

# Development of Terahertz Quantum Cascade Lasers with Novel Quantum Designs

by

Boyu Wen

A thesis  
presented to the University of Waterloo  
in fulfillment of the  
thesis requirement for the degree of  
Doctor of Philosophy  
in  
Electrical and Computer Engineering

Waterloo, Ontario, Canada, 2021

© Boyu Wen 2021

### **Examining Committee Membership**

The following served on the Examining Committee for this thesis. The decision of the Examining Committee is by majority vote.

External Examiner	NAME Benjamin Williams Title Professor
-------------------	---

Supervisor(s)	NAME Dayan Ban Title Professor
---------------	-----------------------------------

Internal Member(s)	NAME Youngki Yoon Title Associate Professor
--------------------	--

	NAME Zbig Wasilewski Title Professor
--	---

Internal-external Member	NAME Pavle Radovanovic Title Professor
--------------------------	---

## **Author's Declaration**

I hereby declare that I am the sole author of this thesis. This is a true copy of the thesis, including any required final revisions, as accepted by my examiners.

I understand that my thesis may be made electronically available to the public.

## Abstract

Terahertz (THz) quantum cascade lasers (QCLs) are arguably the most promising THz radiation source, as they have high output power and efficiency. The main limitation of THz QCLs is the need of a cooling system due to the below-room-temperature operation. Therefore, achieving room temperature operation with good frequency-tuning ability are essential for many potential applications of THz QCLs. This thesis simulates THz QCLs' operation, designs and demonstrates the possible THz QCLs with novel quantum designs that have potential to improve the maximum lasing temperature ( $T_{\max}$ ) and frequency-tuning ability of THz QCLs.

Resonant-phonon (RP) and scattering-assisted (SA) schemes are two widely used THz QCLs quantum schemes that show good temperature performance at different frequency ranges. However, both schemes have limitations, such as the pre-threshold electrical instability in RP designs and thermally activated leakage to continuum in SA designs, which have prevented significant temperature improvements in the last eight years. To overcome those limitations, this thesis develops a six-level hybrid extraction/injection design (HEID) scheme in which the RP and the SA-based injection/extraction are combined within a single  $\text{Al}_{0.15}\text{Ga}_{0.85}\text{As}/\text{GaAs}$  based structure. By utilizing extra excited states for hybrid extraction/injection channels, this design minimizes the appearance of an intermediate negative differential resistance (NDR) before the lasing threshold. The final negative differential resistance is observed up to 260 K, and a high characteristic temperature of 259 K is measured. These observations imply very effective suppression of pre-threshold electrical instability and thermally activated leakage current.

Broadband emission of THz QCL is usually demonstrated at low temperature. One possible way of extending THz QCLs' frequency coverage involves activating multiple-lasing transit channels in the device active region (AR). This thesis discusses a dual-lasing channel THz QCL both theoretically and experimentally. The dual-lasing channel device combines two optical transitions at different frequencies under different device biases. The device exhibits a low threshold current density of 550 A/cm<sup>2</sup> at 50 K and a maximum operating temperature of 144 K. It provides 0.3 THz emission frequency coverage with the lowest reported threshold current density among SA THz QCLs. The combination of a dual-lasing channel operation, low lasing threshold current density, and high-temperature performance makes such devices ideal candidates for broadband emission applications and paves the way for achieving high-temperature-performance THz QCLs with a greater frequency-tuning ability.

The thesis also theoretically investigates two further novel designs. One design addresses an issue observed in the first reported HEID structure for  $T_{\max}$  improvement. The second design is a quasi one-well (Q1W) design consisting of the fewest number of layers (three) and lowest thickness per period (~20



nm) of all the THz QCL quantum structures. The Q1W design exhibits sufficient high optical gain in the positive differential resistance (PDR) region up to a lattice temperature above 250 K.

## Acknowledgements

I would like to thank my supervisor Professor Dayan Ban for his guidance and support over the past 6 years. His knowledge, patience and enthusiasm inspired and encouraged me to persevere the challenges and difficulties in my research. My supervisor's support is not limited to academic research but also to my life as a student. I have also experienced much hardship in my private life during these years, and my supervisor shared with me his life stories and supported me as much as possible. I can say that his support and encouragement is one of the main reasons that my research has not been interrupted.

I would like to express my thanks to Professor Zbigniew Wasilewsk for his knowledge, patience, support on MBE growth for 3 wafers and humor. This work would never have been possible without the support and advice from Professor Wasilewsk. I also want to express my gratitude to the members of Professor Wasilewsk's research team, especially Chris Deimert and Man Chun Tam (Alan). Their professional spirit and knowledge deeply impressed me and helped me.

I would like to thank all the committee members, professor Benjamin Williams, professor Youngki Yoon, professor Dayan Ban, professor Zbigniew Wasilewsk and professor Pavle Radovanovic, for their affiliation.

I am grateful to the current and former members of Professor Ban's research team for their company, discussion and support during my PhD program.

I would like to thank Thomas Grange for lending nextnano. NEGF software for simulation results comparison and verification.

I thank the significant contributions of CFREF-TQT, CFI, Industry Canada, Ontario Ministry of Research & Innovation and Mike & Ophelia Lazaridis. I would also like to express my gratitude to the Quantum Nano Center building manager Chris Kleven for his assistance during Covid19 pandemic and all QNC nanofab staff for their assistance on the microfabrication in clean room.

I also want to express my gratitude to all my friends who supported me. I really enjoy the company and the time spent with them.

## Dedication

To my parents and my wife.

# Table of Contents

Author's Declaration .....	iii
Abstract .....	iv
Acknowledgements.....	vi
List of Figures .....	xi
List of Tables .....	xvi
List of Abbreviations .....	xvii
Chapter 1 Introduction .....	1
1.1 Terahertz Radiation Application.....	1
1.2 Terahertz Radiation Sources .....	4
1.3 Electrically Pumped THz QCLs .....	7
1.3.1 Electronic Engineering of THz QCLs.....	8
1.3.2 Photonic Engineering of THz QCLs .....	19
1.4 Motivation and Research Objectives .....	22
1.5 Thesis Organization .....	23
Chapter 2 Carrier Transport Model for Terahertz Quantum Cascade Lasers .....	25
2.1 Computation of Confined Energy State .....	25
2.2 Electrons Transport Mechanisms .....	27
2.2.1 Tunneling Process .....	27
2.2.2 LO Phonon Scattering.....	28
2.2.3 LA Phonon Scattering.....	30
2.2.4 Interface Roughness Scattering.....	31
2.2.5 Ionized Impurity Scattering .....	32
2.2.6 Electron-Electron Scattering .....	33
2.3 THz QCLs Transport Models .....	34
2.3.1 Rate Equation.....	34
2.3.2 Rate Equation-Based Current Density Calculation Method .....	35
2.3.3 Density Matrix-Based Transport Model .....	36
2.3.4 Density Matrix-Based Current Density Calculation .....	43
2.3.5 Optical Gain Calculation.....	44
2.3.6 Model Validation .....	48
Chapter 3 Experiment .....	52
3.1 Wafer Growth .....	52
3.2 Double-Metal Waveguide THz QCLs Fabrication Procedure .....	53

3.2.1 Wafer Bonding Process.....	54
3.2.2 Lapping and Wet-Etching .....	55
3.2.3 Patterning, Top Metal Deposition, and Lift-Off .....	56
3.2.4 Second Patterning and Dry Etching .....	57
3.2.5 Laser Die Mounting and Wire Bonding.....	58
3.3 Characterization System of THz QCLs .....	59
Chapter 4 Dual Lasing Channel THz QCL Based on Scattering Assisted Injection Scheme.....	63
4.1 Introduction.....	63
4.2 THz QCL Design and Simulation.....	65
4.3 Experiment.....	69
4.4 Results and Discussion .....	70
4.4.1 Dual-Lasing Channel Device Characterization Result.....	70
4.4.2 Comparison between Measured Results and Simulated Results.....	71
4.4.3 Leakage Analysis .....	73
4.4.4 Lasing Spectra.....	74
4.5 Additional Simulation Results by Using nextnano.NEGF Model .....	75
4.6 Reproducibility Verification .....	77
4.7 Conclusion .....	79
Chapter 5 Hybrid Extraction/Injection Design (HEID) Replies on Scattering Assisted Injection and Resonant Phonon Injection .....	80
5.1 Introduction.....	80
5.2 Quantum Design and Simulation Results .....	81
5.3 Results and Discussion for the First HEID Design.....	85
5.3.1 Less Leakage from UL to the Higher Excited State in N+1 Period/module and N Period/module.....	86
5.3.2 Impact of Actual Barrier Profile on J-V Simulation .....	86
5.3.3 Hybrid Extraction/Injection Channel .....	88
5.4 Conclusion .....	89
Chapter 6 Novel THz QCL Designs: Theoretical Investigation .....	90
6.1 Quasi One-Well (Q1W) Design.....	90
6.1.1 Q1W Design Concept .....	91
6.1.2 Actual Q1W Designs .....	94
6.1.3 Investigation of Temperature Sensitivity.....	96
6.1.4 Tolerance on Experimental Variation .....	98

6.1.5 Investigation on critical design parameters.....	99
6.2 Second Hybrid Extraction/Injection Design .....	102
6.2.1 Introduction and Motivation for Making the Second HEID .....	102
6.2.2 Conduction Band Diagram.....	103
6.2.3 Simulation Results and Growth Sheet.....	103
6.3 Conclusion .....	105
Chapter 7 Conclusion.....	107
7.1 Summary of the Work.....	107
7.2 Contributions of the Thesis .....	108
7.3 Future Work .....	111
Letters of copyright permission .....	113
References.....	123
Appendices.....	131
Appendix A.....	131
Appendix B .....	132

## List of Figures

Fig. 1-1. Terahertz gap [1].	1
Fig. 1-2 Terahertz radiation applications. (A) Terahertz radiation detecting a hidden knife in shoes [2] . (B) Terahertz radiation testing high-speed circuit faults [3]. (C) Absorption lines of nucleic acid and Amino acid [4]. (D) absorption lines of amino acid [4] . (E) Detected terahertz radiation from gas cloud in space [5]. (F) wireless system in space where terahertz radiation plays a role [6].	3
Fig. 1-3. MIR QCL based gas laser. The diagram of the working principle in (A), and the simulated gas laser frequency coverage and laser power in (B) [10].	5
Fig. 1-4. Summary of state-of-the-art of compact and gyro THz vacuum electron devices [7].	6
Fig. 1-5. Concept diagram of THz QCLs. (a) Vacuum chamber and cold finger mount. (b) Laser bar with several THz QCLs. (c) Diagram of a laser bar. (d) Simulated electron population on two periods of THz QCL quantum structures, which is highlighted by blue box in (c). (e) Two-well DP structure conduction band structure with the upper lasing states (ULS) in red, the lower lasing state (LLS) in blue, and the injector state (injector) in green [14].	7
Fig. 1-6. Electron-LO phonon interaction and schematic diagram of resonant tunneling. Phonon absorption processes are indicated by cyan arrows, and the phonon emission processes are indicated by green arrows. The solid arrow shows the main process that happens in THz QCL. (a) Possible LO phonon scattering processes between states with energy differences smaller than the phonon energy. (b) Possible LO phonon scattering processes between states with energy differences larger than the phonon energy. (c) Schematic diagram of desired tunneling and wrong tunneling paths across the barrier. Black line indicates the injector state, Orange line indicates the upper lasing state, blue line indicates the lower lasing state, arrows indicate tunneling path, and $\Omega$ indicates the coupling energy.	10
Fig. 1-7. (a) Calculated optical gain of the device V775 below 20 THz. (b) Calculated conduction band diagram of the RP structure device V775. The simulation is performed at temperature of 10 K and electric field of 62 mV (14 kV/cm).	12
Fig. 1-8. Schematic diagram of over-barrier leakage mechanism. Black dots indicate the unescaped electrons and orange dots indicate the escaping electrons, grey arrows indicate possible over-barrier leakage path.	13
Fig. 1-9. Schematic of three-well resonant-phonon structure. (a) Simplified schematic diagram. (b) Actual conduction band diagram of three-well resonant phonon structure from [19].	15
Fig.1-10 Schematic diagram of electron transport. (a) Simplified scattering-assisted injection scheme. (b) Simplified phonon-photon-phonon scheme. (c) Actual scattering-assisted injection scheme conduction band diagram from [34]. (d) Actual 3P scheme conduction band diagram from [33].	16
Fig. 1-11. Schematic diagram of electron transport in two-well direct-phonon design. (a) Simplified diagram. (b) Actual conduction band diagram of two-well direct-phonon design from [14].	17

Fig. 1-12. Summary of temperature performance of different state-of-the-art THz QCL designs. The highest operation temperature is achieved in pulsed mode. Violet squares indicate bond-to-continue designs, blue dots indicate resonant-phonon designs, green triangles indicate scattering-assisted designs, cyan diamond indicates split-well direct-phonon design, and orange stars indicate THz QCL based on material systems other than GaAs/AlGaAs. The data are mainly extracted from [68]. The post-world record of 199.5 K is achieved in 2012 [64], the post-world record of 210.5 K is achieved in 2019[14], and current world record of 250 K is reported in 2021 [104]......19

Fig. 1-13. Waveguide and confinement schematic diagram of (a) SISP waveguide, (b) Double-metal waveguide with its electric field intensity [47]. .....20

Fig. 2-1. Comparison of actual barrier profile (in red) and ideal barrier profile (in blue)......26

Fig. 2-2. Schematic diagram of self-consistent iteration. ....34

Fig. 2-3. Diagrams of important coupling and scattering process between subbands.....36

Fig. 2.4 Energy state labeling in the density matrix-based transport model.....37

Fig. 2-5. DM simulated current-voltage curve comparison. (a) Device V775 (RP) at 8 K. (b) Hybrid extraction/injection design at 70 K. Insets shows corresponding conduction band diagram at design bias. ....49

Fig. 2-6. RE simulation results in comparison with experimental data. (a) 3P structure V962. (b) SA structure G216. (c) The first Hybrid extraction/injection design. Insets shows corresponding conduction band diagram at design bias. ....50

Fig. 2-7. Optical gain calculation of V775 at 200 K. ....51

Fig. 3-1. Diagram of grown THz QCL active region on GaAs substrate. ....53

Fig. 3-2. Schematic diagram of THz QCLs major fabrication steps. ....54

Fig. 3-3 Comparison of bonding interface among the devices. (a) Cu-Cu bonding interface, (b) Au-Au bonding interface, and (c) In-Au bonding interface.....55

Fig. 3-4. Substrate removal process. (a) Mounting wafer on glass pad with wax. (b) Lapping process on lapping machine. (c) Device during wet-etching process. ....56

Fig. 3-5. Top metal mask for patterning in MLA direct-write UV lithography system. Ridge width are 144  $\mu\text{m}$ , 116  $\mu\text{m}$ , 80  $\mu\text{m}$ , 60  $\mu\text{m}$ , and 40  $\mu\text{m}$ . Disk radius is 72  $\mu\text{m}$ . ....57

Fig. 3-6. Mesa etch mask for the second patterning. Ridge width are 152  $\mu\text{m}$ , 122  $\mu\text{m}$ , 82  $\mu\text{m}$ , 58  $\mu\text{m}$ , and 38  $\mu\text{m}$ . Disk radius is 75  $\mu\text{m}$ . ....58

Fig. 3-7. SEM image of fabricated ridges. (a) Au-Au waveguide. (b) Cu-Cu waveguide.....58

Fig. 3-8. Packaged laser bar used in the test. ....59

Fig. 3-9. Chamber design schematics for cryogenic cooler.....60

Fig. 3-10. Circuit board diagram. ....61

Fig. 3-11. Optical path setup for spectra measurement.....62



Fig. 4-1. Dual lasing channel SA-based structure conduction band diagram and scattering time. Conduction band diagram at electric field of 15.4 kV/cm (a) and 17.5 kV/cm (b). (c) Simulation of scattering time between state 3-1 (green), state 2-1 (red), state 3-2 (blue), state 5-4 (brown), and state 4-3 (pink) versus electric field at 30 K [63].....65

Fig. 4-2. Schematic diagram of electric field dependent lasing transition behavior. (a) Single 4-3 lasing transition at  $\sim 15.5$  kV/cm. (b) Dual lasing transition with main lasing transition between state 4 and state 3. (c) Dual lasing transition with main lasing transition between state 3 and state 2. ....67

Fig. 4-3. Current Density-Voltage curve at 40 K and light-current density curve after lasing threshold from 20 K to 130 K [63].....71

Fig. 4-4. Simulation results in comparison with experimental result. (a) Simulated JV curve (orange solid line) in comparison with experimental IV curve at 90 K (black dots). Schottky junction voltage drop of 1.2 V is considered. (b) Simulated optical gain (non-lasing case) between state 4-3 (red) and 3-2 (green dotted line) in comparison between measured Light-Voltage curve (black dots) at 30 K. A Schottky voltage drop of 1.2 V is assumed. Two channels are distinguished by light curve, while the 4-3 transition dominates the first channel and switch to second channel while 4-3 optical gain becomes too weak. [63].....72

Fig. 4-5. Normalized output light power and conduction band diagram of inter-period leakage path. (a) Normalized output light intensity of the first peak (black dots) and the second peak (red dots) in light-current curve versus temperature in plot of  $(1 - P_{out}(T)/P_{outmax})$  with fits (dashed lines). Two peaks show different trends until 113 K. (b) Conduction band diagram shows possible inter-period leakage path from states 4 and 3 to state I. The energy spacing between states 4-I and state 3-I are 5.4 meV and 14.7 meV respectively [63]. 74

Fig. 4-6. Experimental lasing spectra (blue solid lines) in comparison with simulated optical gain of state 4-3 (red dashed line), state 3-2 (green dashed line), and total (black solid line) at 30 K under different bias. The main center frequency of state 3-2 at different bias is marked as red solid line to show contrast with experimental center frequency which is determined by total optical gain [63]. ....75

Fig. 4-7. NEGF model simulated conduction diagram and resolved optical gain at different electric field [55]. .....77

Fig. 4-8. Simulated optical gain in comparison with measured spectra. (a) Simulated peak gain of state 4-3 (green dotted line) and state 3-2 (red dotted line) in comparison with experiment light-voltage result at 30 K (blue dotted line). (b) Simulated gain of state 4-3 at 15.4 kV/cm in comparison with spectrum at 15.4 kV/cm. (c) Simulated gain of state 4-3 and state 3-2 at 17.5 kV/cm in comparison with spectrum at 17.5 kV/cm. (d) Simulated gain of state 4-3 and state 3-2 at  $\sim 16$  kV/cm in comparison with spectrum at  $\sim 16$  kV/cm. Electric field is calculated based on device thickness (10  $\mu$ m) and voltage drop on Schottky junction ( $\sim 1.2$  V). .....79

Fig. 5-1. (a) Conduction band diagram of HEID device at electric field of 12 kV/cm. (b) Hybrid extraction/injection diagram of The HEID device. The first and second channel are labeled by yellow and green arrows in diagram respectively. Layer thickness starting from the extractor barrier are: **44/158/42/70/10/41/23.8/72.5** with barrier labeled in bold and delta doped layer underlined. [43].....83

Fig. 5-2. Simulated function of additional hybrid extraction/injection channels at 70 K. (a) Comparison of extraction tunneling time. (b) Comparison of injection scattering time. (c) Simulated population inversion with/without additional hybrid extraction/injection channels. [43] .....	84
Fig. 5-3. Characterization result of HEID device. (a) L-I-V measurement. (b) Spectra measurement employing Thermo fisher FTIR purged with dry nitrogen gas and Si bolometer as detector. [43] .....	85
Fig. 5-4. Thermally activated leakage analysis. (a) shows extracted characteristic temperature. (b) shows the highest temperature that NDR can be observed on the HEID wafer [43]. .....	86
Fig. 5-5. Impact of accurate barrier profile on simulation results. (a) Plot of the conduction band of HEID device with ideal barrier profile assumption and actual barrier profile in blue/red, respectively. (b) Comparison of simulated J-V curve with ideal barrier profile assumption and actual barrier profile (green/red) and measured J-V curve (blue) at heat sink temperature of 70 K [43]. .....	88
Fig. 5-6. Contribution of two extraction/injection channels. (a) Current contributed by two extraction/injection channels at lattice temperature of 70 K. (b) Measured differential resistance on a 40 $\mu\text{m}$ wide ridge device at heat sink temperature of 30 K and simulated differential resistance at lattice temperature of 30 K [43]. .....	89
Fig. 6-1. Conduction band diagram and resolved 2D optical gain at 100 K. (a) Conduction band diagram of a Q1W design at a design bias of 72 mV. (b) Frequency- and position-dependent optical gain distribution at an electric bias of 72mV and a temperature of 100 K. (c) Conduction band diagram of a Q1W design at zero bias. ....	93
Fig. 6-2. Finalized Q1W design B simulation result by NEGF model. (a) Conduction band diagram. (b) Calculated temperature-dependent optical gain. (c) Voltage-Current density curve at 100 K. ....	94
Fig. 6-3. Temperature dependent calculations using RE model. (a)Temperature dependent optical gain, (b) LO phonon scattering time from $UL_n$ to $LL_n$ (solid line) and scattering time from $LL_n$ to $UL_{n+1}$ (dashed line), and (c) Over-barrier leakage current based on RE model. Blue curve is two-well DP structure G652, green curve is RP structure V775, and red curve is quasi one-well design B. ....	98
Fig. 6-4. Simulation performance of three quasi one-well designs at 100 K. (a) JV curves at 100 K. (b) Optical gain at 100 K. Testcase 3: <b>2.7</b> (25%Al)/ <b>7</b> (7%Al)/10.4(GaAs), testcase 2: <b>1.7</b> (25%Al)/ <b>7</b> (7%Al)/11.4(GaAs), testcase 1: <b>1.7</b> (25%Al)/ <b>8</b> (7%Al)/11.4(GaAs). Layer thickness are shown in nm, and numbers in bold indicates barriers. The underlined layers are averagely doped to achieve sheet density of $3 \times 10^{10} \text{ cm}^{-2}$ . Testcase 1-3 failed during subsequent investigation conducted in section 6.1.3. ....	100
Fig. 6-5. Effect of a parasitic energy level. (a) Conduction band diagram of Q1W testcase 2 at 62 mV. (b) Calculated optical gain of testcase 2 with high energy leakage levels at 250 K. ....	101
Fig. 6-6. Conduction band diagram of the second HEID design. The structure layer thickness: <b>2.9</b> (23%Al)/5.45/ <b>1.2</b> (23%Al)/7.1/ <b>1.7</b> (23%Al)/8.2/ <b>3.2</b> (23%Al)/6.2/5/5 nm. Bold numbers indicate barriers, and underlined number is the doped area. ....	103

Fig. 6-7. NEGF Simulation performance of 2<sup>nd</sup> HEID at 200 K. (a) JV curve at lattice temperature of 200 K. (b) Simulated optical gain at 66mV. ....104

Fig. 6-8. Simulated temperature dependent peak optical gain of 1<sup>st</sup> HEID from RE model (blue solid line), 2<sup>nd</sup> HEID from RE model (red solid curve), and NEGF model [103] (green solid curve). The estimated threshold gain is 22/cm, as indicated by black dashed line. ....104

Fig. 6-9. Growth sheet of the second HEID design. ....105

Fig. A-1. Representative LIV measurement of G405 (a) and G312 (b). G405 exhibits a maximum lasing temperature of 60K and G312 exhibits a maximum lasing temperature of 100K. ....131

Fig. A-2. Measured spectra of G405-2-2-D12 at 20K. The lasing frequency is from ~4.5 THz to 4.8THz. ....132

## List of Tables

Table 1-1. Summary of progress of exploring THz QCLs based on material systems other than GaAs/AlGaAs system. ....8

Table 2-1. Comparison of major scattering time in V775 structures at 150 K and 200 K. ....31

Table 4-1. SA-based THz QCL structure key parameters and performance summary [55]. ....64

Table 4-2. Interface roughness scattering, LO phonon scattering and leakage to continuum calculation for different barrier height at lattice temperature of 160K and applied electric field of 15.5kV/cm. ....68

Table 6-1. Summary of optimized designs. Design A: **3.0**(27%Al)/**8**(7%Al)/8.7(GaAs). Design B: **3.0**(27%Al)/**7.5**(7%Al)/8.0(GaAs). Design C: **3.0**(25%Al)/**8**(7%Al)/8.7(GaAs). Design D: **3.0**(27%Al)/**8.3**(5%Al)/7.5(GaAs). Design E: **3.0**(30%Al)/**7.5**(7%Al)/8.0(GaAs). Layer thickness are shown in nm, and numbers in bold indicate barriers. The underlined layers are averagely doped. The operation bias and electric field is calculated by NEGF model. ....96

Table 6-2. NEGF Simulation results on quasi one-well structures with variation in barrier height and well width. Design B: **3.0**(27%Al)/**7.5**(7%Al)/8.0(GaAs). The simulation is performed using nextnano.NEGF simulation tool from [90] .....98

## List of Abbreviations

3P	phonon-photon-phonon	NDR	negative differential resistance
AR	active region	NEGF	Non-Equilibrium Green's Functions
BTC	bound to continuum	PDR	positive differential resistance
DFB	distributed feedback laser	PSE	power slope efficiency
DFG	differential frequency generation	Q1W	quasi one-well
DI	deionized	QCL	quantum cascade laser
DM	density matrix	RE	rate equation
FP	Fabry-Perot	RP	resonant-phonon
FTIR	Fourier-transform infrared spectroscopy	RT	resonant-tunneling
FWHM	full-width-half-maximum	RWA	rotating-wave approximation
GHz	gigahertz	SA	scattering assisted
HEID	hybrid extraction/injection design	SISP	semi-insulating surface-plasmon
HR-XRD	High-resolution x-ray	TEM	transmission electron microscopy
diffraction		THz	Terahertz
IPA	isopropyl alcohol	TMM	transfer matrix method
LA	longitudinal acoustic	$T_{\max}$	maximum lasing temperature
L-I	Light-current	UL	upper lasing state
LIV	Light-Current-Voltage	VED	vacuum electronic devices
LL	lower lasing state	V-J	voltage-current density
LO	longitudinal optical	WPE	wall-plug efficiency
MBE	Molecular beam epitaxy	$\Delta N/N_{\text{tot}}$	population inversion
MIR	mid-infrared		

# Chapter 1 Introduction

## 1.1 Terahertz Radiation Application

The terahertz (THz) region of the electromagnetic spectrum is defined by the frequency of ~300GHz–10THz, which is located between the microwave radiation and infrared radiation regions. As is shown in Fig. 1-1, an alternative word —terahertz gap— is widely-acknowledged to describe the same frequency range because of the lack of technology of radiation sources at the terahertz region relative to microwave radiation and infrared radiation regions [1].

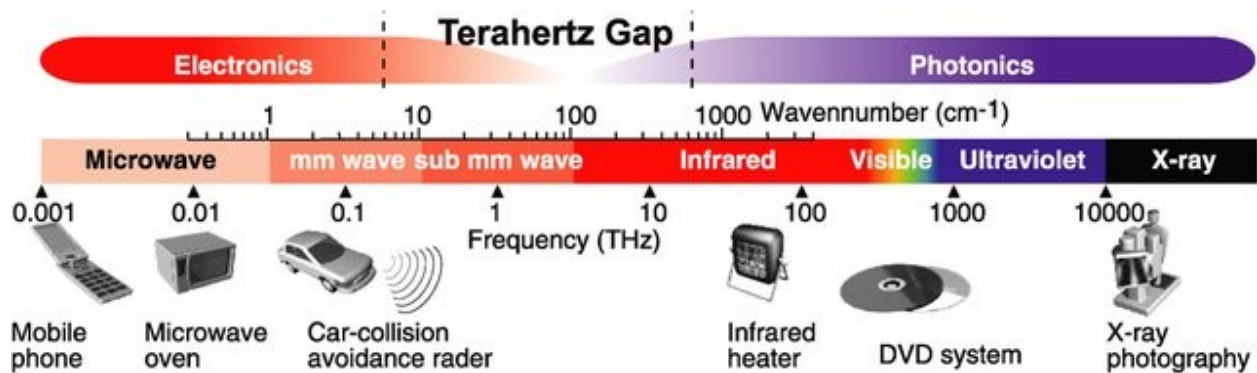


Fig. 1-1. Terahertz gap [1]\*.

The study and applications of terahertz radiation have rapidly expanded in the past decades (Fig. 1-2). Its applications span from fundamental science to everyday use. For example, terahertz radiation is able to penetrate through many common materials such as clothes, plastic and cards. Compared to ultraviolet radiation, the terahertz radiation has relatively lower photon energy, which explains why it is used for security purposes to identify explosive gas and highly excitable species without causing their destruction. An example of a terahertz image of a hidden knife is shown in Fig. 1-2(A) [2]. The non-destructive testing is not only useful in security applications but also semiconductor industry. The fault isolation and defect detection system can achieve higher spatial resolution when using shorter wavelength inspecting radiation. With the development of microelectronics towards higher speed and bandwidth beyond a few gigahertz (GHz), terahertz radiation with a frequency higher than the circuit's operation frequency is required for very high-resolution fault isolation and defect detection systems, as indicated in Fig 1-2(B) [3].

Fig. 1-2(C) and (D) show the figure print absorption lines of chemical species such as nucleic acid and amino acid in the terahertz region. Terahertz radiation can be used in spectroscopy and imaging to

---

\* Reproduced from [K. Fukunaga and M. Picollo, "Terahertz spectroscopy applied to the analysis of artists' materials," *Applied Physics A* **100**(3), 591–597 (2010).], with the permission.

identify chemical species since its photon energy is comparable to molecular vibration, molecular rotation, hydrogen bond and van der Waals energy [4]. Terahertz radiation can achieve a good sensitivity for tumors without causing radiation hazard.

The applications of terahertz also include space exploration. A discovery in 2016 showed that some gas clouds in space emit terahertz radiation corresponding to ionized nitrogen and carbon as shown in Fig. 2(E) [5]. The study of star formation from dust and gas has been greatly enhanced by terahertz technology. In addition, the attenuation of terahertz in space is greatly reduced. Terahertz radiation is considered a promising candidate for space wireless communication because it has higher frequency than microwave and larger tolerance of misalignment than visible light [6]. A wireless system where terahertz radiation plays an important role is shown in Fig 1-2(F).

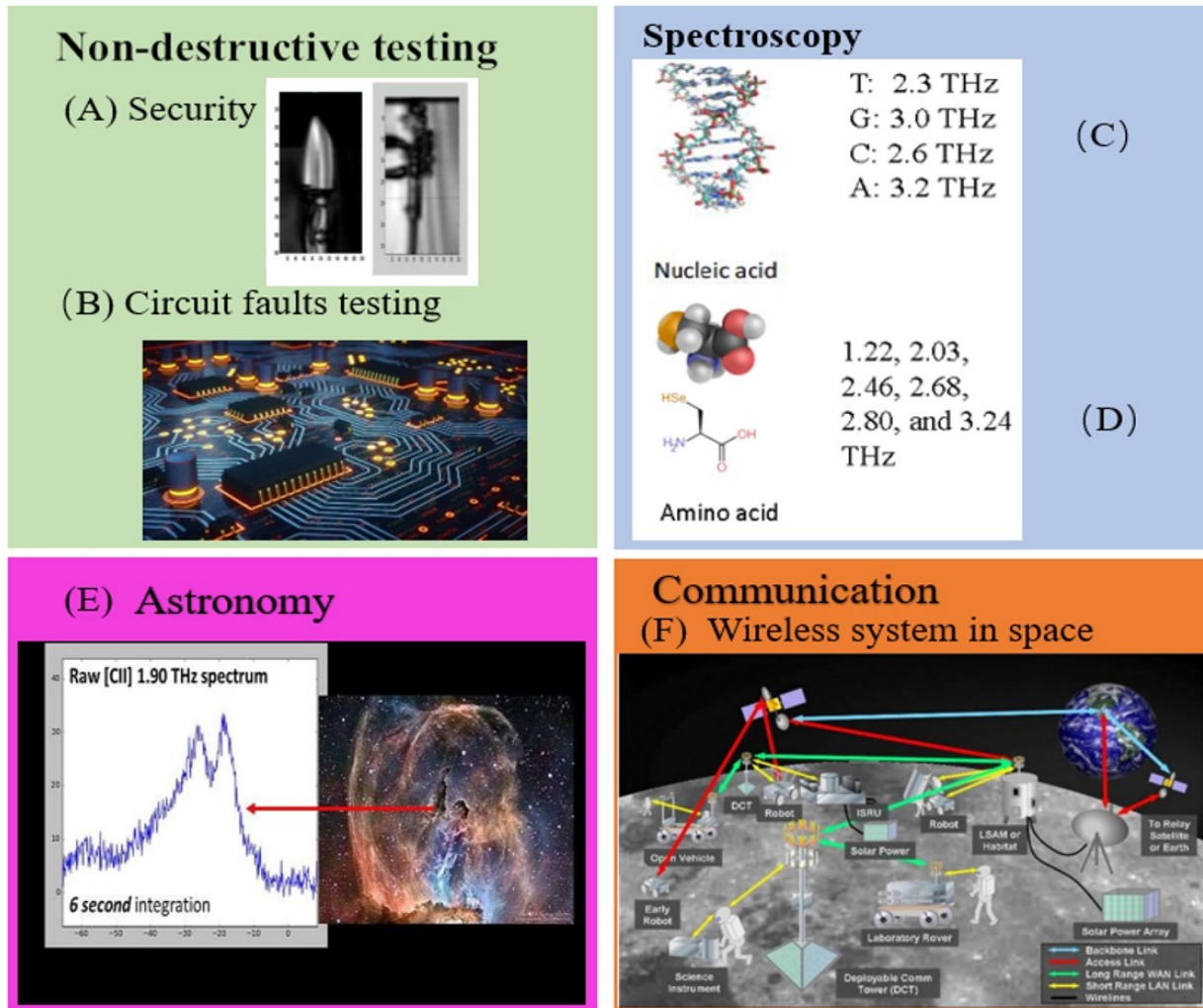


Fig. 1-2 Terahertz radiation applications. (A) Terahertz radiation detecting a hidden knife in shoes [2]<sup>†</sup>. (B) Terahertz radiation testing high-speed circuit faults [3]<sup>‡</sup>. (C) Absorption lines of nucleic acid and Amino acid [4]<sup>§</sup>. (D) absorption lines of amino acid [4]<sup>\*\*</sup>. (E) Detected terahertz radiation from gas cloud in space [5]<sup>††</sup>. (F) wireless system in space where terahertz radiation plays a role [6]<sup>‡‡</sup>.

---

<sup>†</sup> Reproduced from [Q. Song, Y. Zhao, A. Redo-Sanchez, C. Zhang, and X. Liu, "Fast continuous terahertz wave imaging system for security," *Optics Communications*, **282**(10), 2019-2022 (2009).], with the permission.

<sup>‡</sup> Reproduced from [Y. Cai, Z. Wang, and D. Goyal, "Applications of terahertz technology in the semiconductor industry," In *Handbook of Terahertz Technology for Imaging, Sensing and Communications* (Woodhead Publishing, 2013), pp. 624–640.], with the permission.

<sup>§</sup> Reproduced from [X. Yang, X. Zhao, K. Yang, Y. Liu, Y. Liu, W. Fu, and Y. Luo, "Biomedical applications of terahertz spectroscopy and imaging," *Trends in Biotechnology* **34**(10), 810–824 (2016).], with the permission.

<sup>\*\*</sup> Reproduced from [X. Yang, X. Zhao, K. Yang, Y. Liu, Y. Liu, W. Fu, and Y. Luo, "Biomedical applications of terahertz spectroscopy and imaging," *Trends in Biotechnology* **34**(10), 810–824 (2016).], with the permission.

<sup>††</sup> Reproduced from [Delft University of Technology, (2017, Jan 22) "STO2 landed and data secured." <https://phys.org/news/2017-01-sto2.html>], with the permission.

<sup>‡‡</sup> Reproduced from [S. U. Hwu, K. B. de Silva, and C. T. Jih, "Terahertz (THz) wireless systems for space applications," in *2013 IEEE Sensors Applications Symposium Proceedings* (2013), pp. 171–175.], with the permission.



## 1.2 Terahertz Radiation Sources

Due to the numerous applications of terahertz, several explorative researches have been conducted to explore compact terahertz radiation sources that can bridge the terahertz gap with sufficient output power. Four types of terahertz radiation sources are attractive to researchers: (1) laser-based THz sources, (2) THz vacuum electronics, (3) accelerator-based light source, and (4) THz quantum cascade lasers (QCLs) [7]. This section discusses and compares the major advantages and challenges of each type of terahertz radiation sources.

Laser-based THz source requires an additional optical pumping source with emission frequency in the visible or infrared region. Here, the terahertz radiation can be generated by (1) optical rectification using tilted pulse front excitation [8], (2) differential frequency generation using a high nonlinear constant material [9], and (3) gas excitations [10]. The optical rectification techniques use LiNbO<sub>3</sub> or organic crystals to generate terahertz radiation [7]. This can be easily assembled in a lab for basic science study. The drawback of this technique is its low damage threshold of  $\sim 1$  mJ/cm<sup>2</sup> and the small size of the crystal [7]. Differential frequency generation (DFG) technique using mid-infrared (MIR) QCL is widely used for tunable and broadband sources. THz DFG QCLs utilizes two MIR QCLs and mixes two MIR waves in high susceptibility active region to generate terahertz radiation via three-wave mixing effect [9]. THz DFG QCLs are compact and widely tunable, but low conversion efficiency. Gas laser is an early-stage concept for generating terahertz radiation discontinuously in the terahertz region. In a recent study, widely tunable ( $\sim 1$  THz) gas lasers pumped by MIR QCL are reported [10]. Fig. 1-3 from [10] shows the working principle behind the widely tunable gas lasers. The electrons are excited by pumping laser to excited vibrational states and transit between rotational levels by emitting terahertz radiation. A widely tunable N<sub>2</sub>O gas laser has been demonstrated and well explained by theoretical model that considers the pumping transition, dipole-dipole collision, thermal collision and diffusion [10]. The concept is universal for other gas lasers, and it is proposed to achieve 1 THz frequency coverage and milliwatt output intensity. The tuning of MIR QCL emitting frequency and laser cavity pressure is critical in gas laser operation, since those parameters directly affect the transition strength and population inversion between the desired rotational lasing levels.

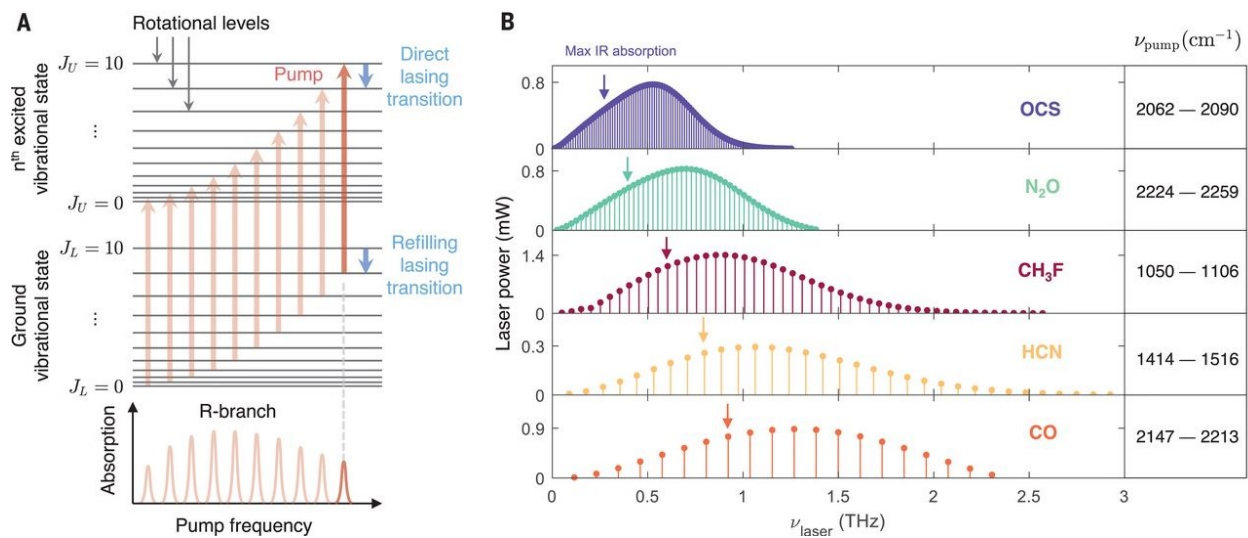


Fig. 1-3. MIR QCL based gas laser. The diagram of the working principle in (A), and the simulated gas laser frequency coverage and laser power in (B) [10]<sup>§§</sup>.

The vacuum electronic device (VED) generates terahertz radiation by accelerating an electron beam through electromagnetic waveguides or cavities. The state-of-the-art gyro THz vacuum electron devices are summarized in Fig. 1-4 [7]. VED converts electrical power into electron kinetic energy to generate radiation, hence it is more compact than the optically pumped laser. The emitting frequency is limited by the fabrication technologies and  $1/\text{frequency}(f)$  power scaling relation, as shown in Fig. 1-4.

<sup>§§</sup> Reproduced from [P. Chevalier, A. Armizhan, F. Wang, M. Piccardo, S. G. Johnson, F. Capasso, and H. O. Everitt, “Widely tunable compact terahertz gas lasers,” *Science* **366**(6467), 856–860 (2019).], with the permission.

### Compact and Gyro THz sources and amplifiers

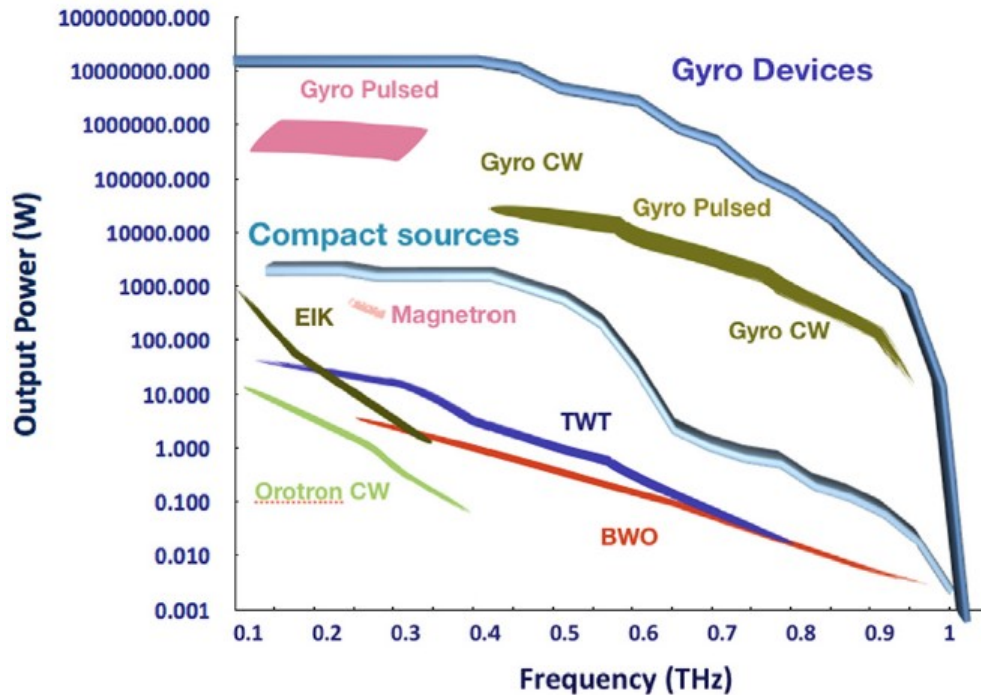


Fig. 1-4. Summary of state-of-the-art of compact and gyro THz vacuum electron devices [7]\*\*.

The accelerator-based sources have been widely used for spectroscopy in the UV to X-ray regime. In the past, researchers have been interested in utilizing the accelerator-based source of the infrared and THz regime. The accelerator-based sources are usually longer than 30 m which is relatively larger than the table-top THz source discussed in previous paragraphs [11]. This source has the advantage of continuous frequency coverage, and high spectral power.

QCLs utilize confined energy states in the conduction band to achieve population inversion. THz QCL was first reported in 2002[11], and has become one of the most promising coherent radiation sources. To date, THz QCLs have been reported to cover frequency of ~1.3-5.4 THz and to produce watt-level output power in pulse mode [8]. The typical size of THz QCLs ridge waveguides is about a few millimeters in length and around one hundred micrometers in width. The major limitation of THz QCL and its application is the operating temperature. Next section will present a thorough discussion on this topic.

\*\*\* Reproduced from [S. S. Dhillon, M. S. Vitiello, E. H. Linfield, A. G. Davies, M. C. Hoffmann, J. Booske, C. Paoloni, M. Gensch, P. Weightman, G. P. Williams, and E. Castro-Camus, "The 2017 terahertz science and technology roadmap," *Journal of Physics D: Applied Physics* **50**(4), 043001 (2017).], with the permission.

### 1.3 Electrically Pumped THz QCLs

The first QCL is demonstrated in mid-infrared (MIR) range in 1994 [13], and the first THz QCL is demonstrated in 2002[11]. Fig. 1-5 shows a simplified diagram of THz QCL from ETH Zurich/D-PHYS, Faist group [14]. Fig. 1-5(a) shows the vacuum chamber and cold finger setup. Fig. 1-5(b) shows the laser bar with THz QCL laser ridges. Fig. 1-5(c) is an enlarged diagram of the laser bar, and the layered structure indicating the active region. In the active region, different layers with different conduction band offset are grown sequentially to create quantum wells, as shown in Fig. 1-5(d), which creates confined energy states. When an electric field is applied across the device, electrons are injected from the negative pole to the positive pole (from left to right in Fig. 5(d)). The entire active region consists of hundreds of repeating periods of layered structures. Each period includes a pair of lasing states and injector section, all periods are equally doped to maintain the electric field over the whole active core in most of the cases. The designed amount of the electric field can lift the injector state (green state in coupling with red state in Fig 1-5(e)) to the same energy as the upper lasing state (red state described as UL in Fig. 5(e)), and electrons are able to transit from the injector state to the upper lasing state via resonant tunneling (RT), while the lower lasing state (blue energy state described as LL in Fig. 1-5(e)) is depopulated to the ground state via scattering. In this way, population is achieved at the designed electric field. Ideally, each available electron would go through one lasing transition between the lasing states and be reprocessed by the injector for the next period, as depicted in Fig. 1-5(d). In real device, the value is characterized by wall-plug efficiency, which is extracted by the ratio of output power to the inject electrical power.

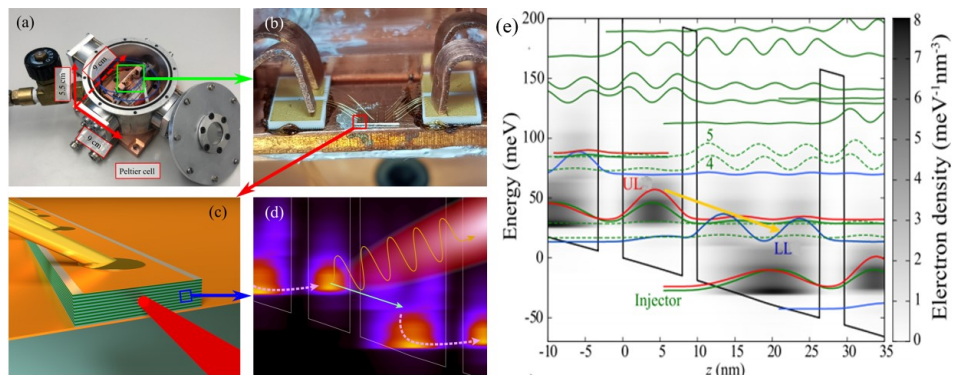


Fig. 1-5. Concept diagram of THz QCLs. (a) Vacuum chamber and cold finger mount. (b) Laser bar with several THz QCLs. (c) Diagram of a laser bar. (d) Simulated electron population on two periods of THz QCL quantum structures, which is highlighted by blue box in (c). (e) Two-well DP structure conduction band structure with the upper lasing states (ULS) in red, the lower lasing state (LLS) in blue, and the injector state (injector) in green [14]<sup>†††</sup>.

<sup>†††</sup> Reproduced from [L. Bosco, M. Franckić, G. Scalari, M. Beck, A. Wacker, and J. Faist, Thermoelectrically cooled THz quantum cascade laser operating up to 210 K, Applied Physics Letters 115(1), 010601 (2019).], with the permission of AIP Publishing

Usually, in comparison to MIR QCLs, THz QCLs are harder to build up high population inversion, because the THz QCLs have energy spacing between the lasing states ( $\sim 4\text{-}25\text{ meV}$ ) closer to the line broadening and longitudinal optical (LO) phonon energy ( $36.5\text{ meV}$  in GaAs). Since the first demonstration of THz QCL in 2002 [12], many efforts have been made in electronic and photonic engineering to further improve the key performance of THz QCLs in relation to the operating temperature, frequency control, beam quality and power efficiency.

### 1.3.1 Electronic Engineering of THz QCLs

To improve the maximum operating temperature of THz QCLs in electronic engineering, several efforts have been made to understand the fundamental electron transport mechanisms and to optimize the existing quantum structural designs. Researchers have also found it necessary to explore new possible quantum structures that might mitigate trade-offs in the state-of-the-art quantum designs and improve the major performance degradation factors. In the past decade, a few promising new quantum structures design schemes, such as resonant-phonon design, two-well direct-phonon designs, extraction-controlled designs, phonon-photon-phonon (3P) designs, scattering-assisted designs, and split-well direct-phonon designs, have been demonstrated and studied [14-35]. As a result of continuous improvement, the latest designs, such as the two-well direct-phonon, scattering-assisted, resonant-phonon, and split-well direct-phonon are among the best schemes with operating temperatures in the main frequency range from  $\sim 2\text{ THz}$  to  $\sim 4\text{ THz}$ . Furthermore, in comparison with other material system-based THz QCL, GaAs/AlGaAs material system-based THz QCL shows the best temperature performance in the experiments so far. The effort on exploration of material system other than GaAs/AlGaAs system is briefly summarized in table 1-1.

Material system	Advantages compared to GaAs/AlGaAs system	Disadvantages compared to GaAs/AlGaAs system	Current stage of development	Reference
GaSb/AlGaSb	Weaker electron-LO phonon interaction	Inter valley scattering is more significant	Theoretical study	Ref. 36
InGaSb/AlInGaSb	Weaker electron-LO phonon interaction; lower intervalley scattering than GaSb well	Growth difficulties and large interface roughness.	Theoretical study	Ref. 37
InGaAs/GaAsSb/InP	Al free system can reduce oxidation issue; Lower effective electron mass; stronger band non-parabolicity	Larger interface roughness	142K	Ref. 38
Si/SiGe or Ge/SiGe	Larger LO phonon energy	Growth difficulties	Demonstrated electroluminescence	Ref. 39
InGaAs/InAlAs	Lower electron effective mass	Conduction band offset is relatively high which is not necessarily to THz QCL	122K	Ref. 40
ZnO/MgZnO	Larger LO phonon energy,	Very material demanding for growing cascade structure in THz domain	Demonstrated electroluminescence	Ref. 41
GaN/AlGaN	Weaker LO phonon interaction	Growth difficulties	Observed spontaneous emission.	Ref. 42

Table 1-1. Brief summary of progress on exploring THz QCLs based on new material systems other than GaAs/AlGaAs system.

### 1.3.1.1 Important Mechanics in THz QCL Design Stages

In THz QCL design stages, a few mechanisms are considered to play important roles, such as RT (including the designed tunneling and wrong tunneling), longitudinal optical phonon scattering, subband absorption (negative optical gain) at terahertz frequency range, elastic scattering (including interface roughness scattering and impurity scattering), electron-electron interaction, over-barrier leakage, thermal distribution, and electrical stability. This section gives a brief account of these mechanics, and the simulation approaches will be discussed in chapter 2.

#### 1.3.1.1.1 Longitudinal Optical Phonon Scattering and Resonant Tunneling (RT)

Longitudinal optical phonon scattering is one of the most significant scattering processes that occur in the THz QCL structure. The optical phonon energy is constant when the wave vector is close to zero, and the atomic displacement is in the same direction as the energy transfer in longitudinal mode. Electron's transport occurs from one subband to another subband by emitting/absorbing phonons. Fig. 1-6 shows a schematic diagram of the electron-phonon interactions is shown in Fig. 1-6. The phonon absorption processes are indicated by cyan arrows, while the phonon emission processes are indicated by green arrows. Fig. 1-6(a) indicates the electron-phonon interaction between the lasing states. Energy spacing between the lasing states in THz QCLs is smaller than phonon energy. In the maximum operating temperature and typical doping density of THz QCL, the major LO phonon scattering processes, which are marked with solid arrows, show the fastest rate in the calculation, Hot electrons from the upper lasing state UL (in orange) can be scattered into the lower lasing state (LL) (in dark blue) by emitting a LO phonon (indicated by green arrow). This process can significantly damage population inversion and is considered to be one of the main factors that limit high temperature performance of THz QCLs. Fig. 1-6(b) indicates the electron-phonon interaction between LL (in cyan) and injector state (in black). The energy spacing between LL and the injector is larger than phonon energy. The possible phonon absorption processes are indicated with cyan arrows, and possible phonon emission processes are indicated with green arrows. The major process which is indicated with solid green arrow between LL and the injector state explains that electrons in LL can be effectively depopulated to the injector state via the phonon emission process. This process is widely used in THz QCL designs for fast depopulating LL.

Resonant tunneling is the key phenomenon used in THz QCL to transport electrons between different periods. When two confined energy levels are aligned, electrons can tunnel through the barriers until the two aligned energy states attain a similar population. To maximize the available electrons for the designed transport path and efficiency, it is important to ensure the electrons to be transported through the desired tunneling path. Fig. 1-6(c) illustrates an example of desired tunneling path and a wrong one. Since the UL and LL in THz QCLs are close to each other with a small energy spacing of 4-20 meV, which is

approximate to the line broadening ( $\sim 4\text{-}6$  meV), electrons can be injected from the injector level to either UL or LL. The injection rate is determined by the coupling energy ( $\Omega_{iu}$  for the injection to UL,  $\Omega_{il}$  for the injection to LL). It is important to ensure that the wrong injection ( $\Omega_{il}$ ) is low enough to achieve population inversion over the lasing states. In a similar way, any undesired parasitic energy levels close to the injector state and the UL in terms of energy can be a leakage path via resonant tunneling. Fig. 1-6 (c) is an example of parasitic energy level ( $P1_{n/n+1}$ ), the grey bar indicates wrong tunneling channel from the injector. It is also important to check if any parasitic energy levels have strong coupling energy ( $\Omega_{ip}$ ) with the injector and UL.

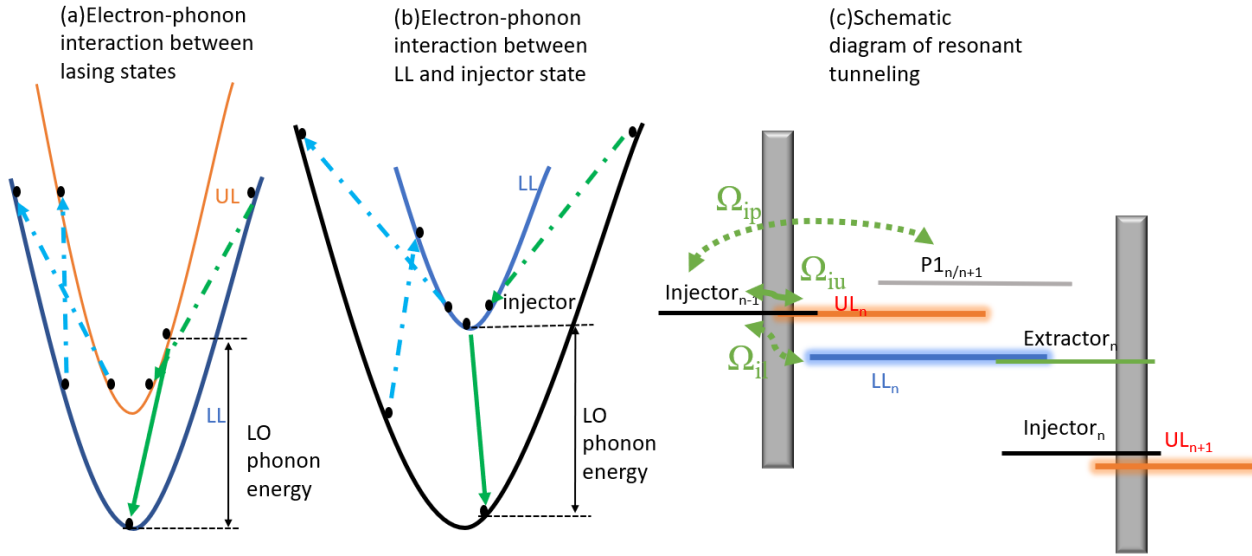


Fig. 1-6. Electron-LO phonon interaction and schematic diagram of resonant tunneling. Phonon absorption processes are indicated by cyan arrows, and the phonon emission processes are indicated by green arrows. The solid arrow shows the main process that happens in THz QCL. (a) Possible LO phonon scattering processes between states with energy differences smaller than the phonon energy. (b) Possible LO phonon scattering processes between states with energy differences larger than the phonon energy. (c) Schematic diagram of desired tunneling and wrong tunneling paths across the barrier. Black line indicates the injector state, Orange line indicates the upper lasing state, blue line indicates the lower lasing state, arrows indicate tunneling path, and  $\Omega$  indicates the coupling energy.

### 1.3.1.1.2 Non-radiative Elastic Scattering and Electrical Stability

Elastic scattering can affect electrons distribution. Interface roughness scattering is induced near the interface between the barrier and well, the scattering rate is dependent on the conduction band offset and the interface quality. The conduction band offset is determined by Al concentration in THz QCLs based on the AlGaAs/GaAs system, while the interface quality is determined by the mean interface roughness height and mean correlation length. In general, a lower conduction band offset and better interface quality would result in a lower interface roughness scattering. Impurity scattering is induced by dopants

embedded in the active region of THz QCLs. The scattering rate is dependent on the dopants' location and doping density while the quantum structure remains the same. Electron-electron interaction on the subbands can cause screening effect and Fermi-Dirac distribution. In terms of the quantum structure, a high population of electrons and dopants can cause conduction band bending effect (for further discussion, see chapter 2).

It is critical to avoid designing operation bias of THz QCLs in a negative differential resistance region. Failing to do so would result in a significant electrical instability and inability to lase in the device [29]. The design bias (at which the device is lasing) should be within a positive differential resistance region (PDR) to ensure that the lasing operation can successfully be initiated and maintained stably.

#### 1.3.1.1.3 Possible Absorption of Terahertz Radiation

The target of designs with the lasing states is to achieve a high population inversion, that is, higher electron population in UL than LL and for a high positive optical gain between the lasing states. However, additional absorption can be created by tens of meV spaced subbands without population inversion, these subbands can absorb the terahertz radiation emitted from the lasing states and mitigate the positive optical gain in the active region. An example of calculated optical gain and absorption in the terahertz range for a device named as V775 from [64] is shown in Fig. 1-7. The major absorption is from the energy states that are spaced around a LO phonon energy. Absorption from other subbands, for example the absorption centered  $\sim 6$  THz in Fig. 1-7, may reduce the peak gain in lasing frequency due to the broadening of absorption peak. Due to the fast-scattering rate of LO phonon scattering, electrons at the higher energy state are efficiently depopulated to the ground state resulting in a very high absorption peak centered around 9 THz. Due to the short life time, the FWHM of the absorption peak could be large, thereby reducing the optical gain in the targeting lasing frequency of  $\sim 1-5$  THz. Therefore, it is necessary to look at the net optical gain that takes into account the optical emission and absorption among all the



major confined energy states in the active region.

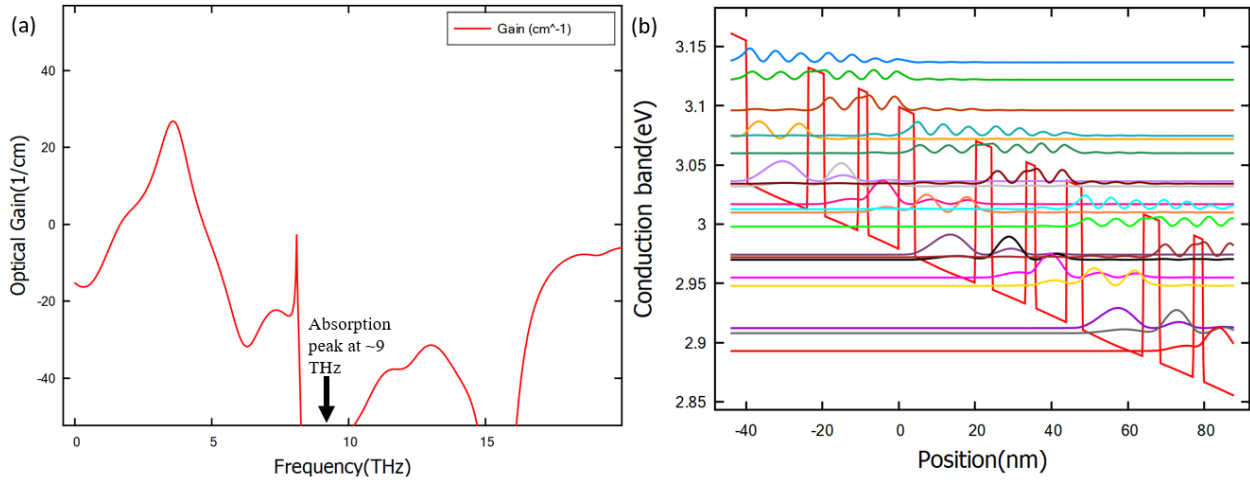


Fig. 1-7. (a) Calculated optical gain of the device V775 below 20 THz. (b) Calculated conduction band diagram of the RP structure device V775. The simulation is performed at temperature of 10 K and electric field of 62 mV (14 kV/cm).

#### 1.3.1.1.4 Over-Barrier Leakage

Over-barrier leakage has been recently recognized as an important performance degradation factor in state-of-the-art diagonal THz QCLs [44]. Despite the THz QCL quantum design to effectively reduce LO phonon scattering and wrong tunneling, at higher temperature, hot electrons can still escape from the UL via over-barrier leakage. Fig. 1-8 shows a schematic diagram of over-barrier leakage, orange dots indicate electrons that are able to escape to the continuum band over-barrier, and black dots indicate electrons with insufficient activation energy to escape. Two paths are available for electrons to escape to the continuum band: (1) hot electrons with enough energy can go over barrier and escape; (2) electrons with relatively low energy can scatter to high energy parasitic levels near barrier edge and tunnel through the barrier edge to the continuum band. Once an electron escapes, its mobility is greatly increased. This will produce a significant leakage current until the escaped electron is recaptured by subsequent periods. The most common way to reduce over-barrier leakage is to increase the barriers' height by adding more Al concentration on the barrier region. It has been reported that increasing barrier height could increase the interface roughness scattering, and high interface roughness scattering is a detrimental phenomenon in

THz QCLs [22].

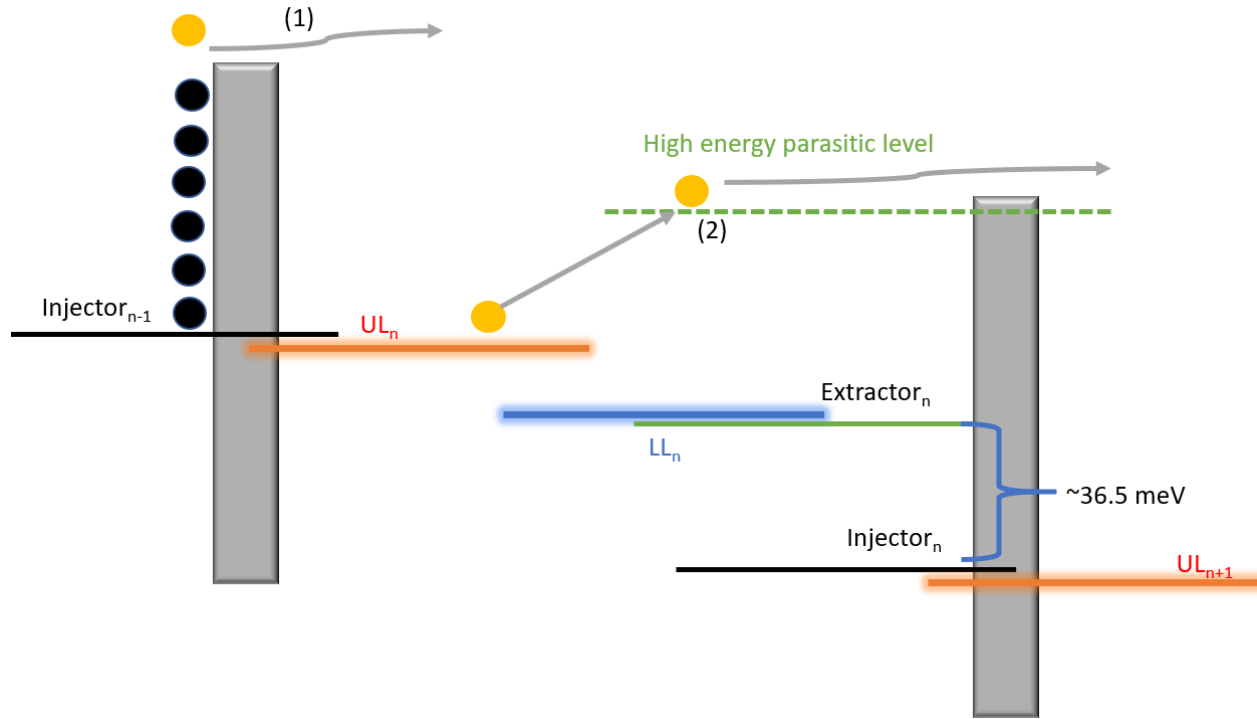


Fig. 1-8. Schematic diagram of over-barrier leakage mechanism. Black dots indicate the unescaped electrons and orange dots indicate the escaping electrons, grey arrows indicate possible over-barrier leakage path.

### 1.3.1.2 Resonant-Phonon Structure

The three-well RP based design scheme is among the earliest developed designs. It is currently one of the most promising structures that can achieve maximum operating temperature above 190 K [19]. The other scheme that can achieve operating temperature above 190 K is 2-well direct-phonon scheme [14], and it is discussed in the next section. Fig. 1-9 is a schematic diagram of the three -well resonant-phonon based design. Electrons are directly injected into the UL and extracted from the LL via the RT process. Electrons on the extractor state can easily transit to the injector state via LO phonon scattering.

In the resonant-phonon based design, three potential performance degradation factors are often encountered: (1) the appearance of an intermediate NDR before the lasing threshold [19, 29], (2) the disappearance of the final NDR at high temperatures due to leakage to the continuum band [15, 17, 18] and (3) the theoretical limit of maximum population inversion ( $\Delta N/N_{\text{tot}}$ ) of 50% in resonant-tunneling (RT) based injection/extraction processes. The appearance of an intermediate NDR before the lasing threshold constrains the operation and design of the device, especially in diagonal designs with low oscillator strength, by preventing the device from reaching the designed lasing bias [19, 29]. This effect results from the presence of significant current-leakage channels, such as a resonant-tunneling leakage

from the injector state to the extractor state before the designed lasing bias [19, 29]. One way to reduce the appearance of the intermediate NDR is to ensure that the current density at the lasing threshold is significantly higher than any local current density peaks at the lower bias. The observation of a well-defined final NDR is considered as a strong evidence that the device does not suffer a significant leakage due to higher energy states and continuum at the measurement temperature [17, 18]. However, the final NDR usually disappears at higher temperatures and the threshold current density dramatically increases due to the fact that electrons possess enough kinetic energy to enable leakage path to continuum at high temperature, and consequently degrade the performance of the device [17-20, 22]. One way to reduce this leakage is to increase the barrier height for better carrier confinement. A high barrier height can potentially increase the interface roughness scattering rate [15, 22,30,31, 44]. Various barrier height growth is often very demanding for a typical molecular beam epitaxy (MBE) growth system. E. Dupont pointed that the direct pump scheme via RT process in a typical three-well resonant-phonon based THz QCLs results in a theoretically limited maximum population inversion ( $\Delta N/N_{\text{tot}}$ ) of 50% [27]. In RT based injection and extraction scheme, the electron population on the UL is limited and similar to the injector state, meaning that UL can hold only half of the available electrons; similarly, the LL and extractor state hold a similar electron population which means that only half of the accumulated electrons on LL can be extracted.

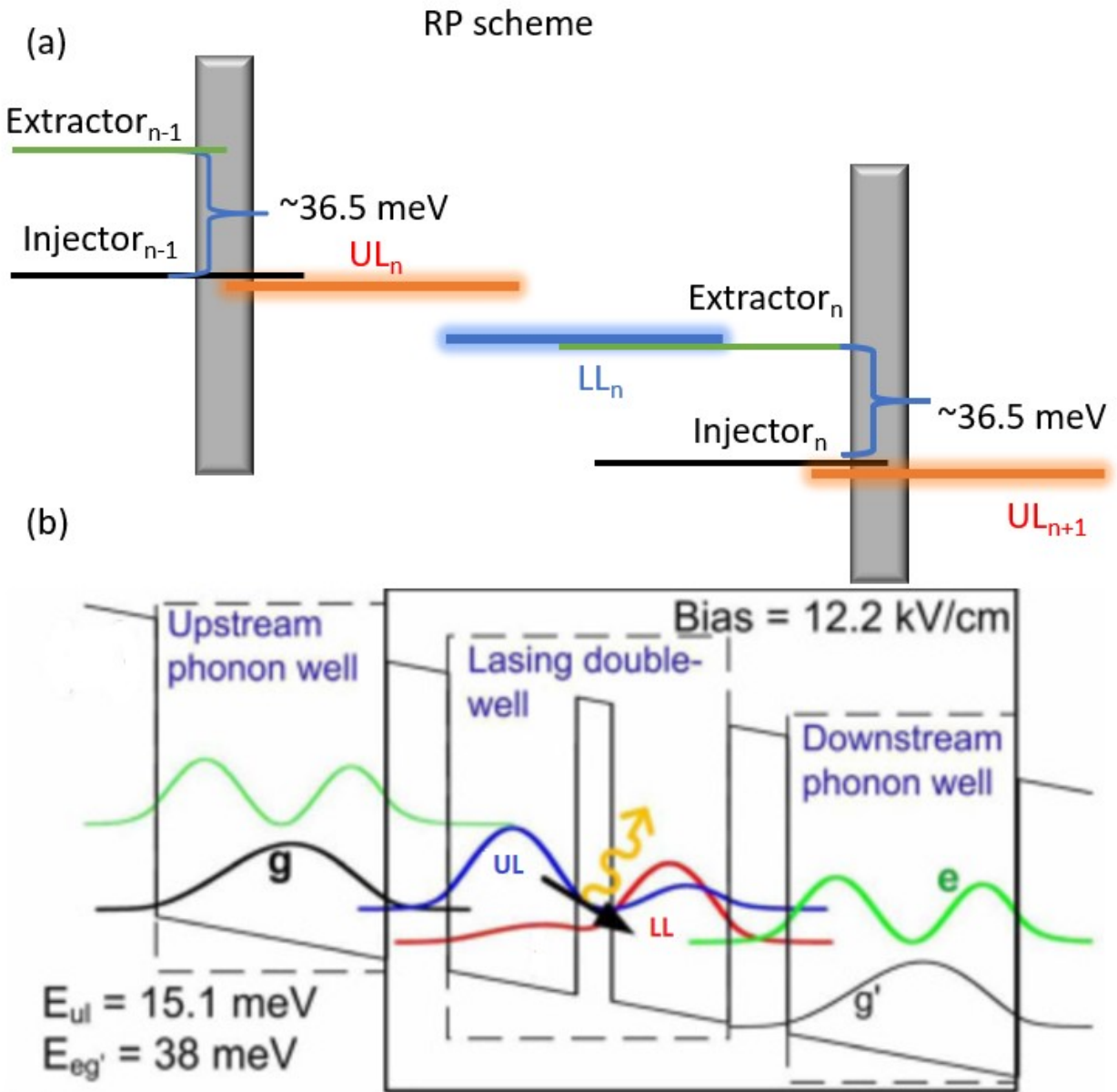


Fig. 1-9. Schematic of three-well resonant-phonon structure. (a) Simplified schematic diagram. (b) Actual conduction band diagram of three-well resonant phonon structure from [19]<sup>†††</sup>.

### 1.3.1.3 Scattering Assisted Structure

To partially overcome the limitations aforementioned in the last paragraph, some SA and 3P injection/extraction schemes have been explored with a resulting better performance than the RP-based

<sup>†††</sup> Reproduced from [S. Fathololoumi, E. Dupont, Z. R. Wasilewski, C. W. I. Chan, S. G. Razavipour, S. R. Laframboise, S. Huang, Q. Hu, D. Ban, and H. C. Liu, "Effect of oscillator strength and intermediate resonance on the performance of resonant phonon-based terahertz quantum cascade lasers," Journal of Applied Physics 113(11), 113109 (2013).], with the permission of AIP Publishing

design when the main lasing frequency is lower than 3.5 THz [32-34]. Fig. 1-10 (a) shows a schematic diagram of the scattering-assisted (SA) design, and Fig. 1-10(b) shows a schematic diagram of the phonon-photon-phonon (3p) design. In the SA design, electrons are extracted from the LL to the extractor via the RT process, but electrons are injected from the injector to the UL via direct LO phonon scattering. In the 3P design, electrons are extracted and injected via direct LO phonon scattering only. SA-based and 3P-based devices require a relatively higher electric field for lasing threshold and show higher leakage to continuum, therefore a relatively higher barrier height and lower energy spacing between the lasing states are preferred [32-34].

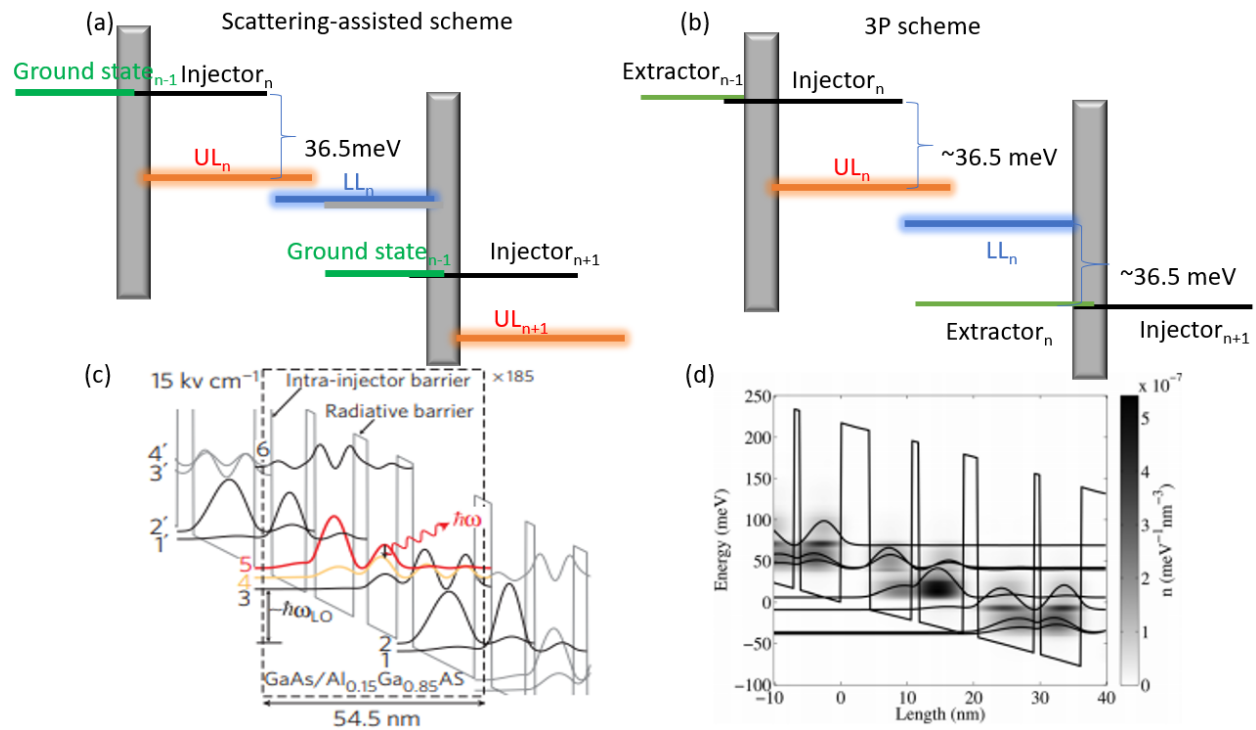


Fig.1-10 Schematic diagram of electron transport. (a) Simplified scattering-assisted injection scheme. (b) Simplified phonon-photon-phonon scheme. (c) Actual scattering-assisted injection scheme conduction band diagram from [34]<sup>§§§</sup>. (d) Actual 3P scheme conduction band diagram from [33]<sup>\*\*\*\*</sup>.

<sup>§§§</sup> Reproduced from [S. Kumar, C. W. I. Chan, Q. Hu, and J. L. Reno, "A 1.8-THz quantum cascade laser operating significantly above the temperature of  $\hbar \omega/kB$ ," *Nature Physics* 7(2), 166–171 (2011).], with the permission.

<sup>\*\*\*\*</sup> Reproduced from [S. G. Razavipour, E. Dupont, S. Fatholouloumi, C. W. I. Chan, M. Lindskog, Z. R. Wasilewski, G. Aers, S. R. Laframboise, A. Wacker, Q. Hu, and D. Ban, "An indirectly pumped terahertz quantum cascade laser with low injection coupling strength operating above 150 K," *Journal of Applied Physics* 113(20), 203107 (2013).], with the permission of AIP Publishing

### 1.3.1.4 Two-Well Direct-Phonon Design and Split-Well Direct-Phonon Design

The two-well direct-phonon design contains only two wells in one period. Electrons are extracted from the LL via direct LO phonon scattering and then injected into the UL via RT as described in Fig. 1-11 [14]. The two-well direct-phonon design is the narrowest THz QCL quantum design that has been experimentally demonstrated, each period consists of four layers (two barriers and two wells). The split-well direct-phonon design has the same electron transport scheme as the two-well direct-phonon, but with one thin barrier added in the phonon well to further assist electron's extraction from the LL to the extractor/injector state via interface roughness scattering. The current world record of highest operation temperature of THz QCLs in pulse mode is achieved by two-well direct-phonon design [104].

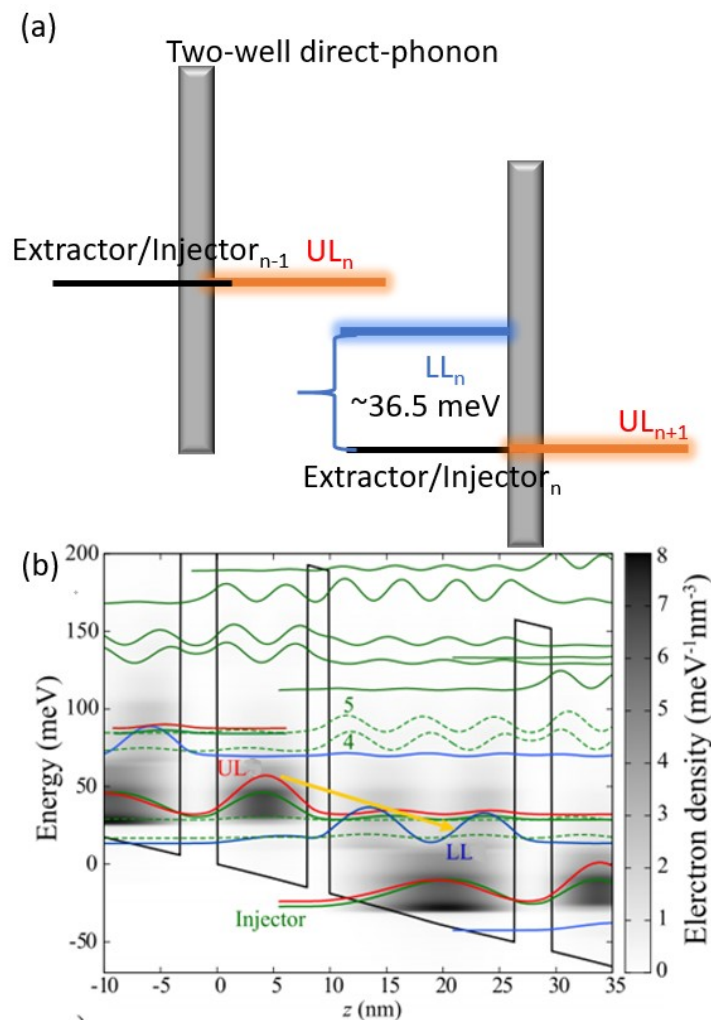


Fig. 1-11. Schematic diagram of electron transport in two-well direct-phonon design. (a) Simplified diagram. (b) Actual conduction band diagram of two-well direct-phonon design from [14]<sup>††††</sup>.

<sup>††††</sup> Reproduced from [L. Bosco, M. Franckić, G. Scalari, M. Beck, A. Wacker, and J. Faist, Thermoelectrically cooled THz quantum cascade laser operating up to 210 K, Applied Physics Letters 115(1), 010601 (2019).], with the permission of AIP Publishing

A summary of published designs of THz QCL with the best operation temperatures at different frequencies is listed in Fig. 1-12. An obvious performance degradation is observed when the lasing frequency is lower than 3 THz or higher than 4 THz in Fig. 1-12. There are multiple reasons for the frequency dependent performance variation. When the lasing frequency is lowered, the energy spacing between the lasing states becomes closer to the line broadening ( $\sim 4$  meV). The closely spaced lasing states can result in poorer selective injection/extraction and higher non-radiative scattering. In the past, the thermal distribution law of  $k_B T = \hbar \omega$  is believed to be an important limiting factor, but multiple latest designs have shown the operation temperatures above the value predicted by  $T \approx \hbar \omega / k_B$  [34]. At higher lasing frequency, the largely separated lasing states can result in more leakage to continuum from the upper lasing state and more LO phonon emission, because electrons in the UL can gain sufficient activation energy to reach barrier edge and a LO phonon energy of 36.5 meV above the energy of the LL.

Furthermore, a clear design dependent performance difference is observed in Fig. 1-12. This suggests that the electron transport scheme plays an important role in the temperature performance. Scattering-assisted designs show better performance at frequencies lower than 3 THz, while the resonant-phonon and the two-well direct-phonon designs show good performance above 3 THz.

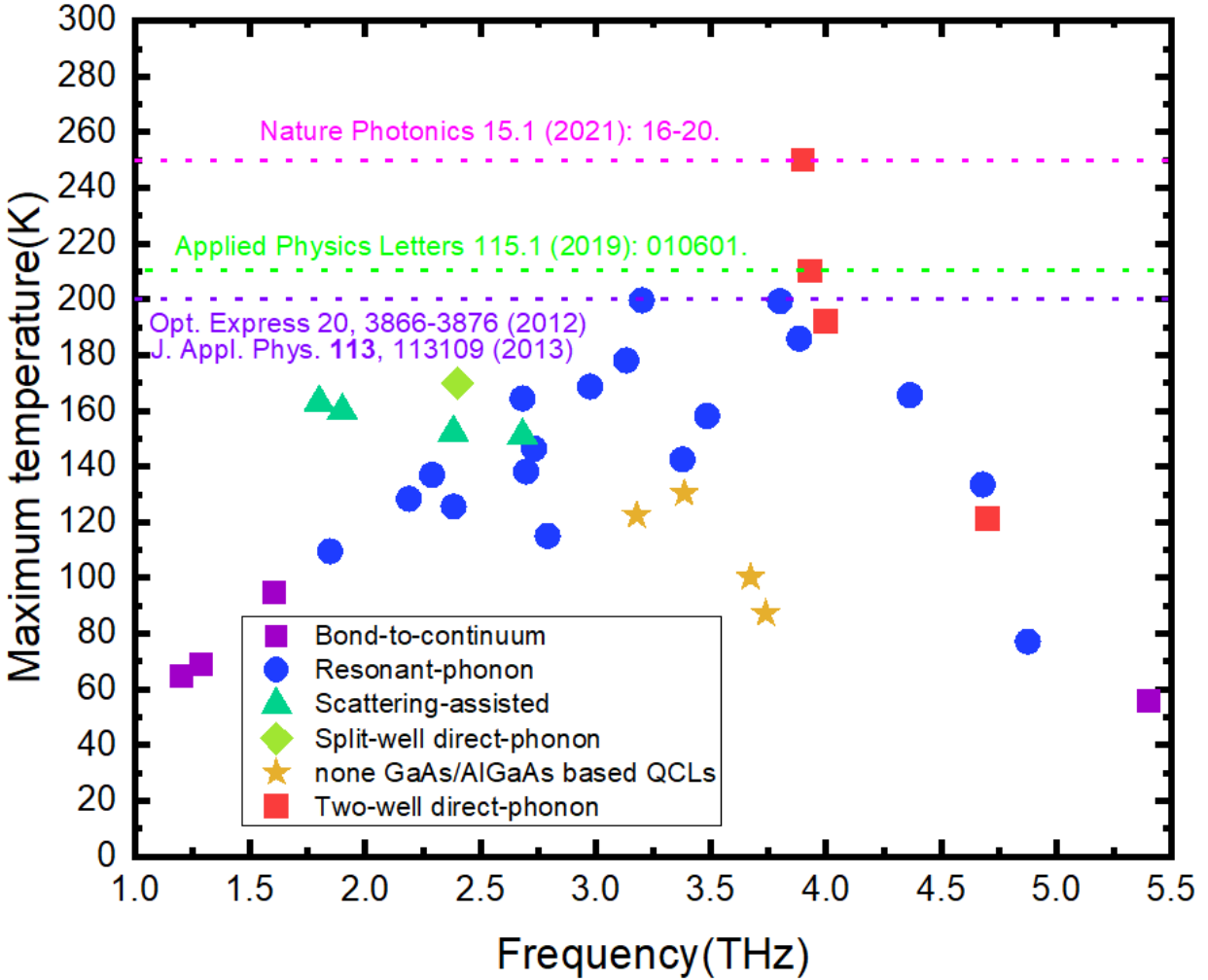


Fig. 1-12. Summary of temperature performance of different state-of-the-art THz QCL designs. The highest operation temperature is achieved in pulsed mode. Violet squares indicate bond-to-continue designs, blue dots indicate resonant-phonon designs, green triangles indicate scattering-assisted designs, cyan diamond indicates split-well direct-phonon design, and orange stars indicate THz QCL based on material systems other than GaAs/AlGaAs. The data are mainly extracted from [68]. The post-world record of 199.5 K is achieved in 2012 [64], the post-world record of 210.5 K is achieved in 2019[14], and current world record of 250 K is reported in 2021 [104].

### 1.3.2 Photonic Engineering of THz QCLs

The emission characteristics can also be improved by photonic engineering. This section presents a brief review of waveguides and recent photonic engineering progress of THz QCLs.

Fabry-Perot (FP) ridge waveguide is the most common waveguide used in THz QCLs. The first invented THz QCL is fabricated into a semi-insulating surface-plasmon (SISP) ridge waveguide [12]. A SISP waveguide contains a high doped layer between the active region (AR) and semi-insulating GaAs substrate. The high doped layer is 0.2-0.8  $\mu\text{m}$  thick with a doping density of  $\sim 10^{18} \text{ cm}^{-3}$  [12]. The high



doped layer has negative dielectric constants and supports surface plasmon. Together with the top metal layer, confinement of light can be achieved in the active region. The mode can be extended into GaAs substrate. SISP waveguide can achieve relatively better beam and high-power emission due to lower facet reflectivity; however, it can result in free carrier loss in the substrate.

In order to improve the mode confinement, a double-metal waveguide has been developed. A double-metal waveguide utilizes two metal layers to sandwich the active regions in between via the metallic wafer bonding method. Compared to the SISP waveguide, the double-metal waveguide provides a more robust frequency independent confinement with confinement factor  $\Gamma \approx 1$ . Threshold gain obeys the rule:

$$g_{th} = (\alpha_w + \alpha_m) / \Gamma, \quad (1.1)$$

where  $\alpha_w$  is the waveguide loss and  $\alpha_m$  is the mirror loss. The double-metal ridge waveguide THz QCL achieves lower threshold gain than that of SISP. Fig. 1-13 shows a schematic diagram of the SISP waveguide and double metal waveguide [47]. Fig. 1-13(a) shows the SISP waveguide and its electric field intensity, (b) shows the double metal waveguide and its electric field intensity.

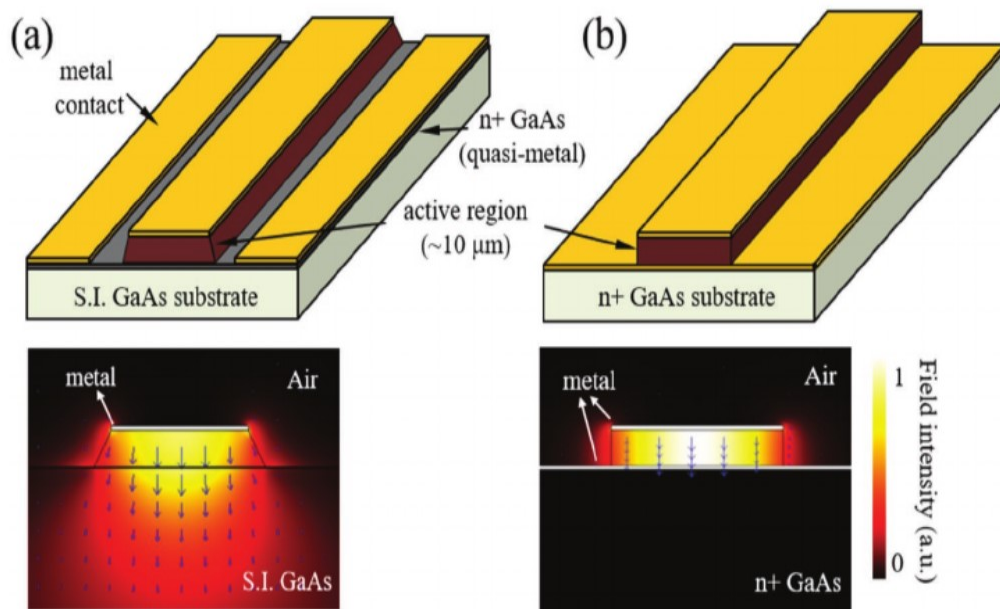


Fig. 1-13. Waveguide and confinement schematic diagram of (a) SISP waveguide, (b) Double-metal waveguide with its electric field intensity [47]††††.

Waveguide material selection is an important factor in the performance of THz QCL. The first fabricated double metal waveguide is Au-Au. Its selection is due to the stable property of Au. Cu is also

†††† Reproduced from [Y. Zeng, B. Qiang, and Q. J. Wang, "Photonic engineering technology for the development of terahertz quantum cascade lasers," *Advanced Optical Materials* **8**(3), 1900573 (2020).], with the permission of AIP Publishing

another suitable double-metal waveguide THz QCLs because it has low waveguide loss and slightly higher thermal conductivity than the Au-Au waveguide [45].

One important emission characteristic is frequency control which includes single mode emission and frequency tuning. Since the radiation wavelength of THz is longer than the thickness of the active region, and the coupling of the mode with the top metal layer is strong, distributed feedback grating can be directly applied to the top metal via photolithography and liftoff process. The feedback frequency can be determined by the following equation:

$$\lambda_0 = 2n_{\text{eff}}\Lambda/n, \quad (1.2)$$

where  $\Lambda$  is the grating period,  $n_{\text{eff}}$  is the effective refractive index in the medium, and  $n$  is the integral number which is defined as diffraction order. The hybrid second- and fourth-order Bragg gratings implemented to THz QCL have achieved a single mode emission and high peak output power of 170 mW with a slope-efficiency of 993 mW/A [46]. Photonic crystal can be used as an external reflection mirror that reflects radiation with certain frequencies falling in its narrow reflectivity band [47]. Active resonators can also be developed using photonic crystals by a 2D periodical patterning. By tuning the air hole size that was drilled through the top metal, a photonic bandgap can be formed and the band-edge resonances can be aligned to gain spectral range of the active region for single-mode operation [47].

Frequency tunability is important for the applications of THz. This paragraph reviews four methods of frequency tuning and their state-of-the-art results. (1) The conventional frequency tuning, which is by modulating the heat-sink temperature, since temperature affects the effective dielectric constant. Due to the relatively low maximum operating temperature of THz QCLs, temperature modulation is usually inefficient. For example, the single-mode distributed feedback laser (DFB) QCL can be tuned only by 12 GHz from temperature 8–97 K [47, 48]. (2) Dielectric layer deposition onto a DFB structure for a larger range of effective dielectric constant tuning [49]. This method achieves mode-hop-free tuning over 57 GHz. (3) External cavity tuning schemes. By changing the external cavity length, the cavity mode can be tuned. This method, when applied to vertical-cavity surface-emitting THz QCLs, achieves 20% (650 GHz) continuous fractional single-mode tuning centered on ~3.47 THz [50]. (4) With the development of the microelectromechanical system, a metal or dielectric layer can be precisely moved in the lateral direction of the laser cavity to efficiently adjust the effective dielectric constant. This method achieves around 330 GHz tuning range centered at 3.85 THz in [51].

Power efficiency is highly desirable in semiconductor lasers for sensing and spectroscopy applications. Power efficiency can be characterized by wall-plug efficiency (WPE) and power slope efficiency (PSE). WPE describes the electrical-to-optical power conversion efficiency. This value can be improved to achieve a low leakage current and thicker THz QCL AR growth for more repeating periods. By growing

an AR of 24  $\mu\text{m}$  in thickness, which is significantly higher than the normal thickness of 10  $\mu\text{m}$  in THz QCL AR, a high output power of 2.4 W and high efficiency of  $\sim 90$  photons per injected electron at 10 K is achieved from a conventional SISP waveguide [52]. The other parameter PSE is defined as

$$\text{PSE} = \eta_{\text{ce}} \times \alpha_{\text{R}} / (\alpha_{\text{W}} + \alpha_{\text{R}}), \quad (1.3)$$

where  $\eta_{\text{ce}}$  is the detector power collection efficiency,  $\alpha_{\text{R}}$  is the radiative loss, and  $\alpha_{\text{W}}$  is the waveguide loss. Two strategies can be employed to enhance PSE via photonic engineering: improve collection efficiency and radiative loss. Collection efficiency can be improved in multiple folds by adding a lens directly in front of the emitting facet. By adding a silicon hyper-hemispherical lens to the facet of the double-metal ridge waveguide, a narrow far-field beam pattern is formed and a high PSE of 296 mW/A is achieved [53]. To improve the out-coupling efficiency (radiative loss), the effective emitting facet can be increased while maintaining phase coherence between the emitting apertures. A vertical-external-cavity surface emitting laser used in a THz QCL achieved a peak power of 1.35 W at 6 K with a high PSE of 767 mW/A [54]. In a recent study, a phase-locked terahertz plasmonic laser array has been employed to coherently combine several short-length cavities. A high peak output power of 2.03 W is detected at 58 K with a PSE of  $1566 \pm 10$  mW/A [55].

## 1.4 Motivation and Research Objectives

Over the past decade, efforts have been made to improve the performance of THz QCLs, as is reviewed in previous section. Compared to the quick improvement in frequency control and power efficiency, temperature performance improved by  $\sim 50$  K for 9 years: from 199.5 K (in 2012 [64]) to 210.5 K (in 2019 [14]) and 250 K (in 2021 [104]). As photonic-engineered THz QCLs usually exhibit lower temperature performance than simple ridge waveguides, a higher temperature performance of THz QCLs is needed for many applications. As shown in Fig. 1-12, the maximum operating temperature is highly dependent on the quantum structure design. Research conducted in the past eight years has focused on optimizing existing quantum structures, such as RP designs, phonon-photon-phonon (3P) designs, and SA designs [14-21, 23-28, 63, 92-93]. However, each design has advantages and limitations regarding temperature performance at different frequency regions, as reviewed in section 1.3.1. The three-well RP-based design scheme has been demonstrated in the early stage. It displays a promising structure for achieving maximum-operating temperatures above 190 K [64]. However, three potential performance degradation factors are often encountered in this design: (1) the appearance of an intermediate NDR before the lasing threshold [29, 64]; (2) the absence of the final NDR at high temperatures due to leakage to the continuum band [17, 18, 20]; and (3) the theoretical limit of maximum population inversion ( $\Delta N/N_{\text{tot}}$ ) of 50% in resonant-tunneling (RT)-based injection/extraction processes [27]. Some SA and 3P

injection/extraction schemes have been explored, and demonstrated better performance than the RP-based designs when the main lasing frequency is lower than 3.5 THz [32-34, 63]. However, SA and 3P-based devices require a relatively high applied electric field for the lasing threshold and show higher leakage to the continuum [27, 32-34]. Therefore, exploring new designs schemes that combine different existing design schemes could overcome some of the aforementioned limitations in the existing designs and pave the path for possible higher temperature performance.

Given the nano scale of each layer in THz QCLs, a high accuracy of device growth and fabrication is needed. Designing shorter period THz QCLs quantum structures compared with existing designs could simplify the design and increase the experimental error tolerance to reach higher temperature operations.

Broadband emission is another challenge that remains to be addressed. This is not only essential for biomolecular terahertz spectroscopy but is also critical for other applications, such as frequency comb operations and tunable THz emission sources [70,71]. Bound-to-continuum (BTC)-based quantum designs are most commonly used for broadband terahertz emissions. However, the broadband gain in BTC structures is often achieved at the expense of device operating temperature performance. As a result, BTC-based THz QCLs lase at lower temperatures than THz QCLs based on RP or SA designs at similar frequencies [68]. Bidirectional THz QCL is another option for achieving broadband emission. Light emission at different terahertz frequencies can be observed when the device bias polarity is switched [72]. Dual color emission operation under the same device bias polarity has been observed when the devices are biased at different voltages. The dual lasing channel design under the same device bias polarity can be integrated with different design schemes and bidirectional THz QCL technique to potentially achieve multiple-lasing frequency over a large frequency range at high temperature.

The goal of this project can be broken down into four major steps: (1) implement and optimize transport models to simulate and optimize THz QCL designs; (2) study and optimize existing design schemes, such as RP- and SA-based schemes; (3) explore new design schemes that combine the RP scheme and SA scheme into one quantum structure; (4) study the dual-lasing channel behavior in THz QCLs; (5) experimentally investigate the performance of the proposed designs; (6) explore the new designs with a shorter period than the existing THz QCL designs.

## **1.5 Thesis Organization**

This thesis presents new designs, including dual-lasing channel design, short-period design, and hybrid extraction/injection designs (HEID) that combine the RP scheme and SA scheme in a single quantum design. First, the density matrix (DM) and rate equation (RE) simulation models are implemented in MATLAB code. Both RP and SA schemes are studied with DM and RE models. Second, a hybrid

extraction/injection scheme is proposed as the first attempt of such a scheme. Third, wafer growth, fabrication, and characterization are performed to experimentally verify the performance of the design.

- Chapter 2 discusses the numerical model implemented for the simulation and design.
- Chapter 3 describes the details of the experiment, including growth, fabrication, and characterization.
- Chapter 4 discusses the design with dual-lasing channels. The results suggest that a THz QCL quantum design that allows for two lasing channels could be a promising approach for achieving wide frequency coverage, low threshold current density, and good device performance at low frequency ( $\sim 2.5$  THz). The results pave the way for designs whose main emission frequency can be electrically tuned over a frequency range of 1 to 5 THz.
- Chapter 5 discusses the design and analysis of the hybrid extraction/injection channels design. The first hybrid extraction/injection design shows good performance with an Au-Au waveguide, comparable to other state-of-the-art THz QCL designs at 2.8 THz. Considering the efforts devoted to optimize the RP- and SA-based designs, the first hybrid extraction/injection design displays potential for high-temperature performance after further quantum design and device optimization.
- Chapter 6 presents the theoretical designs of the novel THz QCL structures. The second hybrid extraction/injection design with two channels are achieved at the same electric field is designed to improve the electrical stability. The narrowest design with only three layers per period is theoretically investigated by using different simulation models.
- Chapter 7 outlines the conclusions and contribution of this thesis and discusses future work.

## Chapter 2 Carrier Transport Model for Terahertz Quantum Cascade Lasers

This chapter describes the build of carrier transport models. THz QCLs' operation highly relies on the electrons transport between subbands via designed transport channels. Due to the multiple confined energy states in each quantum well, it is hard to directly measure which subband contributes the current flowing between quantum wells. It is important to develop the carrier transport models to simulate and study the THz QCLs' operating performance. To simulate carrier transport in terahertz Quantum Cascade Lasers (THz QCLs), density matrix- (DM) and rate equation-based (RE) models are implemented. Fundamental parameters including conduction band shape, confined energy states, major scattering process, and band bending due to the many-body effect are calculated in the models.

### 2.1 Computation of Confined Energy State

In THz QCL, quantum wells are created in the conduction band owing to the band gap difference between  $\text{Al}_x\text{Ga}_{1-x}\text{As}$  and GaAs. Growth of  $\text{Al}_x\text{Ga}_{1-x}\text{As}$  /GaAs is relatively mature; therefore, researchers usually assume that the quantum wells and quantum barriers are formed sharply in the interface [56,57].

However, recent transmission electron microscopy (TEM) results show that the interface is not chemically sharp, and some transition areas actually depend on interface roughness [56]. This nonuniform phenomenon is previously overlooked in many THz QCL simulations due to its difficult implementation, this thesis, however, proves it to be important during simulation and design. The narrowest barriers and wells in THz QCL can be less than 10 Å and comparable to the typical interface roughness with a mean height of ~3 Å in  $\text{Al}_x\text{Ga}_{1-x}\text{As}$ /GaAs-based THz QCL. The actual conduction band profile rather than the perfect square barriers profile should be adopted. The actual conduction band profile can be produced based on the equation suggested in [57]:

$$x_n = \frac{x_0}{1+e^{-(d+(N_w/2))/L^l}} \quad \text{for } d < 0 \text{ (lower interface),} \quad (2.1)$$

$$x_n = \frac{x_0}{1+e^{-(d+(N_w/2))/L^u}} \quad \text{for } d > 0 \text{ (upper interface),} \quad (2.2)$$

where  $x_0$  is the mole fraction of actual Al,  $d$  is the position,  $d = 0$  is the desired center of the barrier,  $N_w$  is the nominal barrier width, and  $L$  is the interface roughness mean height for the upper and lower interface. The interface roughness on both sides of the barrier is usually assumed to be the same, but it is actually different depending on the growth direction. The roughness at the interface grown from GaAs to  $\text{Al}_x\text{Ga}_{1-x}\text{As}$  (the lower interface) is generally smoother than the one grown from  $\text{Al}_x\text{Ga}_{1-x}\text{As}$  to GaAs (the upper interface). In the simulation, the interface roughness mean height is assumed around 1.5 Å / 3 Å for the lower

interface/upper interface, respectively. A comparison of the actual and ideal barrier profiles is shown in Fig. 2-1.

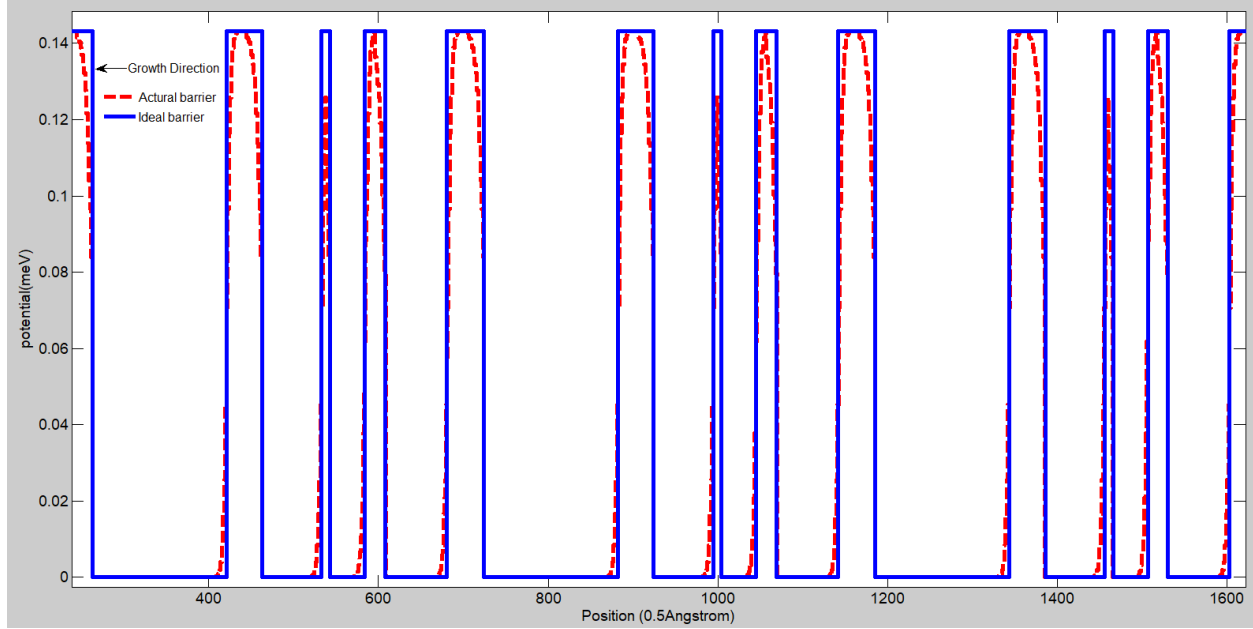


Fig. 2-1. Comparison of actual barrier profile (in red) and ideal barrier profile (in blue).

Once the quantum well is created in the conduction band, eigen energies and the corresponding wavefunctions can be calculated by solving Schrödinger's equation. The transfer matrix method (TMM) is suitable for simulation purpose here. The general solutions to Schrödinger's equation are given as:

$$\psi(z) = A \times \exp(+k \times z) + B \times \exp(-k \times z) \quad (E < V), \quad (2.3)$$

and

$$\psi(z) = C \times \sin(k \times z) + D \times \cos(k \times z) \quad (E > V), \quad (2.4)$$

where (A,B,C,D) are coefficients,  $k$  is the wave vector defined as  $\frac{2|V-E|m^*}{\hbar^2 k^2}$ ,  $V$  is the local potential energy, and  $E$  is energy. The whole calculated quantum wells can be divided by a small distance of  $\sim 0.5$  angstrom, and the TMM is applied on each interface. For example, at the interface from a low potential position ( $V < E$ ) to a high potential position ( $V > E$ ), the TMM can be written as

$$M_1 = \begin{pmatrix} \sin(k \times a) & \cos(k \times a) \\ \frac{k \times \cos(k \times a)}{m_w^*} & \frac{-k \times \sin(k \times a)}{m_w^*} \end{pmatrix} \quad (2.5)$$

$$M_2 = \begin{pmatrix} \exp(k \times a) & \exp(-k \times a) \\ \frac{k \times \exp(+k \times a)}{m_b^*} & \frac{-k \times \exp(-k \times a)}{m_b^*} \end{pmatrix} \quad (2.6)$$

$$M_1 \begin{pmatrix} A \\ B \end{pmatrix} = M_2 \begin{pmatrix} C \\ D \end{pmatrix}. \quad (2.7)$$

In addition, the transfer matrix for this interface can be written as  $M = M_1^{-1}M_2$ . The box boundary condition is applied to the end of the calculation region. In other words, the element  $M(2,2)$  in the overall transfer matrix ( $M$ ) is zero with eigen energies. This boundary condition can be used to determine eigen energies and corresponding wave functions.

Nonparabolicity is included in the  $\text{Al}_x\text{Ga}_{1-x}\text{As}/\text{GaAs}$ -based quantum well model by inducing a nonparabolicity coefficient,  $\gamma = 4.9 \times 10^{-19} m^2$  [58]. Energy-dependent effective mass can be expressed as

$$m_w^*(E) = m_w^* \times \left(1 + \frac{E}{E_{gw}}\right), \quad (2.8)$$

$$m_b^*(E) = m_b^* \times \left(1 - \frac{V-E}{E_{gb}}\right), \quad (2.9)$$

where  $E_{gw} = \frac{\hbar^2}{2m_w^*\gamma}$  and  $E_{gb} = \frac{\hbar^2}{2m_b^*\gamma}$  are the energy gap between the conduction band and the light-hole valence band in the well and barrier regions, respectively [58]. Generally, eigen states are calculated by including 1-3 periods of a QCL structure.

Nonparabolic effect renders conduction band states non-orthogonal, therefore, normalization should consider valence band states [59] as

$$\langle \varphi_c | \varphi_c \rangle + \langle \varphi_v | \varphi_v \rangle = 1, \quad (2.10)$$

where  $\varphi_c$  is conduction band state wavefunction and  $\varphi_v$  is valence band state wavefunction.

In [60], R. Terazzi translates this condition into a special normalization with only conduction band states as

$$\langle \varphi_c | 1 + T | \varphi_c \rangle = 1 \quad (2.11)$$

$$T = \frac{E_c(z)}{E_c(z) + E_g(z)}. \quad (2.12)$$

## 2.2 Electrons Transport Mechanisms

### 2.2.1 Tunneling Process

Electrons can transport via tunneling and scattering processes. To calculate the tunneling process, coupling energy between states in resonance is needed. The coupled wave function  $\varphi$  Hamiltonian is defined as



$$H|\varphi\rangle = H(\alpha|\varphi_L\rangle + \beta|\varphi_R\rangle) \text{ and } H = p_z \frac{1}{2m(z,E)} p_z + V(z), \quad (2.13)$$

where  $m(z, E)$  is the position and energy-dependent effective mass,  $\varphi_L$  is wavefunction on the left side of interface,  $\varphi_R$  is the wavefunction on the right side of interface, and  $V(z)$  is the conduction band potential, as shown in Fig. 2-1. Coupling and detuning energy can be calculated between states in two different wells by solving the equation

$$\langle\varphi_{L,R}|H\varphi\rangle = \langle\varphi_{L,R}|H(\alpha|\varphi_L\rangle + \beta|\varphi_R\rangle) = ER_{L,R} \cdot \begin{pmatrix} \alpha \\ \beta \end{pmatrix}, \quad (2.14)$$

which can be rewritten as  $E = R^{-1} \begin{pmatrix} \langle\varphi_L|H\varphi_L\rangle & \langle\varphi_R|H\varphi_L\rangle \\ \langle\varphi_R|H\varphi_L\rangle & \langle\varphi_R|H\varphi_R\rangle \end{pmatrix}$  with  $R = \begin{pmatrix} R_L \\ R_R \end{pmatrix} = \begin{pmatrix} \langle\varphi_L|\varphi_L\rangle & \langle\varphi_L|\varphi_R\rangle \\ \langle\varphi_R|\varphi_L\rangle & \langle\varphi_R|\varphi_R\rangle \end{pmatrix}$ .

Coupling energy ( $\hbar\Omega$ ) will be expressed as  $(E_{12} \times E_{21})^{0.5}$  and detuning energy ( $\Delta$ ) as  $E_{11} - E_{22}$ , where subscript note in E indicates the row and column of element in matrix. Coupling and detuning energy will be used in the DM and the RE models to compute the coherent tunneling process.

## 2.2.2 LO Phonon Scattering

Four major scattering transitions are being considered in the model: ionized impurity scattering, interface roughness scattering, LO phonon scattering, and electron-electron scattering. Longitudinal acoustic phonon scattering is optional because of its low scattering rate and high computing time. Every type of scattering, except electron-electron scattering, is summarized in terms of Fermi's golden rule. An electron in an initial state  $|i\rangle$  experiences a time-dependent perturbation, and can be scattered into final state  $|f\rangle$  with different energy. The scattering time of this process can be described by

$$\frac{1}{\tau_i} = \frac{2\pi}{\hbar} \sum |\langle f|\check{H}|i\rangle|^2 \delta(E_f^e - E_i^e). \quad (2.15)$$

In semiconductors, atoms vibrate around an equilibrium position. Based on the vibration phase and direction, four phonons are determined: transverse acoustic, transverse optical, longitudinal acoustic (LA), and longitudinal optical (LO). The acoustic mode describes atom vibration in the phase while optical mode describes neighboring atoms vibrate in the opposite direction. In other words, acoustic phonon energy varies with wave vector  $K$ , while optical phonon energy is a constant when the wave vector is close to zero. longitudinal mode describes atomic displacement in the same direction as that of the energy transfer, and transverse mode describes atomic displacement in the perpendicular direction to the energy transfer. Hence, longitudinal phonons can assist electron transport between layers in THz QCLs.

One of the most important reasons for the failure of THz QCL to operate at high temperature (room temperature) is thermally activated LO phonon scattering. By following the work of Harrison Paul and

Alex Valavanis, the following equations in this section (2.2.1) are quoted and rewritten from [59], LO phonon density can be calculated by

$$N_0 = \frac{1}{\exp\left(\frac{\hbar\omega}{kT}\right) - 1}, \quad (2.16)$$

where  $\hbar\omega$  is the LO phonon energy ( $\sim 36$  meV in GaAs), and T is the electron temperature. QCL is a 2D system, and the electron wave function can be described by components along the z-axis (growth direction) and the x-y direction (plane of the layers) [59]. The electron-phonon interaction Hamiltonian is the sum of the dispersionless phonon wave vector in the  $K_z$  and  $K_{x-y}$  direction, which can be expressed as

$$\check{H} = e \sum_{K_{xy}} \sum_{K_z} \left( \frac{\hbar\omega P}{2(|K_{xy}|^2 + |K_z|^2)} \right)^{\frac{1}{2}} \frac{e^{-K_{xy}r_{xy}}}{A^{\frac{1}{2}}} \frac{e^{-K_z z}}{L^{\frac{1}{2}}} \quad (2.17)$$

with

$$P = \left( \frac{1}{\epsilon_\infty} - \frac{1}{\epsilon_s} \right) \left( N_0 + \frac{1}{2} \pm \frac{1}{2} \right). \quad (2.18)$$

The minus sign represents absorption, the plus sign represents phonon emission, and parameters  $\epsilon_\infty$  and  $\epsilon_s$  are 10.92 and 12.9, respectively. The initial electron energy ( $E_i^e$ ) and final energy ( $E_f^e$ ) after electron-phonon interaction satisfies equations

$$E_i^e = E_i + \frac{\hbar^2 k_i^2}{2m^*} \pm \hbar\omega \quad (2.19)$$

And

$$E_f^e = E_f + \frac{\hbar^2 (k_i^2 + K_{xy}^2 + 2k_i K_{xy} \cos(\alpha))}{2m^*}, \quad (2.20)$$

where  $E_i$  and  $E_f$  represents the energy band minima of the initial and final state, and angle  $\alpha$  is the angle between the initial wave vector and the phonon vector. By substituting into equation (2.2.3), the scattering rate at the specific initial wave vector can be expressed as

$$\frac{1}{\tau_{k_i}} = \frac{\pi e^2 \omega P}{(2\pi)^3} \int \int \frac{(\int \varphi_f^*(z) e^{-iK_z z} \varphi_i(z) dz)^2}{K_{xy}^2 + K_z^2} \times \delta(E_f^e - E_i^e) dK_z dK_{xy}. \quad (2.21)$$

To reduce the number of variables,  $K_{xy}$  can be expressed by  $k_i$  as

$$K_{xy} = k_i \cos(\alpha') \pm \sqrt{k_i^2 \cos^2(\alpha') - \frac{2m^*(E_f - (E_i \pm \hbar\omega))}{\hbar^2}} \quad (2.22)$$

with

$$\alpha' = \pi - \alpha. \quad (2.23)$$

After taking the integral over angle  $\alpha'$ , the LO scattering rate at certain initial wave vector can be simplified as

$$\frac{1}{\tau_{k_i}} = \frac{\pi e^2 \omega P}{(2\pi)^3} \int \frac{(\int \varphi_f^*(z) e^{-iK_z z} \varphi_i(z) dz)^2}{\sqrt{K_z^2 + 2K_z^2 (2k_i^2 - \frac{2m^* E_f - (E_i \pm \hbar\omega)}{\hbar^2}) + (\frac{2m^* (E_f - (E_i \pm \hbar\omega))}{\hbar^2})}} dK_z \quad (2.24)$$

with

$$k_i > \sqrt{\frac{2m^* (E_f - (E_i \pm \hbar\omega))}{\hbar^2}}. \quad (2.25)$$

To consider the screening effect,  $K_z$  in equation 2.2.1.9 can be replaced by  $K_z^2 (1 + \frac{\lambda_s^2}{K_z^2})^2$ , and  $\lambda_s^2 = \frac{e^2}{\pi \hbar^2 \epsilon_s} \sum_j [\frac{\sqrt{2m^* E_j} m^* f^{FD}(E_j)}{\pi \hbar}]$  is the inverse screening length as described by Park's screening model [59,61].

### 2.2.3 LA Phonon Scattering

Longitudinal acoustic phonon scattering can have some impact on electron transportation in THz QCLs. Different from LO phonon which has constant energy at the phonon wave vector close to zero, LA phonon energy linearly depends on the phonon wave vector when the wave vector is close to zero. The angular frequency can be described by

$$w_s = v_s K, \quad (2.28)$$

where  $v_s = 5117.0 \text{m}^{-1}$  is the velocity of sound. By applying Fermi's golden rule similar to LA phonon as described in the textbook [59], LA phonon scattering can be calculated by

$$\frac{1}{\tau_{k_i}} = \frac{D_A}{2\rho v_s (2\pi)^2} \left( N_0 + \frac{1}{2} \pm \frac{1}{2} \int \int_0^{2\pi} \int \frac{(\int \varphi_f^*(z) e^{-iK_z z} \varphi_i(z) dz)^2 \times (-k_i \cos(\theta) + \sqrt{k_i^2 \cos^2(\theta) - \frac{2m^* \Delta E}{\hbar^2}}) \times \sqrt{(-k_i \cos(\theta) + \sqrt{k_i^2 \cos^2(\theta) - \frac{2m^* \Delta E}{\hbar^2}})^2 + K_z^2}}{2\sqrt{k_i^2 \cos^2(\theta) - \frac{2m^* \Delta E}{\hbar^2}}} dK_z dK_i \right)$$

for  $\sqrt{k_i^2 \cos^2(\theta) - \frac{2m^* \Delta E}{\hbar^2}} > k_i \cos(\theta)$ , and

$$\frac{1}{\tau_{k_i}} = \frac{D_A}{2\rho v_s (2\pi)^2} \left( N_0 + \frac{1}{2} \pm \frac{1}{2} \int \int_0^{2\pi} \int \frac{(\int \varphi_f^*(z) e^{-iK_z z} \varphi_i(z) dz)^2 \times (-k_i \cos(\theta) - \sqrt{k_i^2 \cos^2(\theta) - \frac{2m^* \Delta E}{\hbar^2}}) \times \sqrt{(-k_i \cos(\theta) - \sqrt{k_i^2 \cos^2(\theta) - \frac{2m^* \Delta E}{\hbar^2}})^2 + K_z^2}}{2\sqrt{k_i^2 \cos^2(\theta) - \frac{2m^* \Delta E}{\hbar^2}}} dK_z dK_i \right)$$

for  $\sqrt{k_i^2 \cos^2(\theta) - \frac{2m^* \Delta E}{\hbar^2}} < k_i \cos(\theta)$ ,

where  $D_A = 7 \text{ eV}$  is the deformation potential, and  $N_0$  the phonon population calculated as in (2.16).

Because of the necessary integration over the phonon wave vector for LA phonons with different energy, the computing time for LA phonon energy is significantly longer than that of LO phonon scattering calculation. The typical LA phonon-electron scattering time in GaAs/AlGaAs-based THz QCL is in tens of picoseconds, which is not significant. Table. 2-1 shows a comparison of major scattering processes in V775 structure at 150 K and 200 K. V775 structure is reported in [19] with an operation temperature of ~200 K. LA phonon scattering is significantly slower than LO phonon, Impurity, and interface roughness scattering.

	Electrons scattering time from UL to LL (at 150 K) V775	Electrons scattering time from UL to LL (at 200 K) V775
LO phonon scattering	2.9 ps (emission) 22 ps (absorption)	2.3 ps (emission) 10 ps (absorption)
Impurity scattering	28 ps	27 ps
Interface roughness scattering	14 ps	15 ps
LA phonon scattering	90 ps (emission) 97 ps (absorption)	68 ps (emission) 71 ps (absorption)

Table 2-1. Comparison of major scattering time in V775 structures at 150 K and 200 K.

## 2.2.4 Interface Roughness Scattering

Another important scattering mechanism is interface roughness scattering. Interface roughness is mainly caused by alloy disorder and growth imperfections at the interface of two semiconductor alloys. This section (2.2.3) quotes the computing formulae from R. Terazzi's PhD thesis to estimate interface roughness scattering in THz QCL [60]. The mean height of roughness ( $\Delta$ ) is described in section 2.1, and correlation length ( $\Lambda$ ) is estimated around  $\Lambda = 68 \text{ \AA}$ . The strength of interaction is defined as

$$F_{i,j} = -\delta V(Z)\varphi_i(Z)\varphi_j(Z) \quad (2.29)$$

where  $\delta V(Z) = V(Z^+) - V(Z^-)$  is the position-dependent conduction band voltage difference.  $V(Z^+)$  and  $V(Z^-)$  are the voltage potential at the next larger and previous smaller  $Z$  positions, respectively.

By assuming the initial electron wave vector as  $k_i$ , the final electron wave vector after elastic scattering can be expressed as

$$k_f^2 = \frac{m^*_i}{m^*_f} k_i^2 + \frac{2m^*_i(E_f - E_i)}{\hbar^2}. \quad (2.30)$$

The exchanged momentum can be expressed as

$$q^2 = \left(1 + \frac{m^*_i}{m^*_f}\right) k_i^2 + \frac{2m^*_i(E_f - E_i)}{\hbar^2} - 2k \sqrt{\frac{m^*_i}{m^*_f} k_i^2 + \frac{2m^*_i(E_f - E_i)}{\hbar^2}} \cos(\alpha), \quad (2.31)$$

where  $\alpha$  is the angle between the initial wave vector and the final wave vector after scattering.

The intersubband interface roughness scattering rate at certain initial wave vector can be calculated by

$$\frac{1}{\tau_{k_i}} = \frac{m^*_f \Delta^2 \Lambda^2}{\hbar^3} F_{i,j} \int_0^\pi e^{-q^2 \frac{\Lambda^2}{4}} d\alpha. \quad (2.32)$$

The intrasubband interface roughness scattering rate can be calculated by

$$\frac{1}{\tau_{k_i}} = \frac{\Delta^2 \Lambda^2}{\hbar^2} [m^*_i F_{i,i}^2 + m^*_f F_{f,f}^2 - (m^*_i + m^*_f) F_{i,i} F_{j,j}] \int_0^\pi \exp(-q_{intra}^2 \Lambda^2 / 4) d\alpha, \quad (2.33)$$

where  $q_{intra}^2 = 2k^2(1 - \cos(\alpha))$ .

## 2.2.5 Ionized Impurity Scattering

Doping in each period is necessary in THz QCLs, as dopants are important for maintaining homogeneity of the electric field domain across the major part of active region at most pumping biases. It is necessary to consider dopant-induced ionized impurity scattering and conduction band bending for THz QCL simulation. This section discusses ionized impurity scattering. The calculating formula in this section (2.2.4) is adopted from [61] and implemented into MATLAB code.

The intersubband scattering between the initial-state  $\varphi_i$  and final-state  $\varphi_f$  can be calculated by

$$\frac{1}{\tau_{k_i}} = \frac{m^*_i q_0^2}{4\pi\epsilon_0 \hbar^2} \int dZ N(Z) \frac{1}{\epsilon^2(Z)} \int_0^\pi d\alpha \times \left[ \frac{1}{\sqrt{q^2 + q_s^2}} \int dz \varphi_i(z) \varphi_f(z) \exp\left(-\sqrt{q^2 + q_s^2} |z - Z|\right) \right]^2, \quad (2.34)$$

where  $q$  is the exchanged wave vector as described in equation (2.2.3.3), and  $q_s = \sqrt{\frac{q_0^2 N_s}{\epsilon_0 \epsilon_s k_B T_e}}$  is a screening wave vector based on the Debye model.  $N_s$  is the sheet carrier density per period.

The intrasubband scattering at the initial and final state can be calculated by

$$\frac{1}{\tau_{k_i}} = \frac{m^*_i q_0^4}{4\pi\epsilon_0 \hbar^2} \int_0^\pi d\alpha \times \left[ \frac{1}{\sqrt{q_{intra}^2 + q_s^2}} \int dz (\varphi_i^2(z) - \varphi_f^2(z)) \exp\left(-\sqrt{q_{intra}^2 + q_s^2} |z - Z|\right) \right]^2, \quad (2.35)$$

where  $q_{intra}^2 = 2k^2(1 - \cos(\alpha))$ .

The doping profile  $N(Z)$  can be the average doping over a period or delta doping that is dependent on MBE growth. Considering the segregation, the delta doping profile is modified as

$$N(Z) = \exp\left(-\frac{(Z-X_0)}{20\text{\AA}}\right) (Z > X_0) \quad (2.36)$$

$$N(Z) = 0 (Z < X_0), \quad (2.37)$$

where  $X_0$  is the delta doping location, and  $z$  is the position that increases along the growth direction,

## 2.2.6 Electron-Electron Scattering

Electron-electron scattering is included by multiple functions, such as thermal distribution, screening effect (as described in the previous section), and the self-consistently solving Hartree potential and exchange-correlation potential.

Thermal distribution on subbands is a result of electron-electron scattering. Electrons are not equally distributed in the initial state, and filled states in the final subband can prevent electrons from scattering into them. The average scattering rate over subband populations in the initial and final state can be modified as

$$\frac{1}{\tau_{if}} = \frac{\int \frac{1}{\tau_i} f_i^{FD}(E) f_f^{FD}(E - \hbar\omega) dE}{\int f_i^{FD}(E) dE}, \quad (2.38)$$

where  $f_i^{FD}$  and  $f_f^{FD}$  are the Fermi-Dirac distribution function in the initial and final state, respectively. In the 2D case and low doping concentration, the Fermi level is calculated by

$$E_f = K_B T \log(e^{\frac{n\pi\hbar^2}{K_B T m^*}} - 1), \quad (2.39)$$

where  $n$  is the carrier density.

Difference of a few meV in conduction band potential can be introduced by embedded dopants and carrier's distribution. The total conduction potential becomes

$$V(z) = V_0(z) + Ed(z) + V_H(z) + V_{xc}(z), \quad (2.40)$$

where  $V_0(z)$  is the initial conduction band profile at zero doping and zero electric bias,  $Ed(z)$  is the potential induced by external electric bias,  $V_H(z) = \frac{e}{\epsilon_s \epsilon_0} \int_{-\infty}^z (z - z') (N_D(z') - n(z')) dz'$  is the Hartree potential induced by dopants density ( $N_D(z)$ ) and electrons density ( $n(z)$ ), and  $V_{xc}(z) =$

$$\frac{-V_H}{\pi \left(\frac{9\pi}{4}\right)^{\frac{-1}{3}} \frac{m_e}{\epsilon_s m_0} \left(\frac{4\pi n(z)}{3}\right)^{\frac{-1}{3}}} \left(1 + 0.6213 \times \frac{m_e}{\epsilon_s m_0} \left(\frac{4\pi n(z)}{3}\right)^{\frac{-1}{3}} \ln\left(1 + \frac{\left(\frac{9\pi}{4}\right)^{\frac{-1}{3}}}{\frac{m_e}{\epsilon_s m_0} \left(\frac{4\pi n(z)}{3}\right)^{\frac{-1}{3}}}\right)\right)$$

is the exchange-correlation potential induced by dopants and redistributed electrons [82]. The calculation diagram is shown in Fig. 2-2.

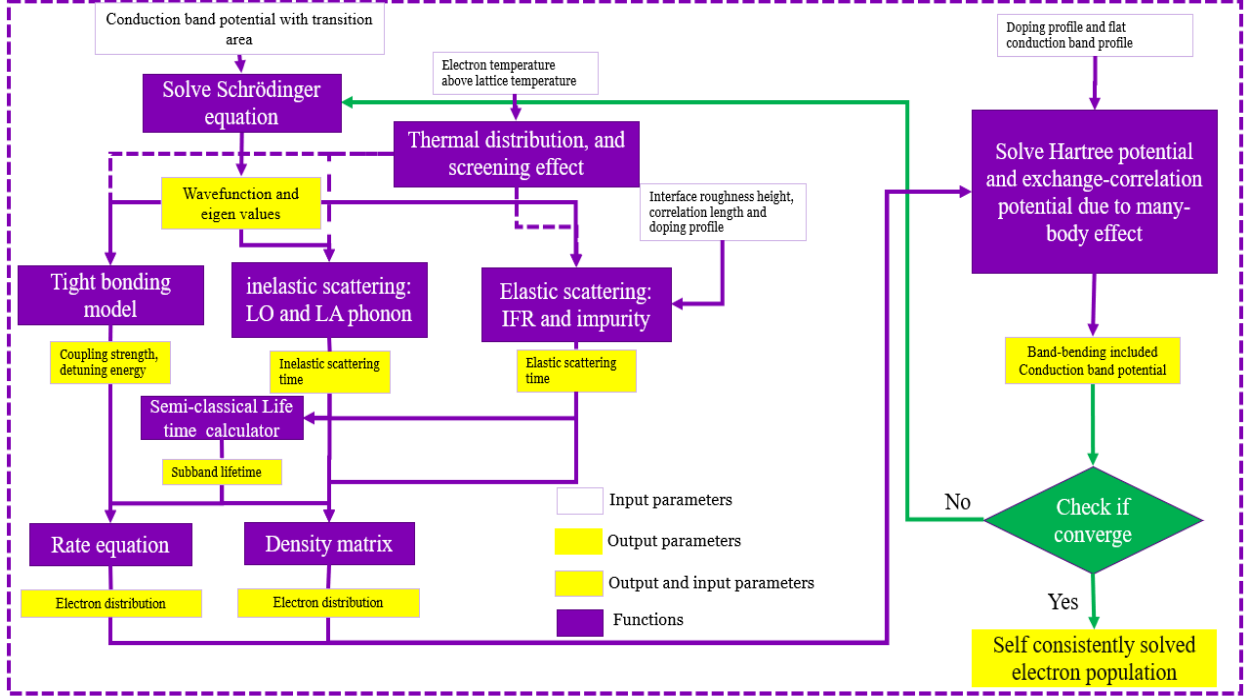


Fig. 2-2. Schematic diagram of self-consistent iteration.

## 2.3 THz QCLs Transport Models

With knowledge of calculated energy states, scattering rate, and coupling strength, one can employ compact and effective transport models such as RE and DM to calculate electron distribution on each subband for a complete cycle shown in Fig. 2-2.

### 2.3.1 Rate Equation

The general RE can be described as

$$\frac{d\rho_i(t)}{dt} = -\frac{\rho_i(t)}{\tau_i} - \sum_f \frac{\rho_i(t)}{T_{if}} + \sum_f \frac{\rho_f(t)}{\tau_{fi}} + \sum_f \frac{\rho_f(t)}{T_{fi}} \quad (2.41)$$

$$\frac{1}{\tau_i} = \sum_{s-inter} \sum_j \frac{1}{\tau_{ij}} \quad (2.42)$$

$$T_{fi} = \frac{(1+\Delta^2 t_{fi}^2)}{2\Omega^2 t_{fi}} \quad (2.43)$$

$$\frac{1}{t_{fi}} = \frac{0.5}{\tau_i} + \frac{0.5}{\tau_f} + \frac{0.5}{\tau_{fi}^*} \quad (2.44)$$

$$\frac{1}{\tau_{fi}^*} = \sum_{s-intra} \frac{1}{\tau_{fi-intra}}, \quad (2.45)$$

where  $s - inter$  is the intersubband scattering mechanism and  $s - intra$  is the intrasubband scattering mechanism mentioned in section (2.2),  $\Delta$  is the detuning energy, and  $\Omega$  is the coupling strength.  $T$  is described as the tunneling time, and  $t_{fi}$  is the dephasing time between state  $f$  and  $i$ .

An example of a six-level RE can be written as

$$\begin{pmatrix} -\frac{1}{\tau_6} - \sum_j \frac{1}{T_{6j}} & \frac{1}{\tau_{56}} + \frac{1}{T_{56}} & \frac{1}{\tau_{46}} + \frac{1}{T_{46}} & \frac{1}{\tau_{36}} + \frac{1}{T_{36}} & \frac{1}{\tau_{26}} + \frac{1}{T_{26}} & \frac{1}{\tau_{16}} + \frac{1}{T_{16}} \\ \frac{1}{\tau_{65}} + \frac{1}{T_{65}} & -\frac{1}{\tau_5} - \sum_j \frac{1}{T_{5j}} & \frac{1}{\tau_{45}} + \frac{1}{T_{45}} & \frac{1}{\tau_{35}} + \frac{1}{T_{35}} & \frac{1}{\tau_{25}} + \frac{1}{T_{25}} & \frac{1}{\tau_{15}} + \frac{1}{T_{15}} \\ \frac{1}{\tau_{64}} + \frac{1}{T_{64}} & \frac{1}{\tau_{54}} + \frac{1}{T_{54}} & -\frac{1}{\tau_4} - \sum_j \frac{1}{T_{4j}} & \frac{1}{\tau_{34}} + \frac{1}{T_{34}} & \frac{1}{\tau_{24}} + \frac{1}{T_{24}} & \frac{1}{\tau_{14}} + \frac{1}{T_{14}} \\ \frac{1}{\tau_{63}} + \frac{1}{T_{63}} & \frac{1}{\tau_{53}} + \frac{1}{T_{53}} & \frac{1}{\tau_{43}} + \frac{1}{T_{43}} & -\frac{1}{\tau_3} - \sum_j \frac{1}{T_{3j}} & \frac{1}{\tau_{23}} + \frac{1}{T_{23}} & \frac{1}{\tau_{13}} + \frac{1}{T_{13}} \\ \frac{1}{\tau_{62}} + \frac{1}{T_{62}} & \frac{1}{\tau_{52}} + \frac{1}{T_{52}} & \frac{1}{\tau_{42}} + \frac{1}{T_{42}} & \frac{1}{\tau_{32}} + \frac{1}{T_{32}} & -\frac{1}{\tau_2} - \sum_j \frac{1}{T_{2j}} & \frac{1}{\tau_{12}} + \frac{1}{T_{12}} \\ 1 & 1 & 1 & 1 & 1 & 1 \end{pmatrix} \begin{pmatrix} \rho_6 \\ \rho_5 \\ \rho_4 \\ \rho_3 \\ \rho_2 \\ \rho_1 \end{pmatrix} = \begin{pmatrix} 0 \\ 0 \\ 0 \\ 0 \\ 0 \\ 1 \end{pmatrix}, \quad (2.46)$$

where subscript numbers 1-6 correspond to energy levels, and  $\rho_i$  is the  $i$ th state's electron population over the total electron density in one period. Population inversion can be calculated from (2.46). Electron population can be used to calculate  $V_e(z)$  in equation (2.40). Calculated electron population is the key to complete the self-consistent iteration in Fig. 2.2.

### 2.3.2 Rate Equation-Based Current Density Calculation Method

The method of current density calculation is also called second-order current density calculation [68], as it considers the effect of carriers' distribution in each state. The tunneling-induced current can be defined as

$$J_{ij} = \frac{2\Omega_{ij}t_{ij}}{1+\Delta_{ij}^2t_{ij}^2} (\overline{\Omega}_{ij}\rho_i - \overline{\Omega}_{ji}\rho_j) \quad (2.47)$$

$$\overline{\Omega}_{ij} = \Omega_{ij}\sigma_i(\Delta_{ji}) \quad (2.48)$$

$$\overline{\Omega}_{ji} = \Omega_{ij}\sigma_j(\Delta_{ij}) \quad (2.49)$$

$$\sigma_i(\Delta_{ji}) = \theta(-\Delta_{ji}) + \theta(-\Delta_{ji}) \exp\left(\frac{\hbar\Delta_{ji}}{k_B T}\right), \quad (2.50)$$

where  $\Delta_{ji}$  is the detuning energy and  $\Omega_{ij}$  is the coupling strength between state  $j$  and state  $i$ .

A simplified formula that does not consider the effect of carrier distribution is described as  $J_{12} = eN_{2D}\left(\frac{\rho_1}{T_{12}} - \frac{\rho_2}{T_{21}}\right)$ . (2.51)

Fig. 2-3 shows a simplified diagram indicating important coupling energy values and scattering times between energy states in the hybrid extraction/injection design (HEID) structure. Fig. 2-3(a) shows important coupling energy values that need to be calculated in the HEID by the RE model. Green arrows indicate the designed main RT process, and red arrows indicate a weak undesired RT process and its corresponding coupling energy. Fig. 2-3(b) shows the semiclassical scattering time that needs to be considered in the HEID by the RE model. Green arrows indicate a scattering process with the designed forward-scattering time  $\tau_{ij}$  (from state  $i$  to state  $j$ ) and undesired back-scattering time (from state  $j$  to state



i), and red arrows indicate a scattering process with undesired forward-scattering and beneficial back-scattering time in the HEID by the RE model.

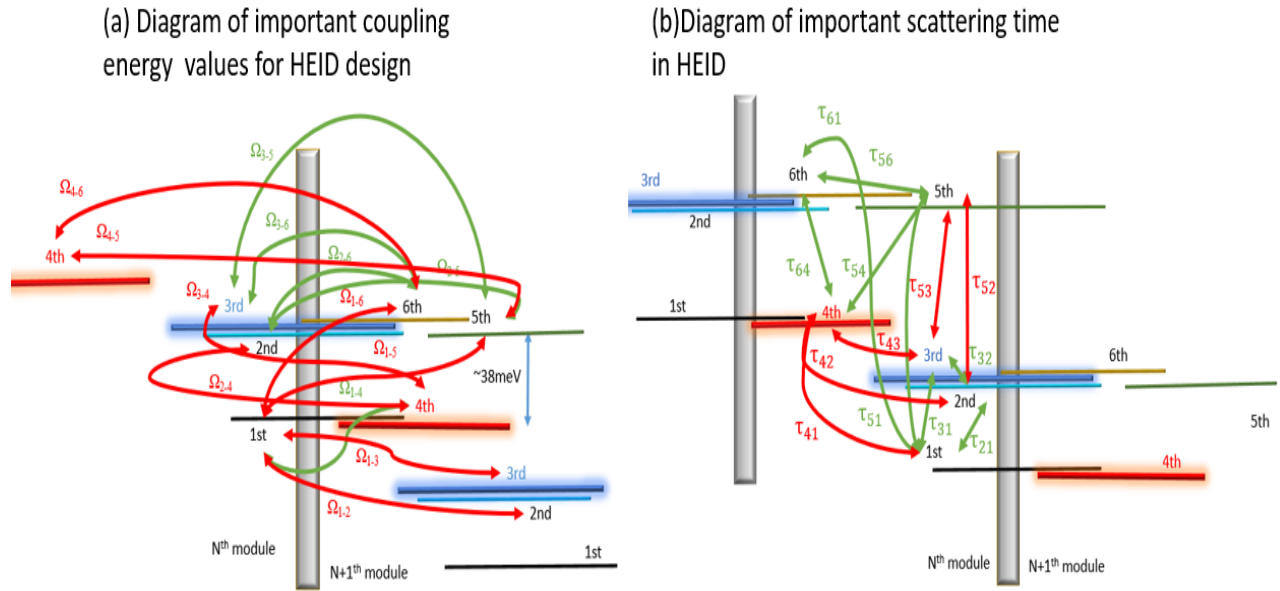


Fig. 2-3. Diagrams of important coupling and scattering process between subbands.

### 2.3.3 Density Matrix-Based Transport Model

The DM method allows correlations between states to describe tunneling effect and effects of coherence terms between states on gain spectra. The past-world record of three-well RP structure is designed by employing a four-state DM model [19]. This section discusses the DM model and its extension to a six-state system. The labeling of energy states in the DM model, which is shown in Fig. 2.4, is different from RE where the numbers correspond to the confined state energy.

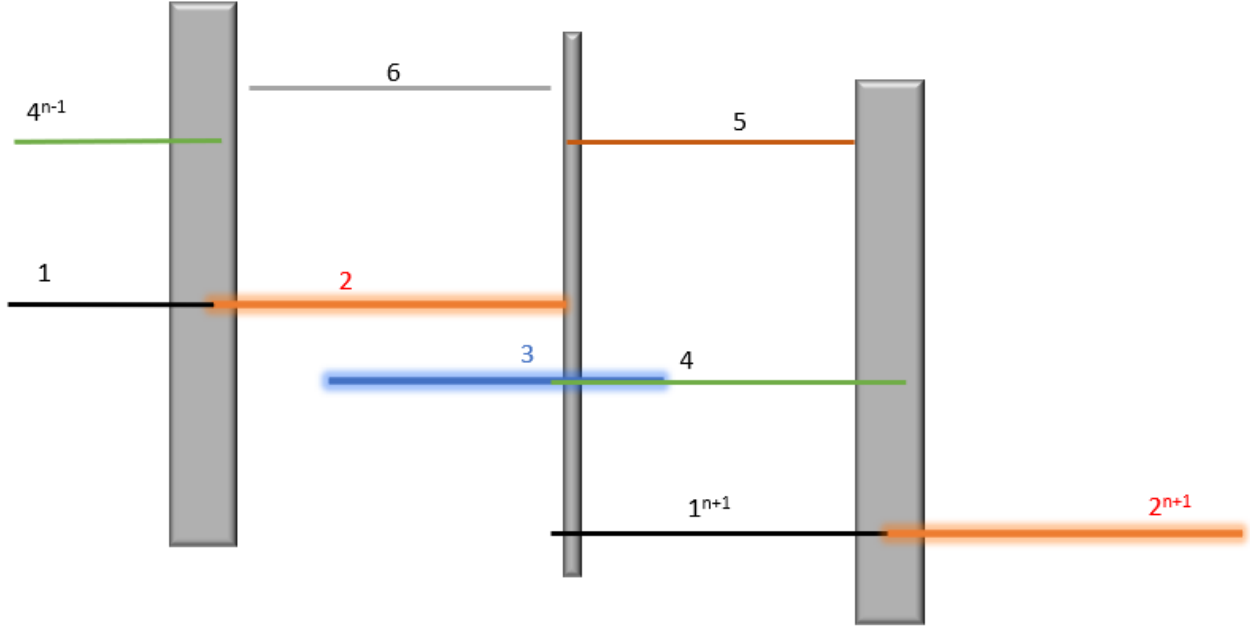


Fig. 2.4 Energy state labeling in the density matrix-based transport model.

The DM of an isolated quantum system begins from the Liouville-von Neumann equation:

$$\frac{d\rho}{dt} = -\frac{i}{\hbar}[H, \rho] - \tau, \quad (2.52)$$

where  $H$  is the Hamiltonian matrix,  $\tau$  is the scattering rate matrix, and  $\rho$  is the carrier DM.

For the four-state system, the aforementioned matrixes can be described as

$$\rho = \begin{bmatrix} \rho_{11} & \rho_{12} & \rho_{13} & \rho_{14} \\ \rho_{21} & \rho_{22} & \rho_{23} & \rho_{24} \\ \rho_{31} & \rho_{32} & \rho_{33} & \rho_{34} \\ \rho_{41} & \rho_{42} & \rho_{43} & \rho_{44} \end{bmatrix} \quad (2.53)$$

$$H = \begin{bmatrix} E_1 & \hbar\Omega_{12} & \hbar\Omega_{13} & \hbar\Omega_{14} \\ \hbar\Omega_{12} & E_2 & 0 & \hbar\Omega_{24} \\ \hbar\Omega_{13} & 0 & E_3 & \hbar\Omega_{34} \\ \hbar\Omega_{14} & \hbar\Omega_{24} & \hbar\Omega_{34} & E_4 \end{bmatrix} \quad (2.54)$$

$$\tau^{-1} = \begin{bmatrix} \tau_{11}^{-1}\rho_{11} - \tau_{44}^{-1}\rho_{44} & \tau_{12}^{-1}\rho_{12} & \tau_{13}^{-1}\rho_{13} & \tau_{14}^{-1}\rho_{14} \\ \tau_{12}^{-1}\rho_{21} & \tau_{22}^{-1}\rho_{22} - \tau_{33}^{-1}\rho_{33} & \tau_{23}^{-1}\rho_{23} & \tau_{24}^{-1}\rho_{24} \\ \tau_{13}^{-1}\rho_{31} & \tau_{23}^{-1}\rho_{32} & \tau_{33}^{-1}\rho_{33} - \tau_{22}^{-1}\rho_{22} & \tau_{34}^{-1}\rho_{34} \\ \tau_{14}^{-1}\rho_{41} & \tau_{24}^{-1}\rho_{42} & \tau_{34}^{-1}\rho_{43} & -\tau_{11}^{-1}\rho_{11} + \tau_{44}^{-1}\rho_{44} \end{bmatrix}, \quad (2.55)$$

where  $\tau_{||ij} = t_{ij}$  as described in equation (2.44).

By plugging equations (2.53) to (2.55) into equation (2.52), equation (2.52) can be rewritten as

$$\begin{pmatrix}
 j\Omega_{12} & 0 & 0 & 0 & -j\Omega_{24} & 0 & 0 & 0 \\
 j\Omega_{12} & 0 & 2j\Omega_{13} & 0 & j\Omega_{24} & 0 & 0 & 0 \\
 0 & 0 & 0 & 0 & j\Omega_{24} & 0 & j\Omega_{34} & 0 \\
 0 & 0 & 0 & 0 & 0 & 0 & 0 & 0 \\
 j\tau_{||12}^{-1} & \Delta_{12} & 0 & 0 & 0 & \Omega_{14} & 0 & 0 \\
 -\Delta_{12} & j\tau_{||12}^{-1} & 0 & 0 & -\Omega_{14} & 0 & 0 & 0 \\
 0 & 0 & j\tau_{||13}^{-1} & \Delta_{13} & 0 & 0 & 0 & \Omega_{14} \\
 0 & 0 & -\Delta_{13} & j\tau_{||13}^{-1} & 0 & 0 & -\Omega_{14} & 0 \\
 0 & -\Omega_{14} & 0 & 0 & j\tau_{||24}^{-1} & \Delta_{24} & 0 & 0 \\
 \Omega_{14} & 0 & 0 & 0 & -\Delta_{24} & j\tau_{||24}^{-1} & j\tau_{||34}^{-1} & \Delta_{34} \\
 0 & 0 & 0 & -\Omega_{14} & 0 & 0 & 0 & 0 \\
 0 & 0 & \Omega_{14} & 0 & 0 & 0 & -\Delta_{34} & j\tau_{||34}^{-1} \\
 0 & -\Omega_{24} & 0 & -\Omega_{34} & 0 & \Omega_{12} & 0 & -\Omega_{13} \\
 -\Omega_{24} & 0 & -\Omega_{34} & 0 & \Omega_{12} & 0 & \Omega_{13} & 0 \\
 0 & -\Omega_{13} & 0 & \Omega_{12} & 0 & -\Omega_{34} & 0 & \Omega_{24} \\
 \Omega_{13} & 0 & \Omega_{12} & 0 & -\Omega_{34} & 0 & -\Omega_{24} & 0
 \end{pmatrix}
 \begin{pmatrix}
 0 \\
 2j\Omega_{14} \\
 j\Omega_{14} \\
 0 \\
 0 \\
 -\Omega_{24} \\
 -\Omega_{24} \\
 -\Omega_{34} \\
 -\Omega_{34} \\
 \dots \\
 0 \\
 \Omega_{12} \\
 0 \\
 \Omega_{13} \\
 \Omega_{13} \\
 j\tau_{||14}^{-1} \\
 -\Delta_{14} \\
 0 \\
 0
 \end{pmatrix}
 \begin{pmatrix}
 0 & 0 & 0 & 0 & 0 & -\tau^{-1}_2 & \tau^{-1}_3 & 0 \\
 0 & 0 & 0 & 0 & 2\tau^{-1}_1 & -\tau^{-1}_2 & \tau^{-1}_3 & -\tau^{-1}_4 \\
 0 & 0 & 0 & 0 & \tau^{-1}_1 & 0 & 0 & -\tau^{-1}_4 \\
 0 & -\Omega_{24} & 0 & \Omega_{13} & 1 & 1 & 1 & 1 \\
 -\Omega_{24} & 0 & -\Omega_{13} & 0 & -2\Omega_{12} & 2\Omega_{12} & 0 & 0 \\
 0 & -\Omega_{34} & 0 & \Omega_{12} & 0 & 0 & 0 & 0 \\
 -\Omega_{34} & 0 & -\Omega_{12} & 0 & -2\Omega_{13} & 0 & 2\Omega_{13} & 0 \\
 \dots & 0 & \Omega_{12} & 0 & 0 & 0 & 0 & 0 \\
 \Omega_{12} & 0 & -\Omega_{34} & 0 & 0 & -2\Omega_{24} & 0 & 2\Omega_{24} \\
 0 & \Omega_{13} & 0 & -\Omega_{24} & 0 & 0 & 0 & 0 \\
 \Omega_{13} & 0 & \Omega_{24} & 0 & 0 & 0 & -2\Omega_{34} & \Omega_{34} \\
 j\tau_{||14}^{-1} & \Delta_{14} & 0 & 0 & -2\Omega_{14} & 0 & 0 & 0 \\
 -\Delta_{14} & j\tau_{||14}^{-1} & 0 & 0 & 0 & 0 & 0 & 2\Omega_{14} \\
 0 & 0 & j\tau_{||23}^{-1} & \Delta_{23} & 0 & 0 & 0 & 0 \\
 0 & 0 & -\Delta_{23} & j\tau_{||23}^{-1} & 0 & 0 & 0 & 0
 \end{pmatrix}
 \times
 \begin{pmatrix}
 \rho_{21} - \rho_{12} \\
 \rho_{21} + \rho_{12} \\
 \rho_{31} - \rho_{13} \\
 \rho_{31} + \rho_{13} \\
 \rho_{42} - \rho_{24} \\
 \rho_{42} + \rho_{24} \\
 \rho_{43} - \rho_{34} \\
 \rho_{43} + \rho_{34} \\
 \rho_{41} - \rho_{14} \\
 \rho_{41} + \rho_{14} \\
 \rho_{32} - \rho_{23} \\
 \rho_{32} + \rho_{23} \\
 \rho_{11} \\
 \rho_{22} \\
 \rho_{33} \\
 \rho_{44}
 \end{pmatrix}
 =
 \begin{pmatrix}
 0 \\
 0 \\
 0 \\
 0 \\
 1 \\
 0 \\
 0 \\
 0 \\
 0 \\
 0 \\
 0 \\
 0 \\
 0 \\
 0 \\
 0 \\
 0 \\
 0 \\
 0 \\
 0
 \end{pmatrix}
 \tag{2.56}$$

where  $j = 1i$ . Electron population can be calculated from equation (2.56). The four-state DM is simplified to simulate four main energy states in the three-well RP structure [62]. Lasing energy is labeled as state 2 and 3, the injector state is labeled as state 1, and the extractor state is labeled as state 4. Tight binding is applied between the phonon well and the lasing well in a four-state DM scheme.

The four-state DM lacks genericity to other QCL schemes. An extended six-state DM is derived and presented here. Since the major confined energy states in state-of-the-art THz QCL design are around 6 (4 main states and 2 parasitic states), arbitrarily large DM method is necessary to simulate this type of devices [83-85]. This section derives 6-state DM formula that is not limited to the RP scheme but also applicable to hybrid extraction/injection designs.

$$\begin{pmatrix}
 -j^{-1}\Omega_{12} & 2 & -j^{-1}\Omega_{13} & 0 & 0 & 0 & 0 & 0 & -j^{-1}\Omega_{16} \\
 j^{-1}\Delta_{12} & -\tau_{||12}^{-1} & 0 & 0 & -j^{-1}\Omega_{24} & 0 & -j^{-1}\Omega_{25} & 0 & 0 \\
 0 & 0 & 0 & 0 & 0 & 0 & 0 & 0 & 0 \\
 -j^{-1}\Omega_{24} & 0 & -j^{-1}\Omega_{34} & 0 & j^{-1}\Delta_{14} & -\tau_{||14}^{-1} & 0 & 0 & -j^{-1}\Omega_{46} \\
 -j^{-1}\Omega_{25} & 0 & -j^{-1}\Omega_{35} & 0 & 0 & 0 & j^{-1}\Delta_{15} & -\tau_{||15}^{-1} & -j^{-1}\Omega_{56} \\
 0 & 0 & 0 & 0 & -j^{-1}\Omega_{46} & 0 & -j^{-1}\Omega_{56} & 0 & j^{-1}\Delta_{16} \\
 -\tau_{||12}^{-1} & j^{-1}\Delta_{12} & 0 & 0 & 0 & -j^{-1}\Omega_{24} & 0 & -j^{-1}\Omega_{25} & 0 \\
 0 & 0 & -\tau_{||13}^{-1} & j^{-1}\Delta_{13} & 0 & -j^{-1}\Omega_{34} & 0 & -j^{-1}\Omega_{35} & 0 \\
 0 & -j^{-1}\Omega_{24} & 0 & -j^{-1}\Omega_{34} & -\tau_{||14}^{-1} & j^{-1}\Delta_{14} & 0 & 0 & 0 \\
 0 & -j^{-1}\Omega_{25} & 0 & -j^{-1}\Omega_{35} & 0 & 0 & -\tau_{||15}^{-1} & j^{-1}\Delta_{15} & 0 \\
 0 & 0 & 0 & 0 & 0 & -j^{-1}\Omega_{46} & 0 & -j^{-1}\Omega_{56} & -\tau_{||16}^{-1} \\
 j^{-1}\Omega_{12} & 0 & 0 & 0 & 0 & 0 & 0 & 0 & 0 \\
 j^{-1}\Omega_{13} & 0 & j^{-1}\Omega_{12} & 0 & 0 & 0 & 0 & 0 & 0 \\
 0 & 0 & 0 & 0 & j^{-1}\Omega_{12} & 0 & 0 & 0 & 0 \\
 0 & 0 & 0 & 0 & 0 & 0 & j^{-1}\Omega_{12} & 0 & 0 \\
 j^{-1}\Omega_{16} & 0 & 0 & 0 & 0 & 0 & 0 & 0 & j^{-1}\Omega_{12} \\
 0 & -j^{-1}\Omega_{13} & 0 & j^{-1}\Omega_{12} & 0 & 0 & 0 & 0 & 0 \\
 0 & 0 & 0 & 0 & 0 & j^{-1}\Omega_{12} & 0 & 0 & 0 \\
 0 & 0 & 0 & 0 & 0 & 0 & 0 & j^{-1}\Omega_{12} & 0 \\
 0 & -j^{-1}\Omega_{16} & 0 & 0 & 0 & 0 & 0 & 0 & 0 \\
 0 & 0 & j^{-1}\Omega_{13} & 0 & 0 & 0 & 0 & 0 & 0 \\
 0 & 0 & 0 & 0 & j^{-1}\Omega_{13} & 0 & 0 & 0 & 0 \\
 0 & 0 & 0 & 0 & 0 & 0 & j^{-1}\Omega_{13} & 0 & 0 \\
 0 & 0 & 0 & 0 & 0 & j^{-1}\Omega_{16} & 0 & 0 & j^{-1}\Omega_{13} \\
 0 & 0 & 0 & 0 & 0 & j^{-1}\Omega_{13} & 0 & 0 & 0 \\
 0 & 0 & 0 & 0 & 0 & 0 & 0 & j^{-1}\Omega_{13} & 0 \\
 0 & 0 & 0 & -j^{-1}\Omega_{16} & 0 & 0 & 0 & 0 & 0 \\
 0 & 0 & 0 & 0 & 0 & 0 & 0 & 0 & 0 \\
 0 & 0 & 0 & 0 & 0 & 0 & 0 & 0 & 0 \\
 0 & 0 & 0 & 0 & j^{-1}\Omega_{16} & 0 & 0 & 0 & 0 \\
 0 & 0 & 0 & 0 & 0 & 0 & 0 & 0 & 0 \\
 0 & 0 & 0 & 0 & 0 & -j^{-1}\Omega_{16} & 0 & 0 & 0 \\
 0 & 0 & 0 & 0 & 0 & 0 & 0 & 0 & 0 \\
 0 & 0 & 0 & 0 & 0 & 0 & j^{-1}\Omega_{16} & 0 & 0 \\
 0 & 0 & 0 & 0 & 0 & 0 & 0 & -j^{-1}\Omega_{16} & 0 \\
 0 & 0 & 0 & 0 & 0 & 0 & 0 & 0 & j^{-1}\Omega_{16}
 \end{pmatrix}$$

$$\begin{array}{cccccccc}
0 & 0 & 0 & 0 & 0 & 0 & 0 & 0 \\
0 & -j^{-1}\Omega_{13} & 0 & 0 & 0 & 0 & 0 & -j^{-1}\Omega_{16} \\
0 & 0 & 0 & 0 & 0 & 0 & 0 & 0 \\
0 & 0 & 0 & j^{-1}\Omega_{12} & 0 & 0 & 0 & 0 \\
0 & 0 & 0 & 0 & 0 & j^{-1}\Omega_{12} & 0 & 0 \\
-\tau_{||16}^{-1} & 0 & 0 & 0 & 0 & 0 & 0 & j^{-1}\Omega_{12} \\
0 & 0 & j^{-1}\Omega_{13} & 0 & 0 & 0 & 0 & j^{-1}\Omega_{16} \\
0 & 0 & j^{-1}\Omega_{12} & 0 & 0 & 0 & 0 & 0 \\
-j^{-1}\Omega_{46} & 0 & 0 & 0 & j^{-1}\Omega_{12} & 0 & 0 & 0 \\
-j^{-1}\Omega_{56} & 0 & 0 & 0 & 0 & 0 & j^{-1}\Omega_{12} & 0 \\
j^{-1}\Delta_{16} & 0 & 0 & -j^{-1}\Omega_{24} & 0 & -j^{-1}\Omega_{25} & 0 & 0 \\
0 & j^{-1}\Delta_{23} & -\tau_{||23}^{-1} & -j^{-1}\Omega_{34} & 0 & -j^{-1}\Omega_{35} & 0 & 0 \\
0 & -j^{-1}\Omega_{34} & 0 & j^{-1}\Delta_{24} & -\tau_{||24}^{-1} & 0 & 0 & -j^{-1}\Omega_{46} \\
0 & -j^{-1}\Omega_{35} & 0 & 0 & 0 & j^{-1}\Delta_{25} & -\tau_{||25}^{-1} & -j^{-1}\Omega_{56} \\
0 & 0 & 0 & -j^{-1}\Omega_{46} & 0 & -j^{-1}\Omega_{56} & 0 & j^{-1}\Delta_{26} \\
0 & -\tau_{||23}^{-1} & j^{-1}\Delta_{23} & 0 & -j^{-1}\Omega_{34} & 0 & -j^{-1}\Omega_{35} & 0 \\
... & 0 & j^{-1}\Omega_{34} & -\tau_{||24}^{-1} & j^{-1}\Delta_{24} & 0 & 0 & -j^{-1}\Omega_{46} \\
0 & 0 & -j^{-1}\Omega_{35} & 0 & 0 & -\tau_{||25}^{-1} & j^{-1}\Delta_{25} & 0 \\
j^{-1}\Omega_{12} & 0 & 0 & 0 & -j^{-1}\Omega_{46} & 0 & -j^{-1}\Omega_{56} & -\tau_{||26}^{-1} \\
0 & 0 & 0 & 0 & 0 & 0 & 0 & 0 \\
0 & j^{-1}\Omega_{24} & 0 & 0 & 0 & 0 & 0 & 0 \\
0 & j^{-1}\Omega_{25} & 0 & 0 & 0 & 0 & 0 & 0 \\
0 & 0 & 0 & 0 & 0 & 0 & 0 & 0 \\
0 & 0 & -j^{-1}\Omega_{24} & 0 & 0 & 0 & 0 & 0 \\
0 & 0 & -j^{-1}\Omega_{25} & 0 & 0 & 0 & 0 & 0 \\
j^{-1}\Omega_{13} & 0 & 0 & 0 & 0 & 0 & 0 & 0 \\
0 & 0 & 0 & j^{-1}\Omega_{24} & 0 & 0 & 0 & 0 \\
0 & 0 & 0 & j^{-1}\Omega_{25} & 0 & j^{-1}\Omega_{24} & 0 & 0 \\
0 & 0 & 0 & 0 & 0 & 0 & j^{-1}\Omega_{24} & 0 \\
0 & 0 & 0 & 0 & -j^{-1}\Omega_{25} & 0 & j^{-1}\Omega_{24} & 0 \\
0 & 0 & 0 & 0 & 0 & 0 & 0 & j^{-1}\Omega_{24} \\
0 & 0 & 0 & 0 & 0 & j^{-1}\Omega_{25} & 0 & 0 \\
0 & 0 & 0 & 0 & 0 & 0 & 0 & j^{-1}\Omega_{25} \\
0 & 0 & 0 & 0 & 0 & 0 & 0 & -j^{-1}\Omega_{25} \\
0 & 0 & 0 & 0 & 0 & 0 & 0 & 0
\end{array}$$

$$\begin{array}{cccccccccc}
0 & 0 & 0 & 0 & 0 & 0 & 0 & 0 & 0 & 0 \\
0 & 0 & 0 & 0 & 0 & 0 & 0 & 0 & 0 & 0 \\
0 & 0 & 0 & 0 & 0 & 0 & 0 & 0 & 0 & 0 \\
j^{-1}\Omega_{13} & 0 & 0 & 0 & 0 & 0 & 0 & 0 & 0 & -j^{-1}\Omega_{16} \\
0 & 0 & j^{-1}\Omega_{13} & 0 & 0 & 0 & 0 & 0 & 0 & 0 \\
0 & 0 & 0 & 0 & j^{-1}\Omega_{13} & 0 & 0 & 0 & 0 & 0 \\
0 & 0 & 0 & 0 & 0 & 0 & j^{-1}\Omega_{16} & 0 & 0 & 0 \\
0 & j^{-1}\Omega_{13} & 0 & 0 & 0 & 0 & 0 & 0 & 0 & 0 \\
0 & 0 & 0 & j^{-1}\Omega_{13} & 0 & 0 & 0 & 0 & 0 & 0 \\
0 & 0 & 0 & 0 & 0 & j^{-1}\Omega_{13} & 0 & 0 & 0 & 0 \\
0 & 0 & 0 & 0 & 0 & 0 & 0 & 0 & 0 & 0 \\
-j^{-1}\Omega_{24} & 0 & -j^{-1}\Omega_{25} & 0 & 0 & 0 & 0 & 0 & 0 & 0 \\
0 & 0 & 0 & 0 & 0 & 0 & -j^{-1}\Omega_{25} & 0 & 0 & 0 \\
0 & 0 & 0 & 0 & 0 & 0 & j^{-1}\Omega_{24} & 0 & 0 & 0 \\
0 & 0 & 0 & 0 & 0 & 0 & 0 & 0 & j^{-1}\Omega_{24} & 0 \\
0 & j^{-1}\Omega_{24} & 0 & j^{-1}\Omega_{25} & 0 & 0 & 0 & 0 & 0 & 0 \\
0 & 0 & 0 & 0 & 0 & 0 & 0 & j^{-1}\Omega_{25} & 0 & 0 \\
... & 0 & 0 & 0 & 0 & 0 & 0 & 0 & j^{-1}\Omega_{24} & 0 & ... \\
0 & 0 & 0 & 0 & 0 & 0 & 0 & 0 & 0 & 0 \\
-j^{-1}\Omega_{34} & 0 & -j^{-1}\Omega_{35} & 0 & 0 & 0 & 0 & 0 & 0 & 0 \\
j^{-1}\Delta_{34} & -\tau_{||34}^{-1} & 0 & 0 & -j^{-1}\Omega_{46} & 0 & -j^{-1}\Omega_{35} & 0 & 0 & 0 \\
0 & 0 & j^{-1}\Delta_{35} & -\tau_{||35}^{-1} & -j^{-1}\Omega_{56} & 23 & j^{-1}\Omega_{34} & 0 & 0 & 0 \\
-j^{-1}\Omega_{46} & 0 & -j^{-1}\Omega_{56} & 0 & j^{-1}\Delta_{36} & -\tau_{||36}^{-1} & 0 & j^{-1}\Omega_{35} & 0 & j^{-1}\Omega_{34} \\
-\tau_{||34}^{-1} & j^{-1}\Delta_{34} & 0 & 0 & 0 & -j^{-1}\Omega_{46} & 0 & j^{-1}\Omega_{35} & 0 & 0 \\
0 & 0 & -\tau_{||35}^{-1} & j^{-1}\Delta_{35} & 0 & -j^{-1}\Omega_{56} & 0 & j^{-1}\Omega_{34} & 0 & 0 \\
0 & -j^{-1}\Omega_{46} & 0 & -j^{-1}\Omega_{56} & -\tau_{||36}^{-1} & j^{-1}\Delta_{36} & 0 & 0 & 0 & -j^{-1}\Omega_{46} \\
j^{-1}\Omega_{34} & 0 & 0 & 0 & 0 & 0 & j^{-1}\Delta_{45} & -\tau_{||45}^{-1} & -j^{-1}\Omega_{56} & 0 \\
j^{-1}\Omega_{35} & 0 & j^{-1}\Omega_{34} & 0 & 0 & 0 & -j^{-1}\Omega_{56} & 0 & j^{-1}\Delta_{46} & 0 \\
0 & 0 & 0 & 0 & j^{-1}\Omega_{34} & 0 & 0 & -\tau_{||45}^{-1} & j^{-1}\Delta_{45} & 0 \\
0 & -j^{-1}\Omega_{35} & 0 & j^{-1}\Omega_{34} & 0 & 0 & 0 & -\tau_{||45}^{-1} & j^{-1}\Delta_{45} & 0 \\
0 & 0 & 0 & 0 & 0 & j^{-1}\Omega_{34} & 0 & -j^{-1}\Omega_{56} & -\tau_{||46}^{-1} & 0 \\
0 & 0 & j^{-1}\Omega_{35} & 0 & 0 & 0 & 0 & 0 & 0 & 0 \\
0 & 0 & 0 & 0 & j^{-1}\Omega_{35} & 0 & j^{-1}\Omega_{46} & 0 & 0 & 0 \\
0 & 0 & 0 & 0 & 0 & j^{-1}\Omega_{35} & 0 & -j^{-1}\Omega_{46} & 0 & 0 \\
0 & 0 & 0 & 0 & 0 & 0 & 0 & 0 & 0 & j^{-1}\Omega_{46}
\end{array}$$

$$\begin{pmatrix}
0 & 0 & 0 & -\tau_1^{-1} & 0 & 0 & \tau_{41}^{-1} & \tau_{51}^{-1} & 0 \\
0 & 0 & 0 & 0 & 0 & 0 & 0 & 0 & 0 \\
0 & 0 & 0 & 1 & 1 & 1 & 1 & 1 & 1 \\
0 & 0 & 0 & 0 & 0 & 0 & 0 & 0 & 0 \\
0 & -j^{-1}\Omega_{16} & 0 & 0 & 0 & 0 & 0 & 0 & 0 \\
0 & 0 & 0 & 0 & 0 & 0 & 0 & 0 & 0 \\
0 & 0 & 0 & -2j^{-1}\Omega_{12} & 2j^{-1}\Omega_{12} & 0 & 0 & 0 & 0 \\
0 & 0 & 0 & -2j^{-1}\Omega_{13} & 0 & 2j^{-1}\Omega_{13} & 0 & 0 & 0 \\
j^{-1}\Omega_{16} & 0 & 0 & 0 & 0 & 0 & 0 & 0 & 0 \\
0 & 0 & j^{-1}\Omega_{16} & 0 & 0 & 0 & 0 & 0 & 0 \\
0 & 0 & 0 & -2j^{-1}\Omega_{16} & -\tau_2^{-1} & \tau_{32}^{-1} & 0 & 0 & 2j^{-1}\Omega_{16} \\
0 & 0 & 0 & 0 & 0 & 0 & 0 & 0 & -\tau_{62}^{-1} \\
0 & 0 & 0 & 0 & 0 & 0 & 0 & 0 & 0 \\
0 & 0 & 0 & 0 & 0 & 0 & 0 & 0 & 0 \\
0 & 0 & 0 & 0 & 0 & 0 & 0 & 0 & 0 \\
0 & j^{-1}\Omega_{25} & 0 & 0 & 0 & 0 & 0 & 0 & 0 \\
0 & 0 & 0 & 0 & 0 & 0 & 0 & 0 & 0 \\
0 & 0 & 0 & 0 & 0 & 0 & 0 & 0 & 0 \\
0 & 0 & 0 & 0 & -2j^{-1}\Omega_{24} & 0 & 2j^{-1}\Omega_{24} & 0 & 0 \\
... & 0 & 0 & 0 & -2j^{-1}\Omega_{25} & 0 & 0 & 2j^{-1}\Omega_{25} & 0 \\
j^{-1}\Omega_{24} & 0 & j^{-1}\Omega_{25} & 0 & 0 & 0 & 0 & 0 & 0 \\
0 & 0 & 0 & 0 & \tau_{23}^{-1} & -\tau_3^{-1} & 0 & 0 & \tau_{63}^{-1} \\
0 & 0 & 0 & 0 & 0 & 0 & 0 & 0 & 0 \\
0 & 0 & 0 & 0 & 0 & 0 & 0 & 0 & 0 \\
0 & j^{-1}\Omega_{35} & 0 & 0 & 0 & 0 & 0 & 0 & 0 \\
0 & 0 & 0 & 0 & 0 & 0 & 0 & 0 & 0 \\
0 & 0 & 0 & 0 & 0 & -2j^{-1}\Omega_{34} & 2j^{-1}\Omega_{34} & 0 & 0 \\
0 & 0 & 0 & 0 & 0 & -2j^{-1}\Omega_{35} & 0 & 2j^{-1}\Omega_{35} & 0 \\
j^{-1}\Omega_{34} & 0 & j^{-1}\Omega_{35} & 0 & 0 & 0 & 0 & 0 & 0 \\
0 & 0 & 0 & \tau_{14}^{-1} & 0 & 0 & -\tau_4^{-1} & \tau_{54}^{-1} & 0 \\
0 & -j^{-1}\Omega_{46} & 0 & 0 & 0 & 0 & 0 & 0 & 0 \\
-\tau_{||46}^{-1} & 0 & 0 & 0 & 0 & 0 & 0 & 0 & 0 \\
-j^{-1}\Omega_{56} & 0 & j^{-1}\Omega_{46} & 0 & 0 & 0 & 0 & 0 & 0 \\
j^{-1}\Delta_{46} & 0 & 0 & 0 & 0 & 0 & -2j^{-1}\Omega_{46} & 0 & 2j^{-1}\Omega_{46} \\
0 & -j^{-1}\Omega_{56} & 0 & 0 & 0 & 0 & \tau_{45}^{-1} & -\tau_5^{-1} & 0 \\
0 & j^{-1}\Delta_{56} & -\tau_{||56}^{-1} & \tau_{15}^{-1} & 0 & 0 & 0 & 0 & 0 \\
0 & -\tau_{||56}^{-1} & j^{-1}\Delta_{56} & 0 & 0 & 0 & 0 & -2j^{-1}\Omega_{56} & 2j^{-1}\Omega_{56} \\
0 & j^{-1}\Omega_{56} & 0 & 0 & \tau_{26}^{-1} & \tau_{36}^{-1} & 0 & 0 & -\tau_6^{-1}
\end{pmatrix} \times$$





$$Z = \begin{bmatrix} Z_{11} & 0 & 0 & Z_{14} \\ 0 & Z_{22} & Z_{23} & 0 \\ 0 & Z_{23} & Z_{33} & 0 \\ Z_{14} & 0 & 0 & Z_{44} \end{bmatrix}. \quad (2.60)$$

The dipole matrix for the six-state DM is written as

$$Z = \begin{bmatrix} Z_{11} & 0 & 0 & Z_{14} & Z_{15} & 0 \\ 0 & Z_{22} & Z_{23} & 0 & 0 & Z_{26} \\ 0 & Z_{23} & Z_{33} & 0 & 0 & Z_{36} \\ Z_{14} & 0 & 0 & Z_{44} & Z_{45} & 0 \\ Z_{15} & 0 & 0 & Z_{45} & Z_{55} & 0 \\ 0 & Z_{26} & Z_{36} & 0 & 0 & Z_{66} \end{bmatrix}. \quad (2.61)$$

### 2.3.5 Optical Gain Calculation

The optical gain of the active region can be estimated by the product of dipole moment and population inversion with Lorentzian shape assumption and calculated full-width-half-maximum (FWHM). The general optical gain can be described by

$$g(\omega) = \frac{\pi \hbar e^2}{2nc\epsilon_0 m^*} f_{ab} \Delta N L(\hbar\omega - \Delta_{ab}) \quad (2.62)$$

and

$$f_{ab} = \frac{2m^* \omega}{\hbar} Z_{ab}^2 \quad (2.63)$$

where  $f_{ab}$  is the oscillator strength,  $Z_{ab}$  is the dipole moment,  $n$  is the refractive index,  $c$  is the speed of light,  $\Delta N$  is the population inversion, and  $L$  is the Lorentz function. The dipole moment is generally defined as

$$Z_{ij} = |\langle \varphi_c^i | Z | \varphi_c^j \rangle|, \quad (2.64)$$

where  $Z$  is the position operator. The typical linewidth of THz QCL is around 1 THz, and can be estimated in frequency by  $\frac{1}{t_{fi}}$  from equation (2.50).

An alternative way to calculate optical gain without taking the Lorentzian shape assumption is presented in the DM-based model. The static tunneling-induced coherence is rewritten as  $\rho_{ij}^{(0)}$ , and the laser-induced coherence between state  $i$  and  $j$  is written as  $\widetilde{\rho}_{ij}$  or  $\widetilde{A}_{ij}$  and  $\widetilde{B}_{ij}$ . Hence, the total coherence is written as

$$\rho_{ij} = \widetilde{A}_{ij} e^{-j\omega t} + \widetilde{B}_{ij} e^{j\omega t} + \rho_{ij}^{(0)} \quad (i < j), \quad (2.65)$$

$$\rho_{ji} = \widetilde{A}_{ji} e^{j\omega t} + \widetilde{B}_{ji} e^{-j\omega t} + \rho_{ji}^{(0)} \quad (i < j, \widetilde{A}_{ji} = \widetilde{A}_{ij}^* \text{ and } \widetilde{B}_{ji} = \widetilde{B}_{ij}^*). \quad (2.66)$$

To simplify the calculation, rotating-wave approximation (RWA) is applied to rewrite coherence as

$$\rho_{ij} = \widetilde{\rho}_{ij} e^{-j\omega t} + \rho_{ij}^{(0)} \quad (i < j) \quad (2.67)$$



$$\begin{array}{cccccc}
0 & 0 & 0 & 0 & 0 & 0 \\
0 & 0 & \Delta_{13} - j\tau_{||13}^{-1} + \omega & -\Omega_{34} & \Omega_{12} & 0 \\
0 & 0 & 0 & 0 & 0 & 0 \\
0 & 0 & -\Omega_{34} & \Delta_{14} - j\tau_{||14}^{-1} + \omega & 0 & \Omega_{12} \\
0 & 0 & 0 & 0 & 0 & 0 \\
0 & 0 & \Omega_{12} & 0 & \Delta_{23} - j\tau_{||23}^{-1} + \omega & \Omega_{34} \\
0 & 0 & 0 & 0 & 0 & 0 \\
\Omega_{34} & 0 & 0 & \Omega_{12} & -\Omega_{34} & \Delta_{14} - j\tau_{||14}^{-1} + \omega \\
-\Omega_{34} & 0 & 0 & 0 & 0 & 0 \\
0 & 0 & 0 & 0 & 0 & 0 \\
\dots -\Delta_{14} - j\tau_{||14}^{-1} + \omega & -\Omega_{12} & 0 & 0 & 0 & \dots \\
0 & 0 & 0 & 0 & 0 & 0 \\
-\Omega_{12} & -\Delta_{24} - j\tau_{||24}^{-1} + \omega & 0 & 0 & 0 & 0 \\
0 & 0 & 0 & 0 & 0 & 0 \\
0 & 0 & 0 & 0 & 0 & 0 \\
0 & \Omega_{14} & 0 & -\Omega_{24} & 0 & 0 \\
0 & 0 & 0 & 0 & 0 & 0 \\
0 & 0 & 0 & \Omega_{13} & 0 & 0 \\
\Omega_{24} & 0 & 0 & 0 & -\Omega_{13} & -\Omega_{14} \\
0 & 0 & 0 & 0 & 0 & 0 \\
-\Omega_{13} & 0 & \Omega_{14} & 0 & \Omega_{24} & 0 \\
0 & 0 & 0 & 0 & 0 & 0 \\
0 & 0 & 0 & 0 & -\Omega_{24} & 0 \\
0 & 0 & 0 & 0 & 0 & 0 \\
0 & 0 & 0 & 0 & 0 & 0 \\
0 & 0 & 0 & 0 & 0 & -\Omega_{13} \\
0 & 0 & 0 & 0 & 0 & 0 \\
0 & 0 & 0 & 0 & 0 & -\Omega_{14} \\
-\Delta_{13} - j\tau_{||13}^{-1} - \omega & -\Omega_{12} & -\Omega_{34} & 0 & 0 & 0 \\
0 & 0 & 0 & 0 & 0 & 0 \\
\Omega_{12} & \Delta_{23} + j\tau_{||23}^{-1} + \omega & 0 & -\Omega_{34} & -\Omega_{13} & 0 \\
0 & 0 & 0 & 0 & 0 & 0 \\
\dots & \dots & -\Delta_{14} - j\tau_{||14}^{-1} - \omega & -\Omega_{12} & 0 & \Omega_{24} \\
\Omega_{34} & 0 & 0 & 0 & 0 & 0 \\
0 & 0 & 0 & 0 & 0 & 0 \\
0 & \Omega_{34} & -\Omega_{12} & -\Delta_{14} - j\tau_{||14}^{-1} + \omega & \Omega_{14} & 0 \\
0 & \Omega_{13} & 0 & \Omega_{14} & \Delta_{12} - j\tau_{||12}^{-1} - \omega & 0 \\
-\Omega_{14} & -\Omega_{24} & 0 & 0 & 0 & 0 \\
0 & 0 & 0 & 0 & 0 & 0 \\
0 & 0 & \Omega_{24} & 0 & 0 & 0 \\
0 & 0 & -\Omega_{13} & 0 & 0 & 0 \\
0 & 0 & -\Omega_{13} & 0 & 0 & 0 \\
0 & 0 & 0 & 0 & 0 & 0
\end{array}$$

$$\begin{pmatrix}
0 & 0 & 0 & 0 & 0 & \Omega_{14} \\
0 & -\Omega_{14} & 0 & 0 & 0 & 0 \\
\Omega_{13} & 0 & 0 & 0 & 0 & 0 \\
0 & 0 & -\Omega_{24} & 0 & \Omega_{13} & 0 \\
0 & 0 & 0 & \Omega_{34} & 0 & 0 \\
0 & \Omega_{24} & 0 & 0 & 0 & 0 \\
0 & 0 & 0 & -\Omega_{14} & 0 & 0 \\
0 & 0 & 0 & 0 & 0 & 0 \\
0 & 0 & 0 & 0 & -\Omega_{14} & 0 \\
-\Omega_{14} & 0 & 0 & 0 & 0 & 0 \\
0 & 0 & -\Omega_{13} & 0 & \Omega_{24} & 0 \\
\Omega_{24} & 0 & 0 & 0 & 0 & 0 \\
\vdots & 0 & -\Omega_{13} & 0 & 0 & 0 \\
0 & 0 & 0 & \Omega_{24} & 0 & \Omega_{13} \\
0 & 0 & \Omega_{14} & 0 & 0 & 0 \\
0 & 0 & 0 & 0 & 0 & 0 \\
0 & 0 & 0 & 0 & 0 & 0 \\
0 & 0 & \Delta_{12} - j\tau_{||12}^{-1} + \omega & 0 & 0 & 0 \\
\Delta_{34} - j\tau_{||34}^{-1} - \omega & 0 & 0 & 0 & 0 & 0 \\
0 & 0 & 0 & 0 & \Delta_{34} - j\tau_{||34}^{-1} + \omega & 0 \\
0 & 0 & 0 & -\Delta_{12} - j\tau_{||12}^{-1} - \omega & 0 & 0 \\
0 & 0 & 0 & 0 & 0 & -\Delta_{34} - j\tau_{||34}^{-1} - \omega \\
0 & -\Delta_{34} - j\tau_{||34}^{-1} + \omega & 0 & 0 & 0 & -\Delta_{34} - j\tau_{||34}^{-1} - \omega \\
0 & 0 & 0 & 0 & 0 & 0
\end{pmatrix} \times$$

$$\frac{2}{\Omega_L} = \begin{pmatrix}
\widetilde{A}_{13} \\
\widetilde{A}_{14} \\
\widetilde{A}_{23} \\
\widetilde{A}_{24} \\
\widetilde{A}_{31} \\
\widetilde{A}_{32} \\
\widetilde{A}_{41} \\
\widetilde{A}_{42} \\
\widetilde{B}_{13} \\
\widetilde{B}_{14} \\
\widetilde{B}_{23} \\
\widetilde{B}_{24} \\
\widetilde{B}_{31} \\
\widetilde{B}_{32} \\
\widetilde{B}_{41} \\
\widetilde{B}_{42} \\
\widetilde{A}_{12} \\
\widetilde{A}_{21} \\
\widetilde{A}_{34} \\
\widetilde{A}_{43} \\
\widetilde{B}_{12} \\
\widetilde{B}_{21} \\
\widetilde{B}_{34} \\
\widetilde{B}_{43}
\end{pmatrix} = \begin{pmatrix}
\rho_{12}^{(0)} \\
\rho_{12}^{(0)} \\
0 \\
0 \\
\rho_{22}^{(0)} - \rho_{33}^{(0)} \\
\rho_{22}^{(0)} - \rho_{33}^{(0)} \\
-\rho_{34}^{(0)} \\
-\rho_{34}^{(0)} \\
-\rho_{21}^{(0)} \\
-\rho_{21}^{(0)} \\
\rho_{22}^{(0)} - \rho_{33}^{(0)} \\
\rho_{22}^{(0)} - \rho_{33}^{(0)} \\
0 \\
0 \\
\rho_{43}^{(0)} \\
\rho_{43}^{(0)} \\
\rho_{13}^{(0)} \\
\rho_{13}^{(0)} \\
-\rho_{24}^{(0)} \\
-\rho_{24}^{(0)} \\
-\rho_{31}^{(0)} \\
-\rho_{31}^{(0)} \\
\rho_{42}^{(0)} \\
\rho_{42}^{(0)}
\end{pmatrix}.$$

(2.71)

Static tunneling-induced coherence  $\rho_{ij}^{(0)}$  has been solved in section 2.3.4. Optical gain is related to the imaginary part of susceptibility  $\chi''(\omega)$  as

$$g(\omega) = \chi''(\omega) \frac{\omega n g}{c}. \quad (2.72)$$

Susceptibility is related to polarization as described by

$$P = \varepsilon_0 \varepsilon_r \chi(\omega) E_z (e^{i\omega t} + e^{-i\omega t}) + c. c = \frac{|e|\langle \varphi | Z | \varphi \rangle}{V_{ar}}$$

$$\begin{aligned}
&= \frac{|e|}{V_{ar}} (|C_u|^2 Z_{uu} + |C_l|^2 Z_{ll} + C_u^* C_l Z_{ul} + C_l^* C_u Z_{lu}) \\
&= \frac{|e|}{V_{ar}} (0 + 0 + \rho_{ul}(w) Z_{ul} + \rho_{lu}(-w) Z_{lu}) + c. c \\
&= \frac{|e|}{V_{ar}} (\widetilde{A}_{ul}(w) Z_{ul} e^{-j\omega t} + \widetilde{B}_{ul} Z_{ul}(w) e^{j\omega t} + \widetilde{A}_{lu}(-w) Z_{lu} e^{-j\omega t} + \widetilde{B}_{lu}(-w) Z_{lu} e^{j\omega t}) + c. c,
\end{aligned} \tag{2.73}$$

where  $|\varphi\rangle = C_u|U\rangle + C_l|L\rangle$  is the mixed state for the two-state system of the upper lasing state (U) and the lower lasing state (L),  $V_{ar}$  is the volume of the active region,  $Z_{ij}$  is the dipole moment between states  $i$  and  $j$ , and  $E(e^{i\omega t} + e^{-i\omega t})$  is the external optical field, and only the electric field component in the Z growth direction is considered because of the intersubband polarization selection rule. The gain equation can be written as

$$\begin{aligned}
g(\omega) &= \frac{n_g \omega}{c} \text{Im} \left( \frac{|e| Z_{ul}}{V_{ar} \epsilon_0 E_z} (\widetilde{A}_{ul}(w) + \widetilde{A}_{lu}(-w)) \right) \\
&= \frac{n_g \omega}{c} \left( \frac{|e| Z_{ul}}{V_{ar} \epsilon_0 E_z} \text{Im} (2 \widetilde{A}_{ul}(w)) \right).
\end{aligned} \tag{2.74}$$

The electric dipole interaction term between lasing states can be described as

$$\hbar \Omega_L = |e| Z_{ul} E_z. \tag{2.75}$$

The overall optical gain ( $G(\omega)$ ) can be written as

$$G(\omega) = N g(\omega) = N_{3D} \frac{n_g \omega}{c} \frac{|e|^2 Z_{ul}^2}{\epsilon_r \epsilon_0 \hbar} \text{Im} \left( \frac{\widetilde{A}_{ul}(w)}{\frac{\Omega_L}{2}} \right), \tag{2.76}$$

where  $N$  is the total number of electrons, and  $N_{3D}$  is the doping concentration.

## 2.3.6 Model Validation

This section tests transport models by comparing simulated data with historical QCL experimental data.

### 2.3.6.1 Density Matrix-Based JV Simulation

DM model has been used to optimize resonant-phonon design and achieved the previous record-holder design (F47) [19]. The previous simplified DM for resonant-phonon optimization uses estimated pure dephasing time, and includes only four main states, so it is not suitable to design and simulate structures using six states, such as hybrid extraction/injection designs. The model presented in this thesis is extended to six states, and intrawell pure dephasing time is calculated using intrasubband scattering time as presented in section 2.2. Fig. 2-5(a) and (b) illustrate simulated IV curves and measured IV curves of V775 from [19] and the first hybrid extraction/injection design from [43]. The simulated IV curves are nonlasing curves, since lasing-induced current can be affected by factors, such as mirror loss from

fabrication, rather than from quantum design. For RP-based V775, the DM model-simulated IV curve agrees well with experimental data from zero bias up to the lasing threshold, as shown in Fig. 2-5(a). In Fig. 2-5(b), the DM model-simulated IV curve matches experimental data from 8 kV/cm to 12 kV/cm, which is the most important electric range that includes a lasing operating electric field. Compared with the RE model, the DM model tends to describe more energy level interaction via coherent tunneling than semiclassical scattering, and the approaches overestimate the current density for HEID devices at low electric field bias (no proper alignments) when electrons distribute semiclassically.

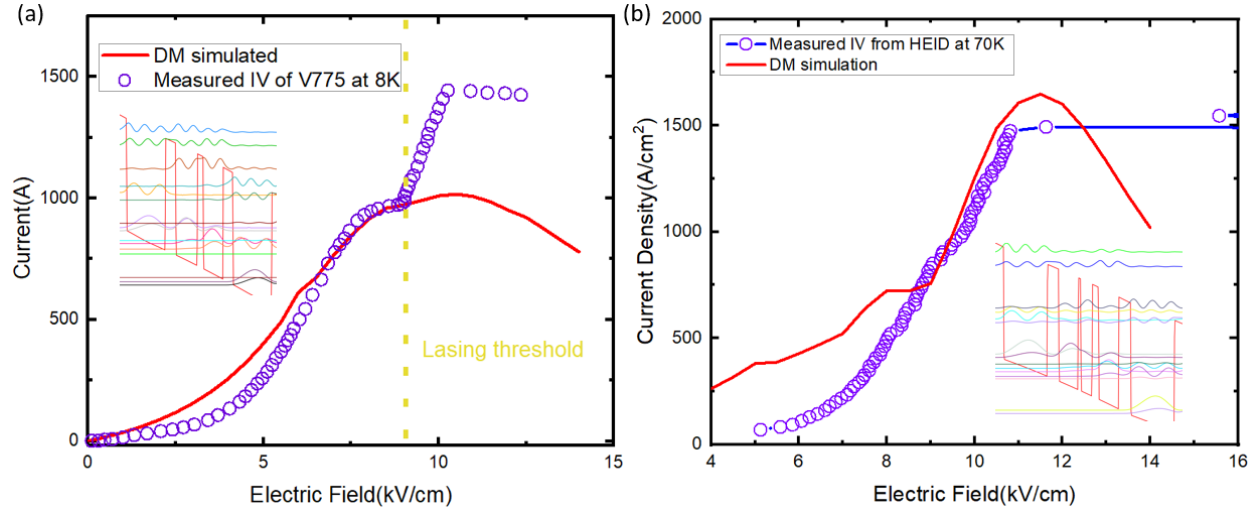


Fig. 2-5. DM simulated current-voltage curve comparison. (a) Device V775 (RP) at 8 K. (b) Hybrid extraction/injection design at 70 K. Insets shows corresponding conduction band diagram at design bias.

### 2.3.6.2 Rate Equation Model-Based JV Simulation.

RE model has more flexibility than DM model when applied to different structures. RE has been applied to simulate scattering-assisted designs, phonon-photon-phonon designs, and the first extraction/injection designs in this thesis. Because growth condition varies with time, the mean height of interface roughness is slightly adjusted for different designs grown at different benches. 3P designs are used to validate the simulation in Fig. 2-6(a) with an interface roughness mean height of 2.85 Å and a correlation length of 128 Å. A simulation result for the scattering-assisted structure in [63] is presented in Fig. 2-6(b), interface roughness mean height is assumed as 4 Å, and correlation length is kept at 128 Å. In Fig. 2-6(c), the first hybrid extraction/injection design from [63] is simulated with a mean interface roughness mean height of 3 Å/1.5 Å at the upper/lower interface, respectively, and a correlation length of 128 Å/65 Å at the upper/lower interface, respectively, as discussed in section 2.1. The interface roughness parameters interface roughness mean height and correlation length are adjustable parameters used from reasonable ranges of 6–15 nm and 2.85–5 Å, respectively [75].

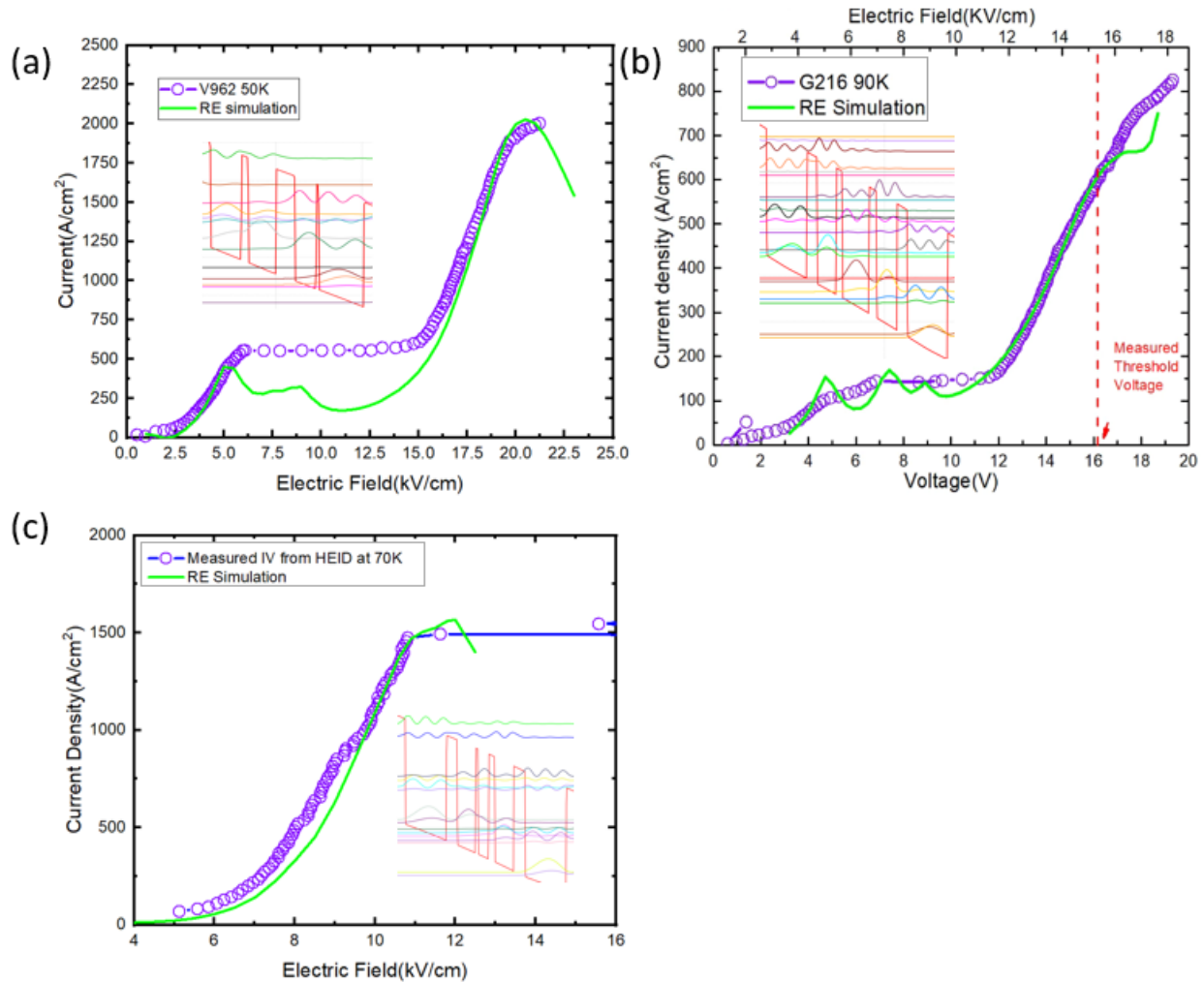


Fig. 2-6. RE simulation results in comparison with experimental data. (a) 3P structure V962. (b) SA structure G216. (c) The first Hybrid extraction/injection design. Insets shows corresponding conduction band diagram at design bias.

### 2.3.6.3 Optical Gain Calculation Validation.

A simulated optical gain of V775 at 200 K is shown in Fig. 2-7. Threshold optical gain is generally agreed around 25 /cm in the literature [19,64]. Simulated optical gain peaks at ~3.2 THz with a magnitude of 25 /cm. In [19,64], V775 targeted ~3.6 THz during the designing stage, but the experimental results show a slightly different lasing frequency of 3.22 THz at 199.5 K. Clearly, in terms of frequency, our approach agrees better with experimental results from [64]. The improvement is mainly due to the consideration of the non-chemically sharp interface described in section 2.1.

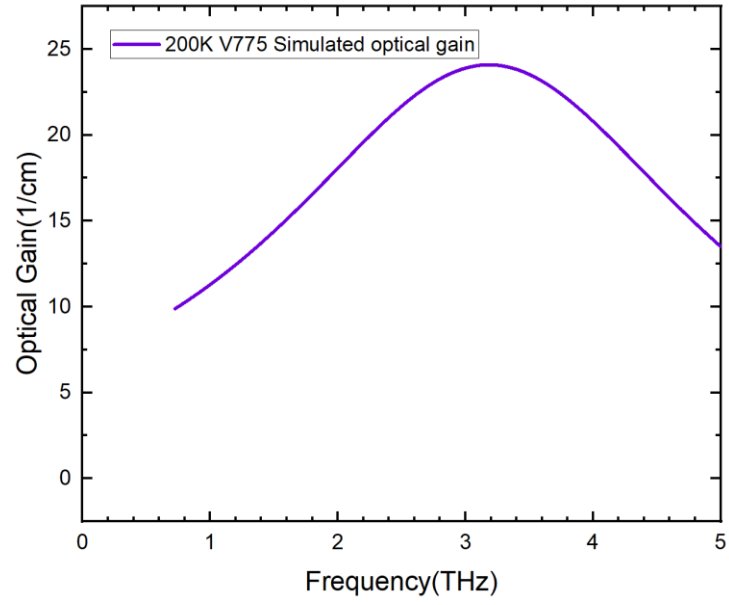


Fig. 2-7. Optical gain calculation of V775 at 200 K.



## Chapter 3 Experiment

To experimentally generate THz radiation and test the performance of THz QCL quantum structure design, the design has to be fabricated into actual device with optical cavity and characterized. The thickness of each GaAs/AlGaAs layer in the design is in nano scale and needs to be grown accurately with high quality to ensure that the quantum wells are well created in the design. Electrically pumped laser operation needs high quality optical cavity and electrical connection which is achieved by double metal waveguide fabrication. The actual device needs to be accurately characterized to know its performance for application and further improvement. This chapter summarizes the experimental method of THz QCLs fabrication and characterization.

### 3.1 Wafer Growth

The designed THz QCLs quantum structure is grown via molecular beam epitaxy (MBE) by Professor Wasilewski and his research team. The growth is performed on a semi-insulating GaAs substrate. A 0.2  $\mu\text{m}$  buffer layer is first grown on top of the substrate, after which a 0.3  $\mu\text{m}$   $\text{Al}_{0.5}\text{Ga}_{0.5}\text{As}$  is grown at 550  $^{\circ}\text{C}$  as the etch-stop layer. Active regions are sandwiched between a 100  $\text{\AA}$  undoped GaAs spacer followed by a  $1000 \text{\AA}/5 \times 10^{18} \text{ cm}^{-3} \text{ n}^+$  GaAs, then a 100  $\text{\AA}$  undoped GaAs spacer followed by a top stack of  $5 \times 10^{18} \text{ cm}^{-3} / 4 \times 10^{19} \text{ cm}^{-3}$  (500  $\text{\AA}/100 \text{\AA}$ )  $\text{n}^+$  GaAs layers, and finally capped with a 35  $\text{\AA}$  low-temperature grown GaAs layer.

The morphology is assessed under a Nomarski differential interference contrast microscopy to estimate the defect density which is one of the parameters to determine the growth quality. The defect density for wafer G499, referred to as the HEID wafer in the subsequent chapters, is 4  $\text{mm}^{-2}$  for large defects and 8  $\text{mm}^{-2}$  for all defects. High-resolution x-ray diffraction (HR-XRD) is employed to estimate the actual layer thicknesses and composition of the actual structure grown. The HR-XRD results of the G499 center area reveal that the thickness of the active region period is only 0.3% thinner than the target, and the magnitude of random variation in the layer thickness is  $\pm 0.2\%$ . A diagram of wafer G499 is illustrated in Fig. 3-1.

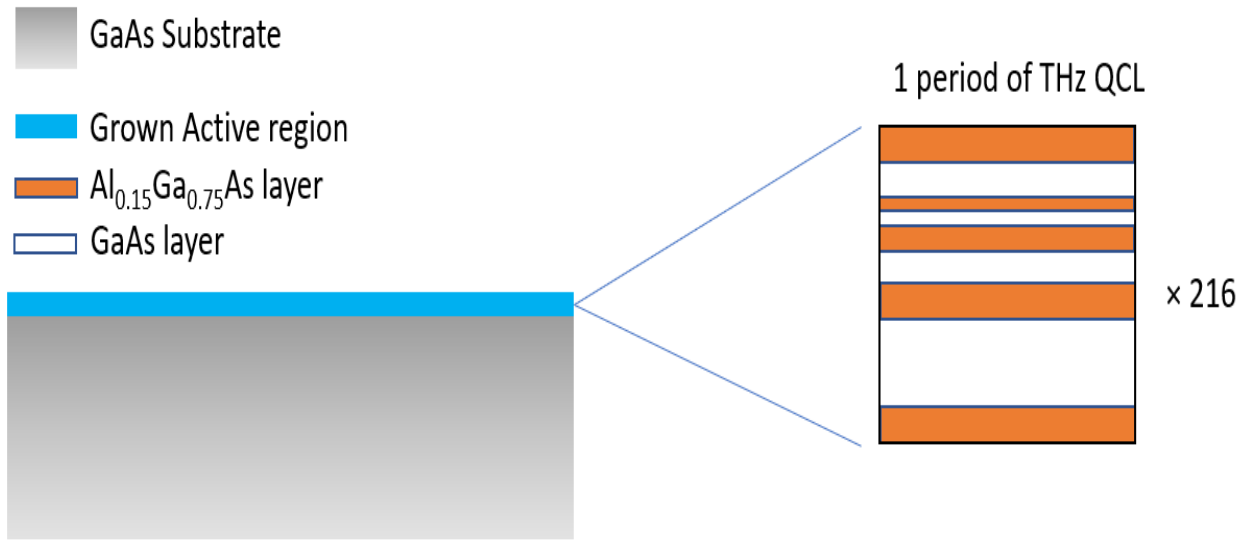


Fig. 3-1. Diagram of grown THz QCL active region on GaAs substrate.

### 3.2 Double-Metal Waveguide THz QCLs Fabrication Procedure

This section describes the fabrication procedure for THz QCL ridge waveguides conducted by the author in cleanroom. The fabrication procedure begins from a wafer grown in accordance with the procedure described in Section 3.1. The wafer is then cleaved into 1 cm × 1 cm pieces for fabrication. The general fabrication process can be summarized in seven steps, as depicted in Fig. 3-2. In Fig. 3-2, blue layers indicate the AR, while orange layers indicate the metal layers. After wafer cleaving, metal is deposited on top of the THz QCL wafer and receptor wafer, as presented in step 1. For example, the Ti/Au layers are deposited for Au-Au double metal waveguide fabrication, while the Ti/Cu layers are deposited for Cu-Cu double metal waveguide fabrication. The receptor wafers are cleaved into ~ 1.3 cm-1.3 cm pieces for the wafer bonding process. A die bonder is used during the wafer bonding process in step 2. Wafers are permanently bonded with the assistance of heat and pressure, as described in the following sections. For Cu-Cu bonding, the Cu metal on the receptor wafer that is not covered by QCL wafer will be quickly oxidized due to the heat and have no impact on subsequent steps of device fabrication, while the bonding area between the QCL wafer and receptor wafer is well bonded. After the bonding process, the ~600 μm GaAs substrate of the QCL wafer is removed by lapping and wet-etching process to expose the AR in step 3. Concentrated HF is used to remove the etch-stop layer. After the etch-stop layer is removed, photoresist is spin-coated and patterned for top metal deposition. In step 4, Ti/Au layers are deposited on top for Au-Au waveguide fabrication, while Ti/Cu/Au layers are deposited for Cu-Cu waveguide fabrication. A thin layer of Au is deposited on top of Cu to avoid oxidation and assist wire bonding in the

last step. Step 5 illustrates the result when photoresist is removed by PG removal during lift process. Once again, the photoresist is spin-coated and patterned for dry-etching process. The AR area that is not covered by metal/photoresist will be etched off to the fabricated ridge waveguide lasers in step 6. In the final step (7), Au is deposited on the backside of the receptor wafer, and the fabricated piece is cleaved into a 1-2 mm long laser die and bond on copper package via Au-In bonding. Wires are bonded on top of the ridge waveguide and the top of the receptor wafer as electrodes for Au-Au waveguides. Wires are bonded to the top of the ridge waveguide and the top of the copper package for electrical connections for Cu-Cu waveguide devices. The following sections provide detailed account of each step.

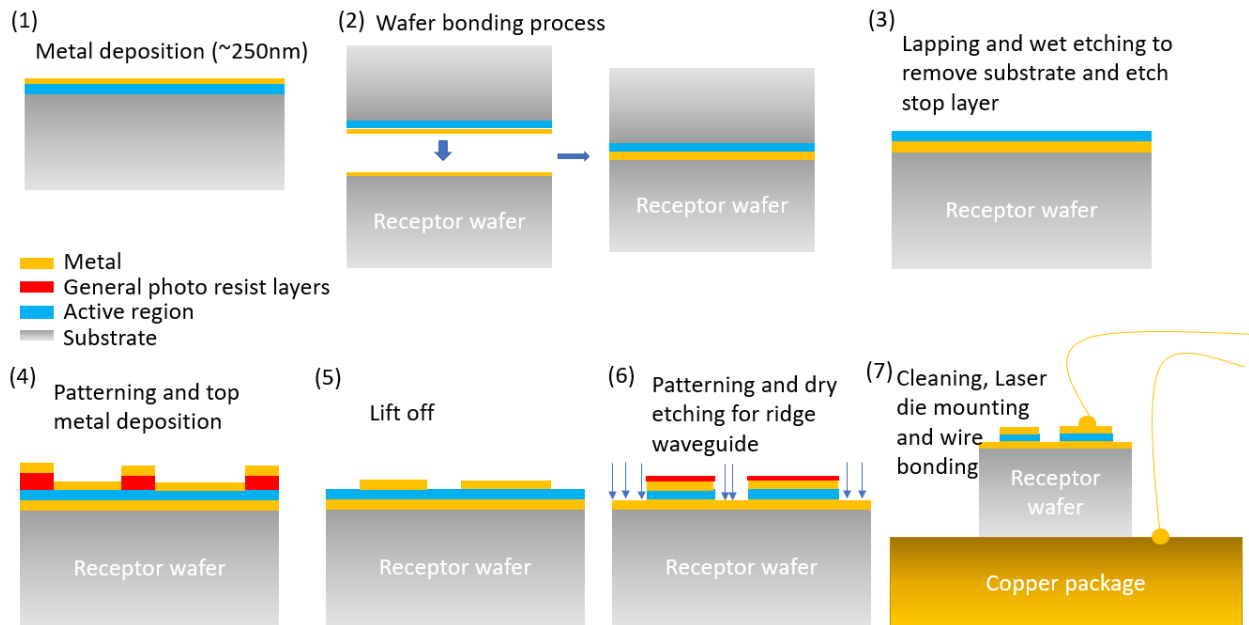


Fig. 3-2. Schematic diagram of THz QCLs major fabrication steps.

### 3.2.1 Wafer Bonding Process

Three bonding methods have been tested in this thesis, and their scanning electron microscope (SEM) images are illustrated in Fig. 3-3. The most common metal used for fabrication is Au because of its stable chemical properties. In the first step, both QCL wafers and receptor wafers are coated by Ti/Au film via E-beam evaporation. The thin layer of Ti serves as an adhesion layer. Special care is needed during the bonding process to avoid Ti diffusion into the surface to form  $TiO_2$ , which can prevent good Au-Au bonding [65,66]. Conversely, Au is not very likely to diffuse through Ti layers to the active region side [66]. Temperature ramps relatively fast to the targeting temperature of 300 °C in 30 minutes, and a 3.5 Mpa pressure is maintained for the bonding wafers during the bonding process. The bonding interface of Au-Au bonding is depicted in Fig. 3-3(b). In-Au bonding is also performed in early stage, in which a  $\sim 1 \mu m$  In layer is deposited on the receptor wafer, and a Ti/Au file is deposited on THz QCL wafer via E-

beam evaporation and electrode plating. During the In-Au bonding process, temperature ramps to 200 °C in 15 minutes and remains at 200 °C for 30 minutes with a pressure of 0.5 Mpa on top of the two bonding wafers. The bonding interface of In-Au bonding is presented in Fig. 3-3(c). Cu-Cu bonding has been reported in the literature to demonstrate good temperature performance of THz QCLs. In the final step, Cu-Cu bonding is tested and fabricated. Both 250 nm Ti/Cu layers are deposited on THz QCL and receptor wafers, making the total thickness of the bonding interface at ~500 nm, which is relatively thinner than that of Au-Au and In-Au bonding. A targeting temperature of 285 °C and pressure of 3.5 Mpa are used in the bonding process. The Cu-Cu bonding interface is characterized by SEM, as presented in Fig. 3-3(a). The bonding interfaces are characterized when the wafers are developed into ridge waveguide devices after step 6 in Fig 3-2.

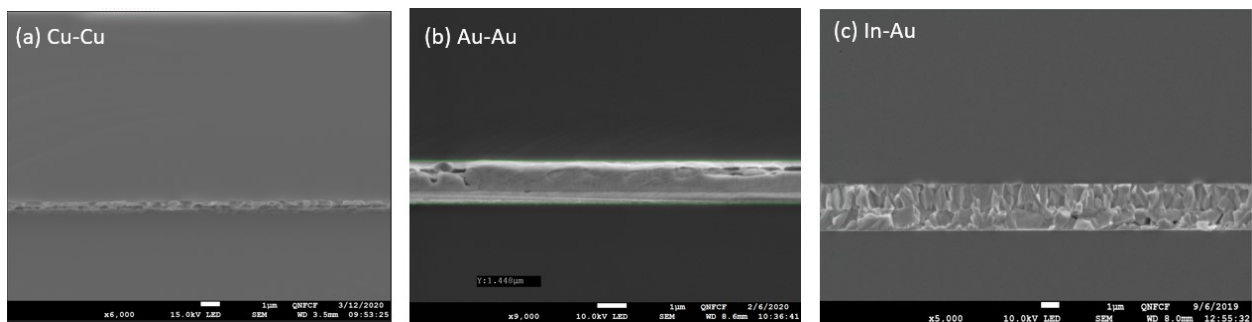


Fig. 3-3 Comparison of bonding interface among the devices. (a) Cu-Cu bonding interface, (b) Au-Au bonding interface, and (c) In-Au bonding interface.

### 3.2.2 Lapping and Wet-Etching

The typical GaAs substrate used for MBE growth is ~600 μm in thickness and is completely removed by lapping and wet-etching. Lapping is achieved with a lapping machine, and the wafer is mounted to a glass pad by wax, as illustrated in Fig. 3-4(a). Fig. 3-4(b) shows the lapping machine we used in the procedure. Our lapping solution is a mixture of 3 μm Al<sub>2</sub>O<sub>3</sub> with water in a ratio of 1:10. A ~500 μm substrate is removed during the lapping process. The design of lapping machine can roughly ensure the lapping is in parallel to the device surface; additionally, around 100 μm substrate is left on purpose to avoid damage of AR from imperfect parallel lapping process. The receptor wafer is mounted on a Si wafer with photoresist, and the sidewalls are carefully covered with photoresist to avoid etching at the backside. Fig. 3-4(c) shows the sidewalls. The remaining substrate is removed via wet etching by dipping the wafer into a solution comprised of 100 g citric acid and 33 mL hydrogen peroxide diluted in 100 mL DI water. The wet etching solution should be highly selective to etch GaAs and stop etching at the etch-stop layer, which is Al<sub>0.5</sub>Ga<sub>0.5</sub>As layer. Regular cleaning process with acetone, isopropyl alcohol (IPA), and deionized (DI) water removes photoresist and prepare the wafer for subsequent steps. To remove the etch-stop layer Al<sub>0.5</sub>Ga<sub>0.5</sub>As, the device is cleaned with acetone, IPA, and DI water, and then dipped in

concentrated HF solution for 50 seconds. A rainbow of color changes should be observed during the etch-stop layer removal process.

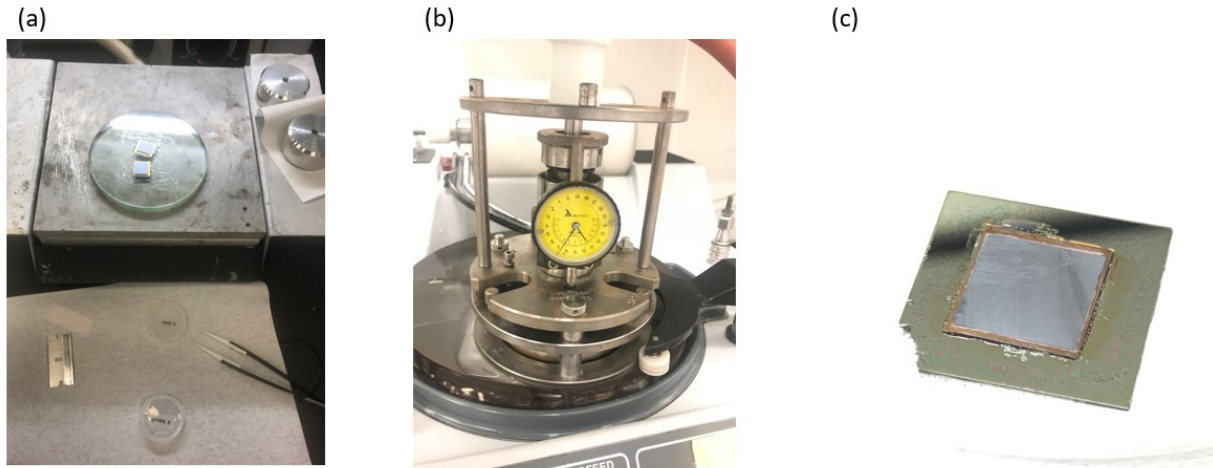


Fig. 3-4. Substrate removal process. (a) Mounting wafer on glass pad with wax. (b) Lapping process on lapping machine. (c) Device during wet-etching process.

### 3.2.3 Patterning, Top Metal Deposition, and Lift-Off

This step focuses on depositing metal for top contact and consists of three main parts: bi-layer photoresist patterning, metal deposition, and lift-off process.

In the bi-layer photoresist patterning step, PGMI-SF7 is applied uniformly on the wafer via a spin-coating process as a lift-off photoresist, and the wafer is baked at  $\sim 180$  °C on a hot plate for 90 seconds. Photoresist S1811 is uniformly applied as the second layer for imaging, and the wafer is baked again at  $\sim 120$  °C for 90 seconds. Patterning is achieved using MLA 150 direct-write UV lithography system. An e-version mask for patterning is displayed in Fig. 3-5. In the figure, the covered parts are ridges of 150  $\mu\text{m}$ , 120  $\mu\text{m}$ , 80  $\mu\text{m}$ , 60  $\mu\text{m}$ , and 40  $\mu\text{m}$  in width. The round shape is for disk device with radius of 75  $\mu\text{m}$ . Small-size disk device can be used to extract the IV curve with minimized extra voltage drop on the wire resistance. The exposed photoresist is developed in MF-319 for imaging.

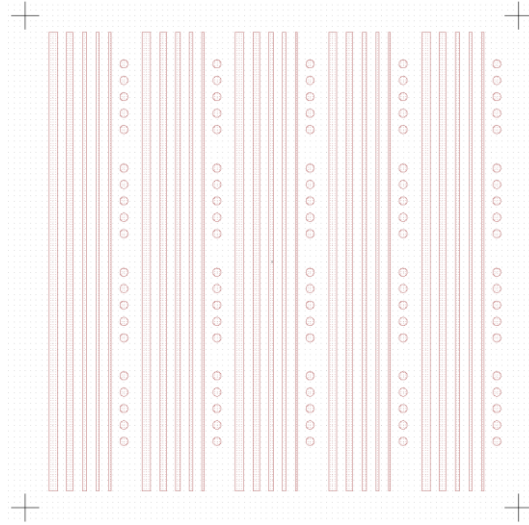


Fig. 3-5. Top metal mask for patterning in MLA direct-write UV lithography system. Ridge width are 144  $\mu\text{m}$ , 116  $\mu\text{m}$ , 80  $\mu\text{m}$ , 60  $\mu\text{m}$ , and 40  $\mu\text{m}$ . Disk radius is 72  $\mu\text{m}$ .

Top metal is deposited by E-beam evaporation system. For Au-Au waveguide devices, 10/250 nm Ti/Au layers are deposited, while 10/200/50 nm Ti/Cu/Au layers are deposited for Cu-Cu waveguide devices. During the lift-off process, Au-Au waveguide device can be dipped in PG-remover at 95 °C overnight to complete the lift-off process. Cu-Cu waveguide device must be handled with caution during the lift-off process. Normally, 4-hour dipping in PG-remover at 95 °C is sufficient to remove most of the lift-off resist, and the residuals can be rinsed off with IPA/Acetone. It has been reported that Ta might be better suited as adhesive layer than Ti layer for Cu-Cu waveguide, but Ta is not permitted in our E-beam evaporation system in NanoFab at the time of writing. After the lift-off process, the wafer is cleaned with acetone, IPA, and DI water, as mentioned in previous steps.

### 3.2.4 Second Patterning and Dry Etching

The purpose of the second patterning is to cover the metal area with photoresist to avoid etching on the metal, which can cause chamber contamination and metal re-deposition. A sample of the mask for the second patterning is presented in Fig. 3-6. The width of the ridges is slightly increased by a few  $\mu\text{m}$  to fully cover the metal area. The exposed photoresist is developed in AZP400K for imaging.

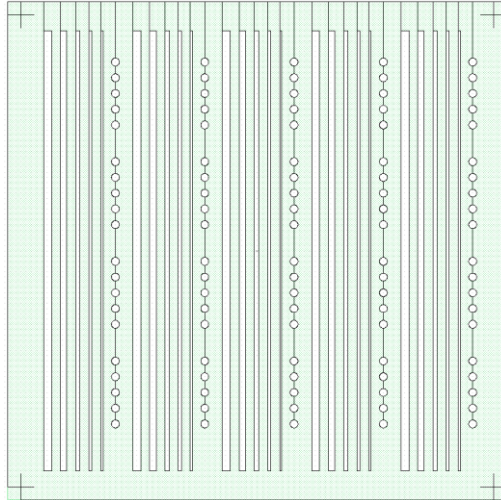


Fig. 3-6. Mesa etch mask for the second patterning. Ridge width are 152  $\mu\text{m}$ , 122  $\mu\text{m}$ , 82  $\mu\text{m}$ , 58  $\mu\text{m}$ , and 38  $\mu\text{m}$ .  
Disk radius is 75  $\mu\text{m}$ .

Dry etching is conducted with a meta reactive ion etching system.  $\text{Cl}_2$ ,  $\text{BCL}_3$ , and Ar are used as etching receipts. The sidewalls of the ridges are depicted in Fig. 3-7. After dry-etching, the wafer is again cleaned with PG-remover, acetone, IPA, and DI water.

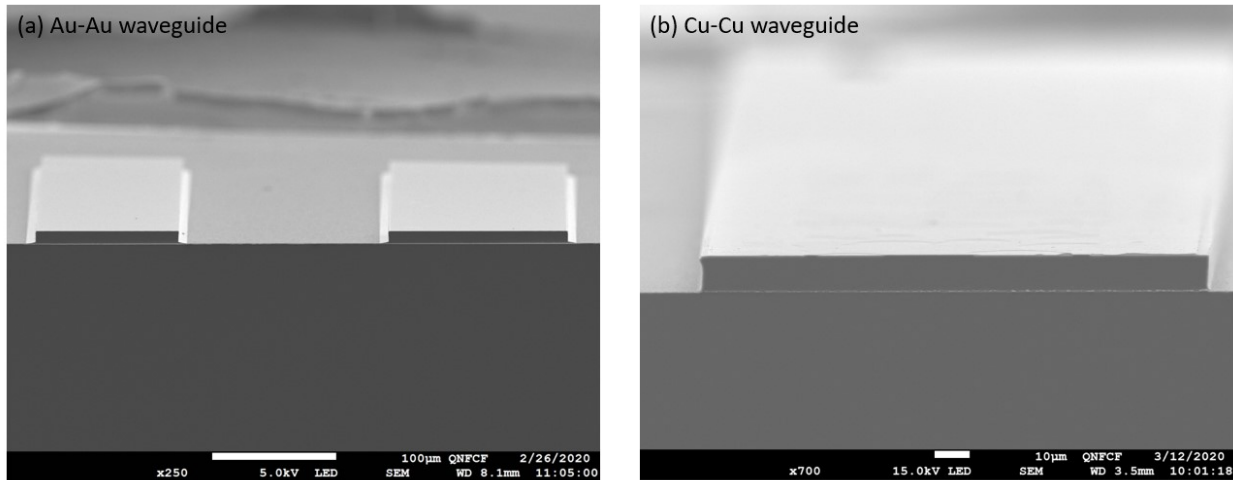


Fig. 3-7. SEM image of fabricated ridges. (a) Au-Au waveguide. (b) Cu-Cu waveguide.

### 3.2.5 Laser Die Mounting and Wire Bonding

Fabricated wafers are cleaved into 1-2 mm long laser dies which in turn are mounted on a gold-coated copper package via In-Au bonding. During laser die mounting step, a glass slide is used to place a thin indium piece on the copper package. The copper package is placed on a hot plate targeting  $\sim 170^\circ\text{C}$  to melt indium. Blade coating technique is used to uniformly coat the indium around the mounting area on the gold-coated copper package. After indium coating, a heat proof tweezers is used to gently place a laser bar on the indium coated area. The gold deposited substrate is towards the indium film, and the laser bar



is gently pressed to ensure good contact between the gold layer and indium film. Hot plate is then turned off, and the gold-coated copper package is allowed time to return to room temperature. After the laser die is mounted, gold wire is used to connect the bonding pad and laser ridges via a ball bonder. The first bonding point is on the package gold pad which is designed for wire bonding, and the second bonding point is on the laser ridge. The ultrasonic power is reduced to 300, which is an arbitrary unit in system programming panel, and the force is set low to avoid damage on laser ridge waveguide. After some trials, the ball bonder (west bond model 747677E series) in QNC cleanroom is able to wire bond to ridge waveguide as narrow as 40 $\mu$ m without causing any damage. For the Au-Au waveguide, a wire can bond from ground bonding pad to the gold substrate to form good grounding. A highly doped substrate is used for Cu-Cu waveguide to ensure good grounding connection, because the wire bonding on the substrate is difficult to achieve due to copper's susceptibility to oxidation. A packaged laser bar ready for characterization is presented in Fig. 3-8.

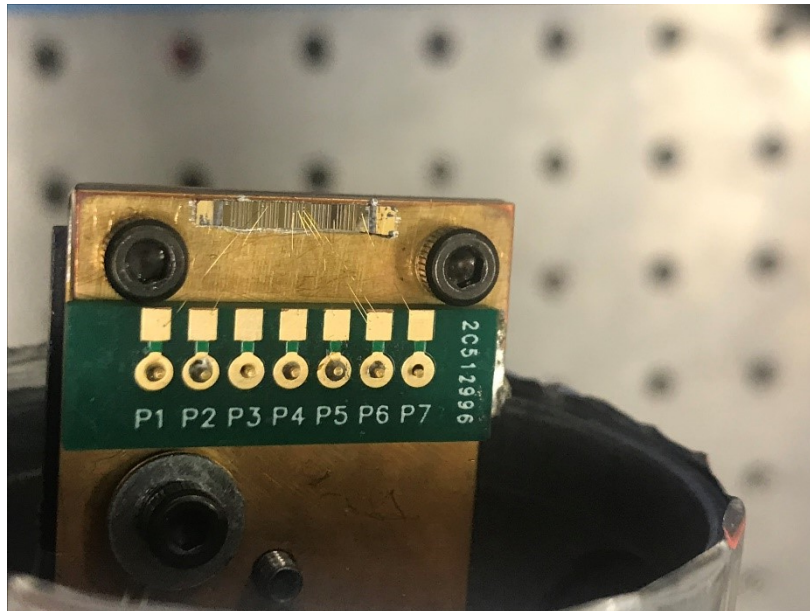


Fig. 3-8. Packaged laser bar used in the test.

### 3.3 Characterization System of THz QCLs

Two characterization methods are commonly used for THz QCLs: light-current-voltage (LIV) measurement and spectra measurement. This section described the methods used by the author.

At the time of writing, the operation of THz QCLs is still limited to the temperature lower than room temperature. A cryogenic cooler is required for THz QCLs to lase at frequency of  $\sim$ 1–5.4 THz. To cool down the device to lower than 0  $^{\circ}$ C, a sufficient vacuum is needed to prevent moisture condensation and freezing on the device. A vacuum chamber for the cryogenic cooler is designed using Solidwork software. Fig. 3-9 illustrates the construction of the vacuum chamber. The cryogenic cooler used is a Sumitomo



(SHI) CH-110 Cryocooler. The out chamber is used to create a vacuum seal with double O rings, and the inner shield is designed for heat radiation flux blocking. A laser device is mounted on a 7-pin package. A device package and temperature sensor are mounted on the cold finger, which in turn is mounted on a cryostat cold head through a copper connector. A heater is tightly attached to the cold finger to adjust the temperature for temperature-dependent measurement. The newly constructed system can work at 20 K, which is the designed lowest cooling temperature of Sumitomo (SHI) CH-110. It can still work at ~30 K after 5 years of use, the possible reason for the minimum temperature rising could be the slight loss of recycled helium gas and accumulated particles which is hard to be removed by vacuum pump.

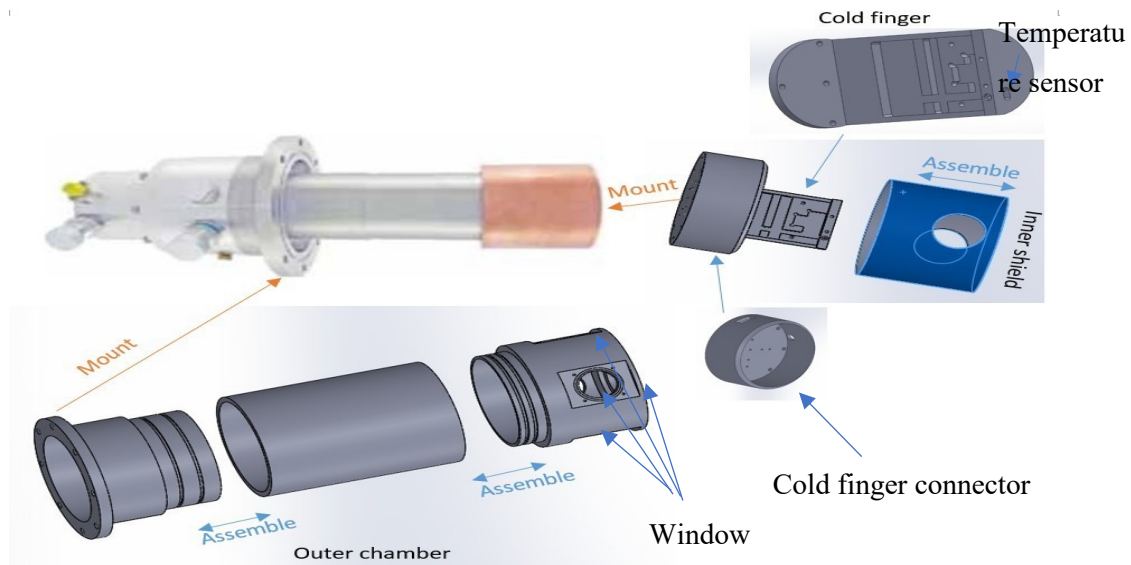


Fig. 3-9. Chamber design schematics for cryogenic cooler.

The device is electrically pumped by AVTECH (AVO-6C-B) pulse generator in pulse mode. A pulse with repeating frequency of 500 Hz and pulse width of 500 ns is regularly used for our measurement. A circuit, as illustrated in Fig. 3-10, is constructed to monitor the current and voltage on the QCL device in measurement. A 40 Ohm resistance is added for impedance-matching.

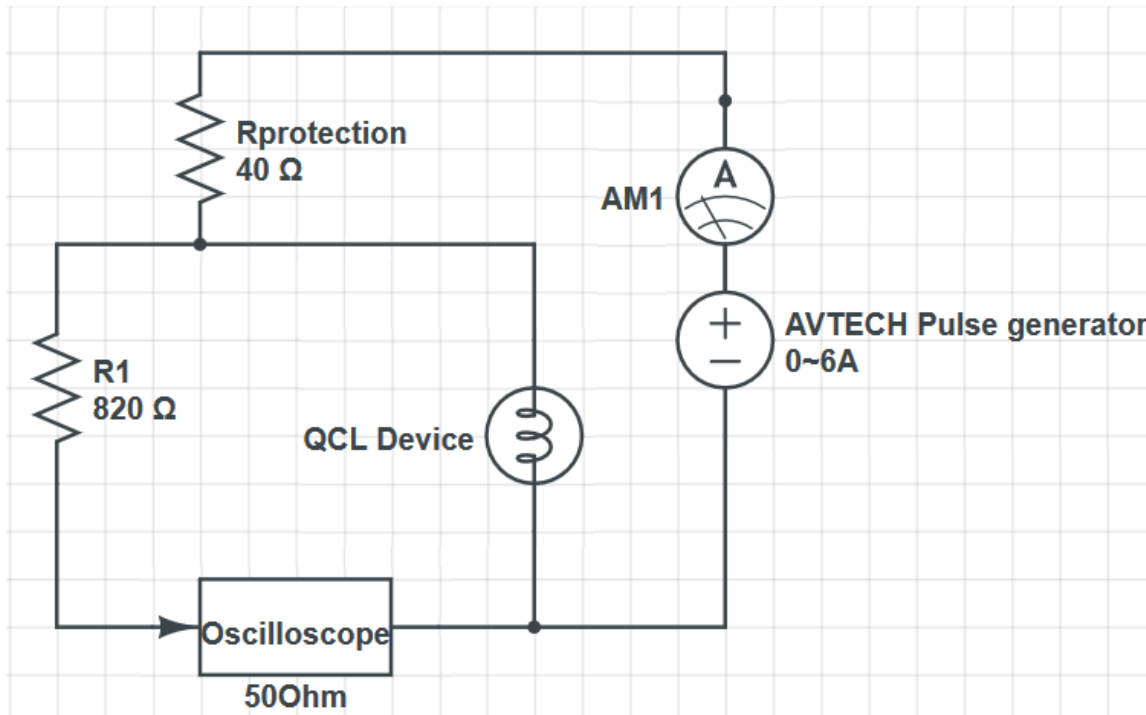


Fig. 3-10. Circuit board diagram.

The light signal is measured by a Golay cell and amplified using a lock-in amplifier. An extra pulse generator is used to modulate low-frequency pulse (20 Hz) due to the slow response time of Golay cell. The extra pulse generator, with 50 ms pulse width and 20 Hz frequency, is injected into the reference-in port in the lock-in amplifier and the gate port in the AVETECH pulse generator, which pumps THz QCLs.

Since the broadband signal can be measured by Golay cell in LIV measurement, it is necessary to measure spectra to confirm the frequency of emitting radiation from THz QCL devices. The spectra of THz QCL are measured by using Fourier-transform infrared spectroscopy (FTIR) spectrometer and Si-bolometer. A QCL device for spectra measurement is set as external light source, and a Si-bolometer is set as external detector for FTIR spectrometer. The optical path diagram is presented in Fig. 3-11. The entire optical path is purged with dry nitrogen to reduce water absorption. Substantial optical alignments are needed to enhance signal-to-noise ratio in spectra measurements.

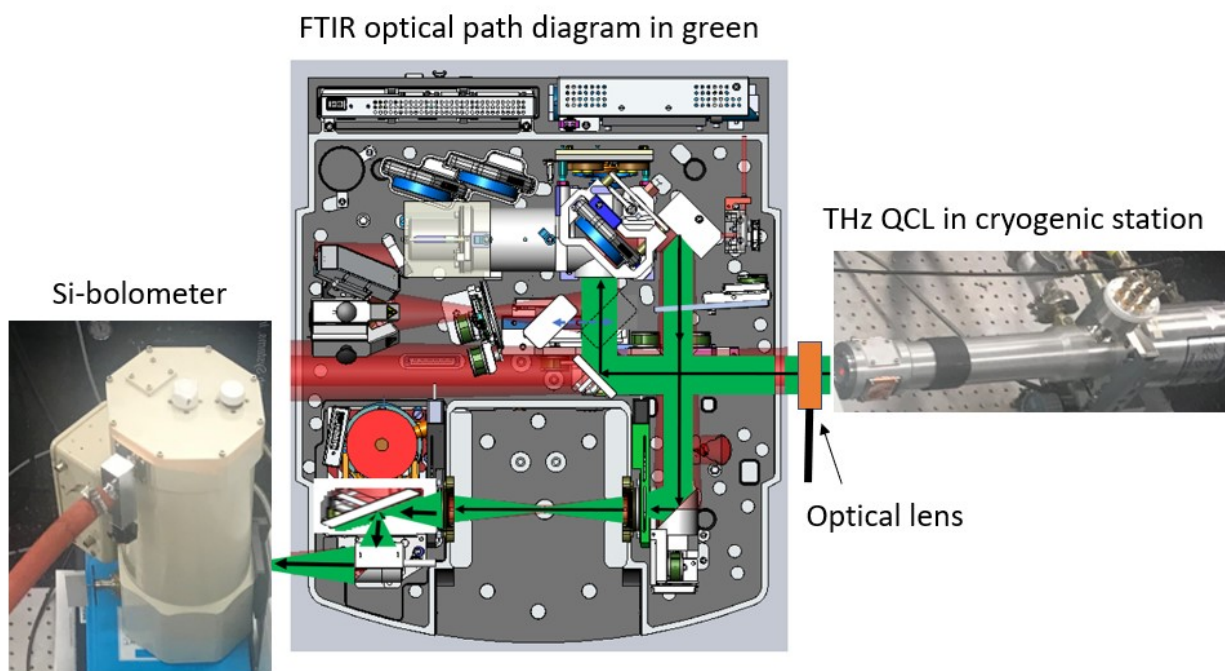


Fig. 3-11. Optical path setup for spectra measurement.

# Chapter 4 Dual Lasing Channel THz QCL Based on Scattering Assisted Injection Scheme

## 4.1 Introduction

Terahertz Quantum Cascade Laser has been recognized as one of the most promising coherent radiation sources in EM band since its inception [7,67]. To date, THz QCLs can cover a wide frequency of ~1–5 THz [68] and produce watt-level output power in pulse mode [55,69]. THz QCLs have been used in some practical applications, but technical difficulties, such as cryogenic operating temperature [14,64,104] and poorer performance at lower frequencies (<2.5 THz) [68], prevent further and wider deployment of this device technology. Since the characteristic absorption of many biomolecules is located in the THz range, largely at frequencies below 2.5 THz [4], it is of scientific interest and technological importance to develop THz QCLs at these frequencies. Broadband emission is another challenge that remains to be addressed, which is not only essential for the biomolecular terahertz spectroscopy but also critical for other applications such as frequency comb operation and tunable THz emission sources [70,71]. Bound to continuum-based quantum designs are most commonly used for broadband terahertz emission. However, the broadband gain in the bound to continuum (BTC) structures is achieved often at the expense of device operating temperature performance. As a result, BTC-based THz QCLs can lase only at lower temperatures compared to THz QCLs based on RP or scattering-assisted designs at the similar frequencies [68]. Bidirectional THz QCL is another option to achieve broadband emission – light emission at different terahertz frequencies when the device bias polarity is switched [72]. Dual color emission operation under the same device bias polarity is also observed when the devices are biased at different voltages. The THz QCL in [34] first lased at ~4 THz at lower bias (a lower current injection), then at ~1.8 THz at higher bias, which is attributed to sequential turn-on of two different lasing transition channels. A substantial spectral gap ( $4 - 1.8 = 2.2$  THz) is present between the two lasing frequencies.

This chapter analyzes four-well GaAs/Al<sub>0.17</sub>Ga<sub>0.83</sub>As THz QCLs based on the scattering-assisted scheme that lases up to 144 K. The Al composition of AlGaAs barriers is 17%, providing better suppression for leakage current to continuum band at higher temperature than conventional designs with 15% Al composition. This statement is evidenced by a lower threshold current density than that of the existing SA-based designs listed in table 4-1. A large injection coupling strength (1.7 meV) is adopted here. Numerical simulations predict that two lasing channels contribute to device optical gain, which is supported by experimental results. The devices exhibit lasing emission spectra covering 2.3-2.6 THz and a large dynamic range of ~550–825 A/cm<sup>2</sup> (at 20 K). The study shows that THz QCL quantum design allowing two lasing channels might be a promising approach to achieve wide frequency coverage, low

threshold current density, and good device performance at low frequency (~2.5 THz). Compared to the device reported in [73] that emits light in similar frequency, our device achieves 26% lower threshold current density, wider frequency coverage (0.3 THz to 0.13 THz), and the same maximum operation temperature are achieved. A summary of previous scattering-assisted structures with top temperature performance is listed in table 4-1.

Design	Material System	Main frequency	T <sub>max</sub>	Current Density (heatsink temperature)	Injection coupling strength $\hbar\Omega$	Oscillator strength
Kumar et al. [34]	GaAs/Al <sub>0.15</sub> Ga <sub>0.85</sub> As	1.8 THz and 4THz	163 K	865 A/cm <sup>2</sup> (10 K)	1.5 meV	0.6
Dupont et al. [27]	GaAs/Al <sub>0.25</sub> Ga <sub>0.75</sub> As	3.2 THz	138 K	1170 A/cm <sup>2</sup> (10 K)	1.14 meV	0.39
Razavipour et al. [33]	GaAs/Al <sub>0.25</sub> Ga <sub>0.75</sub> As	2.4 THz	153 K	800 A/cm <sup>2</sup> (10 K)	0.845 meV	0.27
Razavipour et al. [32]	GaAs/Al <sub>0.25</sub> Ga <sub>0.75</sub> As	2.67 THz	151 K	1440 A/cm <sup>2</sup> (10 K)	1.54 meV	0.27
Khanal et al. [73]	GaAs/Al <sub>0.15</sub> Ga <sub>0.85</sub> As	2.1 THz	144 K	745 A/cm <sup>2</sup> (46 K)	~1.55 meV	0.39
This work	GaAs/Al <sub>0.17</sub> Ga <sub>0.83</sub> As	2.4 THz	144 K	550 A/cm <sup>2</sup> (50 K)	1.7 meV	0.44 and 0.27

Table 4-1. SA-based THz QCL structure key parameters and performance summary [63].

## 4.2 THz QCL Design and Simulation

(a) Conduction band diagram at 15.4kV/cm (b) Conduction band diagram at 17.5kV/cm (c) Scattering time

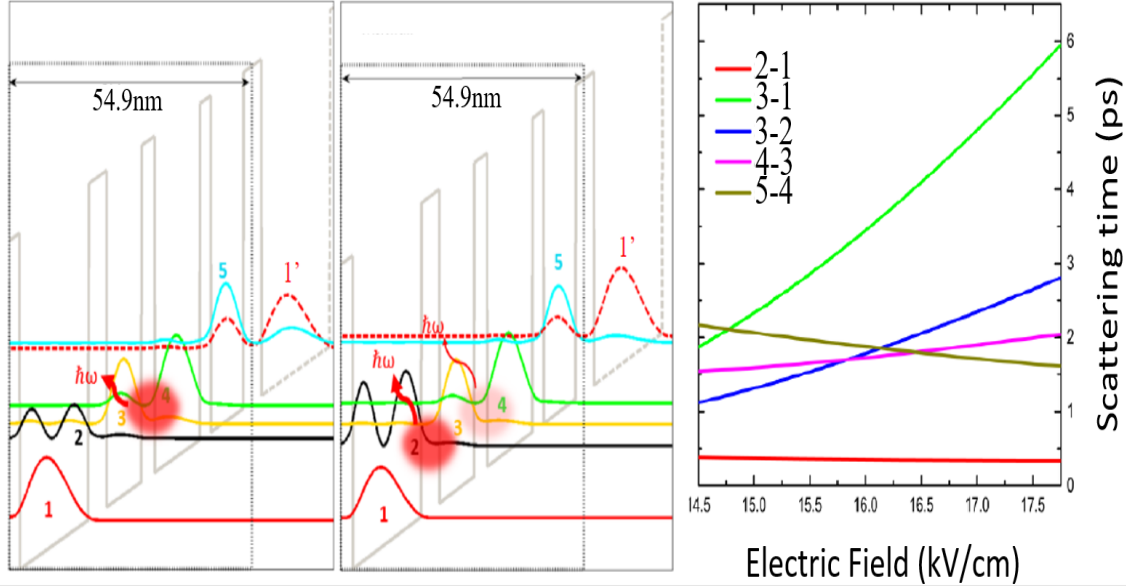


Fig. 4-1. Dual lasing channel SA-based structure conduction band diagram and scattering time. Conduction band diagram at electric field of 15.4 kV/cm (a) and 17.5 kV/cm (b). (c) Simulation of scattering time between state 3-1 (green), state 2-1 (red), state 3-2 (blue), state 5-4 (brown), and state 4-3 (pink) versus electric field at 30 K [63]. Scattering-assisted design schemes show the best temperature performance at low frequency (<2.5 THz) because of its efficient and selective charge carrier injection [68,65]. At low frequencies, the energy spacing ( $\sim 10$  meV) between lasing states is comparable to the energy broadening ( $\sim 4$  meV) [24], so, it is more challenging to selectively inject carriers to the upper lasing state rather than the lower lasing state [73]. In order to sustain higher population inversion to achieve high optical gain for wide frequency coverage, a GaAs/ $\text{Al}_{0.17}\text{Ga}_{0.83}\text{As}$  quantum design based on scattering-assisted pumping scheme is adopted. Each period consists of four quantum wells and four barrier layers, the thickness of the actual layer extracted from HRXRD measurement in angstrom are **40.3/74.4/24.1/103.6/29.7/79.7/40.3/156.7**, starting from the rightmost barrier in the period (shown in Fig. 4-1) with barriers indicated in bold fonts and doped layer underlined. The widest well is n-doped with Si at  $2.02 \times 10^{16} \text{ cm}^{-3}$ , and average sheet doping density in one period is  $3.17 \times 10^{10} \text{ cm}^{-2}$ .

The conduction band diagrams at electric fields of 15.4 and 17.5 kV/cm are shown in Fig. 4-1 (a) and (b), respectively, together with energy levels and square of their corresponding wavefunctions. In one period, carrier transport and potential optical transition basically involve five lowest quantum states (1-5). State 5 is highly coupled with state 1' from previous period for effective electron inter-period transport.

Population inversion can potentially be built up between state 4 and 3, and between state 3 and 2, yielding two stimulated emission transitions, as denoted in Fig. 4-1.

State 5 is located  $\sim 30.3$  meV- $32.7$  meV above state 4 at electric fields from  $15.4$  to  $17.5$  kV/cm. Though the energy separation is slightly less than GaAs LO phonon energy ( $36$  meV), the electron- LO phonon scattering from state 5 to 4 is adequately efficient [27, 33]. As shown in Fig 4-1(c), the calculated scattering time  $\tau_{54}$  is below  $2.5$  ps in this electric field range and decreases as the increasing of the electric field. The scattering times for other transitions ( $\tau_{21}$ ,  $\tau_{42}$ ,  $\tau_{32}$ ,  $\tau_{43}$ ) are also plotted in Fig. 4-1(c). The states 3 and 2 are aligned at an electric field of  $12.4$  kV/cm, while the state 1' aligns with the state 5 at  $15.4$  kV/cm. At a lower bias ( $\sim 15$  kV/cm), the state 3 is depopulated via scattering and resonant tunneling to the state 2 (only semi-classical scattering is included in Fig. 4-1(c)), and electron population inversion is achieved between states 4 and 3. This yields the first stimulated optical transition (so-called the first lasing channel thereafter). Simulation shows that lasing frequency of subbands 4-3 is  $2.27$  THz ( $9.4$  meV) at  $15.4$  kV/cm. While the applied electric field is increased to  $17.5$  kV/cm, the states 3 and 2 become misaligned and the electron transport from 3 to 2 is significantly slowed down. As shown in Fig. 4-1(c),  $\tau_{32}$  increases from  $\sim 1$  ps at  $14.5$  kV/cm to  $\sim 3$  ps at  $17.75$  kV/cm in Fig. 4-1(c). Nevertheless, state 3 continues to be populated directly from the state 4 via nonradiative scattering or stimulation emission transition or even directly from the state 5 via LO phonon scattering ( $\tau_{53}$  is  $6-9$  ps which is not shown). In particular,  $\tau_{32}$  exceeds  $\tau_{43}$  beyond the electric field of  $\sim 15.8$  kV/cm. Electrons are therefore accumulated at the state 3 and population inversion is built up between the states 3 and 2, yielding the second stimulated optical transition (the second lasing channel). Electrons at the state 2 can be quickly depopulated via fast LO phonon scattering to the ground state 1 as  $\tau_{21}$  remains very short at  $\sim 0.4$  ps over the whole electric field range of interest.

The electric field dependent dual lasing process is described by a cartoon diagram in Fig. 4-2. At low electric field of  $\sim 15.5$  kV/cm, the main lasing transition is between state 4 and 3 due to its above threshold optical gain, as shown in Fig. 4-2(a). As electric field increases to  $16$  kV/cm, state 2 and state 3 are not perfectly aligned and population inversion starts build between state 3 and 2. The lasing transition between state 3 and 2 starts to show up, but it is not as manifest as that between state 4 and 3. At high electric field of  $17.5$  kV/cm, both 4-3 and 3-2 lasing transition occur. In contrast with 4-3 lasing transition as the main lasing transition at lower electric field, however, 3-2 lasing transition is the main lasing transition at high electric field.

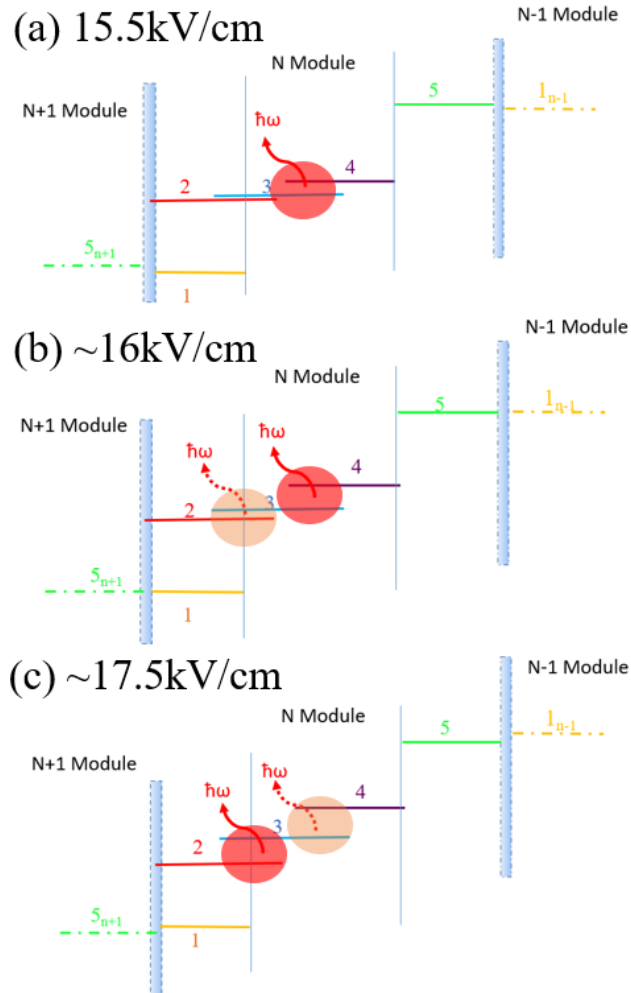


Fig. 4-2. Schematic diagram of electric field dependent lasing transition behavior. (a) Single 4-3 lasing transition at  $\sim 15.5$  kV/cm. (b) Dual lasing transition with main lasing transition between state 4 and state 3. (c) Dual lasing transition with main lasing transition between state 3 and state 2.

Several key parameter differences can be discerned between our device and other SA-based structures. First, energy spacing between state 4 and 5 changes from 30.3 meV to 32.7 meV from electric field of 15.4 kV/cm to 17.5 kV/cm. The energy spacing is closer to phonon energy comparing to [34] so that high frequency radiative emission between subbands 5 and 4 is prevented. Second, barriers of  $\text{Al}_{0.17}\text{Ga}_{0.83}\text{As}$  are adopted, the barrier height (154 meV) is tuned to be lower than [27-32], but higher than those in [34, 73]. This is a trade-off for reducing interface roughness while effectively suppressing carrier leakage into continuum band. In [73], S. Khanal et al. proved that scattering-assisted design can be utilized with low barrier material system ( $\text{Al}_{0.15}\text{Ga}_{0.85}\text{As}/\text{GaAs}$ ), and low threshold current density of  $745 \text{ A/cm}^2$  has been achieved because of the lower interface roughness scattering. However, it is suspected that the device in Ref.14 is damaged by leakage to continuum, which is supported by the absence of negative differential resistance (NDR) at even 46 K. A tradeoff between interface roughness scattering and leakage to



continuum has been pointed out in [30, 31]. A numerical simulation for the device reported in this chapter shows that an increase of barrier height from 15% Al to 17% Al can reduce leakage current to continuum from 418 A/cm<sup>2</sup> to 204 A/cm<sup>2</sup>, while interface roughness scattering time between state 4 and 3 decreases from 3.05 ps to 2.53 ps. A further increased barrier height may result even less leakage to continuum, but it is on risk to make interface roughness scattering faster than LO phonon scattering (~2.4 ps at 160 K) as another dominant scattering mechanism as shown in table 2. The three parameters are calculated when barrier height is the only variable. In order to reduce threshold current density without introducing too much interface roughness scattering, a barrier height of 17% Al is suitable for this structure. Thirdly, High injection coupling strength is chosen to maintain high optical gain peak value. The coupling energy ( $\hbar\Omega_{1,5}$ ) is 1.7 meV. The value is set higher than other scattering-assisted designs based on the same material system, as summarized in table 1. Fourth, the alignment of state 3 and 2 is detuned to an electric field lower than that of state 5 and 1' alignment, and the energy spacing between state 3 and 2 increased to ~9.9 meV at 17.5 kV/cm for the second lasing channel operation.

	15%Al	17%Al	19%Al
Interface roughness scattering between state 4 and 3 (ps)	3.05	2.53	2.16
LO phonon scattering between state 4 and 3 (ps)	2.34	2.39	2.46

Table 4-2. Interface roughness scattering, LO phonon scattering and leakage to continuum calculation for different barrier height at lattice temperature of 160K and applied electric field of 15.5kV/cm. [63]

The theoretical modeling of non-lasing device is based on rate equation approach, as it is proved to be reliable for simulating THz QCLs based on scattering-assisted pumping scheme [32, 33]. Tight binding method is applied only between periods, and all transitions within one period are treated semi-classically, because state 3 and 2 is not perfectly aligned at design bias and electron transports between state 1 and state 5 rely on effective tunneling at design bias. Interface roughness, LO phonon, and impurity scattering have been included in intersubband scattering, and electron distribution on each energy level is considered to be obeying Fermi-Dirac distribution. When calculating the interface roughness scattering, the mean height of roughness and the correlation length are 4 Å and 128 Å, respectively, and the product of these two values is similar to the product of values used in [74] for GaAs/AlGaAs-based QCL. The interface roughness may vary between different growth conditions. The typical experimental values of correlation length of 6–15 nm, and roughness height varies around 2 monolayers [75]. The parameters are estimated in this range. The current density-voltage (J-V) curve calculation is based on second order rate equation which includes the effect of carrier thermal distribution in different states on charge carrier tunneling [76]. Electron temperature is set to be 90 K above heat sink temperature.

The leakage to continuum is calculated by obtaining electron density that has ability to escape to continuum. Electrons density on upper lasing state with energy above the barrier edge are included by Eq. (4.1):

$$N_{2D} \approx \frac{m}{\pi\hbar^2} k_B T \exp\left(\frac{-E_{act}}{k_B T}\right), \quad (4.1)$$

where  $E_{act}$  is the thermal activation energy which equals the energy difference between the barrier edge and the Fermi level in the upper lasing state that are calculating. Additionally, electrons with energy lower than barrier edge might also be able to scatter into energy levels are slightly lower than the barrier edge and tunnel into continuum. Hence, electrons with lower thermal energy than activation energy are also considered to have possibility to escape to continuum via scattering-assisted tunneling [77,78], and can be calculated in Eq. (4.2) [79]:

$$N_{2DLE} = \int_{E_1}^{E_b} \frac{m}{\pi\hbar^2} T(E, F) [1 + \exp\left(\frac{E-E_f}{k_B T}\right)]^{-1} dE, \quad (4.2)$$

where

$$T(E, F) = \exp\left[-2 \int_0^{Z_c} dz \sqrt{2m_b(E_b - E - eFz)}/\hbar\right] \quad (4.3)$$

is the transmission coefficient,  $E_1$  is the electron energy that is lower than  $E_b$  (barrier edge energy),  $Z_c = (E_b - E/eF)$  is the classical turning point or barrier thickness through which electron might tunnel at the calculating energy, and  $F$  is the applied electric field [78]. Finally, the leakage current can be calculated with formula [79]:

$$J = e \frac{(N_{2D} + N_{2DLE})}{L_p} v(F) \quad (4.4)$$

and

$$v(F) = \frac{\mu F}{[1 + (\mu F/v_{sat})^2]^{\frac{1}{2}}}, \quad (4.5)$$

where  $L_p$  is the length of one period,  $\mu \approx 12000 \text{ cm}^2\text{Vs}^{-1}$  is the mobility, and  $v_{sat} \approx 0.72 \times 10^7 \text{ cm}\cdot\text{s}^{-1}$  is the saturated drift velocity [80,81].

### 4.3 Experiment

The quantum structure presented in Fig. 1 is grown on semi-insulating GaAs substrate by using molecular beam epitaxy with 172 repeating periods in 10  $\mu\text{m}$  thickness active region core. The widest well in each period is uniformly doped to achieve a sheet doping density of  $3.17 \times 10^{10} \text{ cm}^{-2}$  per period. The active region is sandwiched between a 100 angstrom un-doped GaAs spacer followed by a 100

nm/ $5 \times 10^{18} \text{ cm}^{-3}$  n+GaAs, and a 100 angstrom un-doped GaAs spacer followed by a top stack of  $5 \times 10^{18} \text{ cm}^{-3} / 5 \times 10^{19} \text{ cm}^{-3}$  (50 nm/10 nm) n+ GaAs layers and capped with a 3.5 nm low temperature growth GaAs layer.

The laser devices are processed with the conventional In-Au wafer bonding and Ti/Au double metal ridge waveguide. The laser ridge is 150  $\mu\text{m}$  in width and cleaved into 2.22 mm in length. The measured maximum lasing temperature of the fabricated device is 144 K, which is the same as reference device in [73]. The fabricated device also shows low threshold current density of 550 A/cm<sup>2</sup> at 50 K. To eliminate high order mode competition in the wide ridge waveguide which often yields kinks on measured light-current curves of THz QCLs [86], two side strips of 6.5  $\mu\text{m}$  width of the n-GaAs contact layer are uncovered by the top metal along the ridge waveguide of the device, and the n-GaAs layer is not etched. In other words, n<sup>+</sup> doped top contact layer between the top metal and active region at the laser ridge waveguide edges is uncovered by the top metal. High order optical modes will suffer from higher loss at the sides of ridge, while the fundamental optical mode that mostly locates in the center of laser ridge remains unaffected. Thus, the fundamental optical mode dominates the output [86].

## 4.4 Results and Discussion

### 4.4.1 Dual-Lasing Channel Device Characterization Result

Fig. 4-3 shows light (L)-current density (J) characteristics of the fabricated device from 20 to 130 K in pulse mode, with pulse frequency of 500 Hz and pulse width of 500 ns. The measured L-J curves at temperatures below 120 K exhibit a substantial slump in optical output power between two peaks before reaching the negative differential resistance (NDR) point. Correspondingly, a turning point in the slope of the voltage (V)-current density (J) curve at 40 K is observed right after the first optical output peak, denoted by dashed line in Fig. 4-3. A clear NDR is measured at high bias on Voltage-Current density curve, and NDR is observed up to 120 K, while a similar device in [73] did not show clear NDR at 46 K. Observation of NDR region up to 120 K and a 26% reduction on threshold current density together prove an improvement of 17% Al barrier on leakage current suppression. Considering a wider emission spectrum (0.3 THz compare to 0.13 THz) and the same maximum operation temperature, this device should have achieved larger population inversion.

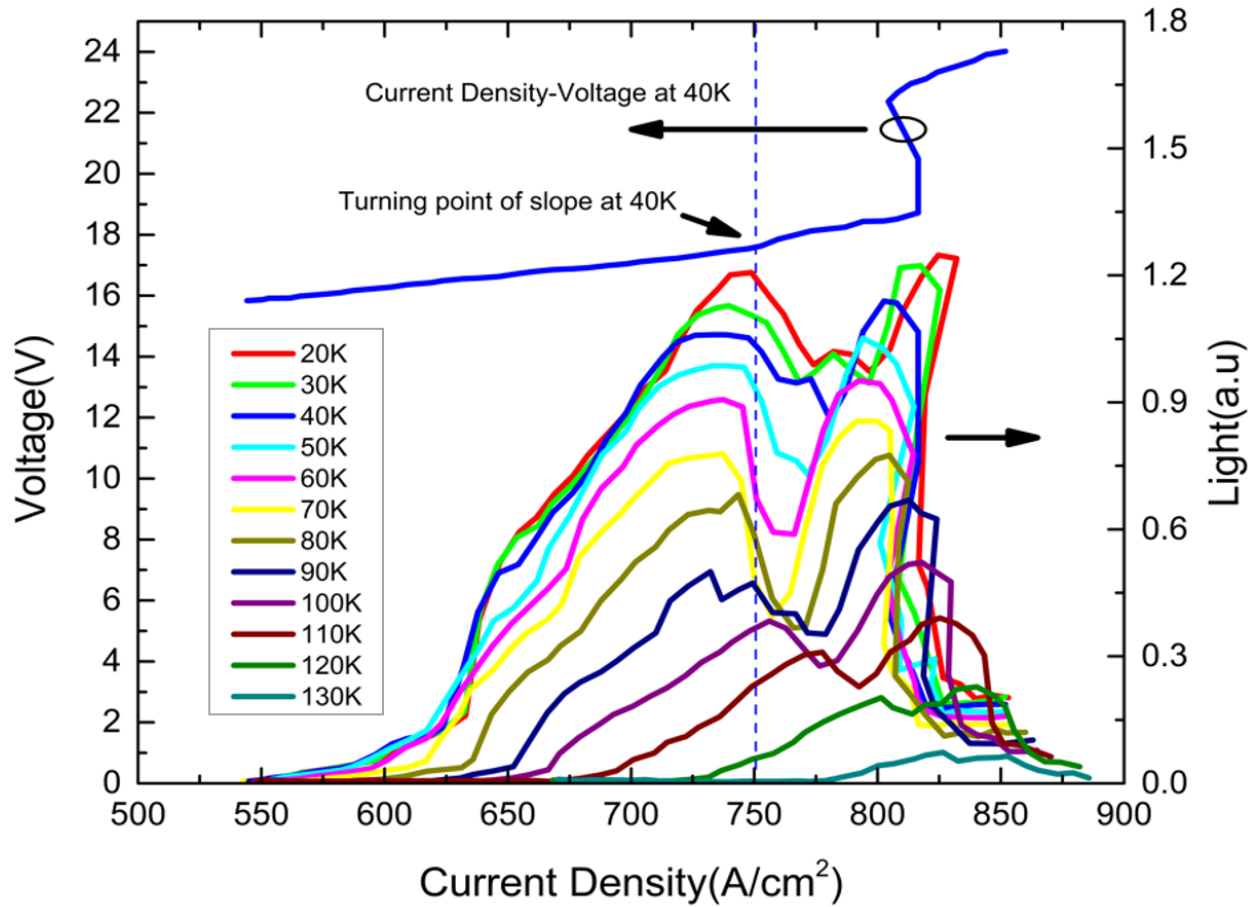


Fig. 4-3. Current Density-Voltage curve at 40 K and light-current density curve after lasing threshold from 20 K to 130 K [63].

The experimental J-V curve is compared to the simulation results of a non-lasing structure, as shown in Fig. 4-4(a). After including the extra voltage drop ( $\sim 1.2$  V) on contacts, the simulation and experimental curves are in good agreement. Three pre-threshold tunneling resonances are observed at device biases of 4.7 V (for 1'-4), 7.4 V (1'-3), and 8.9 V (1'-2), respectively, corresponding well with the two shoulders in the experimental curve. The measured threshold voltage at 90 K is 16.1 V, as denoted by dashed line in Fig. 4-4(a). The device enters NDR region at  $\sim 19$  V at 90 K.

#### 4.4.2 Comparison between Measured Results and Simulated Results

In order to understand the double peaks observed in the optical output power curve, the light-voltage (L-V) curve at 30 K is re-plotted in Fig. 4-4(b). The figure also illustrates the calculated optical gain peak values (in non-lasing case) as a function of device bias for the first (4-3 transition) and the second lasing channels (3-2 transition). The 4-3 transition peak gain reaches its maximum of  $31.19 \text{ cm}^{-1}$  at  $\sim 15.7 \text{ kV/cm}$  with an oscillator strength of 0.44, while that of the 3-2 transition reaches  $42.78 \text{ cm}^{-1}$  at  $\sim 17.5 \text{ kV/cm}$  with an oscillator strength of 0.27 at 30 K. The first lasing channel is first turned on at low biases ( $\sim 15.8$  V,

14.6 kV/cm), leading to the ignition and increase of the lasing emission. The lasing emission is peaked around 17.3 V (~16.1 kV/cm), corresponding well to the bias at which the 4-3 transition optical gain (the red curve) is maximized. Beyond this bias, the states 3 and 2 become more and more misaligned and the fast resonant tunneling from 3 to 2 slows down. Charge carriers therefore pile up at state 3 and the population inversion between 4 and 3 is diminishing, leading to the quick reduction of the corresponding peak gain value. The shut-down of the first lasing channel contributes to the observed reduction in the lasing optical output power.

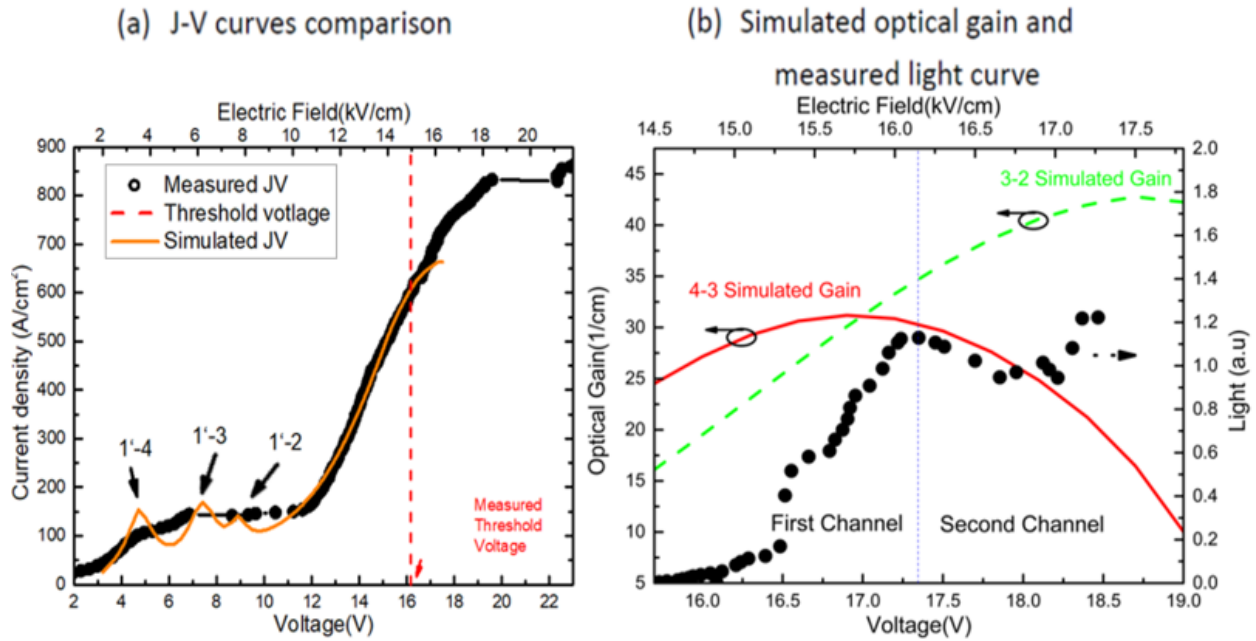


Fig. 4-4. Simulation results in comparison with experimental result. (a) Simulated JV curve (orange solid line) in comparison with experimental IV curve at 90 K (black dots). Schottky junction voltage drop of 1.2 V is considered.

(b) Simulated optical gain (non-lasing case) between state 4-3 (red) and 3-2 (green dotted line) in comparison between measured Light-Voltage curve (black dots) at 30 K. A Schottky voltage drop of 1.2 V is assumed. Two channels are distinguished by light curve, while the 4-3 transition dominates the first channel and switch to second channel while 4-3 optical gain becomes too weak. [63]

The second lasing channel (the 3-2 transition) is turned on at higher biases. As the optical transitions from the 4-3 pair and the 3-2 pair do not overlap exactly in lasing frequency (to be shown in Fig. 4-6 shortly), the increase of the 3-2 transition peak gain is not necessarily compensating the reduction of the 4-3 transition peak gain at the 4-3 lasing frequency. As a result, the measured overall lasing emission power does not bounce back until a bias of ~17.8 V, at which the 3-2 transition gain is high enough to overcome the optical loss at its corresponding lasing frequency, and reaches its second peak at ~18.5 V (~17.3 kV/cm), when the second lasing channel is fully opened up. And device enters NDR region

immediately after 18.5 V at 30 K. This explains the double peak in the light-current density curves in Fig. 4-3.

The lasing channel switching is also indirectly manifested in the measured current density-voltage (J-V) curve. The slope of the J-V curve in Fig. 4-3 exhibits a sudden change at the bias of  $\sim 17.58$  V at 40 K because the current-carrying capacity of the first lasing channel (4-3) is higher than that of the second (3-2). The sudden change marks the switching point of the dominant lasing channel transition.

#### 4.4.3 Leakage Analysis

In order to further reveal the difference in that the underlying mechanisms responsible for the two lasing emission peaks are different, the normalized peak value ( $P_{out}(T)$ ) of the two optical emission peaks in the L-J curves of Fig. 4-3 is plotted as a function of  $1/T$  in Fig. 4-5(a), where  $T$  is the temperature. For both peaks, the value of  $P_{out}(T)$  decreases with the increase of  $T$ . An activation energy ( $E_a$ ) can be extracted from high temperature end ( $>90$  K) by using equation  $\ln(1 - \frac{P_{out}(T)}{P_{outmax}}) \approx \ln(a) - \frac{E_a}{k_B T}$  [18], where  $P_{outmax}$  is the maximum output power at the lowest temperature (20 K).

At low temperatures (below 113 K), the fitting to the emission peak curve from the first lasing channel (4-3) yields an activation energy  $E_{a4-3} = 8.3$  meV, while the value is  $E_{a3-2} = 18.4$  meV for the second lasing channel (3-2). The emission peak from the first lasing channel diminishes faster than that from the second lasing channel, and gradually becomes indistinguishable at temperatures higher than 120 K. The different activation energy derived from the fitting can be explained by the energy difference between the states 4 and 3. As described earlier, the first lasing emission peak (at lower biases) is mainly contributed from the 4-3 transition where 4 is the upper lasing state (UL) and 3 is the lower lasing state (LLS), while the second peak (at higher biases) from the 3-2 transition where 3 is the UL and 2 is the LLS. At the design bias, an inter period leakage level (labeled as state 1) is  $\sim 5.4$  meV above the first UL (4) and  $\sim 15$  meV above the second UL (3) as shown in Fig. 4-5(b). Hence  $E_{a3-2}$  is  $\sim 10$  meV larger than  $E_{a4-3}$ . Because of the lower activation energy, 4-3 transition plays a substantial role only at lower temperatures (i.e.,  $< \sim 113$  K) and the 3-2 transition becomes more dominant at higher temperatures.

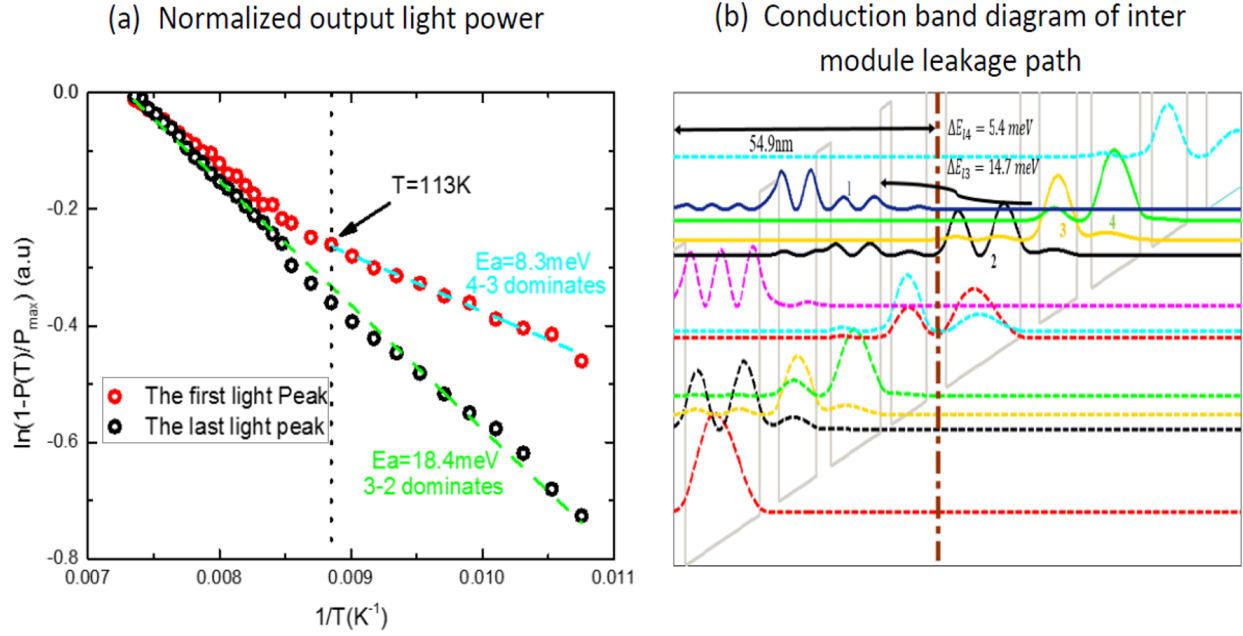


Fig. 4-5. Normalized output light power and conduction band diagram of inter-period leakage path. (a) Normalized output light intensity of the first peak (black dots) and the second peak (red dots) in light-current curve versus temperature in plot of  $(1 - \frac{P_{out}(T)}{P_{outmax}})$  with fits (dashed lines). Two peaks show different trends until 113 K. (b) Conduction band diagram shows possible inter-period leakage path from states 4 and 3 to state 1. The energy spacing between states 4-1 and state 3-1 are 5.4 meV and 14.7 meV respectively [63].

#### 4.4.4 Lasing Spectra

The switching hypothesis of two lasing channels can be verified ultimately by measuring the lasing spectra at different device biases (current injection). Fig. 4-6 present the measured lasing spectra at different devices biases (16.5, 17.2, 18.2, 18.46 V) at 30 K and simulated gain spectra due to 4-3 transition and 3-2 transition under corresponding conditions. Optical gain is calculated in non-lasing case and is proportional to the product of population inversion and oscillator strength. At the lower bias of 16.5 V, the lasing is observed at a frequency of  $\sim 2.3$  THz, corresponding well with the peak frequency of 4-3 transition gain spectrum (dashed red curve). As the device bias increases, the peak gain of the first lasing channel (4-3) diminishes. In addition, due to the Stark effect, 4-3 transition peak frequency (marked by brown solid squares at each bias) almost linearly shifts to higher values (blue-shift, denoted by brown solid line). The optical gain due to the second lasing channel (3-2) (green dashed line) starts to emerge on the lower frequency side at the bias of 17.2 V. As a result, the calculated overall gain (black solid line) exhibits a slower-paced blue shift. At higher biases, such as 18.2 V and 18.4 V, the lasing spectra overlap well with the peak of the overall gain spectra, which is dominated by optical gain contribution from the second lasing channel (3-2). The lasing spectra clearly demonstrate the transitions of the two lasing

channels during device operation. Due to the dual lasing channels, the lasing spectrum spans a range of  $\sim 6.5\%$  of the central frequency of 2.35 THz at  $1.317 J_{th}$  and  $7.9\%$  of the central frequency of 2.51 THz at  $1.48 J_{th}$ . The frequency coverage is from 2.3 THz to 2.62 THz.

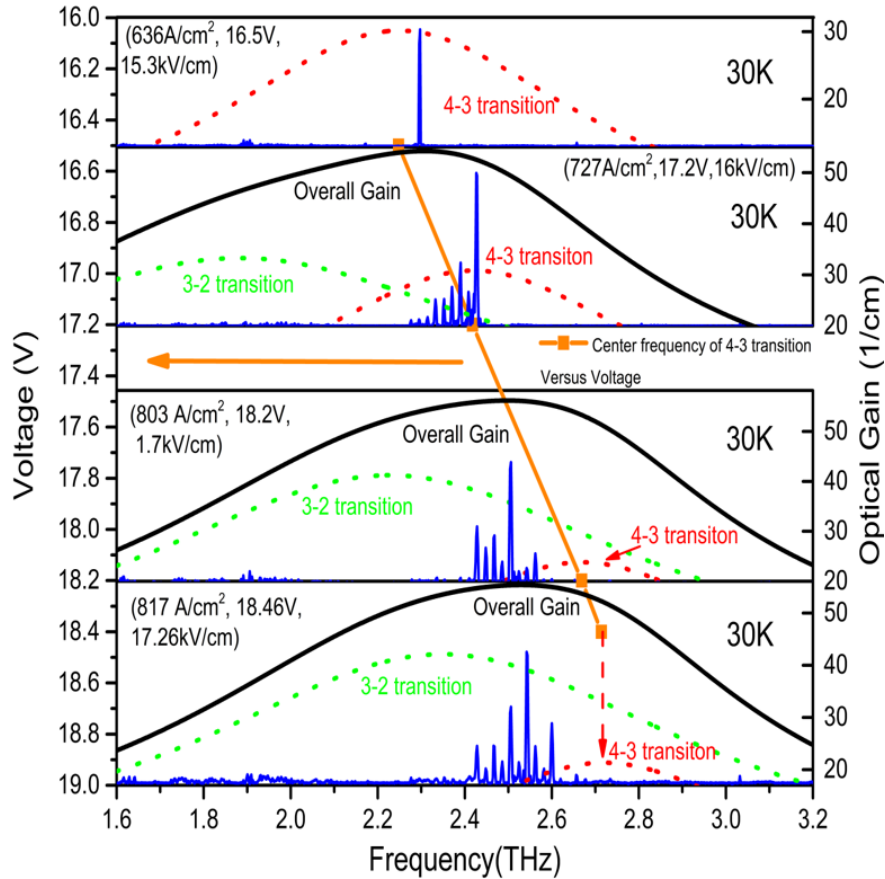


Fig. 4-6. Experimental lasing spectra (blue solid lines) in comparison with simulated optical gain of state 4-3 (red dashed line), state 3-2 (green dashed line), and total (black solid line) at 30 K under different bias. The main center frequency of state 3-2 at different bias is marked as red solid line to show contrast with experimental center frequency which is determined by total optical gain [63].

#### 4.5 Additional Simulation Results by Using nextnano.NEGF Model

This section presents the simulation results obtained from Non-Equilibrium Green's Functions formalism (NEGF) model for comparison and validation. In 2017, a commercialized powerful simulation tool named nextnano.NEGF is developed by Thomas Grange [103]. Fig. 4-7 show the simulated wavefunction diagrams and corresponding resolved optical gain at electric fields of 15 kV/cm, 16.5 kV/cm, and 17.5 kV/cm. At 15 kV/cm, only one significant lasing optical gain is observed, centered around 2.5 THz ( $\sim 10$  meV) in frequency and located at 50 nm and -30 nm in position. This optical gain corresponds to the 4-3 transition and peak optical gain located at the radiation barrier between state 4 and state 3. At 16.5 kV/cm, dual optical gain peaks are observed. The optical gain peak located at the same position around 50 nm and



-30 nm corresponds to 4-3 transition as 15 kV/cm, while another presenting optical gain peak located around 60 nm and 5 nm at the radiation barrier between state 3 and state 2, as shown in the conduction band diagram. This observation proves that optical gain with slightly lower center frequency of 2 THz ( $\sim 8$  meV) corresponds to 3-2 transition. Finally, the main optical gain peaks at 2.37 THz (9.5 meV) in frequency, 60 nm and 5 nm in position at high electric field of  $\sim 17.5$  kV/cm. 3-2 transition contributes the most into the optical gain at  $\sim 17.5$  kV/cm. The simulation results agree well with that of the RE simulation and measured results shown in section 4.1-4.4.

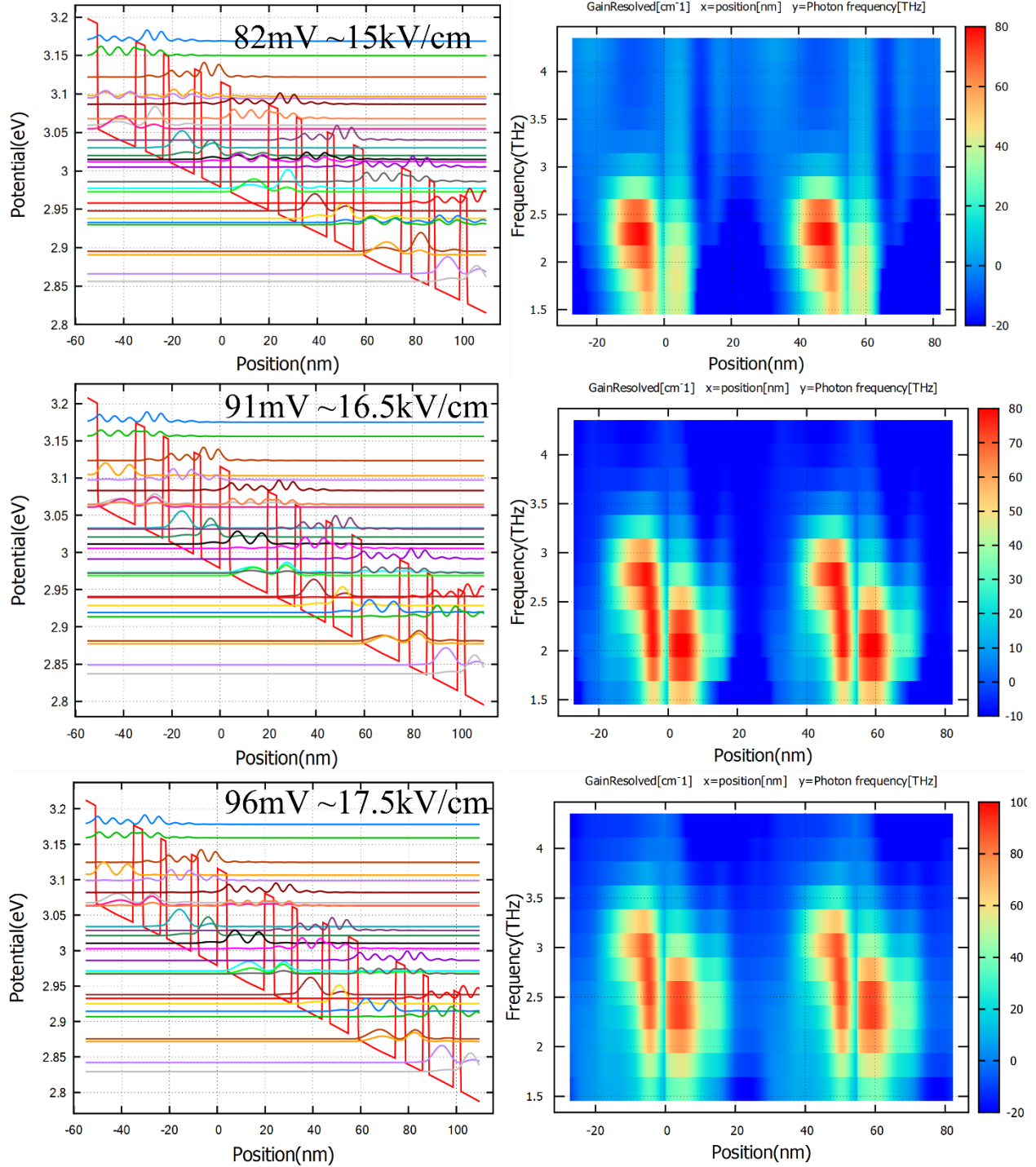


Fig. 4-7. NEGF model simulated conduction diagram and resolved optical gain at different electric field [55].

## 4.6 Reproducibility Verification

Two patches of fabrication are performed to verify the observation. The laser device (device B) is processed with the conventional In-Au wafer bonding and Au-Au ridge waveguide. The conduction band

diagram and light-current-voltage (LIV) results are shown in Fig. 4-8(b) and Fig. 4-8(a). The  $T_{\max}$  of this device (device B) is 144 K. Apart from the high temperature performance, this device shows a low threshold current density and dual color lasing around 2.12 THz and 2.32 THz at 30 K. The low threshold current density is resulted from dual color lasing and lower leakage to continuum band. Calculated gain for state 4-3 and 3-2 is compared to the light-voltage (LV) results at 30 K in Fig. 4-8 (a) and the measured lasing spectrums in Fig. 4-8(b)-(d). The rate equation-based simulation shows that the peak gain from 4-3 transition is  $14.5 \text{ cm}^{-1}$  at  $\sim 15 \text{ kV/cm}$  with an oscillator strength of  $\sim 0.40$ , and the peak gain from 3-2 transition is  $16.2 \text{ cm}^{-1}$  at  $\sim 17.5 \text{ kV/cm}$  with an oscillator strength of  $\sim 0.28$  by assuming the same line width of 1 THz. As a result, the lasing emission (Fig. 4-8(b)) due to 4-3 transition is observed at lower biases (region I in Fig. 4-8(a)), the lasing emission (Fig. 4-8(c)) due to 3-2 transition is observed at higher biases (region III), and the lasing emission from both transitions (Fig. 4-8(d)) is observed at intermediate biases (region II). The switching and transition of the lasing channels are clearly revealed by the measured lasing spectra at different device biases. This observation corresponds well to the features in the LV. The optical gain calculated by the RE model in Fig. 4-8 (b)-(d) uses a constant broadening of 1THz rather than the calculated broadening in Fig. 4-5. The different approach of optical gain broadening does not affect center frequency, and both of them support the measured spectra measurement.

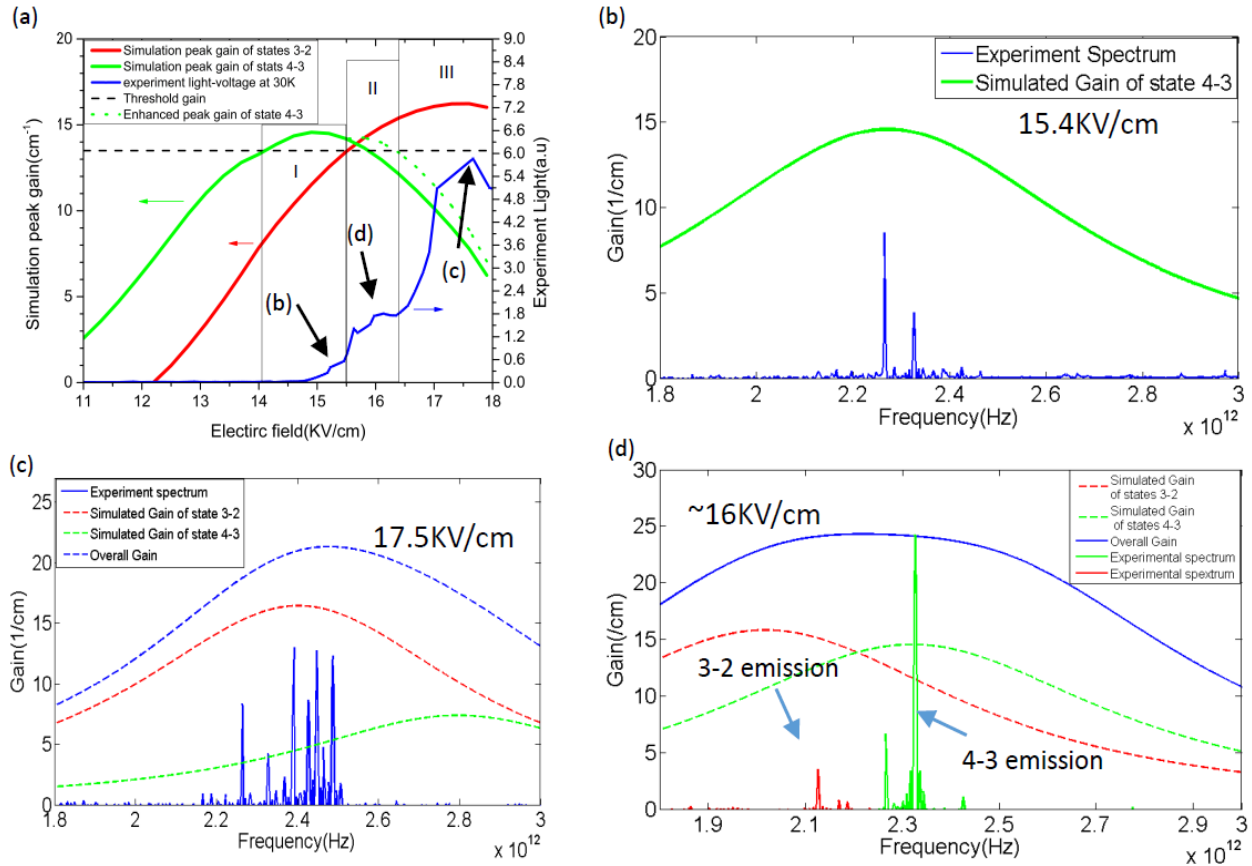


Fig. 4-8. Simulated optical gain in comparison with measured spectra. (a) Simulated peak gain of state 4-3 (green dotted line) and state 3-2 (red dotted line) in comparison with experiment light-voltage result at 30 K (blue dotted line). (b) Simulated gain of state 4-3 at 15.4 kV/cm in comparison with spectrum at 15.4 kV/cm. (c) Simulated gain of state 4-3 and state 3-2 at 17.5 kV/cm in comparison with spectrum at 17.5 kV/cm. (d) Simulated gain of state 4-3 and state 3-2 at ~16 kV/cm in comparison with spectrum at ~16 kV/cm. Electric field is calculated based on device thickness (10  $\mu\text{m}$ ) and voltage drop on Schottky junction (~1.2 V).

## 4.7 Conclusion

In this chapter, I present and analyze a dual lasing channel QCL, which emits light from 2.3 THz to 2.62 THz at 30 K, based on a scattering-assisted injection scheme in the GaAs/ $\text{Al}_{0.17}\text{Ga}_{0.83}\text{As}$  material system. The device exhibits a low threshold current density of  $550 \text{ A/cm}^2$  at 50 K and a maximum operating temperature of 144 K. It is proved that this dual lasing structure scheme can provide 0.3 THz frequency coverage at low frequencies with the lowest reported threshold current density based on SA structures and a temperature performance close to the highest operating temperature recorded in this frequency range. Devices from different fabrication benches are characterized to verify the robustness of experimental observation, and both the NEGF model and RE model are used for simulation to verify the consistency of our analysis.

## Chapter 5 Hybrid Extraction/Injection Design (HEID) Replies on Scattering Assisted Injection and Resonant Phonon Injection

This chapter presents the development of a six-level scheme THz QCL design, in which RP and SA injection/extraction are combined within a single  $\text{Al}_{0.15}\text{Ga}_{0.85}\text{As}/\text{GaAs}$ -based structure. Such structure has never been reported in theoretical or experimental results before the date of publication of [43].

### 5.1 Introduction

Since their first demonstration in 2002 [12], THz QCLs have become one of the most promising light sources that can cover a terahertz gap from  $\sim 1.2$  THz to  $\sim 5.4$  THz [87-91]. Improving maximum operating temperature of THz QCLs [14, 64,104] is an important research topic for many applications, such as, non-destructive imaging, spectroscopic identification of chemical and biological species, and ultra-high-speed communication. To improve the maximum operating temperature of THz QCLs, many efforts have been made to understand the fundamental electron transport mechanisms and optimize existing quantum structure designs. Researchers have also found it necessary to explore new possible quantum structures that may mitigate many trade-offs in state-of-the-art quantum designs and improve major performance degradation factors. In the past decade, several promising new quantum structures design schemes, such as two-well direct-phonon designs, extraction-controlled designs, phonon-photon-phonon (3P) designs, scattering-assisted designs, and split well direct-phonon designs, have been demonstrated and studied. [14-21,24-28,63,92-94]. three-well RP-based design scheme was demonstrated in early stage, and it is now one of the most promising structures that can achieve maximum operating temperature above 190K [64]. However, three potential performance degradation factors are often encountered: (1) the appearance of intermediate NDR before lasing threshold [29,64], (2) the missing of the final NDR at high temperatures due to leakage to continuum band [17,18,20], and (3) the theoretical limit of maximum population inversion ( $\Delta N/N_{\text{tot}}$ ) of 50% in resonant-tunneling (RT) based injection/extraction processes [27].

The appearance of intermediate NDR before lasing threshold constrains device operation and design, especially on diagonal designs with low oscillator strength, by preventing devices from reaching the designed lasing bias [19, 29]. This effect arises from the presence of significant current-leakage channels, such as a resonant-tunneling leakage from injector state to extractor state before the designed lasing bias [19,29]. One way to reduce the appearance of the intermediate NDR is to ensure that the current density at

the lasing threshold is significantly higher than any local current density peaks at lower bias, and this approach is examined – theoretically and experimentally – in this chapter.

The observation of a well-defined final NDR is considered as a strong evidence that device is not suffering from significant leakage to higher energy states and continuum at the measured temperature [18,20]. However, at higher temperatures final NDR usually disappears and threshold current density increases dramatically, because electrons possess sufficient kinetic energy to enable the leakage path to continuum and degrade devices performance [15-18, 20]. One way to reduce this leakage is to increase the barrier height for better carrier confinement. High barrier height would have a potential to increase the interface roughness scattering rate [30,31,63]. Various barrier height growth is often very demanding for a typical Molecular beam epitaxy (MBE) growth system. Therefore, this chapter presents a different approach to reduce the leakage to continuum without increasing barrier height by utilizing higher excited energy states as additional extraction/injection states.

E. Dupont pointed out that the RT-based direct pump scheme in the typical three-well RP-based THz QCLs results in a theoretically limited maximum population inversion ( $\Delta N/N_{\text{tot}}$ ) of 50% [27]. In RT-based injection and extraction scheme, electron population on upper lasing state (UL) is limited to be similar to injector state which means that UL can hold only half of available electrons; similarly, lower lasing state (LL) and extractor state hold similar electron population which means that only half of accumulated electrons on LL can be extracted. To overcome this limitation, some SA and 3P injection/extraction schemes have been explored and demonstrated better performance than that of RP-based design when the main lasing frequency is lower than 3.5 THz [32,33,63]. However, SA and 3P-based devices require a relatively higher applied electric field for lasing threshold and show higher leakage to continuum, therefore a relatively higher barrier height and lower energy spacing between lasing states are preferred [27,32,33]. Hence, designing a hybrid extraction/injection structure that combines both SA- and RP-based schemes can potentially reduce the thermally activated leakage current, minimize the appearance of intermediate NDR, and further increase the population inversion [35].

## 5.2 Quantum Design and Simulation Results

In this section, we present a new six-level scheme THz QCL with hybrid extraction/injection channels. The hybrid extraction/injection channels design (HEID) uses a material system of GaAs/Al<sub>0.15</sub>Ga<sub>0.85</sub>As. The design is expected to have advantages in reducing pre-threshold instability and suppressing thermally activated leakage to excited states and continuum. This study also discusses function of hybrid extraction/injection channels in this design and possible modification for better performance.

We design a six-level hybrid extraction/injection scheme quantum cascade laser active region to lase at  $\sim 2.8$  THz based on GaAs/Al<sub>0.15</sub>Ga<sub>0.85</sub>As material system. The conduction band diagram of this structure, which is calculated by using an effective two-band model, is shown in Fig. 1(a). An electrons transport schematic diagram of the design is shown in Fig. 1(b).

In the new design (Fig. 5-1), there are 6 main confined energy states in one period/module and they are all included in the simulation. At the design bias of 12 kV/cm, the injector state ( $1_{n-1}$ ) is aligned with the UL, and the LL is in resonance with both states  $5_{n+1}$  and  $6_{n+1}$ . The difference between RP-based designs and this design is that state  $5_{n+1}$ th and  $6_{n+1}$ th have been finely tuned to align with LL for additional hybrid extraction/injection channels, and the closest higher leakage energy level is suppressed to be  $\sim 38$ meV above UL to become an injection state. The first injection/extraction channel allows electrons to flow from LL to state 2 via resonant-tunneling, and then flow from state 2 to state 1 via LO-phonon scattering, and finally flow to the upper lasing state in the next period/module via tunneling. The second injection channel enables an additional electron flow path from the LL to state 5 and state 6 via resonant-tunneling, and from state 5 and state 6 to the UL via scattering-assisted injection as indicated by green arrows in Fig. 1(b). To ensure the selective injection from the second injection/extraction states (5 and 6) to the UL, the energy difference between two states is kept  $\sim 38$  meV. In addition, oscillator strength between the second injection/extraction states (5 and 6) and UL is made larger than that between the second injection/extraction states (5 and 6) and LL by tuning the thickness of two lasing barriers.

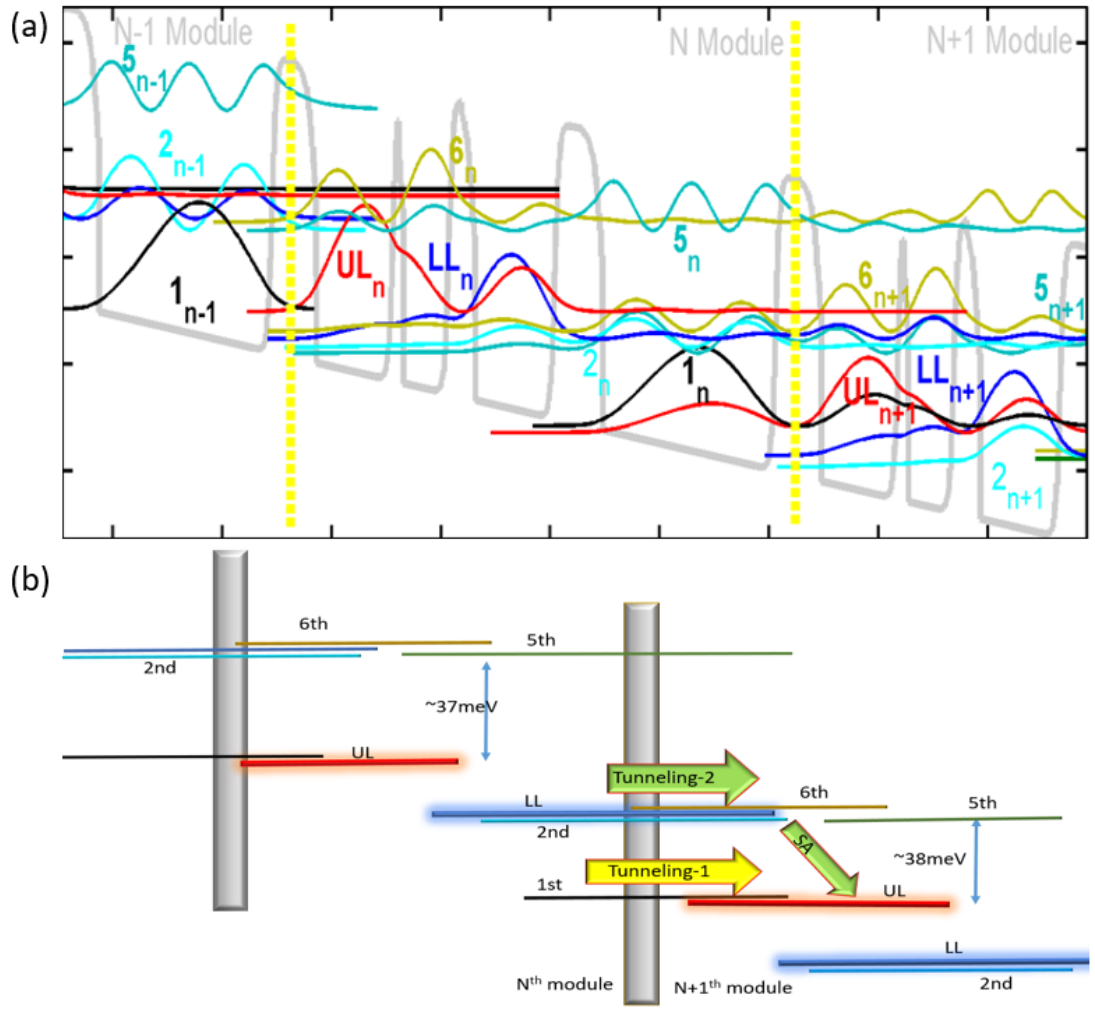


Fig. 5-1. (a) Conduction band diagram of HEID device at electric field of 12 kV/cm. (b) Hybrid extraction/injection diagram of The HEID device. The first and second channel are labeled by yellow and green arrows in diagram respectively. Layer thickness starting from the extractor barrier are: **44/158/42/70/10/41/23.8/72.5** with barrier labeled in bold and delta doped layer underlined. [43]

The second extraction/injection channel can help the accumulated electrons in LL to further depopulate to states 5,6 and inject more electrons to the UL with assistance of LO phonon scattering. In contrast, the RP-based device relies only on resonant-tunneling for injection (from state  $1_{n-1}$  to UL) and extraction (from  $LL_n$  to state  $2_{n+1}$ ). In addition, the new structure also pushes up any low-lying excited energy levels in both periods/modules N and N+1 to  $\sim 38$  meV above the upper lasing state, in contrast to the value of  $\sim 9$  meV in the three-well RP structure [19, 98]. The use of higher excited energy levels is an advantage of this HEID structure, while higher excited energy levels are detrimental in three-well RP structure as they play as leakage energy levels and damage population inversion [19, 29].

Important design parameters for hybrid extraction/injection channels are shown in Fig.5-2. In the electric field of 10.3–11.8 kV/cm, electrons are extracted from LL to states 5 and 6 via resonant-tunneling



at very fast rates while the wrong extraction rates from UL to states 5 and 6 are negligible as shown in Fig. 5-2(a). States 5 and 6 are also playing roles as additional injection states, because desired scattering-assisted injection rates (from states 5 and 6 to UL) are consistently higher than undesired wrong scattering-assisted injection rates (from state 5 and 6 to LL) as shown in Fig. 5-2(b). In order to further understand benefits of the additional extraction/injection channel, simulation results including 4 states (violet) and 6 states (red) are compared in Fig. 5-2(c). The simulation using only 4 states (violet curve in Fig. 5-2(c)) can be considered as a structure relies only on RT extraction/injection channel which is similar to RP design device, while full hybrid extraction/injection channels are included in the simulation using full 6 states (red curve in Fig. 5-2(c)). Owing to the help of states 5 and 6 as an additional hybrid extraction/injection channel, peak population inversion is enhanced by  $\sim 41.7\%$  than the case that the second extraction/injection channel is not included in simulation as shown in Fig. 5-2(c). The simulation is performed at a lattice temperature of 70 K with electron temperature of 140 K above lattice temperature. As a result, the six-level scheme hybrid extraction/injection design, which is achieved and named by HEID, is expected to be able to achieve higher population inversion and a better suppression of the electrons leakage to both higher parasitic excited states and continuum band without increasing the barrier height.

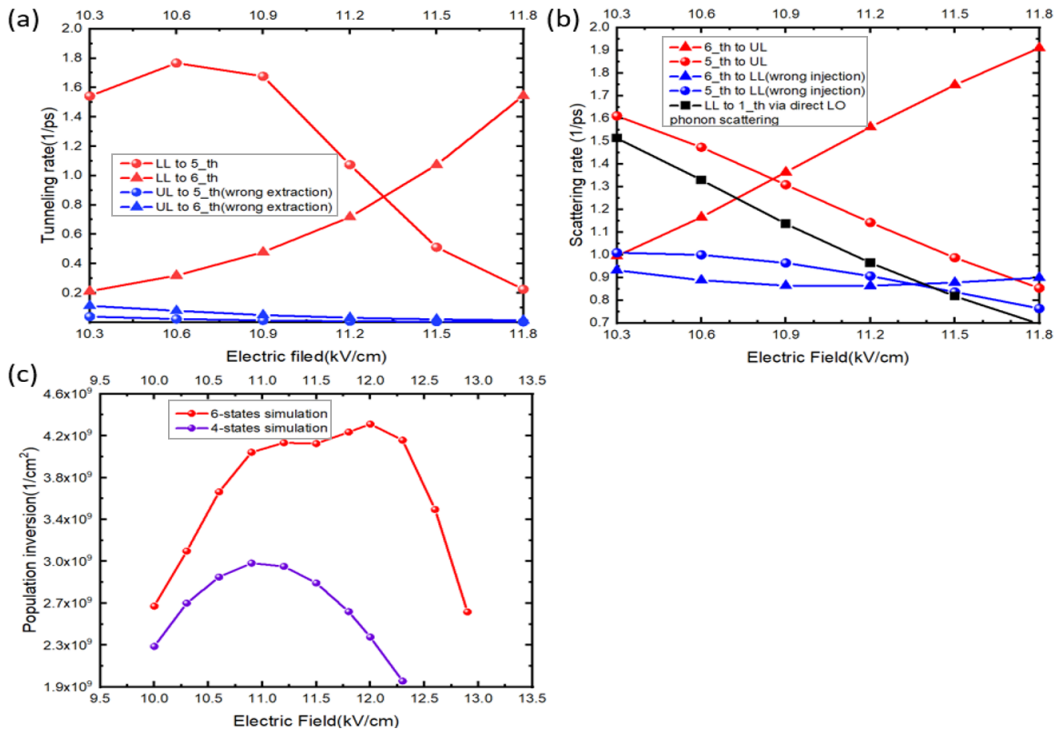


Fig. 5-2. Simulated function of additional hybrid extraction/injection channels at 70 K. (a) Comparison of extraction tunneling time. (b) Comparison of injection scattering time. (c) Simulated population inversion with/without additional hybrid extraction/injection channels. [43]

### 5.3 Results and Discussion for the First HEID Design.

The HEID active region is 10  $\mu\text{m}$  thick and consists of 216 repeats of the period/module presented in Fig. 5-1. The wafer is grown by using MBE on semi-insulating GaAs substrates from WaferTech, and their active regions are sandwiched between a 100  $\text{\AA}$  undoped GaAs spacer followed by a 1000  $\text{\AA}/5 \times 10^{18} \text{ cm}^{-3} \text{ n}^+$  GaAs and a 100  $\text{\AA}$  undoped GaAs spacer followed by a top stack of  $5 \times 10^{18} \text{ cm}^{-3}/4 \times 10^{19} \text{ cm}^{-3}$  (500  $\text{\AA}/100 \text{\AA}$ )  $\text{n}^+$  GaAs layers and capped with a 35  $\text{\AA}$  low temperature grown GaAs layer. The active region of HEID device is Si doped to  $3.8 \times 10^{10} \text{ cm}^{-2}$ . Lasing devices are processed to Au-Au waveguides and bonded with epi-side up.

Fig. 5-3(a) shows the light-current-voltage (L-I-V) characteristic curves of a HEID device fabricated from wafer G499, which is measured in pulse mode (pulse width of 400 ns and pulse repetition frequency of 400 Hz) at heat sink temperature of 40 K. It is worth noting that no intermediate NDR before lasing threshold is observed as it usually exists in three-well RP structures [19, 29]. This observation confirms that the design reduces threshold instability problem caused by pre-lasing leakage channels. The HEID device lases at  $\sim 2.58 \text{ THz}$  to  $\sim 2.85 \text{ THz}$ , and the lasing spectra are normalized and vertically shifted for a clear view in Fig. 5-2(b). The size of the measured ridge device in Fig.2 is 150  $\mu\text{m}$  wide and 1.90 mm long with lasing spectra mode spacing of  $\sim 21.9 \text{ GHz}$ .

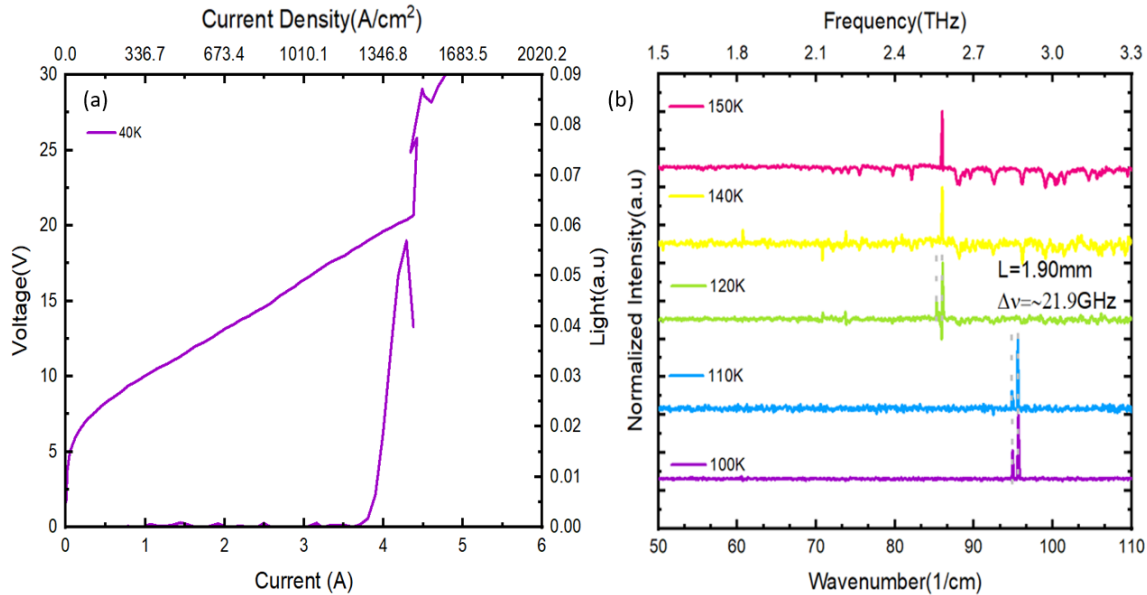


Fig. 5-3. Characterization result of HEID device. (a) L-I-V measurement. (b) Spectra measurement employing Thermo fisher FTIR purged with dry nitrogen gas and Si bolometer as detector. [43]

To reveal underlying physics and to better understand the HEID device performance, more simulation and experimental results are analyzed in the following section. The following sections focus on the

thermally activated leakage current, the effect of actual conduction band profile, current density - voltage features, and the impact of the additional extraction/injection channel.

### 5.3.1 Less Leakage from UL to the Higher Excited State in N+1 Period/module and N Period/module.

One of the accomplishments of this work is the successful suppression of the leakage current from UL to higher excited leakage energy levels without increasing barrier height. This statement can be verified by the characteristic temperature and the highest temperature that the final NDR appears. The higher characteristic temperature and the higher temperature of the final NDR appearance in HEID device reflect the fact that fewer thermally activated electrons escape to higher excited states and continuum [14,85,86]. Fig. 5-4(a) shows the extracted characteristic temperature of 259 K from the measured L-I-V data from Fig. 3(a) by using the function  $J_{th}(T)=J_0\exp(T/T_0)$ . Fig. 5-4(b) shows the appearance of the final NDR up to 260 K measured in a round disk device fabricated from the same HEID wafer. This value is the highest reported among THz QCLs that employ a material system of GaAs/Al<sub>0.15</sub>Ga<sub>0.85</sub>As with lasing frequencies from 2.6 THz to 2.85 THz.

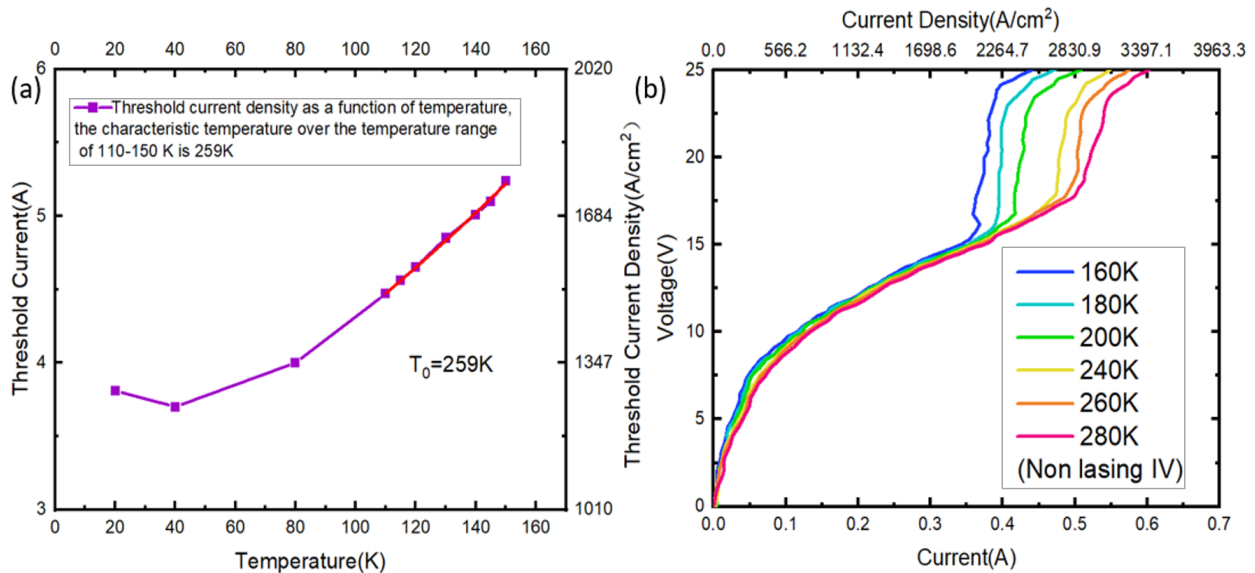


Fig. 5-4. Thermally activated leakage analysis. (a) shows extracted characteristic temperature. (b) shows the highest temperature that NDR can be observed on the HEID wafer [43].

### 5.3.2 Impact of Actual Barrier Profile on J-V Simulation

X. Lü and E. Luna have experimentally investigated the actual barrier profile in III-V semiconductor heterostructures that is neither chemically sharp nor perfect square shaped, as described by ideal barrier profile assumption, but there are transition areas at interfaces [56,57]. In addition, the thickness of

quantum barriers and the composition of maximum Al differ from target value particularly when designed barriers and wells are narrow and Al composition in barriers is high in the active region [56,98]. In our HEID device, we employ a relatively narrow barrier of 10 Å. Hence, it is necessary to study the impact of actual barrier profile and Al composition on device performance. We calculate conduction band diagram with ideal barrier profile assumption and actual conduction band diagram at 11 kV/cm, as shown in Fig. 5(a). In actual conduction band diagram calculation, we implement the growth direction dependent transition area as suggested in [57], and consider the interfaces as non-identical along two sides of the barrier. We find that the maximum Al composition is lower than the expected value and reduces maximum barrier height by  $\sim 10$  meV.

We present the simulated J-V curves of a non-lasing HEID device by using ideal barrier profile assumption and actual barrier profile in comparison with measured J-V curve, as shown in Fig. 5(b). In the measured J-V curve, we consider a  $\sim 2.2 \Omega$  extra wire resistance in series and deduct it in the plot to reveal the actual electric field applied to the device. We find a better agreement between the measured J-V and simulated J-V curve with the actual barrier thickness profile below threshold region. The discrepancy between the two simulated J-V curves becomes substantial beyond  $\sim 7$  kV/cm, and the maximum discrepancy in the simulated current density is  $\sim 500$  A/cm<sup>2</sup> (at  $\sim 11$  kV/cm), as shown in Fig. 5(b). The discrepancy is attributed to the difference between the actual potential profile of the actual quantum system (red dotted line in Fig. 5(a)) and that of the ideal square-well system (blue solid line), particularly near the top of the potential barriers. We use the same mean interface roughness height parameter of 3 Å/1.5 Å and roughness correlation length of 128 Å/65 Å at two sides of each barrier in the interface roughness scattering calculation in both simulations (the ideal barrier profile assumption and actual barrier profile). The only implemented difference is conduction band shape shown in Fig. 5-5(a). The inset in Fig. 5-5(b) shows simulated optical gain at 11 kV/cm which is centered at 2.8 THz and agrees well with measured lasing spectra at 2.58–2.85 THz.

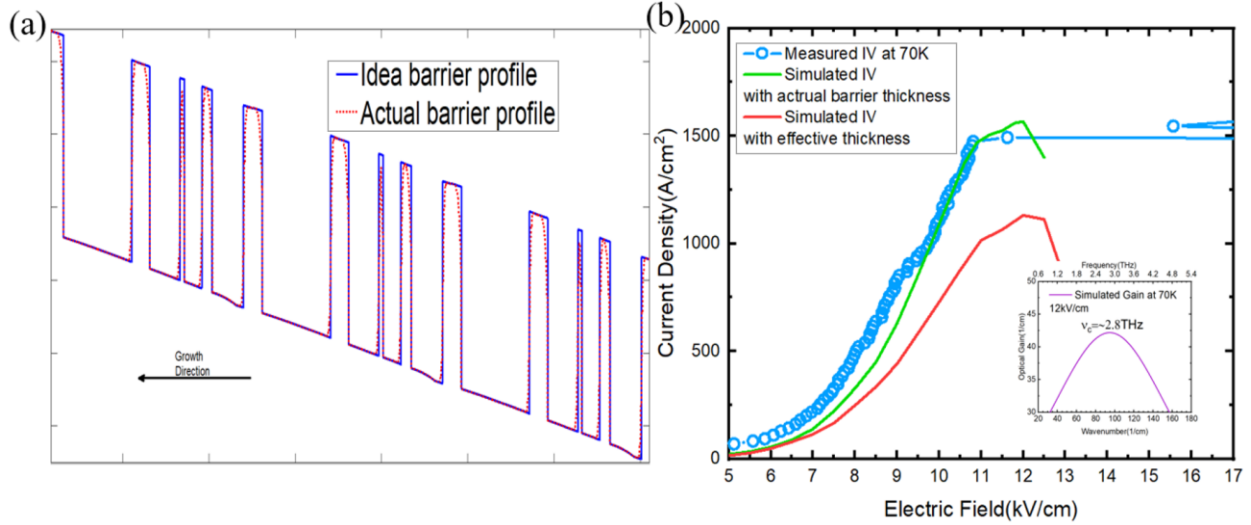


Fig. 5-5. Impact of accurate barrier profile on simulation results. (a) Plot of the conduction band of HEID device with ideal barrier profile assumption and actual barrier profile in blue/red, respectively. (b) Comparison of simulated J-V curve with ideal barrier profile assumption and actual barrier profile (green/red) and measured J-V curve (blue) at heat sink temperature of 70 K [43].

### 5.3.3 Hybrid Extraction/Injection Channel

Fig. 5-6 (a) presents the simulated current density carried through the RP channel (red curve), the SA channel (green curve), and the combination of the two (blue curve) for comparison. The curves are simulated at lattice temperature of 70 K and electron temperature of 140 K above lattice temperature. The peak current density through the first extraction/injection channel (RP channel) is observed at an electric field of  $\sim 11$  kV/cm, and that through the second extraction/injection channel (SA channel) is at  $\sim 12$  kV/cm, showing a difference of  $\sim 1$  kV/cm in the electric field. The difference might enable a wider bias dynamic range for lasing operation. However, if the two channels can be tuned to reach their maximum current carrying capacity at the same electric field, the electrical instability can be further suppressed, and the population inversion can be improved [100].

Fig. 5-6 (b) compares the plot of simulated differential resistance and measured differential resistance from a small laser device ( $40 \mu\text{m}$  wide and  $\sim 2$  mm long). We select the small device for comparison due to its small total injection current and small extra voltage drop on wire resistance. It is worth noting that a ridge of  $40 \mu\text{m}$  in width shows higher threshold current density and low  $T_{\text{max}}$  of 100 K due to higher loss compared to the best device that is presented in Fig. 5-3. We observe two peaks (A and B) on both simulated and measured differential resistance curves (Fig. 5-6 (b)). Peak A appears at the electric field when injector state ( $1_{n-1}$ ) passes extractor state ( $2_n$ ), and peak B appears at the electric field when the first RP-based extraction/injection channel passes its peak current capability. In a  $40 \mu\text{m}$  wide device, lasing happens after peak B, which is another strong evidence to show that the second extraction/injection

channel (SA channel) contributes population inversion and benefits lasing operation, particularly for devices with high optical loss, or operation at higher temperature.

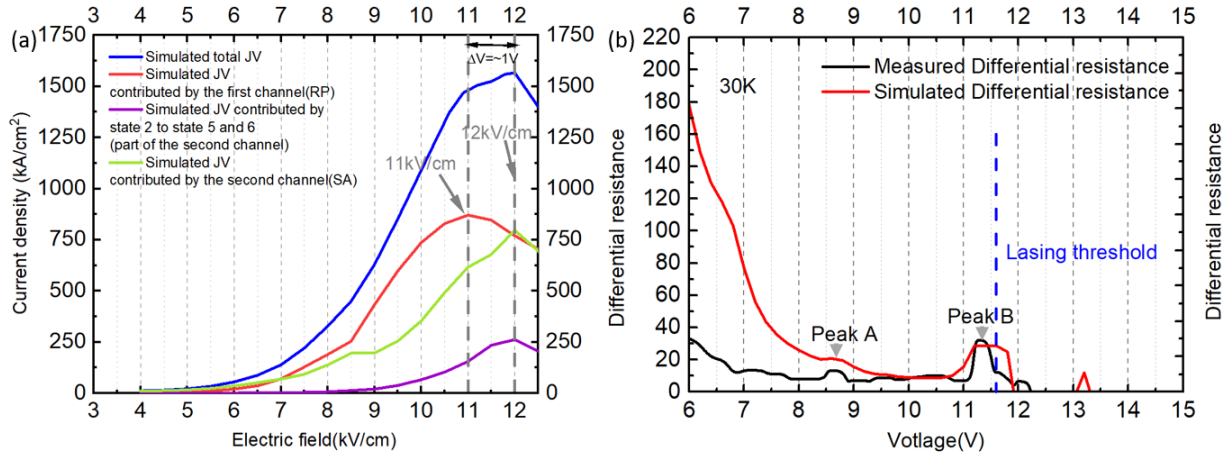


Fig. 5-6. Contribution of two extraction/injection channels. (a) Current contributed by two extraction/injection channels at lattice temperature of 70 K. (b) Measured differential resistance on a 40  $\mu\text{m}$  wide ridge device at heat sink temperature of 30 K and simulated differential resistance at lattice temperature of 30 K [43].

## 5.4 Conclusion

This chapter demonstrates a new THz QCL design with hybrid extraction/injection channels, in which both resonant-phonon and scattering-assisted injection/extraction are employed. In comparison with other THz QCL designs with the same material system of GaAs/Al<sub>0.15</sub>Ga<sub>0.85</sub>As, this hybrid extraction/injection design structure shows advantages in reducing pre-threshold electrical instability and suppressing thermally activated current leakage to higher excited states and continuum. As a result, the measured current density-voltage curves are free of intermediate NDR, and the final NDR is still observable at a temperature as high as 260 K. In addition, the HEID device also exhibits a high characteristic temperature of 259 K, showing promising potential for higher-temperature operation after further quantum design and device optimization.

---

This chapter is a slightly modified version of (Boyu Wen, Chris Deimert, Siyi Wang, Chao Xu, Sm Shazzad Rassel, Zbigniew Wasilewski, and Dayan Ban, Opt. Express 28, 26499-26508) Copyright (2020) Optical Society of America.

## Chapter 6 Novel THz QCL Designs: Theoretical Investigation

Previous sections have reviewed the maximum operating temperature of THz QCLs highly relates to THz QCLs quantum structure designs. Exploring the new possible THz QCL structures and optimizing the existing structures are important for developing high-performance THz QCLs. The first HEID has been designed and demonstrated, and the experimental result shows advantages in reducing pre-threshold electrical instability and suppressing thermally activated current leakage to higher excited states and continuum. However, the first attempt of such design could not achieve record-breaking high operating temperature. Considering the substantial study and efforts on RP and two-well direct-phonon design, a second design based on HEID structure would be necessary to reveal its real potential on temperature performance. The second HEID structure is investigated theoretically, but not experimentally, due to the MBE growth lag behind schedule. In addition, a short period design with narrowest period width and lowest number of layers per period can simplify the design, increase its tolerance for experimental error, and reduce the injection wells that may provide negative optical gain on terahertz region. This chapter presents the shortest design named quasi one-well (Q1W) design, with only 3 layers per period. The design is investigated theoretically via NEGF model [103] and rate equation model. Both models show that the Q1W designs can exhibit a higher optical gain than the state-of-the-art THz QCL devices (V775 and G652). In particular, the nextnano. NEGF simulation results show the optimized Q1W design can achieve optical gain of around  $35 \text{ cm}^{-1}$  at 250K and around  $20 \text{ cm}^{-1}$  at 300 K.

### 6.1 Quasi One-Well (Q1W) Design

Since the first demonstration of a terahertz (THz) quantum cascade laser (QCL) in 2002 [12], improving the operating temperature performance is one of the most important topics for THz QCL and its applications. Researchers have found that THz QCL quantum structure designs are critical for temperature performance of the device [14,21,34,64,91,104] and have made great efforts to explore different THz QCL quantum structure designs. Multiple quantum designs, such as the bound-to-continuum (BTC) design [87,101], resonant-phonon (RP) design [64], scattering-assisted (SA) design [34], dual lasing design [63], phonon-photon-phonon (3p) design [32,33], direct-phonon design [14,35], split-well direct-phonon design [28,102], and hybrid extraction/injection design [43], have been experimentally demonstrated and exhibited good temperature performance at different frequency at 1.2–5.4 THz. The most recent world record is demonstrated using two-well direct-phonon design [104]. At the time of writing, the two-well direct-phonon is the reported shortest quantum cascade design with the lowest number of layers per period (four layers per period). It has been argued that maximum lasing temperature tends to increase as the number of layers per period decreases [14]. Furthermore, a narrower

THz QCL design enables the epi-growth of more repeating periods in the active region (AR), which is typically around 10  $\mu\text{m}$  in thickness. A higher number of repeating periods means that the electrons can go through more photon generation cycles.

In a typical THz QCL quantum design demonstrated so far, a radiation barrier between lasing states and an injection barrier between repeating periods are essentially critical for achieving a sufficiently high optical gain and reaching the device design bias before entering a negative differential resistance (NDR) region. Without a well-engineered radiative barrier and an injection barrier, the design bias is very likely to locate in the NDR region [107], in which inhomogeneous and oscillating electric field domains emerge in the AR and the lasing operation is generally disrupted [29,107]. In some theoretical research attempts, superlattice designs were employed and results show that the device design bias may be attainable in a positive differential resistance (PDR) region, but the extremely diagonal transition in the design failed achieving sufficient optical gain [108]. It is therefore very challenging to design a THz QCL quantum structure that consists of fewer than four semiconductor layers per period but is still capable to achieving a high optical gain and a design bias in a PDR region spontaneously.

This section presents a Q1W design scheme that requires only three layers per period, in which the radiation barrier and the injection barrier are combined by employing one single step-tapered barrier. The Q1W design is verified by using the nextnano. NEGF simulation tool [103]. The design requires the lowest number of layers and the lowest thickness per period among all THz QCL quantum structures. The Q1W design exhibits sufficient high optical gain in the positive differential resistance (PDR) region.

### 6.1.1 Q1W Design Concept

A step-tapered barrier is used to combine radiation barrier and injection barrier, and a three-level system is used for the Q1W design. A simplified concept diagram of a Q1W design with three main energy levels is presented in Fig. 6-1(a). The diagram includes three repeating periods named per. N-1, per. N, and per. N+1, and there are only three layers per period. Each period in Fig. 6-1(a) and (b) is separated by the blue dashed lines. From the left to the right in Fig. 6-1(a) and (b), the first layer is a 1.7 nm thick radiation barrier with 25% Al; the second layer is an 8 nm thick step barrier layer with 7% Al; the third layer is a 11.4 nm GaAs based quantum well. The starting of radiation barrier is set to be the zero position. Each period consists of an upper lasing (UL), a lower lasing (LL), and an injector state, but they are not contributing to the electron transport and photon generation within the same period at the design bias. Moreover, it is worth noting that the  $LL_{n-1}$  in the (N-1)-th period is higher than the  $UL_n$  in the N-th period. As such faster re-injection of electrons from the  $LL_{n-1}$  to the  $UL_n$  can be activated.

Fig. 6-1(b) shows the conduction band diagram at the design bias when the injector<sub>n</sub> is lifted by externally-applied electric field and aligned with the  $UL_n$ . The three main confined energy levels in each



period are named lev.1–3 in order of energy from the highest to the lowest in the same way as Fig. 1(a). The highest confined energy level in the N-th period (lev\_1 per.N) serves as the LL for the (N-1)-th period, the second highest confined energy level in the N-th period (lev\_2 per.N) serves as the UL in the N-th period, and the lowest confined energy level in the N-th period (lev\_3 per.N) serves as the injector/extractor state located around 43 meV, which is  $\sim 7$  meV higher than the LO phonon energy of 36.5 meV, below the  $LL_n$  (lev\_1 per.N+1) and aligns with  $UL_{n+1}$  (lev\_2 per.N+1) in the subsequent period. In this case, each M number of repeating periods accommodate M-1 full pairs of lasing levels, and electrons can finish the cycle of injection-generating photon-collection every  $M/(M-1)$  well. Since a typical 10  $\mu\text{m}$  THz QCL AR accommodates hundreds of repeating periods, the average number of wells needed for one photon generation cycle is close to one. The thickness of one period in this design is only  $\sim 20$  nm, and it is narrower than all demonstrated THz QCL designs; therefore, an AR that is typically 10  $\mu\text{m}$  in thickness can accommodate  $\sim 500$  repeating periods. The injection well that provides negative optical gain in THz frequency region is omitted in Q1W design, the required threshold population inversion between lasing state should be lower due to the lower THz radiation re-absorption.

Fig. 6-1(c) displays the spatial optical gain distribution. The initial designed frequency is approximately 3.75 THz, and the highest optical gain occurs at the position from 10–20 nm in the period, where LL (lev.3 per. N+1) and UL (lev.2 per. N) overlap in the N-th period. Some optical gain is also observed at the position from 0–5 nm, which corresponds to the overlapping of UL and LL for the (N-1)-th period, as illustrated in Fig. 6-1(a). Fig. 6-1(c) confirms that the optical gain results from the designed pair of lasing states. Moreover, Fig. 6-1(c) presents the conduction band diagram at zero bias. Each well consists a LL, UL, and injector state, but they are not used in the same photon generation cycle at design bias. It is worth noting that because LL is the higher energy level than UL in Q1W design scheme, it can enable faster re-injection of electron from  $LL_{n-1}$  to  $UL_n$ .

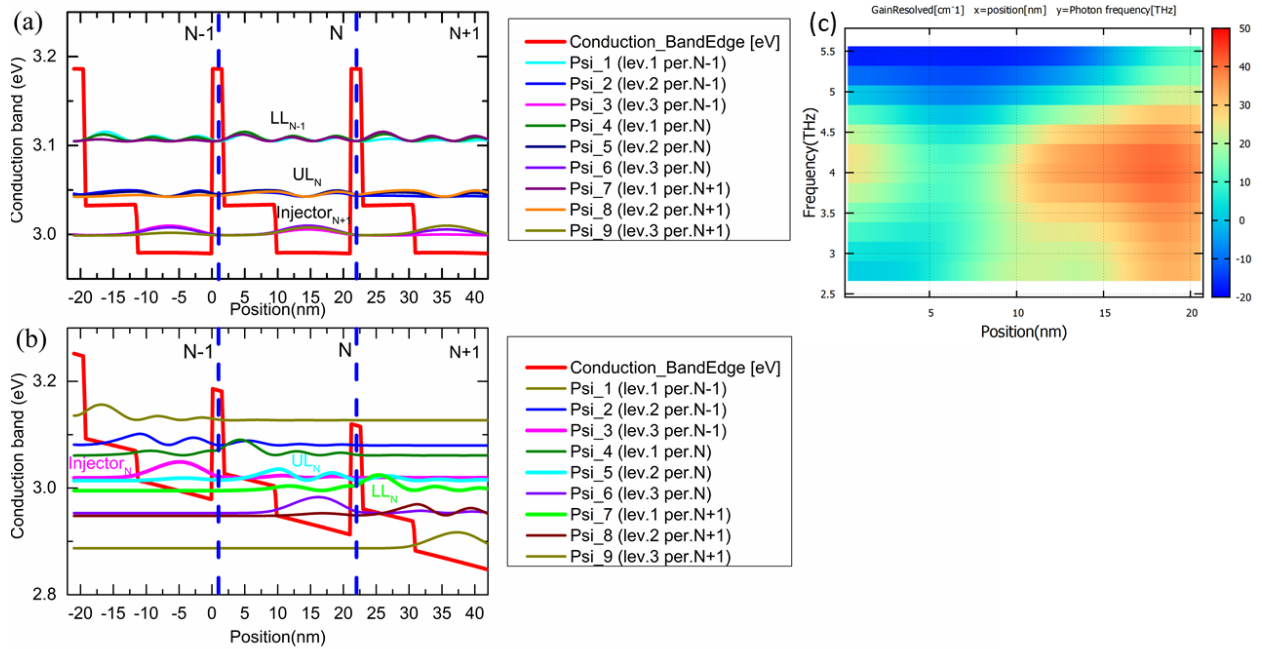


Fig. 6-1. Conduction band diagram and resolved 2D optical gain at 100 K. (a) Conduction band diagram of a Q1W design at a design bias of 72 mV. (b) Frequency- and position-dependent optical gain distribution at an electric bias of 72mV and a temperature of 100 K. (c) Conduction band diagram of a Q1W design at zero bias.

### 6.1.2 Actual Q1W Designs

The conduction band diagram of an actual design targeting emission frequency of 3 THz is illustrated in Fig. 6-2(a). Fig. 6-2(b) displays the simulated optical gain from 100 K to 300 K at a voltage of 72 mV per period. The NEGF simulation results show a sufficient optical gain of around 30 /cm at 300 K. Fig. 6-2(c) presents a simulated voltage-current density curve. Here, the maximum current density is observed at 74 mV/period. Note that the design bias is 72 mV/period, which is lower than the peak current bias (74 mV/period). This satisfies the pre-requisition of achieving population inversion in a PDR region.

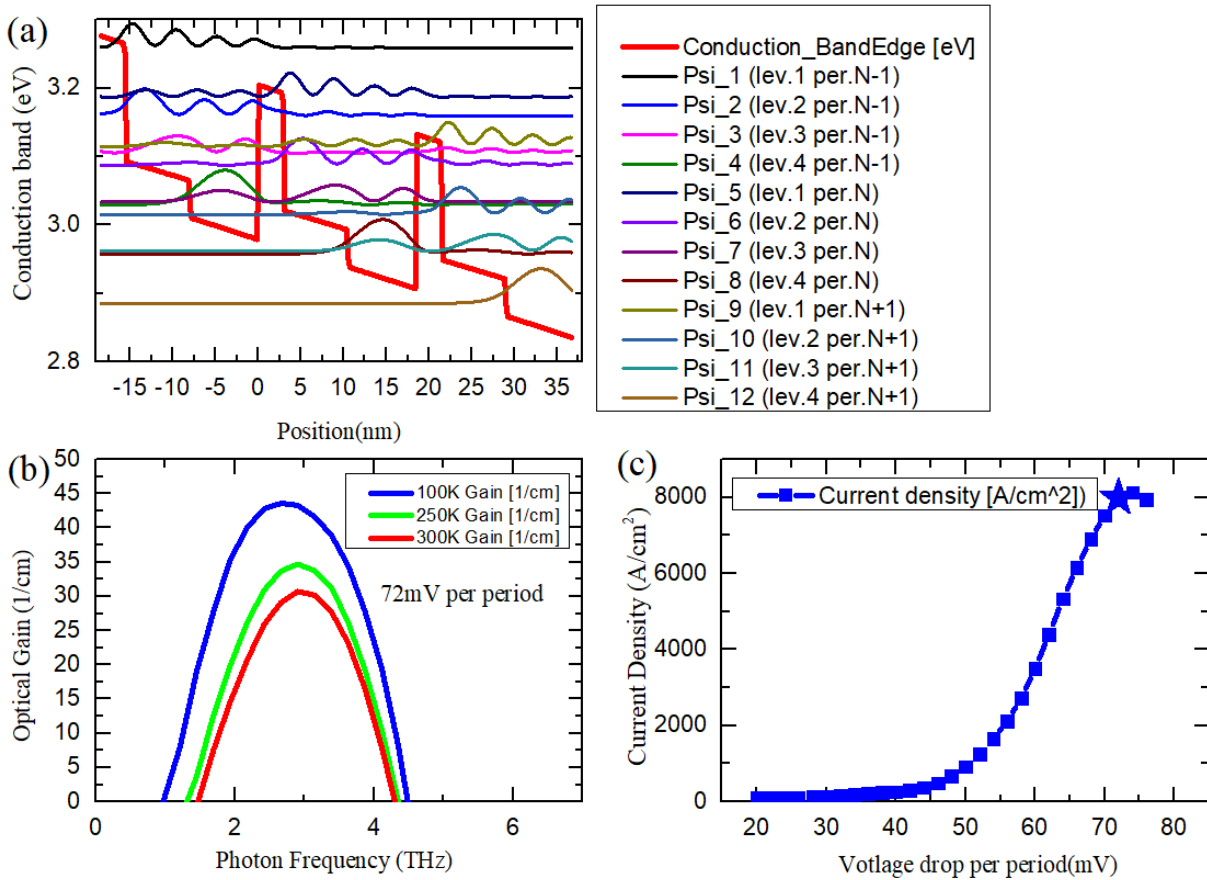


Fig. 6-2. Finalized Q1W design B simulation result by NEGF model. (a) Conduction band diagram. (b) Calculated temperature-dependent optical gain. (c) Voltage-Current density curve at 100 K.

A series of Q1W designs is summarized in Table 6-1. Due to the high and broad absorption centered around phonon energy (from the injector<sub>n</sub> to the LL<sub>n</sub>, and from the UL<sub>n</sub> to the LL<sub>n-1</sub>), which is spatially overlapped with lasing states. The designs with the highest optical gain are found with a center frequency of around 3 THz, such as Q1W design B, C, D and E. There is some value difference between NEGF model [103] and RE model, it is mainly resulted from different model approach on Al<sub>x</sub>Ga<sub>1-x</sub>As band gap [105,106] and different interface roughness parameters. Nevertheless, both models show that Q1W

designs (B, C, D and E) have better simulation performance than G652 at 250 K. The Q1W-B shows highest averaged optical gain calculated by RE and nextnano. NEGF models. Q1W design C2 has a lower doping density of  $3 \times 10^{10} \text{ cm}^{-2}$ , which can reduce operating current density at the cost of lower optical gain. The Q1W-D is an optimization result based on RE with band gap values based on Z. Wasilewski's paper [105], while the Q1W-E is an optimization result based on NEGF model with band gap values based on Vurgaftman's paper [103,106]. Q1W designs exhibit higher operating electric field in comparison with G652 shown in table 6-1. Higher operation current density and higher operation bias are some of the features of the Q1W design scheme. High operation bias might cause high joule heat and high over-barrier leakage. The over-barrier leakage of the Q1W design B is analyzed in section 6.1.3. Joule heat generation in pulse mode operation is relatively easy to solve. Compared to G652, the Q1W design B's operation current increases from  $2.5 \text{ kA/cm}^2$  to  $\sim 8 \text{ kA/cm}^2$  and the operation bias is increased from  $\sim 29 \text{ kV/cm}$  to  $35 \text{ kV/cm}$ . The injected power is increased to 3.86 times higher than G652. However, the injection pulse used to measure G652 up to 250 K is 400 ns wide, while it is common for a pulse generator to generate a narrower pulse of  $\sim 100 \text{ ns}$ . In this case, the total injected power to the Q1W design B can be kept roughly at a similar range with G652. The Q1W design B exhibits the highest operating current density among Q1W design series presented in this section.

Design	NEGF simulated peak optical gain @ 250 K (cm <sup>-1</sup> )	RE simulated peak optical gain @ 250 K (cm <sup>-1</sup> )	Operation bias (mV)	Sheet doping density (cm <sup>-2</sup> )	Period length (nm)	Electric field (kV/cm)
Q1W-A	28.3	16.0	68	4.5×10 <sup>10</sup>	19.7	34.5
Q1W-B	34.7	29.8	72	4.5×10 <sup>10</sup>	18.5	38.9
Q1W-C	32.7	24.6	68	4.5×10 <sup>10</sup>	19.7	34.5
Q1W-C2	22.0	16.4	68	3×10 <sup>10</sup>	19.7	34.5
Q1W-D	28.1	31	66	4.5×10 <sup>10</sup>	18.8	35.1
Q1W-E	35	21.9	72	4.5×10 <sup>10</sup>	18.5	38.9
G652 [104]	16.5	19.0	76	4.03×10 <sup>10</sup>	26.9	28.2
V775 [64]	15.1	6.42	58	3×10 <sup>10</sup>	43.91	13.3

Table 6-1. Summary of optimized designs. Design A: 3.0(27%Al)/**8**(7%Al)/8.7(GaAs). Design B:

3.0(27%Al)/**7.5**(7%Al)/8.0(GaAs). Design C: 3.0(25%Al)/**8**(7%Al)/8.7(GaAs). Design D:

3.0(27%Al)/**8.3**(5%Al)/7.5(GaAs). Design E: 3.0(30%Al)/**7.5**(7%Al)/8.0(GaAs). Layer thickness are shown in nm, and numbers in bold indicate barriers. The underlined layers are averagely doped. The operation bias and electric field is calculated by NEGF model.

### 6.1.3 Investigation of Temperature Sensitivity

Simulated optical gain versus temperature is simulated by RE model and plotted to investigate temperature sensitivity, as shown in Fig. 6-3(a). The simulated V775 is shown in green, the simulated G652 in blue, and the simulated Q1W design B in red curve. The estimated threshold optical gain is usually around 15–25 /cm, and 22 /cm is selected as the estimated threshold optical gain in Fig. 6-5(a). Simulated V775 reaches threshold gain around 205 K, and simulated G652 reaches threshold gain around ~245 K, both values are close to the published results (199.5 K and 250 K) [64,104]. Based on the same simulation method, the Q1W design B has the potential to achieve higher operating temperature because of its relatively lower temperature sensitivity. The reason for the relatively lower temperature sensitivity in the Q1W design B is explained in Fig. 6-3(b). As described in Chapter 1, one of the major temperature dependent performance degradation factors for THz QCL is thermal activated LO phonon scattering. Hot electrons with high kinetic energy can be scattered from UL to LL via phonon emission. This LO phonon scattering at high temperature dominates scattering mechanism between UL and LL, so the population inversion is destroyed. However, in and only in Q1W design, LL<sub>n</sub> is the third lowest energy level and

$UL_{n+1}$  is the second lowest energy level in the same well, as described in Fig. 6-1(c). Hence, the overlapping between  $LL_n$  and  $UL_{n+1}$  is large and electrons tend to scatter to the lower energy level in the same well. In the other words, the scattering time from  $LL_n$  to  $UL_{n+1}$  (dashed line in Fig 6-3(b)) is faster than the LO phonon scattering between diagonally spaced  $UL_n$  to  $LL_n$  (solid line in Fig 6-3(b)) at temperature of 30–290 K, as shown in Fig. 6-3(b). The dominating electrons scattering process is from  $LL_n$  to  $UL_{n+1}$ . The strong scattering may introduce extra broadening to lasing states and results lower peak optical gain than V652 and V775 at temperature lower than  $\sim 150$  K, as shown in Fig. 6-3(a). This scattering process can compensate the detrimental LO phonon scattering from  $UL_n$  to  $LL_n$  to help keeping the population inversion from fast temperature dependent degradation.

Temperature dependent over-barrier leakage current is also calculated and compared between the Q1W design B and the state-of-the-art designs shown in Fig. 6-3(c). Despite the higher operation bias of Q1W design, the leakage current to continuum is limited below  $500 \text{ A/cm}^2$  in Q1W design B and G652, and the V775 shows higher leakage current to continuum than Q1W-B, as shown in Fig. 6-3(c). This simulation result indicates that over-barrier leakage might not be a significant issue in Q1W design.

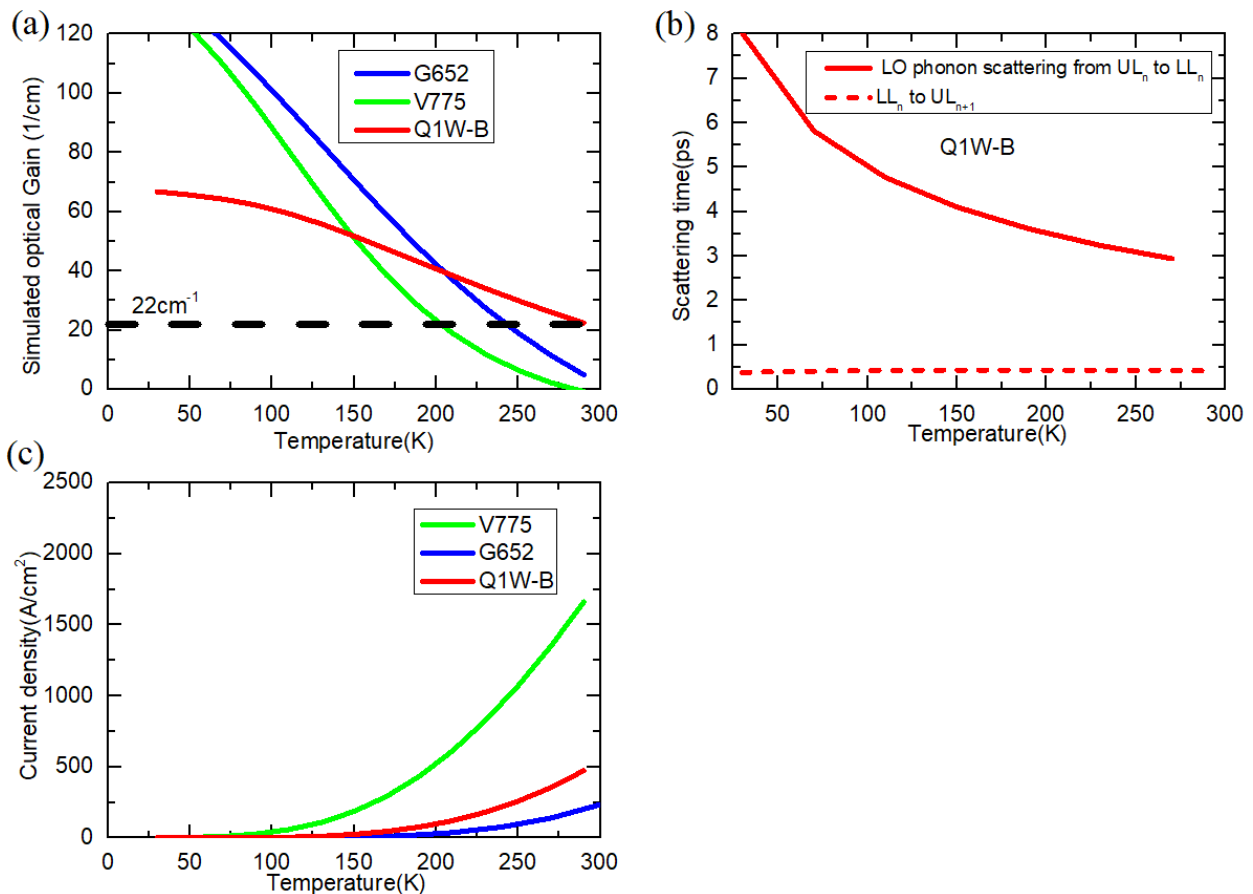


Fig. 6-3. Temperature dependent calculations using RE model. (a) Temperature dependent optical gain, (b) LO phonon scattering time from  $UL_n$  to  $LL_n$  (solid line) and scattering time from  $LL_n$  to  $UL_{n+1}$  (dashed line), and (c) Over-barrier leakage current based on RE model. Blue curve is two-well DP structure G652, green curve is RP structure V775, and red curve is quasi one-well design B.

### 6.1.4 Tolerance on Experimental Variation

Simple optimization process has been performed on Q1W design to produce designs shown in Table 6-1, and experiment error tolerance is included in the optimization process, the error tolerance is discussed in this section as well. Q1W design utilizes a step-tapered barrier, and the actual Al concentration might differ from the design value due to the changing of the flux rate during long-time growth. It is necessary to investigate the tolerance of step-tapered barrier variation, so, we performed a series of simulations based on design B variants with different Al concentration or different well width by using NEGF model from [103]. The barrier height and well width dependent simulation performance degradation is presented in Table 6-2.

Design	Step-tapered barrier	Relative variation on barrier height	Relative variation on well width	Peak optical gain at 250 K (1/cm)	Lasing frequency (THz)
Q1W design B (target value)	27%/7% Al	0%	0%	34.7	3
Q1W design B+	27%/8%Al	+14%	0%	30.1	2.6
Q1W design B-	27%/6%Al	-14%	0%	30	2.8
Q1W design B++	27%/7% Al	0%	+8.7%	31	2.1
Q1W design B--	27%/7% Al	0%	-7%	24	3.2

Table 6-2. NEGF Simulation results on quasi one-well structures with variation in barrier height and well width.

Design B: **3.0**(27%Al)/**7.5**(7%Al)/8.0(GaAs). The simulation is performed using nextnano. NEGF simulation tool from [103]

The simulated design reveals a peak optical gain greater than 30 /cm with a  $\pm 14\%$  relative variation on barrier height. The simulation results also show a peak optical gain greater than 24 /cm with a  $\pm 7\%$  relative variation of well width by using the nextnano. NEGF simulation tool [103]. The experimental errors are typically within these error ranges, so the design is practical in terms of tolerance of experimental errors.

### 6.1.5 Investigation on critical design parameters

This section investigates main critical design parameters that may significantly affect the performance of Q1W design. The step-tapered barrier effective thickness is the key parameter to ensure Q1W design has designed bias at PDR region and maintain a good optical gain. Parasitic energy levels are also need to be carefully tuned to minimized detrimental leakage between short periods.

#### 6.1.5.1 Effect of Step-Tapered Barrier Thickness

Step-tapered barrier affects both JV curve and optical gain, and the effect is discussed by using simplified three-level simulation in this section. The current density-voltage (JV) curves and calculated optical gain are presented in Fig. 6-4. JV curves are important parameters to assess if the Q1W design can achieve design bias before entering the NDR. A THz QCL at design bias usually exhibit the highest population inversion and thus the highest optical gain, and it is important to ensure that a sufficiently high optical gain is achieved in the PDR region to thereby ensure that THz QCL can ignite [29]. To achieve sufficient optical gain in the PDR region for proper lasing operation. To achieve sufficient optical gain in the PDR region, the barrier thickness is the key parameter for tuning the JV curves. In another sentence, the step-tapered barrier can tune the JV curve, so that the design bias will not be in an NDR, so that we can achieve sufficient positive optical gain that is achieved only at the design bias.

Three test cases of how step-tapered barrier thicknesses affect the simulation performance with three main energy levels are presented in Fig. 6-4. In the simplified three-level simulation, all three testcases (testcases 1–3) reveal that the highest optical gain is achieved at the electric bias with the highest current density (marked by stars on the JV curves). The testcase 1 is the optimized structure by using the simplified three-level simulation, and its barrier is 9.7 nm thick which consists of a 1.7 nm thick  $\text{Al}_{0.25}\text{Ga}_{0.75}\text{As}$  based radiation barrier and an 8 nm thick  $\text{Al}_{0.07}\text{Ga}_{0.93}\text{As}$  based step barrier. The GaAs based quantum well is 11.4 nm thick. Testcase 1 shows a peak current density of  $\sim 4500 \text{ A/cm}^2$  at bias of 60 mV in the NEGF model. The peak gain achieved without considering leakage levels is 48 /cm at 100 K.

Testcase 2 presents the structure with a step-tapered barrier that is 1 nm thinner than testcase 1 in thickness, and testcase 3 presents the structure with a step-tapered barrier that is 1 nm thicker than testcase 1 in thickness. The quantum well thickness of testcase 3 is also tuned 1 nm thinner than testcase 1 and testcase 2 to keep the energy spacing between lasing states closer to 3 THz. The normal variation during the growth is typically much less than 1 nm.

The results of testcase 3 and 2 reveal the effect of step-tapered barrier on JV curve and optical gain. On the one hand, a thick barrier is needed to keep the pre-threshold leakage channels sufficiently low to



ensure the peak gain is achieved in PDR region. The step-tapered barrier, which is  $1.7(25\%Al)/7(7\%Al)$ , in testcase 2 is close to the thinnest barrier it can be to ensure a threshold bias in PDR, because the pre-threshold leakage channel at the voltage of 50 mV per period produces almost the same amount of current with design bias of 62 mV per period as shown in Fig. 6-4(a). On the other hand, a thicker barrier reduces injection coupling energy and reduces the maximum population the design can achieve. A thicker barrier, which is  $2.7(25\%Al)/7(7\%Al)$  in testcase 3, reduces peak gain from 48 /cm to  $\sim 26$  /cm at 100 K. Further trials are needed to identify the sweet point of step-tapered barrier thickness. The barrier thickness in this section is tested under the condition of 10.4–11.4 nm well width. Well width should be adjusted according to the barrier thickness and height due to the position change of confined energy levels. However, the effect of step-tapered barrier thickness follows the trend discussed in this section.

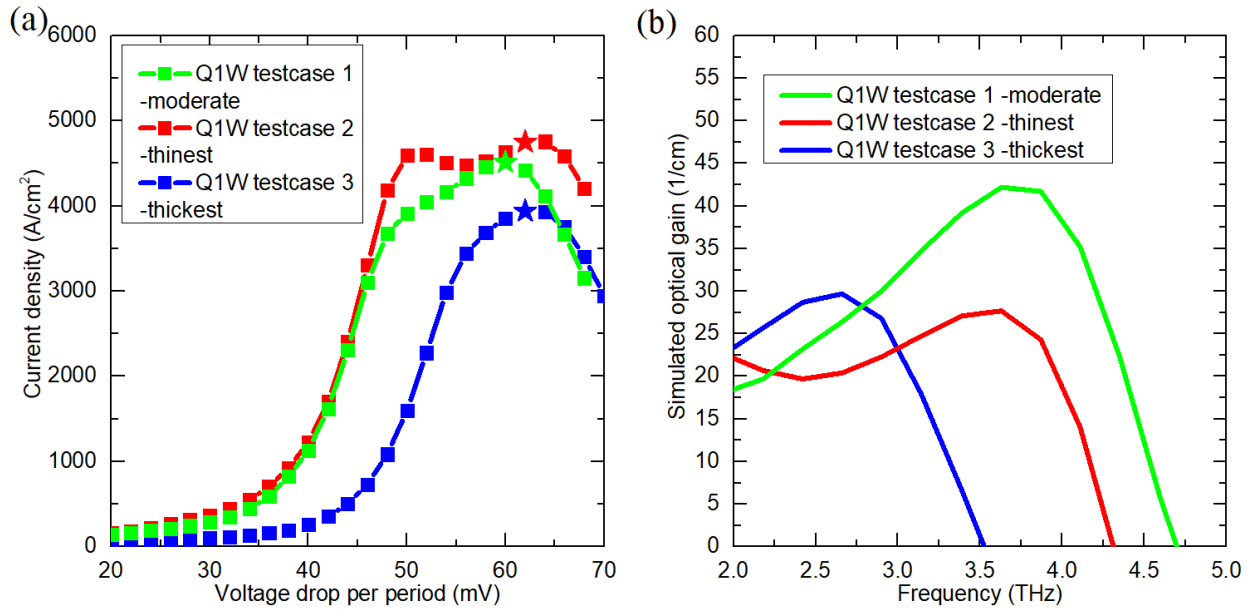


Fig. 6-4. Simulation performance of three quasi one-well designs at 100 K. (a) JV curves at 100 K. (b) Optical gain at 100 K. Testcase 3:  $\underline{2.7}(25\%Al)/7(7\%Al)/10.4(GaAs)$ , testcase 2:  $\underline{1.7}(25\%Al)/7(7\%Al)/11.4(GaAs)$ , testcase 1:  $\underline{1.7}(25\%Al)/8(7\%Al)/11.4(GaAs)$ . Layer thickness are shown in nm, and numbers in bold indicates barriers. The underlined layers are averagely doped to achieve sheet density of  $3 \times 10^{10} \text{ cm}^{-2}$ . Testcase 1-3 failed during subsequent investigation conducted in section 6.1.3.

### 6.1.5.2 Effect of High-energy Parasitic Energy Levels

The principle of the Q1W design scheme is verified by a simplified three-level system in Fig. 6-1, and the effect of step-tapered effective thicknesses is discussed in Fig. 6-4. In order to convert the design idea to a real structure, a full simulation with all confined energy states up to barrier edge for each period is performed to investigate the role of high-energy parasitic energy levels. It is worth noting that the second highest energy level (highlighted by thick lines) in the (N+1)-th period is closely spaced in energy with

UL (lev.4 per. N in Fig. 6-5(a)) in the N-th period. Due to the short period, the two energy states can be strongly coupled at the alignment condition near design bias, as described in Fig. 6-5(a). This strong coupling can create a leakage path that vanishes the gain of testcase 1 at 100 K, as illustrated in Fig. 6-5(b). Around 15 percentages of available electrons remain on the leakage level and vanished optical gain peak at 3.75 THz from Fig. 6-4(b).

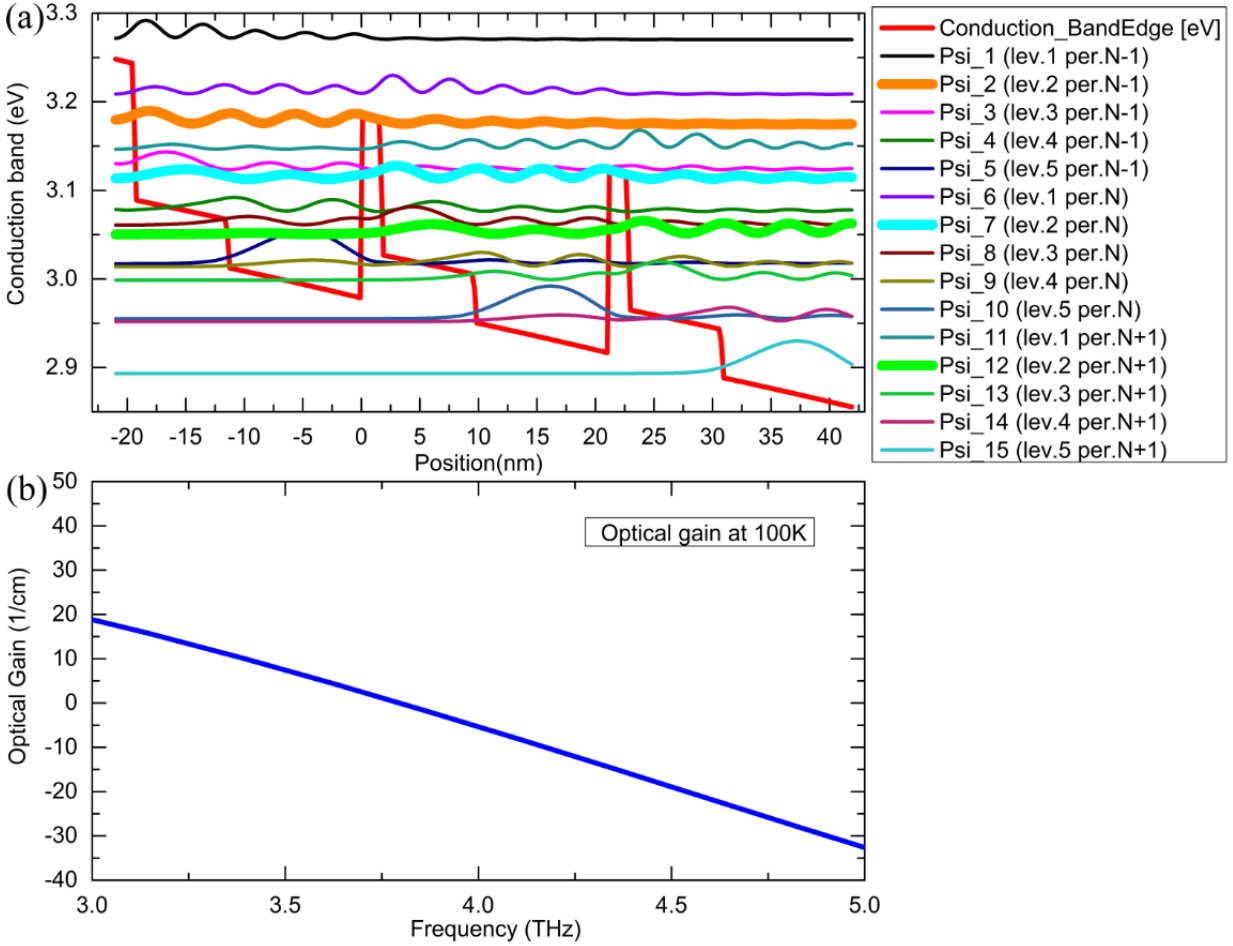


Fig. 6-5. Effect of a parasitic energy level. (a) Conduction band diagram of Q1W testcase 2 at 62 mV. (b) Calculated optical gain of testcase 2 with high energy leakage levels at 250 K.

GaAs well width plays a key role in tuning the parasitic energy levels in the Q1W design. After having performed a large number of trials for this design, we found a good choice for the Q1W thickness, which is shown in Fig 6-2, and successfully tuned the first parasitic channel to an energy higher than UL and thus reduced the coupling strength can improve leakage issue and retain the design bias at PDR region. The step-tapered barrier is also adjusted in accordance with the change of well width. In the optimized designs summarized in Table 6-1, parasitic energy level still creates leakage current, but not so significant as to ruin the population inversion. The optical gain is improved from low values shown in Fig. 6-5 (b) to high values shown in Fig. 6-2(b) by tuning the parasitic energy level.

In conclusion, Q1W design series is developed theoretically by using nextnano. NEGF model [103] and RE model. The Q1W design series consists only three layers per period, and the total thickness per period is below 20 nm which is considered thinner than all demonstrated THz QCL designs. The Q1W design series exhibits sufficient positive gain of  $\sim 35$  /cm at 250K at design electric field of  $\sim 35$ – $39$  kV/cm. The design bias is located at PDR region with peak current density of  $4$ – $8$  kA/cm<sup>2</sup>. The Q1W design series shows good relative error tolerance that the peak optical gain remains above  $24$  /cm with a relative variance of  $7$ – $9\%$  on quantum well width. These features of the Q1W design scheme make it a promising design scheme for THz QCL designs of high-efficiency and high-temperature performance.

## **6.2 Second Hybrid Extraction/Injection Design**

This section presents a hybrid extraction/injection design that combines the SA and RP transport schemes by using an idea similar to that employed in chapter 5. The design used different design parameters, such as injection coupling energy and targeting lasing frequency, than the experimental demonstrated design presented in Chapter 5.

### **6.2.1 Introduction and Motivation for Making the Second HEID**

The terahertz region of the electromagnetic spectrum has remained underdeveloped due to the inadequacies of coherent sources. Despite a number of potential applications, it is always experimentally challenging to produce radiation in terahertz region. THz QCL is one of the most promising coherent radiation sources. It is compact and able to continuously cover frequency of  $1.3$ – $5.4$  THz; however, the operating temperature of THz QCL is below room temperature. Multiple designs, including the scattering-assisted design [34], resonant-phonon design [64], and two-well direct-phonon design [14], demonstrate record-high temperature performance in the past decade. Recently, a novel design that combines the scattering-assisted design and resonant-phonon design in one quantum structure to form a hybrid extraction/injection design (HEID) structure is developed and demonstrated, as presented in Chapter 5. The HEID structure exhibits good suppression of over-barrier carrier leakage and pre-threshold leakage. The high characteristic temperature and high-temperature observation of NDR are believed to be important for high-temperature performance [18,21,104]. Compared with all the attentions the scattering-assisted design, resonant-phonon design, and two-well direct-phonon design have received over past decades, the potentials of HEID scheme have been very much overlooked. The HEID scheme requires more experimental investigation and design structure optimization to reveal its best temperature performance potential. To further study the HEID scheme and optimize the design by using the knowledge obtained from the first HEID in Chapter 5, a second HEID structure is theoretically developed and presented in this chapter.

## 6.2.2 Conduction Band Diagram

The major design concept is based on the design described in Chapter 5. The boundary of a single period/module is marked by blue dashed lines in Fig. 6-6. The injector state is labeled as lev.5 for each period, UL is labeled as lev.6, LL is labeled as lev. 7, and two extractor states are labeled as lev.3 and lev.4. The highest energy level (lev.1 and lev.2 in each period) are parasitic energy levels which have little effect on this structure. Barrier height is the major difference between this design and the first HEID presented in Chapter 5. The Al concentration in barriers is increased from 15% to 23% to further reduce over-barrier leakage.

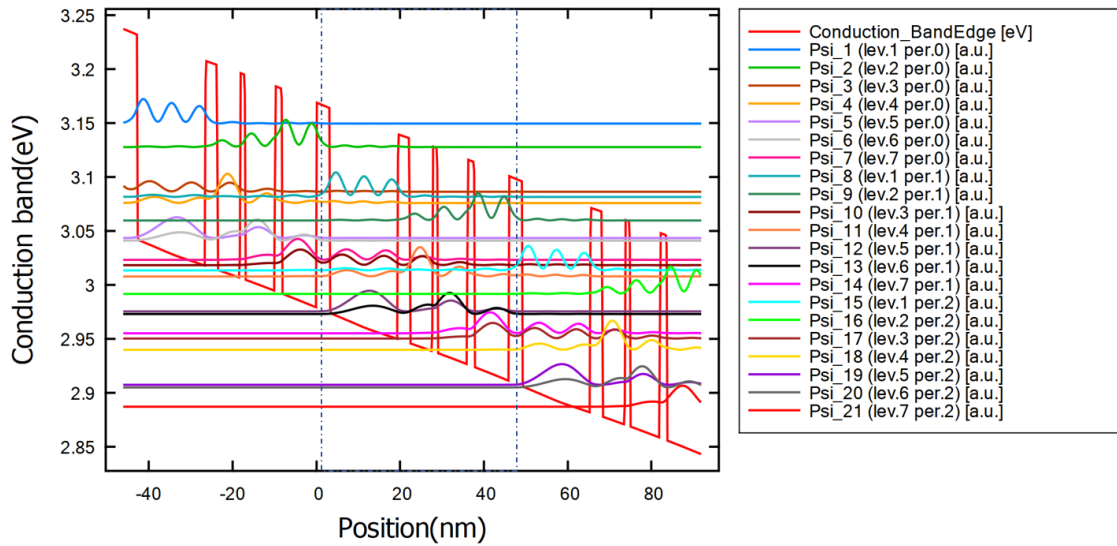


Fig. 6-6. Conduction band diagram of the second HEID design. The structure layer thickness: **2.9**(23%Al)/5.45/**1.2**(23%Al)/7.1/**1.7**(23%Al)/8.2/**3.2**(23%Al)/6.2/5/5 nm. Bold numbers indicate barriers, and underlined number is the doped area.

## 6.2.3 Simulation Results and Growth Sheet

Simulation of this structure is performed by the NEGF model software from nextnano.NEGF [103] at a lattice temperature of 200 K. Fig. 6-7(a) presents the JV curve simulation at 200 K. The simulated  $J_{\max}$  occurs at a potential drop of 66 mV. There is no significant pre-threshold leakage channel to prevent the device from reaching design bias. The current density is relatively lower than the first HEID device, which is believed to reduce Joule heat caused by injected current. Fig. 6-7(b) displays the simulated optical gain at 66 mV. The center frequency is at 4.5 THz, and the peak optical gain is  $\sim 26$  /cm at 200 K from NEGF model [103], indicating the design's promising potential for high-temperature operation on and above 200 K.

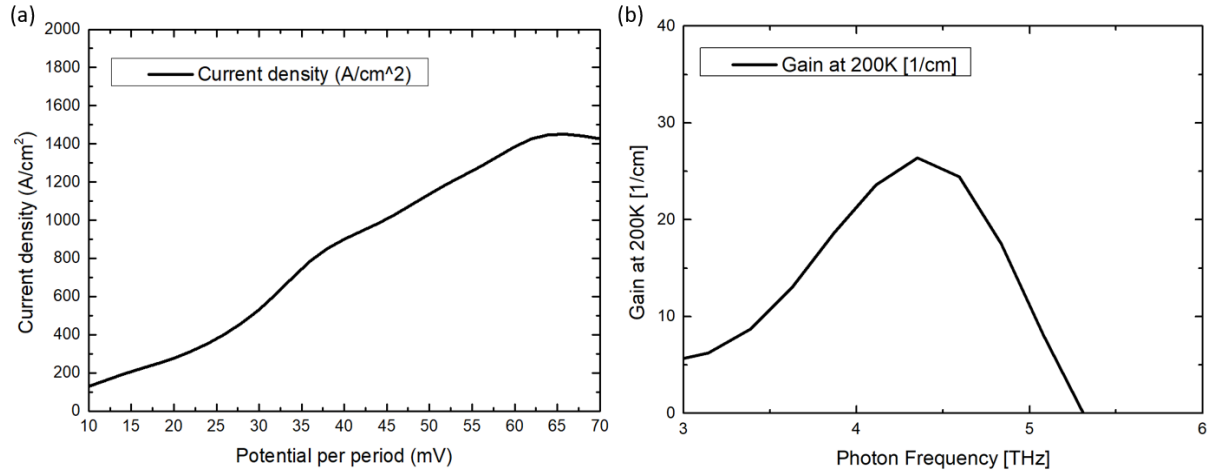


Fig. 6-7. NEGF Simulation performance of 2<sup>nd</sup> HEID at 200 K. (a) JV curve at lattice temperature of 200 K. (b) Simulated optical gain at 66mV.

The second HEID is then tested in RE-based model and NEGF based model to validate its reliability of simulated temperature performance. The temperature dependent peak optical gain is exhibited in Fig. 6-8. Blue curve indicates simulation result from RE model, and green curve indicates simulation result from NEGF model from [103]. The two models show very close simulation results on the second HEID structure, and temperature dependent optical gain curves cross the estimated threshold gain (22 cm<sup>-1</sup>) at ~220 K.

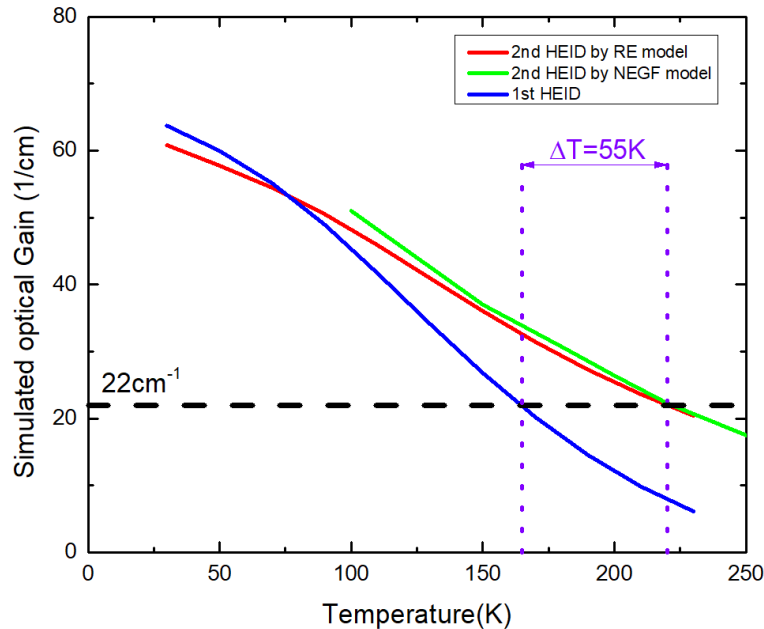


Fig. 6-8. Simulated temperature dependent peak optical gain of 1<sup>st</sup> HEID from RE model (blue solid line), 2<sup>nd</sup> HEID from RE model (red solid curve), and NEGF model [103] (green solid curve). The estimated threshold gain is 22/cm, as indicated by black dashed line.

A detailed growth sheet has been created for growth, as depicted in Fig. 6-9. The total thickness of one period is  $\sim 460 \text{ \AA}$ , and the entire  $\sim 10 \text{ \mu m}$  AR consists of 218 repeating periods. Dopant is implanted at the center 5 nm in the phonon well. The entire AR is sandwiched by a 10 nm spacer, and a  $3 \text{ \mu m}$   $\text{Al}_{0.55}\text{Ga}_{0.45}\text{As}$  layer is grown as the etch-stop layer.

	Comment	Material	x	d [Å]	doping N [cm-3]	reps
	Semi Insulating GaAs					
	Buffer	GaAs		2000.0		1
	Etch Stop	$\text{Al}_x\text{Ga}_{1-x}\text{As}$	0.55	3000.0		1
	Positive bias	GaAs:Si		1000.0	$5.00\text{E}+18$	1
	Spacer	GaAs		100.0		1
218	Injector Barrier	$\text{Al}_x\text{Ga}_{1-x}\text{As}$	0.23	29.0		218
	Phonon Well	GaAs		50.0		218
	<b>Si doping</b>	GaAs:Si		50.0	$7.60\text{E}+16$	218
	Phonon Well	GaAs		62.0		218
	Collector Barrier	$\text{Al}_x\text{Ga}_{1-x}\text{As}$	0.23	32.0		218
	Lower lasing Well	GaAs		82.0		218
	Lasing Barrier	$\text{Al}_x\text{Ga}_{1-x}\text{As}$	0.23	17.0		218
	Upper Lasing Well	GaAs		71.0		218
	injector Barrier 2	$\text{Al}_x\text{Ga}_{1-x}\text{As}$	0.23	12.0		218
	Injector Well	GaAs		54.5		218
	Injector Barrier	$\text{Al}_x\text{Ga}_{1-x}\text{As}$	0.23	29.0		1
	Phonon Well	GaAs		50.0		1
	<b>Si doping</b>	GaAs:Si		50.0	$7.60\text{E}+16$	1
	Phonon Well	GaAs		62.0		1
	Collector Barrier	$\text{Al}_x\text{Ga}_{1-x}\text{As}$	0.23	32.0		1
	Spacer	GaAs		100.0		1
	Top Contact A	GaAs:Si		500.0	$5.00\text{E}+18$	1
	Top Contact B	GaAs:Si		100.0	$5.00\text{E}+19$	1
	Top Contact C	LT GaAs		35.0		

Module Thickness:	459.5
Total Repeating Growth Thickness:	100171
Number of repeats:	218

Doping Sheet Density:	$3.80\text{E}+10$
Doping density	$7.60\text{E}+16$
Average Doping:	$8.27\text{E}+15$

Fig. 6-9. Growth sheet of the second HEID design.

### 6.3 Conclusion

This chapter presents two novel THz QCL designs. One is the second HEID structure that is optimized based on an analysis of the experimental results from the first HEID structure. The performance is investigated theoretically by NEGF model [103] and RE model. Both models indicate that the second HEID structure shows higher optical gain than the best reported RP structure (V775). The other design series is the first Q1W design series that consists of only 3 layers per period. The design is considered to be the shortest period design among all reported THz QCL designs. Q1W design series is also

investigated by NEGF and RE model. Both models show that Q1W designs, specifically, design B and design C, exhibit higher optical gain than the state-of-the-art pulse mode THz QCL designs (V775 and G652).

## Chapter 7 Conclusion

Throughout my Ph.D. program, I have questioned how the performance of THz QCLs can be improved by exploring new quantum designs. In my view, two directions are possible for pursuing high-performance THz QCL designs. One involves consistently improving theoretical models, including parameters used in simulation to improve their accuracy in handling complex structures. THz QCL quantum design is a complex work involving many subbands with energy spacing close to line broadening, and the structure must be designed precisely on angstrom scale. The more quantum wells added into one period, the more freedom there is to tune with trade-offs. However, multiple quantum wells structures are difficult to optimize and rely significantly on the accuracy of the model. The second direction involves developing a quantum structure with fewer layers for it to have high tolerance for experimental and design errors as well as easy optimization.

This chapter presents and summarizes my work and scientific contribution in the development of THz QCLs with novel quantum designs. In addition, it explores avenues for future work.

### 7.1 Summary of the Work

This thesis represents a series of attempts that encompasses theory, computing, quantum structure design, and experimentation to explore novel THz QCL quantum designs which pave the way for room-temperature THz QCLs. The main results of this thesis are summarized as follows:

1. Two sets of efficient numerical simulation codes based on rate equation model and density matrix model, including detailed important scattering processes, an over-barrier leakage estimation, a non-uniform interface, and charge-induced band bending, are developed and implemented with MATLAB code. The efficient numerical simulation codes can well simulate IV curves and optical gain characteristics of THz QCLs.
2. Full fabrication steps of THz QCL from a newly grown wafer to ridge waveguide devices via In-Au bonding, Au-Au bonding, and Cu-Cu bonding process are performed to obtain the experimental results of THz QCL. A cryostat vacuum chamber is designed and assembled for the measurements. LIV and spectra measurements have been performed to characterize the THz QCL devices. Over 300 THz QCL devices are characterized.
3. Dual-lasing channel behavior are characterized and analyzed to provide deeper understanding of dual-lasing channel THz QCLs theoretically and experimentally. The device exhibits a low-threshold current density of  $550 \text{ A/cm}^2$  at 50 K and a maximum operating temperature of 144 K. It is proved that this dual lasing structure scheme is shown to provide 0.3 THz frequency coverage at low frequencies with the lowest-reported threshold current density based on SA



structures and a temperature performance close to the highest operating temperature recorded in this frequency range. Devices from different fabrication benches are characterized to verify the robustness of the experimental observations. NEGF model and RE model are used in the simulation to verify the consistency of the analysis.

4. Simulation models are used to analyze the state-of-the-art THz QCL designs and develop the first hybrid extraction/injection design structure which combines an RP-based scheme and an SA-based scheme in one quantum structure. A novel HEID structure is designed, fabricated, and characterized. Compared with other THz QCL designs with the same material system of GaAs/Al<sub>0.15</sub>Ga<sub>0.85</sub>As, this HEID structure demonstrates the advantages of reducing pre-threshold electrical instability and suppressing thermally activated current leakage to higher excited states and continuum. As a result, the measured current density-voltage curves are free from intermediate NDR, and the final NDR remains observable at temperatures as high as 260 K. In addition, this HEID device also exhibits a high characteristic temperature of 259 K. It, therefore, shows promise for higher-temperature operations after further quantum design and device optimization.
5. The first hybrid extraction/injection design is analyzed, and an improved second-generation HEID structure is developed. The new design leads to a ~55 K performance improvement on the first HEID and ~20 K improvement on the best-reported RP structure (V775).
6. A possible novel design named quasi one-well design that has three layers in each period is explored. This design is the narrowest of all existing THz QCL structures to date. A quasi one-well design series is also investigated using NEGF and RE models. Both models show that the Q1W designs exhibit higher optical gain than state-of-the-art pulse mode operation THz QCL designs (V775 and G652). These results suggest that the novel quasi one-well design is a promising design scheme toward room temperature operation.

## 7.2 Contributions of the Thesis

By making progress in the development of THz QCLs with novel quantum designs, the thesis contributes to scientific understanding and technological development in the field of THz QCL research. The main contributions of the thesis are as follows:

1. This thesis provides a deeper understanding of dual-lasing channel THz QCL based on SA design both theoretically and experimentally. The results are described in Chapter 4 and have been published on the journal Optics express.

2. This thesis developed and demonstrated the first hybrid extraction/injection design structure that combines an RP-based scheme and an SA-based scheme in one quantum structure. Compared with other THz QCL designs with the same material system of GaAs/Al<sub>0.15</sub>Ga<sub>0.85</sub>As, this HEID structure shows advantages in reducing pre-threshold electrical instability and suppressing thermally activated current leakage to higher excited states and continuum. The results are described in Chapter 4 and have been published on Optics express.
3. The first hybrid extraction/injection design is analyzed, and an improved second-generation HEID structure is proposed. The second HEID design can lead to a ~55 K performance improvement on the first HEID and a ~20 K improvement on the best-reported RP structure (V775). The results are presented in detail in section 6.2.
4. This thesis proposes a possible novel quasi one-well design with three layers in each period, which has not been previously reported. This design is the narrowest of all existing THz QCL structures to date. The results are presented in section 6.1. The manuscript is to be submitted.

Publications during the Ph.D. program:

Journal publications:

1. **Wen, B.**, Deimert, C., Wang, S., Xu, C., Rassel, S. S., Wasilewski, Z., & Ban, D. Six-level hybrid extraction/injection scheme terahertz quantum cascade laser with suppressed thermally activated carrier leakage. *Optics Express*, 28(18), pp.26499-26508. (2020).
2. **Wen, B.**, Xu, C., Wang, S., Wang, K., Tam, M.C., Wasilewski, Z. and Ban, D., Dual-lasing channel quantum cascade laser based on scattering-assisted injection design. *Optics express*, 26(7), pp.9194-9204. (2018).
3. **Wen, B.**, Ban, D., Quasi one-well terahertz quantum cascade laser with sufficient optical gain above lattice temperature of 250K. manuscript to be submitted.
4. Ban, D., **Wen, B.**, High temperature terahertz quantum cascade lasers. manuscript in preparation. (Invited)
5. Ban, D., **Wen, B.**, Dhar, R.S., Razavipour, S.G., Xu, C., Wang, X., Wasilewski, Z. and Dixon-Warren, S., 2016. Electrical scanning probe microscopy of electronic and photonic devices: connecting internal mechanisms with external measures. *Nanotechnology Reviews*, 5(3), pp.279-300.

6. Wang, S., Xu, C., Duan, F., **Wen, B.**, Rassel, S. S., Tam, M. C., ... & Ban, D. (2020). Thermal dynamic imaging of mid-infrared quantum cascade lasers with high temporal-spatial resolution. *Journal of Applied Physics*, 128(8), 083106..
7. Khan, A. A., Rana, M. M., Huang, G., Mei, N., Saritas, R., **Wen, B.**, ... & Ban, D. (2020). Maximizing piezoelectricity by self-assembled highly porous perovskite-polymer composite films to enable the internet of things. *Journal of Materials Chemistry A*, 8(27), 13619-13629.
8. Rana, M. M., Khan, A. A., Huang, G., Mei, N., Saritas, R., **Wen, B.**, ... & Ban, D. (2020). Porosity Modulated High-Performance Piezoelectric Nanogenerator Based on Organic/Inorganic Nanomaterials for Self-Powered Structural Health Monitoring. *ACS Applied Materials & Interfaces*, 12(42), 47503-47512.

Conference publications/presentation:

1. **Wen, B.**, Xu, C., Wang, S., Wang, K., He, X., Wasilewski, Z.R., Ban, D., ‘Lasing channels switching in dual color scattering assisted THz quantum-cascade laser’, *The 14th International Conference On intersubband Transition in Quantum Wells*, Sands Expo and Convention Center, Singapore, 11-15 September 2017.
2. **Wen, B.**, Xu, C., Wang, S., Wasilewski, Z.R., Ban, D., ‘Scattering Assisted dual color THz quantum cascade laser operating up to 144K with large dynamic range’, *The 18th Canadian Semiconductor Science and Technology Conference*, Waterloo, Ontario, Canada, 24- 27 August 2017.
3. **Wen, B.**, Ban, D., Watchorn, J., ‘Improved Resonant Phonon-based THz QCL density matrix model’, *The 4th International Quantum Cascade Lasers School and Workshop*, Cambridge, UK, 4 - 9 September 2016.
4. Wang, K., **Wen, B.**, Ban, D., ‘Effect of Dopant Position on Impurity Scattering Time and Optical Gain in Terahertz Quantum Cascade Laser’, *The 18th Canadian Semiconductor Science and Technology Conference*, Waterloo, Ontario, Canada, 24- 27 August 2017.
5. Wang, S., Xu, C., Duan, F., **Wen, B.**, Rassel, S. S., Wasilewski, Z., ... & Ban, D. (2020, May). Time-resolved Thermoreflectance Imaging for Mid-infrared Quantum Cascade Laser. In *CLEO: Applications and Technology* (pp. JTu2G-2). Optical Society of America.
6. Xu, C., Wang, S., **Wen, B.**, He, X., Zhuo, Y., Gosselink, D., Wasilewski, Z.R., Ban, D., Tam, M.C., ‘Broad-band Terahertz Quantum Cascade Lasers’, *The 18th Canadian Semiconductor Science and Technology Conference*, Waterloo, Ontario, Canada, 24- 27 August 2017.

### 7.3 Future Work

The operating temperature is one of the most significant challenges in THz QCL development. The highest operating temperature was kept at 200 K by the RP scheme for seven years, and improved to 210K in 2019 and subsequently to 250K in 2020, using a two-well direct-phonon scheme. It has been shown that THz QCL quantum structure design plays an important role in operating temperature and arguably determines the upper limit of operating temperature of the THz QCL wafer. The two-well direct-phonon structure was first demonstrated in 2010. It took researchers 10 years to reveal its major potential in high-temperature operations. This suggests that substantial optimization and reliable optimization methods are needed for novel THz QCL structures.

Dual-lasing channel designs can be further explored in bi-directional operations to achieve 3–4 lasing channels in a single THz QCL design. Specifically, the dual-lasing channel design could be modified to be more symmetrical while maintaining the dual-lasing operation in forward bias. When applying forward bias, the device can be electrically tuned between two lasing channels targeting different frequency ranges (an example is illustrated in Chapter 4, the targeting frequencies are 2.1 and 2.5 THz); when applying reverse bias, the device can also achieve lasing because of its symmetric design. In such cases, a single QCL can be electrically tuned between 3–4 lasing frequencies, such as with 2 lasing channels in forward bias at a different applied voltage and 1–2 lasing channels in reverse bias. This type of device would be useful for achieving low-cost chemical species identification by measuring its fingerprint absorption in THz range.

The HEID structure is invented and demonstrated for the first time in this thesis. Compared with other existing structures, optimization and experimental trials are needed to pinpoint its true potentials in high-temperature operations. The analysis of the first HEID structure shows that this structure relies on three resonant tunneling, which requires accurate simulation tools. An accurate conduction band shape, confined energy level, and charge-induced conduction band bending simulation are essential for optimization. The HEID structure can theoretically achieve higher population inversion than designs relied on only one resonant tunneling injection; conversely, multiple resonant tunneling processes make HEID structure critical to simulation accuracy during design stage and sensitive to experimental errors.

A short-period design is also worthy of experimental testing. In THz QCLs, the wavelength of the emission radiation is larger than the thickness of the active region, so, it is tightly confined in  $\sim 10 \mu\text{m}$  AR by a double metal waveguide. In the THz QCL structure, the lasing wells can provide positive optical gain, but other GaAs and  $\text{Al}_x\text{Ga}_{1-x}\text{As}$  layers provide absorption from free carriers and multiple confined subbands, which do not have population inversion as lasing states. This absorption from non-lasing wells can reduce the total optical gain produced by AR, as the THz mode is also highly distributed on the

layers. Designing a short-period design can significantly reduce absorption in AR and increase the total number of repeating periods. Further, a short-period design can reduce the need for minimal population inversion between lasing states for lasing operation and increase efficiency because of its low number of absorption layers per period and large number of repeating periods.

# Letters of copyright permission

4/2/2021

RightsLink Printable License

## SPRINGER NATURE LICENSE TERMS AND CONDITIONS

Apr 02, 2021

---

This Agreement between University of Waterloo -- BOYU WEN ("You") and Springer Nature ("Springer Nature") consists of your license details and the terms and conditions provided by Springer Nature and Copyright Clearance Center.

License Number	5041100645497
License date	Apr 02, 2021
Licensed Content Publisher	Springer Nature
Licensed Content Publication	Applied Physics A: Materials Science & Processing
Licensed Content Title	Terahertz spectroscopy applied to the analysis of artists' materials
Licensed Content Author	Kaori Fukunaga et al
Licensed Content Date	Mar 30, 2010
Type of Use	Thesis/Dissertation
Requestor type	non-commercial (non-profit)
Format	print and electronic
Portion	figures/tables/illustrations

Will you be translating?	no
Circulation/distribution	1 - 29
Author of this Springer Nature content	no
Title	Development of Terahertz Quantum Cascade Lasers with Novel Quantum Designs
Institution name	University of Waterloo
Expected presentation date	May 2021
Order reference number	1
Portions	Fig. 1
Requestor Location	University of Waterloo 395 BAMBERG CRES 200 University Avenue West, WATERLOO, ON N2T 0B5 Canada Attn: University of Waterloo
Total	0.00 USD
Terms and Conditions	

ELSEVIER LICENSE  
TERMS AND CONDITIONS

Apr 05, 2021

---

This Agreement between University of Waterloo -- BOYU WEN ("You") and Elsevier ("Elsevier") consists of your license details and the terms and conditions provided by Elsevier and Copyright Clearance Center.

License Number	5042640343685
License date	Apr 05, 2021
Licensed Content Publisher	Elsevier
Licensed Content Publication	Optics Communications
Licensed Content Title	Fast continuous terahertz wave imaging system for security
Licensed Content Author	Qian Song, Yuejin Zhao, Albert Redo-Sanchez, Cunlin Zhang, Xiaohua Liu
Licensed Content Date	May 15, 2009
Licensed Content Volume	282
Licensed Content Issue	10
Licensed Content Pages	4
Start Page	2019
End Page	2022
Type of Use	reuse in a thesis/dissertation



Portion	figures/tables/illustrations
Number of figures/tables/illustrations	5
Format	both print and electronic
Are you the author of this Elsevier article?	No
Will you be translating?	No
Title	Development of Terahertz Quantum Cascade Lasers with Novel Quantum Designs
Institution name	University of Waterloo
Expected presentation date	May 2021
Portions	all figures
Requestor Location	University of Waterloo 395 BAMBERG CRES 200 University Avenue West, WATERLOO, ON N2T 0B5 Canada Attn: University of Waterloo
Publisher Tax ID	GB 494 6272 12
Total	0.00 USD
Terms and Conditions	

SPRINGER NATURE LICENSE  
TERMS AND CONDITIONS

Apr 03, 2021

---

This Agreement between University of Waterloo -- BOYU WEN ("You") and Springer Nature ("Springer Nature") consists of your license details and the terms and conditions provided by Springer Nature and Copyright Clearance Center.

License Number 5041600688378

License date Apr 03, 2021

Licensed Content Publisher Springer Nature

Licensed Content  
Publication Nature PhysicsLicensed Content Title A 1.8-THz quantum cascade laser operating significantly above the temperature of  $\hbar\omega/kB$ 

Licensed Content Author Sushil Kumar et al

Licensed Content Date Dec 12, 2010

Type of Use Thesis/Dissertation

Requestor type academic/university or research institute

Format print and electronic

Portion figures/tables/illustrations

Number of  
figures/tables/illustrations 1<https://is100.copyright.com/AppDispatchServlet>

4/3/2021

RightsLink Printable License

High-res required no

Will you be translating? no

Circulation/distribution 1 - 29

Author of this Springer Nature content no

Title Development of Terahertz Quantum Cascade Lasers with Novel Quantum Designs

Institution name University of Waterloo

Expected presentation date May 2021

Portions all figures

Requestor Location  
University of Waterloo  
395 BAMBERG CRES  
200 University Avenue West,  
WATERLOO, ON N2T 0B5  
Canada  
Attn: University of Waterloo

Total 0.00 USD

SPRINGER NATURE LICENSE  
TERMS AND CONDITIONS

Apr 02, 2021

---

This Agreement between University of Waterloo -- BOYU WEN ("You") and Springer Nature ("Springer Nature") consists of your license details and the terms and conditions provided by Springer Nature and Copyright Clearance Center.

License Number	5041100645497
License date	Apr 02, 2021
Licensed Content Publisher	Springer Nature
Licensed Content Publication	Applied Physics A: Materials Science & Processing
Licensed Content Title	Terahertz spectroscopy applied to the analysis of artists' materials
Licensed Content Author	Kaori Fukunaga et al
Licensed Content Date	Mar 30, 2010
Type of Use	Thesis/Dissertation
Requestor type	non-commercial (non-profit)
Format	print and electronic
Portion	figures/tables/illustrations
Number of figures/tables/illustrations	1

<https://s100.copyright.com/AppDispatchServlet>

4/2/2021

RightsLink Printable License

Will you be translating?	no
Circulation/distribution	1 - 29
Author of this Springer Nature content	no
Title	Development of Terahertz Quantum Cascade Lasers with Novel Quantum Designs
Institution name	University of Waterloo
Expected presentation date	May 2021
Order reference number	1
Portions	Fig. 1
Requestor Location	University of Waterloo 395 BAMBERG CRES 200 University Avenue West, WATERLOO, ON N2T 0B5 Canada Attn: University of Waterloo
Total	0.00 USD

 [Market place logo](#)

Dear BOYU WEN,

Thank you for placing your order on [Marketplace™](#).

**Order Summary:**

Order date: 03 Apr 2021  
Order number: 1109229  
No. of items: 1  
Order total: 0.00 USD

**Billing Summary:**

Payment method: Invoice  
An invoice will be generated and emailed within 24 hours.

To view your order details, click the following link, sign in, and search for your order:  
[Manage Account](#).


How was your experience? [Click here to give us feedback](#)

Please do not reply to this message.

To speak with a Customer Service Representative, call +1-855-239-3415 toll free or +1-978-646-2600 (24 hours a day), or email your questions and comments to [support@copyright.com](mailto:support@copyright.com).

Sincerely,

The CCC Marketplace Team

Tel: 1-855-239-3415 / +1-978-646-2600  [Copyright Clearance Center](#)  
[support@copyright.com](mailto:support@copyright.com)  
[Manage Account](#)

## Thank you for your order!

Dear BOYU WEN,

Thank you for placing your order through Copyright Clearance Center's RightsLink® service.

### Order Summary

Licensee: University of Waterloo  
Order Date: Apr 2, 2021  
Order Number: 5041111112888  
Publication: Trends in Biotechnology  
Title: Biomedical Applications of Terahertz Spectroscopy and Imaging  
Type of Use: reuse in a thesis/dissertation  
Order Total: 0.00 USD

View or print complete [details](#) of your order and the publisher's terms and conditions.

Sincerely,

Copyright Clearance Center

## References

1. K. Fukunaga and M. Picollo, "Terahertz spectroscopy applied to the analysis of artists' materials," *Applied Physics A* **100**(3), 591–597 (2010).
2. Q. Song, Y. Zhao, A. Redo-Sanchez, C. Zhang, and X. Liu, "Fast continuous terahertz wave imaging system for security," *Optics Communications*, **282**(10), 2019–2022 (2009).
3. Y. Cai, Z. Wang, and D. Goyal, "Applications of terahertz technology in the semiconductor industry," In *Handbook of Terahertz Technology for Imaging, Sensing and Communications* (Woodhead Publishing, 2013), pp. 624–640.
4. X. Yang, X. Zhao, K. Yang, Y. Liu, Y. Liu, W. Fu, and Y. Luo, "Biomedical applications of terahertz spectroscopy and imaging," *Trends in Biotechnology* **34**(10), 810–824 (2016).
5. Delft University of Technology, (2017, Jan 22) "STO2 landed and data secured." <https://phys.org/news/2017-01-sto2.html>
6. S. U. Hwu, K. B. de Silva, and C. T. Jih, "Terahertz (THz) wireless systems for space applications," in *2013 IEEE Sensors Applications Symposium Proceedings* (2013), pp. 171–175.
7. S. S. Dhillon, M. S. Vitiello, E. H. Linfield, A. G. Davies, M. C. Hoffmann, J. Booske, C. Paoloni, M. Gensch, P. Weightman, G. P. Williams, and E. Castro-Camus, "The 2017 terahertz science and technology roadmap," *Journal of Physics D: Applied Physics* **50**(4), 043001 (2017).
8. J. Hebling, G. Almasi, I. Z. Kozma, and J. Kuhl, "Velocity matching by pulse front tilting for large-area THz-pulse generation," *Optics Express* **10**(21), 1161–1166 (2002).
9. K. Fujita, S. Jung, Y. Jiang, J. H. Kim, A. Nakanishi, A. Ito, M. Hitaka, T. Edamura, and M. A. Belkin, "Recent progress in terahertz difference-frequency quantum cascade laser sources," *Nanophotonics* **7**(11), 1795–1817 (2018).
10. P. Chevalier, A. Armizhan, F. Wang, M. Piccardo, S. G. Johnson, F. Capasso, and H. O. Everitt, "Widely tunable compact terahertz gas lasers," *Science* **366**(6467), 856–860 (2019).
11. E. Chiadroni, A. Bacci, M. Bellaveglia, M. Boscolo, M. Castellano, L. Cultrera, G. Di Pirro, M. Ferrario, L. Ficcadenti, D. Filippetto and G. Gatti, The SPARC linear accelerator based terahertz source. *Applied Physics Letters* **102**(9), 094101 (2013).
12. R. Köhler, A. Tredicucci, F. Beltram, H. E. Beere, E. H. Linfield, A. G. Davies, D. A. Ritchie, R. C. Iotti, and F. Rossi, "Terahertz semiconductor-heterostructure lasers," in *Conference on Lasers and Electro-Optics* (2002), p. CPDC12.
13. J. Faist, F. Capasso, D. L. Sivco, C. Sirtori, A. L. Hutchinson, and A. Y. Cho, "Quantum cascade laser," *Science* **264**(5158), 553–556 (1994).



14. L. Bosco, M. Franckić, G. Scalari, M. Beck, A. Wacker, and J. Faist, “Thermoelectrically cooled THz quantum cascade laser operating up to 210 K,” *Applied Physics Letters* **115**(1), 010601 (2019).
15. A. Albo, Q. Hu, and J. L. Reno, “Room temperature negative differential resistance in terahertz quantum cascade laser structures,” *Applied Physics Letters* **109**(8), 081102 (2016).
16. C. W. I. Chan, A. Albo, Q. Hu, and J. L. Reno, “Tradeoffs between oscillator strength and lifetime in terahertz quantum cascade lasers,” *Applied Physics Letters* **109**(20), 201104 (2016).
17. A. Albo and Y. V. Flores, “Temperature-driven enhancement of the stimulated emission rate in terahertz quantum cascade lasers,” *IEEE Journal of Quantum Electronics* **53**(1), 1–5 (2016).
18. A. Albo and Q. Hu, “Investigating temperature degradation in THz quantum cascade lasers by examination of temperature dependence of output power,” *Applied Physics Letters* **106**(13), 131108 (2015).
19. S. Fatholouloumi, E. Dupont, Z. R. Wasilewski, C. W. I. Chan, S. G. Razavipour, S. R. Laframboise, S. Huang, Q. Hu, D. Ban, and H. C. Liu, “Effect of oscillator strength and intermediate resonance on the performance of resonant phonon-based terahertz quantum cascade lasers,” *Journal of Applied Physics* **113**(11), 113109 (2013).
20. M. A. Kainz, S. Schönhuber, A. M. Andrews, H. Detz, B. Limbacher, G. Strasser, and K. Unterrainer, “Barrier height tuning of terahertz quantum cascade lasers for high-temperature operation,” *ACS Photonics* **5**(11), 4687–4693 (2018).
21. B. S. Williams, “Terahertz quantum-cascade lasers,” *Nature Photonics* **1**(9), 517–525 (2007).
22. C. W. I. Chan, Q. Hu, and J. L. Reno, “Tall-barrier terahertz quantum cascade lasers,” *Applied Physics Letters* **103**(15), 151117 (2013).
23. G. Scalari, C. Walther, M. Fischer, R. Terazzi, H. Beere, D. Ritchie, and J. Faist, “THz and sub-THz quantum cascade lasers,” *Laser & Photonics Reviews* **3**(1-2), 45–66 (2009).
24. B. S. Williams, H. Callebaut, S. Kumar, Q. Hu, and J. L. Reno, “3.4-THz quantum cascade laser based on longitudinal-optical-phonon scattering for depopulation,” *Applied Physics Letters* **82**(7), 1015–1017 (2003).
25. R. Köhler, A. Tredicucci, C. Mauro, F. Beltram, H. E. Beere, E. H. Linfield, A. G. Davies, and D. A. Ritchie, “Terahertz quantum-cascade lasers based on an interlaced photon-phonon cascade,” *Applied Physics Letters* **84**(8), 1266–1268 (2004) .
26. H. Luo, S. R. Laframboise, Z. R. Wasilewski, G. C. Aers, H. C. Liu, and J. C. Cao, “Terahertz quantum-cascade lasers based on a three-well active module,” *Applied Physics Letters* **90**(4), 041112 (2007).
27. E. Dupont, S. Fatholouloumi, Z. R. Wasilewski, G. Aers, S. R. Laframboise, M. Lindskog, S. G. Razavipour, A. Wacker, D. Ban, and H. C. Liu, “A phonon scattering assisted injection and extraction based terahertz quantum cascade laser,” *Journal of Applied Physics* **111**(7), 073111 (2012).

28. A. Albo, Y. V. Flores, Q. Hu, and J. L. Reno, "Split-well direct-phonon terahertz quantum cascade lasers," *Applied Physics Letters* **114**(19), 191102 (2019).
29. D. O. Winge, E. Dupont, and A. Wacker, "Ignition of quantum cascade lasers in a state of oscillating electric field domains," *Physical Review A* **98**(2), 023834 (2018).
30. Y. V. Flores and A. Albo, "Impact of interface roughness scattering on the performance of GaAs/Al<sub>x</sub>Ga<sub>1-x</sub>As terahertz quantum cascade lasers," *IEEE journal of Quantum Electronics* **53**(3), 1–8 (2017).
31. Y. V. Flores and A. Albo, "Erratum to 'Impact of interface roughness scattering on the performance of GaAs/Al<sub>x</sub>Ga<sub>1-x</sub>As terahertz quantum cascade lasers' [Jun 17 Art. no.2300208]," *IEEE J. of Quantum Electron* **53**(5), 1 (2017).
32. S. G. Razavipour, E. Dupont, C.W. I. Chan, C. Xu, Z. R. Wasilewski, S. R. Laframboise, Q. Hu, and D. Ban, "A high carrier injection terahertz quantum cascade laser based on indirectly pumped scheme," *Applied Physics Letters* **104**(4), 041111 (2014).
33. S. G. Razavipour, E. Dupont, S. Fatholouloumi, C. W. I. Chan, M. Lindskog, Z. R. Wasilewski, G. Aers, S. R. Laframboise, A. Wacker, Q. Hu, and D. Ban, "An indirectly pumped terahertz quantum cascade laser with low injection coupling strength operating above 150 K," *Journal of Applied Physics* **113**(20), 203107 (2013).
34. S. Kumar, C. W. I. Chan, Q. Hu, and J. L. Reno, "A 1.8-THz quantum cascade laser operating significantly above the temperature of  $\hbar \omega/k_B$ ," *Nature Physics* **7**(2), 166–171 (2011).
35. M. Franckić, L. Bosco, M. Beck, C. Bonzon, E. Mavrona, G. Scalari, A. Wacker, and J. Faist, "Two-well quantum cascade laser optimization by non-equilibrium Green's function modelling," *Applied Physics Letters* **112**(2), 021104 (2018).
36. H. Yasuda, "Intervalley scattering in terahertz quantum cascade lasers with GaSb and InGaSb wells," *AIP Adv.* **8**(2), 025125 (2018)
37. H. Yasuda, and I. Hosako, "Non-equilibrium Green's function calculation of AlGaAs-well-based and GaSb-based terahertz quantum cascade laser structures," *Applied Physics Letters*, **106**(11), 111111 (2015).
38. C. Deutsch, H. Detz, T. Zederbauer, M. Krall, M. Brandstetter, A.M. Andrews, P. Klang, W. Schrenk, G. Strasser, and K. Unterrainer, "InGaAs/GaAsSb/InP terahertz quantum cascade lasers," *Journal of Infrared, Millimeter, and Terahertz Waves* **34**(5-6), pp.374-385. (2013).
39. D. Stark, M. Mirza, L. Persichetti, M. Montanari, S. Markmann, M. Beck, T. Grange, S. Birner, M. Virgilio, C. Ciano, and M. Ortolani, "THz intersubband electroluminescence from n-type Ge/SiGe quantum cascade structures," *Applied Physics Letters* **118**(10), p.101101. (2021).
40. M. Fischer, G. Scalari, K. Celebi, M. Amanti, C. Walther, M. Beck, and J. Faist, Scattering processes in terahertz InGaAs/InAlAs quantum cascade lasers. *Applied Physics Letters* **97**(22), 221114. (2010).

41. B. Meng, B. Hinkov, N.M.L. Biavan, H.T. Hoang, D. Lefebvre, M. Hugues, D. Stark, M. Franckić, A. Torres-Pardo, J. Tamayo-Arriola, and M.M. Bajo, “Terahertz Intersubband Electroluminescence from Nonpolar m-Plane ZnO Quantum Cascade Structures,” *ACS Photonics*. (2020).
42. W. Terashima, and H. Hirayama, “Spontaneous emission from GaN/AlGaN terahertz quantum cascade laser grown on GaN substrate,” *physica status solidi c* **8**(7-8), pp.2302-2304. (2011).
43. B. Wen, C. Deimert, S. Wang, C. Xu, S. S. Rassel, Z. Wasilewski, and D. Ban, “Six-level hybrid extraction/injection scheme terahertz quantum cascade laser with suppressed thermally activated carrier leakage,” *Optics Express* **28**(18), 26499–26508 (2020).
44. A. Albo and Y. V. Flores, “Carrier leakage dynamics in terahertz quantum cascade lasers,” *IEEE Journal of Quantum Electronics* **53**(5), 1–8 (2017).
45. M. A. Belkin, J. A. Fan, S. Hormoz, F. Capasso, S. P. Khanna, M. Lachab, A. G. Davies, and E. H. Linfield, “Terahertz quantum cascade lasers with copper metal-metal waveguides operating up to 178 K,” *Optics Express* **16**(5), 3242–3248 (2008).
46. Y. Jin, L. Gao, J. Chen, C. Wu, J. L. Reno, and S. Kumar, “High power surface emitting terahertz laser with hybrid second-and fourth-order Bragg gratings,” *Nature Communications* **9**(1), 1–7 (2018).
47. Y. Zeng, B. Qiang, and Q. J. Wang, “Photonic engineering technology for the development of terahertz quantum cascade lasers,” *Advanced Optical Materials* **8**(3), 1900573 (2020).
48. B. S. Williams, S. Kumar, Q. Hu, and J. L. Reno, “Distributed-feedback terahertz quantum-cascade lasers with laterally corrugated metal waveguides,” *Optics Letters* **30**(21), 2909–2911 (2005).
49. C. Wu, Y. Jin, J. L. Reno, and S. Kumar, “Large static tuning of narrow-beam terahertz plasmonic lasers operating at 78 K,” *APL Photonics* **2**(2), 026101 (2017).
50. C. A. Curwen, J. L. Reno, and B. S. Williams, “Broadband continuous single-mode tuning of a short-cavity quantum-cascade VECSEL,” *Nature Photonics*, **13**(12), 855-859. (2019).
51. Q. Qin, J. L. Reno, and Q. Hu, “MEMS-based tunable terahertz wire-laser over 330 GHz,” *Optics letters* **36**(5), 692–694 (2011).
52. L. H. Li, L.Chen, J. R. Freeman, M. Salih, P. Dean, A. G. Davies, and E. H. Linfield, “Multi-Watt high-power THz frequency quantum cascade lasers,” *Electronics Letters* **53**(12), 799–800 (2017).
53. A. W. M. Lee, Q. Qin, S. Kumar, B. S. Williams, Q. Hu, and J. L. Reno, “High-power and high-temperature THz quantum-cascade lasers based on lens-coupled metal-metal waveguides,” *Optics letters* **32**(19), 2840–2842 (2007).
54. C. A. Curwen, J. L. Reno, and B. S. Williams, “Terahertz quantum cascade VECSEL with watt-level output power,” *Applied Physics Letters* **113**(1), 011104 (2018).

55. Y. Jin, J. L. Reno, and S. Kumar, "Phase-locked terahertz plasmonic laser array with 2 W output power in a single spectral mode," *Optica* **7**(6), 708–715 (2020).
56. X. Lü, E. Luna, L. Schrottke, K. Biermann, and H. T. Grahn, "Determination of the interface parameter in terahertz quantum-cascade laser structures based on transmission electron microscopy," *Appl. Phys. Lett.* **113**(17), 172101 (2018).
57. E. Luna, F. Ishikawa, B. Satpati, J. B. Rodriguez, E. Tournié, and A. Trampert, "Interface properties of (Ga, In)(N, As) and (Ga, In)(As, Sb) materials systems grown by molecular beam epitaxy," *J. Cryst. Growth* **311**(7), 1739–1744 (2009).
58. D. F. Nelson, R. C. Miller, and D. A. Kleinman, "Band nonparabolicity effects in semiconductor quantum wells," *Physical Review B* **35**(14), 7770 (1987).
59. P. Harrison and A. Valavanis, *Quantum Wells, Wires and Dots: Theoretical and Computational Physics of Semiconductor Nanostructures* (John Wiley & Sons, 2016).
60. R. Terazzi, "Transport in quantum cascade lasers," Ph.D. dissertation (ETH Zürich, 2011).
61. S.-H. Park, D. Ann, and Y.-T. Lee, "Screening effects on electron-longitudinal opticalphonon intersubband scattering in wide quantum well and comparison with experiment," *Jpn. J. Appl. Phys* **39**, 6601 (2000).
62. E. Dupont, S. Fatholouloumi, and H. C. Liu, "Simplified density-matrix model applied to three-well terahertz quantum cascade lasers," *Physical Review B* **81**(20), 205311 (2010).
63. B. Wen, C. Xu, S. Wang, K. Wang, M. C. Tam, Z. Wasilewski, and D. Ban, "Dual-lasing channel quantum cascade laser based on scattering-assisted injection design," *Opt. Express* **26**, 9194–9204 (2018).
64. S. Fatholouloumi, E. Dupont, C. W. I. Chan, Z. R. Wasilewski, S. R. Laframboise, D. Ban, A. Mátyás, Jirauschek, C. Q. Hu, and H. C. Liu, "Terahertz quantum cascade lasers operating up to  $\sim 200$  K with optimized oscillator strength and improved injection tunneling," *Opt. Express* **20**, 3866–3876 (2012).
65. T. Matsumae, Y. Kurashima, and H. Takagi, "Surface activated bonding of Ti/Au and Ti/Pt/Au films after vacuum annealing for MEMS packaging," *Microelectronic Engineering* **197**, 76–82 (2018).
66. W. E. Martinez, G. Gregori, and T. Mates, "Titanium diffusion in gold thin films," *Thin Solid Films* **518**(10), 2585–2591 (2010).
67. G. Liang, L. Tao, and Q. Wang, "Recent developments of terahertz quantum cascade lasers," *IEEE J. Sel. Top. Quantum Electron* **23**(4), 1–18 (2017).
68. M.A. Belkin and F. Capasso, "New frontiers in quantum cascade lasers: high performance room temperature terahertz sources," *Phys. Scripta* **90**(11), 118002 (2015).
69. L. Li, L. Chen, J. Zhu, J. Freeman, P. Dean, A. Valavanis, A.G. Davies, and E.H. Linfield, "Terahertz quantum cascade lasers with  $>1$  W output powers," *Electron. Lett.* **50**(4), 309–311 (2014).

70. M. Rösch, G. Scalari, M. Beck, and J. Faist, “Octave-spanning semiconductor laser,” *Nat. Photonics* **9**(1), 42–47 (2015).
71. Y. Yang, D. Burghoff, J. Reno, and Q. Hu, “Achieving comb formation over the entire lasing range of quantum cascade lasers,” *Op. Lett.* **42**(19), 3888 (2017).
72. S. Khanal, L. Gao, L. Zhao, J. L. Reno, and S. Kumar, “High-temperature operation of broadband bidirectional terahertz quantum-cascade lasers,” *Sci. Rep.* **6**, 32978 (2016).
73. S. Khanal, J. L. Reno, and S. Kumar, “2.1 THz quantum-cascade laser operating up to 144 K based on a scattering-assisted injection design,” *Opt. Express* **23**(15), 19689–19697 (2015).
74. H. Yasuda, “Intervalley scattering in terahertz quantum cascade lasers with GaSb and InGaSb wells,” *AIP Advances* **8**(2), 025125 (2018).
75. K. Leosson, J. R. Jensen, W. Langbein, and J. M. Hvam, “Exciton localization and interface roughness in growth-interrupted GaAs/AlAs quantum wells,” *Phys. Rev. B* **61**, 10322, (2000).
76. S. G. Razavipour, “Design, analysis, and characterization of indirectly-pumped terahertz quantum cascade laser,” Ph.D. dissertation (University of Waterloo, 2013).
77. S. V. Meshkov, “Tunneling of electrons from a two-dimensional channel into the bulk,” *Zh. Eksp. Teor. Fiz.* **91**(2252), 196 (1986).
78. H. Schneider and H. C. Liu, *Quantum well infrared photodetectors* (Springer, 2007), Chap. 4.
79. B. F. Levine, C. G. Bethea, G. Hasnain, V. O. Shen, E. Pelve, R. R. Abbott, and S. J. Hsieh, “High sensitivity low dark current 10  $\mu\text{m}$  GaAs quantum well infrared photodetectors,” *Appl. Phys. Lett.* **56** (9), 851–853 (1990).
80. J. S. Blakemore, “Semiconducting and other major properties of gallium arsenide,” *J. Appl. Phys.* **53**(10), R123–181 (1982).
81. R. Quay, C. Moglestue, V. Palankovski, and S. Selberherr, “A temperature dependent model for the saturation velocity in semiconductor materials,” *Mater. Sci. Semicond. Process* **3**(1–2), 149–155 (2000).
82. S. Ferre, S. G. Razavipour and D. Ban, "Terahertz Quantum Well Photodetectors with Improved Designs by Exploiting Many-Body Effects," *Appl. Phys. Lett.* **103**(081105), 1-4 (2013).
83. B.A. Burnett, and B.S. Williams, “Density matrix model for polarons in a terahertz quantum dot cascade laser,” *Physical Review B* **90**(15), 155309. (2014).
84. B.A. Burnett and B.S. Williams, “Origins of terahertz difference frequency susceptibility in midinfrared quantum cascade lasers,” *Physical Review Applied* **5**(3), 034013. (2016).
85. R. Terazzi, and J. Faist, “A density matrix model of transport and radiation in quantum cascade lasers,” *New journal of Physics* **12**(3), 033045. (2010).

86. C. Xu, S.G. Razavipour, Z. Wasilewski, and D. Ban, "An investigation on optimum ridge width and exposed side strips width of terahertz quantum cascade lasers with metal-metal waveguides," *Opt. Express* **26**, 31951–31959 (2013).
87. C. Walther, M. Fischer, G. Scalari, R. Terazzi, N. Hoyler, and J. Faist, "Quantum cascade lasers operating from 1.2 to 1.6 THz," *Appl. Phys. Lett* **91**(13), 131122 (2007).
88. S. Kumar, B. S. Williams, Q. Hu, and J. L. Reno, "1.9 THz quantum-cascade lasers with one-well injector," *Appl. Phys. Lett* **88**(12), 121123 (2006).
89. M. Wienold, B. Röben, X. Lü, G. Rozas, L. Schrottke, K. Biermann, and H. T. Grahn, "Frequency dependence of the maximum operating temperature for quantum-cascade lasers up to 5.4 THz," *Appl. Phys. Lett* **107**(20), 202101 (2015).
90. K. Ohtani, D. Turčinková, C. Bonzon, I. C. Benea-Chelmus, M. Beck, J. Faist, M. Justen, U. U. Graf, M. Mertens, and J. Stutzki, "High performance 4.7 THz GaAs quantum cascade lasers based on four quantum wells," *New J. Phys* **18**(12), 123004 (2016).
91. C. Sirtori, S. Barbieri, and R. Colombelli, "Wave engineering with THz quantum cascade lasers," *Nature Photon* **7**(9), 691–701 (2013).
92. A. Albo, Y. V. Flores, Q. Hu, and J. L. Reno, "Two-well terahertz quantum cascade lasers with suppressed carrier leakage," *Appl. Phys. Lett.* **111**(11), 111107 (2017).
93. S. Kumar and A. W. M. Lee, "Resonant-phonon terahertz quantum cascade lasers and video-rate terahertz imaging," *IEEE J. Sel. Topics Quantum Electron* **14**(2), 333–344 (2008).
94. G. Scalari, C. Walther, M. Fischer, R. Terazzi, H. Beere, D. Ritchie, and J. Faist, "THz and sub-THz quantum cascade lasers," *Laser Photon. Rev.* **3**(1-2), 45–105 (2009).
95. L. Gao, J. L. Reno, and S. Kumar, "Short barriers for lowering current-density in terahertz quantum cascade lasers," *Photonics* **7**(1), 7 (2020).
96. N. Sekine, and K. Hirakawa, Dispersive terahertz gain of a nonclassical oscillator: Bloch oscillation in semiconductor superlattices. *Phys. Rev. Lett.* **94**(5), 057408. (2005).
97. D. O. Winge, M. Franckić, and A. Wacker, "Superlattice gain in positive differential conductivity region." *AIP Advances* **6**(4), 045025. (2016).
98. B. Wen, C. Xu, S. Wang, S. M. Shazzad Rassel, M. Kaniselman, C. Deimert, Z. Wasilewski, and D. Ban, "Novel 4-well THz QCL with channels," in the *Infrared Terahertz Quantum Workshop* (2019).
99. A. Albo and Q. Hu, "Carrier leakage into the continuum in diagonal GaAs/Al<sub>0.15</sub>Ga<sub>0.85</sub>As terahertz quantum cascade lasers," *Appl. Phys. Lett.* **107**(24), 241101 (2015).

100. D. Ban, B. Wen, R. S. Dhar, S. G. Razavipour, C. Xu, X. Wang, Z. Wasilewski, and S. Dixon-Warren, “Electrical scanning probe microscopy of electronic and photonic devices: connecting internal mechanisms with external measures,” *Nanotechnology Reviews* 5(3), 279–300 (2016).
101. C. Worrall, J. Alton, M. Houghton, S. Barbieri, H. E. Beere, D. Ritchie, and C. Sirtori, “Continuous wave operation of a superlattice quantum cascade laser emitting at 2 thz,” *Opt. Express* 14, 171–181 (2006).
102. N. Lander Gower, S. Piperno, and A. Albo, “The Significance of Carrier Leakage for Stable Lasing in Split-Well Direct-Phonon Terahertz Quantum Cascade Lasers,” *Photonics* 2020, 7, 59 (2020).
103. Nextnano.NEGF model,  
[https://nextnanodocu.northeurope.cloudapp.azure.com/dokuwiki/doku.php?id=negf:the\\_nextnano\\_negf\\_software#copyright\\_information](https://nextnanodocu.northeurope.cloudapp.azure.com/dokuwiki/doku.php?id=negf:the_nextnano_negf_software#copyright_information).
104. A. Khalatpour, A. K. Paulsen, C. Deimert, Z. R. Wasilewski, and Q. Hu, “High-power portable terahertz laser systems,” *Nature Photonics* 15(1), 1–5 (2020).
105. Z. R. Wasilewski, M. M. Dion, D. J. Lockwood, P. Poole, R. W. Streater, and A. J. SpringThorpe, “Composition of AlGaAs,” *Journal of Applied Physics* 81(4), 1683–1694 (1997).
106. I. Vurgaftman, J. Á. Meyer, and L. Á. Ram-Mohan, “Band parameters for III-V compound semiconductors and their alloys,” *Journal of Applied Physics* 89(11), 5815–5875 (2001).
107. N. Sekine, and K. Hirakawa, Dispersive terahertz gain of a nonclassical oscillator: Bloch oscillation in semiconductor superlattices. *Phys. Rev. Lett.* 94(5), 057408. (2005).
108. D. O. Winge, M. Franckić, and A. Wacker, “Superlattice gain in positive differential conductivity region.” *AIP Advances* 6(4), 045025. (2016).

# Appendices

## Appendix A

This section exhibits the representative characterization results of THz QCLs that have not been discussed in the main chapters. In the early stage, some of the reported designs are repeated for calibrating growth and fabrication process. G312 and G405 structure is a repeating structure of design f30 from [19]. The LIV characterization result is shown in Fig. A-1. The devices from G405 wafer show a maximum operating temperature of 60K, and devices from G312 wafer show a maximum operating temperature of 100K. Both devices are fabricated into Au-Au waveguide.

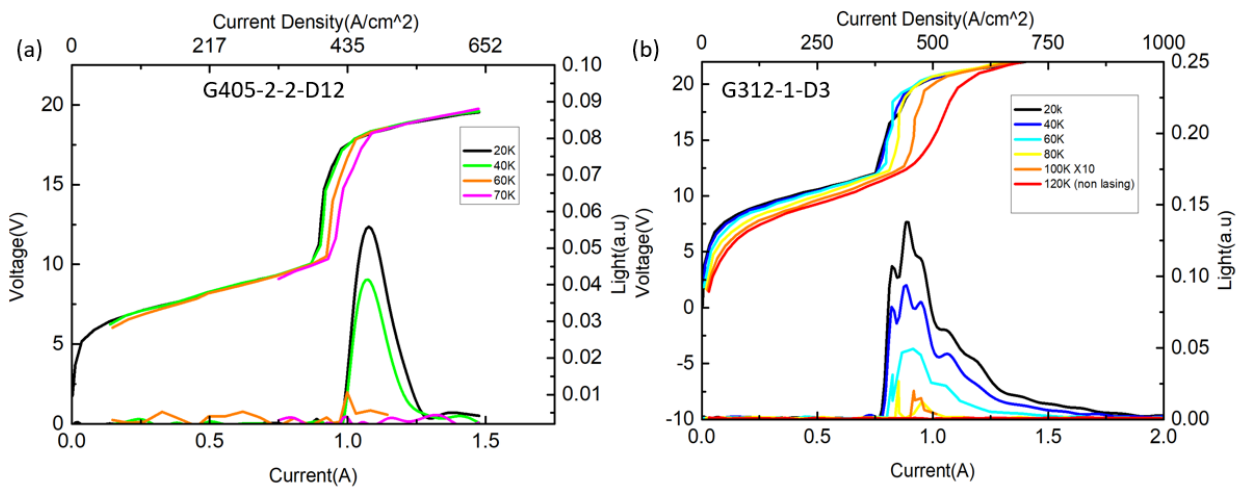


Fig. A-1. Representative LIV measurement of G405 (a) and G312 (b). G405 exhibits a maximum lasing temperature of 60K and G312 exhibits a maximum lasing temperature of 100K.

The spectra have been measured using the method described in section 3.3. The spectra of G405 measured at 20K is shown in Fig. A-2. The measured lasing frequency is from 4.5THz to 4.8THz. This suggests that the energy spacing between lasing states are likely larger than expected value in literature in [19]. The quantum structure difference may cause the different performance from the published data of f30 in [19].



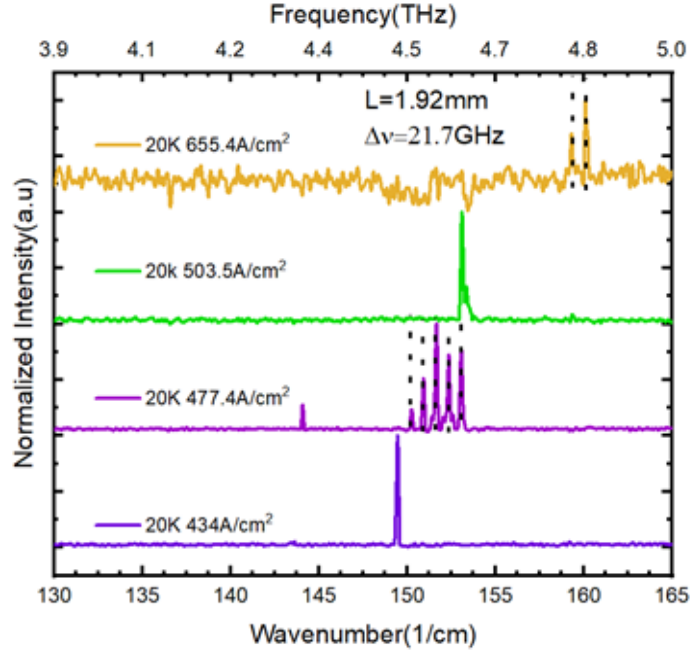


Fig. A-2. Measured spectra of G405-2-2-D12 at 20K. The lasing frequency is from ~4.5 THz to 4.8THz.

## Appendix B

This section lists the main parameters used in RE and DM simulation.

Al composition (x) dependent energy gap	$E_g=1.515+(1.36+0.22x)x$
Conduction band ratio	0.65
Velocity of sound in LA phonon scattering	$5117.0 \text{ m}^{-1}$
LA phonon deformation potential	7 eV
Interface roughness mean height	2.85–5 Å
Interface roughness correlation length	6–15 nm
Electron mass in $\text{Ga}_x\text{Al}_{1-x}\text{As}$	$(0.067+0.083x) m_0$
nonparabolicity coefficient	$\gamma = 4.9 \times 10^{-19} \text{ m}^2$
Escaped electron mobility	$\mu \approx 12000 \text{ cm}^2\text{Vs}^{-1}$
Saturated drift velocity	$v_{\text{sat}} \approx 0.72 \times 10^7 \text{ cm}\cdot\text{s}^{-1}$

Material database in nextnano. NEGF simulation

```
<!-- gallium arsenide -->
<Material>
  <Name>GaAs</Name>
  <CrystalStructure>Zincblende</CrystalStructure>
  <ConductionBandOffset Unit="eV">2.979</ConductionBandOffset>
  <!--<ValenceBandOffset Unit="eV">-0.80</ValenceBandOffset> --> <!-- Vurgaftman -->
  <ValenceBandOffset Unit="eV">1.346</ValenceBandOffset> <!-- S.-H. Wei, A. Zunger, APL 72, 2011
(1998) -->
  <!--<ValenceBandOffset Unit="eV">1.45966666</ValenceBandOffset>--> <!-- E_v,average + 1/3 Delta_so =
1.346 + 1/3 0.341 -->
  <BandGap Unit="eV">1.519</BandGap> <!-- Vurgaftman -->
  <BandGapAlpha Unit="eV/K">0.5405e-3</BandGapAlpha> <!-- Vurgaftman -->
  <BandGapBeta Unit="K">204</BandGapBeta> <!-- Vurgaftman -->
  <ElectronMass Unit="m0">0.067</ElectronMass> <!-- Vurgaftman -->
  <EpsStatic>12.93</EpsStatic>
  <EpsOptic>10.89</EpsOptic> <!-- http://www.ioffe.ru/SVA/NSM/Semicond/GaAs/basic.html -->
  <DeformationPotential Unit="eV">-7.17</DeformationPotential><!-- Vurgaftman -->
  <!--<DeformationPotential Unit="eV">-9.36</DeformationPotential> --> <!-- a_c(Gamma) = a_v +
a_gap(Gamma) = -1.21 - 8.15 = -9.36 (S.-H. Wei, A. Zunger, PRB 60, 5404 (1999)) -->
  <ValenceDefPotHydro Unit="eV">1.16</ValenceDefPotHydro>
  <ValenceDefPotUniaxial_b Unit="eV">-2.0</ValenceDefPotUniaxial_b>
<MaterialDensity Unit="kg/m^3">5.316e3</MaterialDensity>
  <VelocityOfSound Unit="m/s">4.73e3</VelocityOfSound>
  <LOPhononEnergy Unit="eV">36e-3</LOPhononEnergy> <!--
http://www.ioffe.ru/SVA/NSM/Semicond/GaAs/optic.html -->
  <LOPhononWidth Unit="eV">3e-3</LOPhononWidth>
  <TOPhononEnergy Unit="eV">33.86e-3</TOPhononEnergy>
  <AcousticPhononEnergy Unit="eV">5e-3</AcousticPhononEnergy>
  <Ep Unit="eV">28.8</Ep> <!-- Vurgaftman -->
  <S>-2.88</S> <!-- S = 1 + 2F = 1 + 2 (-1.94) = -2.88 [Vurgaftman] -->
  <DeltaSO Unit="eV">0.341</DeltaSO> <!-- Vurgaftman -->
  <Lattice_a Unit="nm">0.565325</Lattice_a> <!-- Vurgaftman -->
  <Elastic_c11 Unit="GPa">122.1</Elastic_c11> <!-- Vurgaftman -->
  <Elastic_c12 Unit="GPa">56.6</Elastic_c12> <!-- Vurgaftman -->
  <Elastic_c44 Unit="GPa">60.0</Elastic_c44> <!-- Vurgaftman -->
  <Piezo_e14 Unit="C/m^2">-0.160</Piezo_e14> <!-- experimental value S. Gironcoli et al., PRL 62(24), 2853
(1989) -->
</Material>
<!-- aluminium arsenide -->
<Material>
  <Name>AlAs</Name>
  <CrystalStructure>Zincblende</CrystalStructure>
  <ConductionBandOffset Unit="eV">4.049</ConductionBandOffset>
  <!--<ValenceBandOffset Unit="eV">-1.33</ValenceBandOffset> --> <!-- Vurgaftman -->
  <ValenceBandOffset Unit="eV">0.857</ValenceBandOffset> <!-- S.-H. Wei, A. Zunger, APL 72, 2011
(1998) -->
  <!--<ValenceBandOffset Unit="eV">0.95033333</ValenceBandOffset> --> <!-- E_v,average + 1/3 Delta_so =
0.857 + 1/3 0.28 -->
  <BandGap Unit="eV">3.099</BandGap> <!-- Vurgaftman -->
  <BandGapAlpha Unit="eV/K">0.885e-3</BandGapAlpha> <!-- Vurgaftman -->
  <BandGapBeta Unit="K">530</BandGapBeta> <!-- Vurgaftman -->
  <ElectronMass Unit="m0">0.15</ElectronMass> <!-- Vurgaftman -->
  <EpsStatic>10.064</EpsStatic>
  <EpsOptic>8.162</EpsOptic>
  <DeformationPotential Unit="eV">-5.64</DeformationPotential> <!-- Vurgaftman -->
```

```

<!--<DeformationPotential Unit="eV">-7.40</DeformationPotential--> <!-- a_c(Gamma) = a_v +
a_gap(Gamma) = 1.53 - 8.93 = -7.40 (S.-H. Wei, A. Zunger, PRB 60, 5404 (1999)) -->
<ValenceDefPotHydro Unit="eV">2.47</ValenceDefPotHydro>
<ValenceDefPotUniaxial_b Unit="eV">-2.3</ValenceDefPotUniaxial_b>
<MaterialDensity Unit="kg/m^3">3.72e3</MaterialDensity>
<VelocityOfSound Unit="m/s">6.4e3</VelocityOfSound>
<LOPhononEnergy Unit="eV">50e-3</LOPhononEnergy> <!-- J. Piprek (low-temperature optical phonon
energy) -->
<LOPhononWidth Unit="eV">3e-3</LOPhononWidth>
<AcousticPhononEnergy Unit="eV">5e-3</AcousticPhononEnergy> <!-- Peter Greck had 2e-3? Reference? -->
<Ep Unit="eV">21.1</Ep> <!-- Vurgaftman -->
<S>0.04</S> <!-- S = 1 + 2F = 1 + 2 (-0.48) = 0.04 [Vurgaftman] -->
<DeltaSO Unit="eV">0.28</DeltaSO> <!-- Vurgaftman -->
<Lattice_a Unit="nm">0.56611</Lattice_a> <!-- Vurgaftman -->
<Elastic_c11 Unit="GPa">125.0</Elastic_c11> <!-- Vurgaftman -->
<Elastic_c12 Unit="GPa">53.4</Elastic_c12> <!-- Vurgaftman -->
<Elastic_c44 Unit="GPa">54.2</Elastic_c44> <!-- Vurgaftman -->
<Piezo_e14 Unit="C/m^2">-0.015</Piezo_e14> <!-- calculated by S. Gironcoli et al., PRL 62(24), 2853 (1989) -
->
</Material>
<!-- aluminium gallium arsenide -->
<Material>
<Name>Al(x)Ga(1-x)As</Name>
<Alloy>AlAs(x)</Alloy>
<Alloy>GaAs(1-x)</Alloy>
<CrystalStructure>Zincblende</CrystalStructure>
<ConductionBandOffset Unit="eV">0.318</ConductionBandOffset> <!-- To match a band offset of 0.120 eV
for GaAs/Al(0.15)Ga(0.85)As -->
<ValenceBandOffset Unit="eV">0</ValenceBandOffset>
<BandGap Unit="eV">-0.127</BandGap>
<BandGap_CUBIC Unit="eV">1.310</BandGap_CUBIC> <!-- Cubic bowing for AlGaAs (see Vurgaftman):
BandGap = (1-x) BandGap(GaAs) + x BandGap(AlAs) - x(1-x)(BandGap(Bowing) + x*BandGap_CUBIC) -->
<BandGapAlpha Unit="eV/K">0</BandGapAlpha>
<BandGapBeta Unit="K">0</BandGapBeta>
<ElectronMass Unit="m0">0</ElectronMass>
<DeltaSO Unit="eV">0</DeltaSO> <!-- I. Vurgaftman, JAP 89, 5815 (2001) -->
<EpsStatic>0</EpsStatic>
<EpsOptic>0</EpsOptic>
<DeformationPotential Unit="eV">0</DeformationPotential>
<MaterialDensity Unit="kg/m^3">0</MaterialDensity>
<VelocityOfSound Unit="m/s">0</VelocityOfSound>
<LOPhononEnergy Unit="eV">0</LOPhononEnergy>
<LOPhononWidth Unit="eV">0</LOPhononWidth>
<AcousticPhononEnergy Unit="eV">0</AcousticPhononEnergy>
<Lattice_a Unit="nm">0</Lattice_a>
<Elastic_c11 Unit="GPa">0</Elastic_c11>
<Elastic_c12 Unit="GPa">0</Elastic_c12>
<Elastic_c44 Unit="GPa">0</Elastic_c44>
<Piezo_e14 Unit="C/m^2">0</Piezo_e14>
</Material>

```